The Dissertation Committee for Christopher Eugene Crabtree
Certifies that this is the approved version of the following dissertation:

Ballooning Stability of the Earth's Magnetosphere

Committee:

C. Wendell Horton, Jr., Supervisor

H.V. Wong

J.W. Van Dam

E. Powers

R. Hazeltine

L. Reichl

Ballooning Stability of the Earth's Magnetosphere

by

Christopher Eugene Crabtree, B.A.

DISSERTATION

Presented to the Faculty of the Graduate School of

The University of Texas at Austin

in Partial Fulfillment

of the Requirements

for the Degree of

DOCTOR OF PHILOSOPHY

THE UNIVERSITY OF TEXAS AT AUSTIN

May 2003

To Kristi.

Acknowledgments

I have found that writing a dissertation is not an individual accomplishment. It is very much a team effort. Consequently, there are countless contributions made by many people. First, I would like to thank my advisor Wendell Horton for his patient guidance and leadership in this endeavour. Secondly, I would like to thank all of my committee members for their support and guidance in reviewing and improving this dissertation. I would like to thank Vernon Wong for countless hours on the black-board where I learned many things. I would like to thank Jim Van Dam for his thoroughness, clarity and excellent advice. I would like to thank my many friends and colleagues: Enrico Rossi for many valuable discussions on physics and other things, Andrew Cole for being an admirable officemate and friend, Ping Zhu for providing discussions on plasma physics, Bob Weigel for helping me to understand space physics, Alex Arefiev for providing solid physics knowledge and a workmanlike attitude, and Trevor Garner for helping me to understand space physics. I would also like to thank the many people that made my life at the IFS so easy: Jim Dibble who kept my computer running and backed up, Suzy Mitchell for being the LaTeX Goddess, Saralyn Stewart for taking care of many administrative nightmares and for providing valuable advice, Leslie Harper for her extraordinary efficiency, helpfulness and cheerfulness, and James Halligan for his efficient help with all things "paper-work". I would also like to thank the people at TACC, especially Dean Nobles and Chuana Guoan, for providing

help with the parallel coding. I would also like to thank Norma Kotz for her tireless efforts to guide me through the administrative machines. I would like to think my family and friends for enduring my constant business and general level of stress. I would like to thank my parents for their support, guidance and love through this long process. Most importantly I would like to thank my wife Kristi-for everything.

Ballooning Stability of the Earth's Magnetosphere

Publication No. _____

Christopher Eugene Crabtree, Ph.D.
The University of Texas at Austin, 2003

Supervisor: C. Wendell Horton, Jr.

A substorm is a frequently occurring ordered sequence of global energetic events in the magnetosphere and ionosphere. The most obvious manifestation of a substorm is auroral brightening, due to an increase in the number of electrons precipitating into the ionosphere. During a substorm, quiet auroral arcs suddenly intensify. Electrojets are produced in the ionosphere, and magnetic disturbances are observed on the surface of the Earth with magnetometers. Plasma instabilities in the inner magnetosphere, in the region where the nightside auroral magnetic field lines cross the magnetic equator, are a candidate to explain the triggering mechanism of these substorms. This region is at a distance of about ten times the radius of the Earth in the midnight sector. In this region the plasma thermal pressure gradient reaches its highest value and the plasma is susceptible to unstable motions.

We have investigated the linear stability of the inner magnetosphere against fast interchange-ballooning dynamics as a possible candidate for the

magnetospheric substorm trigger, using different models of the quiet-time magnetospheric magnetic field. The region most likely unstable to these dynamics is found to map to the lower edge of stable auroral arcs. We then extend the ideal fast-MHD analysis to include local gyrokinetic effects such as wave-particle resonances, in order to explain the low-frequency oscillations that are observed prior to and during the onset of substorms. We generalize the local kinetic analysis to include non-local orbital effects due to the mirroring motion of the particles between the Earth's magnetic poles. We developed a new numerical technique to solve the resulting non-linear integral eigenvalue equations. We also investigated a magnetic compressional trapped particle instability in detail and obtained the conditions for instability as well as the growth rates and mode structures. We invoke this low-frequency drift wave instability to explain compressional Pi2 oscillations observed throughout the substorm onset period and argue that they play an important role in substorm dynamics.

Table of Contents

List of Tables

List of Figures

Chapter 1

Introduction

Simply stated, magnetospheric substorms are disruptions of the equilibrium nature of the magnetosphere. Substorms lead to global reconfiguration of the complex system that consists of the Earth's geomagnetic field, plasma components, and the plasma currents. The first signatures of a substorm are observed in the ionosphere which is coupled to the magnetosphere by field aligned currents.

A magnetospheric substorm has many important observational features. A substorm is most often characterized by an intensification and development of the aurora around both North and South poles. The westward electrojet is a current, formed during substorms, that drives the development of the aurora and produces magnetic perturbations on the ground that serve as a fundamental diagnostic for magnetospheric substorms. The aurora is caused by charged particles, mainly electrons, following geomagnetic field lines and colliding with oxygen atoms in the upper atmosphere. Thus, the intensification of the aurora observed during a substorm is a symptom of processes occurring higher in the magnetosphere. With the advent of satellite technology, these processes have been extensively observed. However, due in part to the diffi-

culty of making satellite observations, the cause and precise development of a magnetospheric substorm is still an unsolved problem and thus remains an exciting topic of research in space physics.

Understanding space-weather events, such as magnetospheric substorms, is important scientifically and valuable to civilization for many reasons. In modern times civilization has relied heavily on advanced satellite communications. High energy electrons that accompany magnetospheric storms and substorms have proven to be particularly devastating to satellite electronics. Thus a high priority for space physics has been to predict when such events are likely to occur. Many ground based communications rely on reflecting radio waves off of the ionosphere, and magnetospheric storms and substorms can change the properties necessary for reflection. Also, because of the large currents flowing in the ionosphere during disruptions large currents can be induced to flow along conductors in the ground such as power lines, telephone lines, and petroleum pipelines [136]. These induced currents can lead to failures of transformers and disruption of power services as well as a reduction of the safety of pipelines. Recently, researchers at MIT, Columbia university and others have proposed magnetic dipole confinement devices for the purpose of controlled fusion. Understanding the principle issues involved in substorms is critical for controlling confinement in these new devices. Besides the practical benefits of understanding magnetospheric substorms there is the intrinsic scientific goal of understanding such a complex system comprised of an interesting plasma where vital assumptions needed for MHD to be appropriate are

violated.

Various plasma instabilities are thought to play major roles throughout the different stages of the development of the substorm. For example, ballooning or interchange modes, primarily an MHD instability, have long been considered as a possible mechanism for the triggering of the onset of the substorm and thus have been considered by many authors. However, the validity of the MHD equations under the conditions necessary to accurately describe the relevant portion of the magnetosphere is doubtful. Consequently more accurate descriptions of the plasma such as the gyrokinetic approximation have recently been used to investigate the kinetic effects on ballooning/interchange and other modes. In this dissertation the stability of various models of the magnetosphere is tested under different levels of approximation such as the MHD approximation and the gyrokinetic approximation. The results of these studies are intended to shed light on the mechanisms involved in the initiation and development of magnetospheric substorms.

This first chapter introduces the magnetic field models used in all preceding calculations. In Section 1.1 the coordinate systems used to describe the magnetic field models are described. In Section 1.2 the commonly used empirical magnetic field model of Tsyganenko and coworkers is discussed and the configuration of the Earth's magnetosphere is discussed in a global sense. Also, the major current systems and how they are modeled are discussed individually. In Section 1.2.1 the ring current is discussed in some detail as well as a calculation of its inductance under different geomagnetic activity levels. In

Section 1.2.2 the magnetotail current is discussed and computed in the noon-midnight meridian. Finally, In Section 1.2.3 the magnetopause and Birkeland currents are discussed. In Section 1.3 the magnetic field models used in this dissertation are discussed in the context of an MHD equilibrium. Also, the plasma pressure is computed using the Tsyganenko magnetic field model and compared with satellite data. In Section 1.4 a simple 2D equilibrium model called the constant current model (CCM) is discussed and compared with the more realistic empirically based models of Tsyganenko. Finally, in Section 1.5 an outline of the remainder of the dissertation is presented.

1.1 Coordinate systems

Many coordinate systems are commonly employed in the study of the Earth's magnetosphere. Most coordinate systems have the center of the Earth as the origin. Spherical coordinates are common in ionospheric work since latitude and longitude are important variables. Various Cartesian systems are also used, with the particular choice depending on whether one is interested in understanding the Sun's influence on the Earth (GSE coordinates), or in studying interior portions of the magnetosphere (GSM coordinates). In this work we will use only one coordinate system (GSM) for studying the magnetosphere at large, although we will employ another system (local flux-tube coordinates) for examining a small localized region of the magnetosphere.

The Geocentric Solar Ecliptic (GSE) coordinate system is depicted in Fig. 1.1. The x-axis lies along the Earth-Sun line, with the positive x-axis

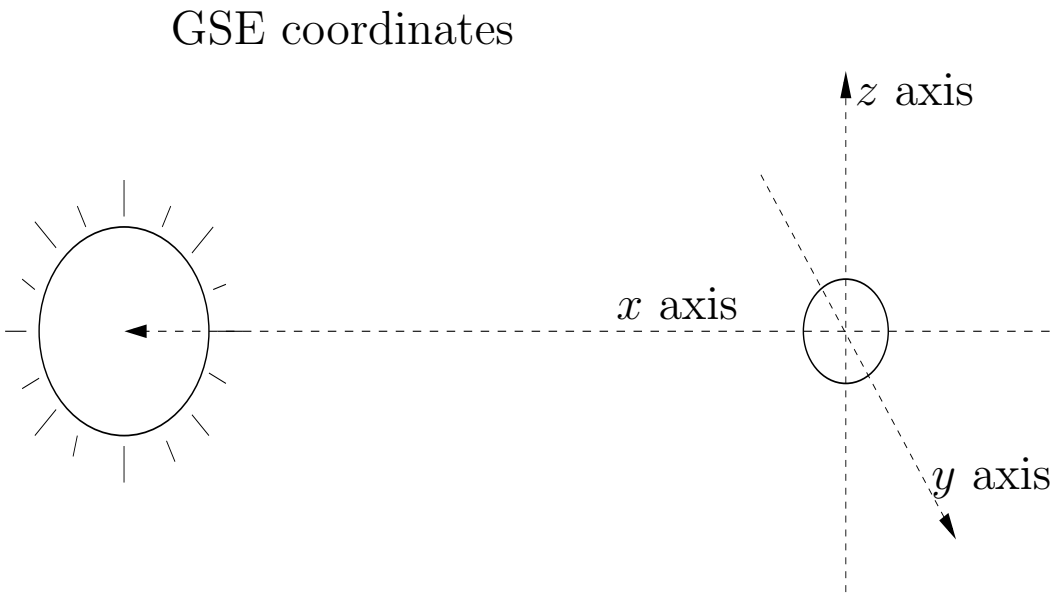

Figure 1.1: Geocentric Solar Ecliptic (GSE) coordinates. The Earth is at the origin of this coordinate system.

pointing towards the Sun and the origin at the center of the Earth. The z-axis is perpendicular to the ecliptic plane defined by the Earth's motion about the Sun, with the positive z-axis pointing towards North. The y-axis is defined such that the coordinate system is right-handed and Cartesian.

Magnetospheric physics commonly employs the Geocentric Solar Magnetospheric (GSM) coordinate system. Most magnetic field models, plasma codes, and satellite data are reported in GSM coordinates. The most common unit of distance in GSM coordinates is the radius of the Earth (R_E), which is approximately $6.37 \cdot 10^6$ m. GSM coordinates are Cartesian, with the x-axis lying along the Earth-Sun line (the positive x-axis pointing towards the Sun) and the origin at the center of the Earth. The z-axis is the projection of the

Earth's magnetic dipole axis onto the y-z plane of the GSE system. Figure 1.2 depicts the GSM coordinate system. Hapgood [78] gives a thorough description of the various coordinate systems used in space physics, as well as the formulas to transform from one coordinate system to another.

At times it will be convenient to follow the observational literature and refer to directions as East (dawn-ward) or West (dusk-ward). To be clear, these directions refer to the points on a compass, and in reference to the GSM coordinates, a vector that is pointing to the East is pointing in the negative $\hat{\mathbf{y}}$ direction and a vector pointing towards the West is pointing in the positive $\hat{\mathbf{y}}$ direction. These designations are used in almost all accounts of satellite and ground-based observations.

Observations are also often given in terms of magnetic local time (MLT). This can be understood as fixing midnight at the negative $\hat{\mathbf{x}}$ axis and noon at the positive $\hat{\mathbf{x}}$ axis, with twelve hours between them. MLT is commonly used when describing an auroral form.

Many simplifications in theoretical analysis can be made by employing a right-handed curvilinear coordinate system (Ψ, y, s), where Ψ is the magnetic flux function, y is the normal GSM coordinate, and s is the suitably normalized distance along a field line. In this coordinate system the magnetic field is expressed as $\mathbf{B} = \nabla\Psi \times \nabla y$. The contravariant system of basis vectors is

$$\mathbf{e}_\Psi = \nabla\Psi \qquad \mathbf{e}_y = \nabla y \qquad \mathbf{e}_s = \nabla s \tag{1.1}$$

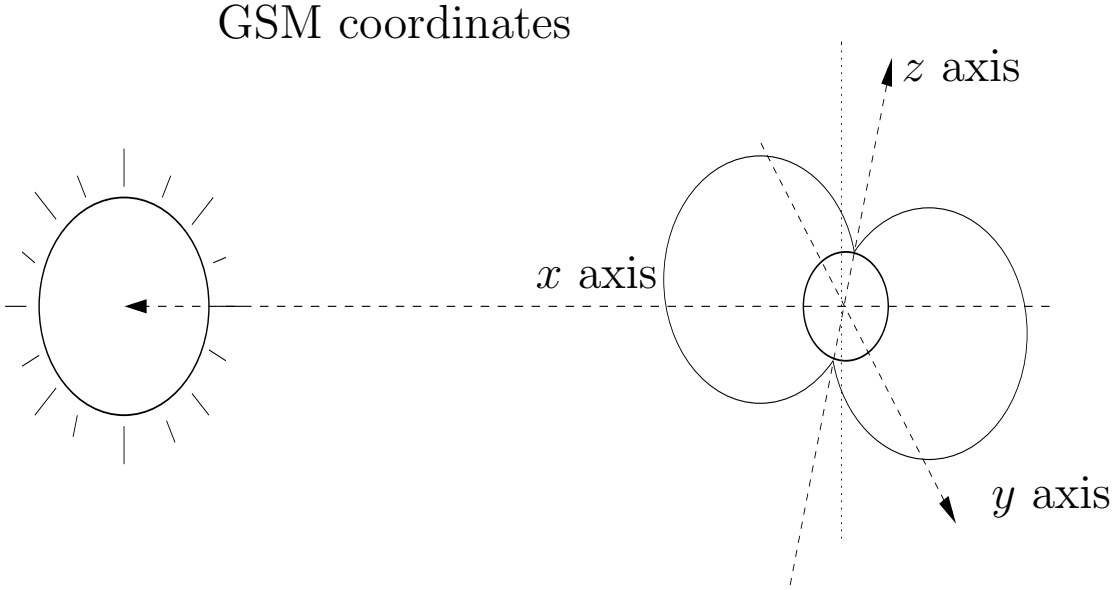

Figure 1.2: Geocentric Solar Magnetic (GSM) coordinates. The Earth's dipolar magnetic field is depicted with the two loops. The vertical dotted line represents the z-axis from the GSE coordinate system. The dashed lines represent the axes in the GSM system.

and the covariant basis is defined as

$$\mathbf{e}^{\Psi} = \frac{\partial \mathbf{r}}{\partial \Psi} \qquad \mathbf{e}^{y} = \frac{\partial \mathbf{r}}{\partial y} \qquad \mathbf{e}^{s} = \frac{\partial \mathbf{r}}{\partial s} = \widehat{\mathbf{b}} \tag{1.2}$$

where in the last equality of Eq. (1.2) we used the facts that $\mathbf{B}$ is tangent to the curve given by $(x(s), y(s), z(s))$ and that $\hat{\mathbf{b}}$ is a unit vector, i.e. $\hat{\mathbf{b}} = \mathbf{B}/B$. To convert any vector from a covariant to a contravariant representation we can use the following identity

$$\mathbf{e}^{\Psi} = \frac{1}{J}\left(\mathbf{e}_y \times \mathbf{e}_s\right) \tag{1.3}$$

and cyclic permutations thereof, where J is the Jacobian. With our representation of the magnetic field and the formula for the covariant representation of the contravariant vector $\mathbf{e}^s$, it is easy to determine that the Jacobian is just the magnitude of the magnetic field, $J = B$.

1.2 Tsyganenko's Magnetic Field Model

Tsyganenko and coworkers have developed a series of increasingly sophisticated empirical magnetic field models that have become the community standard for understanding the three-dimensional structure of the Earth's magnetospheric magnetic field. His models are based on flexible analytical functions that model the major magnetospheric current systems. Each function that models the structure of a current system has parameters that can be used for fitting to satellite measurements of the magnetic field. His models use tens of thousands of vector magnetic field measurements, sorted into bins

according to well defined measures of the solar wind and geomagnetic activity, to determine the parameters of the global model. Thus for any solar wind condition or geomagnetic activity level, the model produces different magnetic field configurations.

The early Tsyganenko models [184, 189] were based on just three major current systems: 1) the ring current (to be discussed in Section 1.2.1), 2) the tail current (to be discussed in Section 1.2.2), and 3) the magnetopause currents (to be discussed in Section 1.2.3). Also these models only used a single parameter, K_p, to describe the geomagnetic activity level. The K_p index is not a simple measurable parameter; rather it is based on a weighted average of magnetic field levels at various stations around the Earth. In these measurements, the diurnal and seasonal variation of the magnetic components are removed and an index of the levels is created. Kivelson and Russell [5] explain in detail how a K_p index is computed.

Later Tsyganenko models [185, 188] included region 1 and 2 Birkeland currents and more detailed representations of the magnetopause currents, including shielding currents at the magnetopause generated by currents inside of the magnetopause. Also, in these newer models there are four parameters to describe the geomagnetic disturbance level. Three of these parameters describe the state of the solar wind: P_{dyn} is the dynamical pressure of the solar wind, measured in units of nano-Pascals; B_y^{IMF} is the magnitude of the $\hat{\mathbf{y}}$ component (in GSE coordinates) of the interplanetary magnetic field (IMF) carried with the solar wind, measured in nano-Teslas; and B_z^{IMF} is the magnitude of the

$\hat{\mathbf{z}}$ component (GSE coordinates) of the IMF, measured in nano-Teslas. The fourth parameter is a measure of the strength of the ring current and is called the DST index (disturbance storm time). The DST index, like the K_p index, is an average over the Earth; however, in this case, the average is for a physical measurement and not an index. The measurement used in the average DST index is the depression of the Earth's internally generated dipole field due to the currents flowing in the ring current and it is measured in nano-Teslas. More will be said about the ring current and the DST index later in this chapter. In all of the Tsyganenko models the Earth's internal currents are not modeled, and for all of our calculations performed with this model we have included a three-dimensional magnetic dipole field with the value for the Earth's dipole moment $M_E = B_0 R_E^3 = 8 \cdot 10^{15} \mathrm{T} \cdot \mathrm{m}^3$.

The Tsyganenko series of magnetic field models serve as the primary tool for understanding the three-dimensional structure of the magnetosphere. However, in using this model we should keep in mind several factors [174]. First, because of finite coverage by satellites, there are regions in the magnetosphere where very few observations have been made. Thus, these regions will have a small weight in the fitting procedure, which may lead to inaccurate results in these sparsely covered regions. For this reason these models are typically not valid tail-ward beyond -60 R_E. Second, the major features of the magnetosphere are specifically built into the model (such as the ring current and tail current). The functions used to represent these systems may lead to systematic errors. Conversely, other features, such as the Birkeland

currents, which are very thin current sheets, are represented through polynomial expansions, and thus these features may be washed out. Third, only the magnetic field data is given. No attempt is given to provide important plasma parameters such as density, temperature, or pressure. More will be said on this in Section 1.3. Finally, because the magnetic field data is sorted into a finite number of bins and then averaged in a sense, the model cannot accurately represent certain dynamic configurations. The sharp features that are seen during dynamic events, *i.e.,* substorm onset, will be averaged out of the database. This is an especially important point, as the time that is of greatest interest in this work, namely the point immediately preceding substorm onset, will not be accurately represented by this model. Nonetheless, the Tsyganenko magnetic field model is the best model currently available.

1.2.1 Ring Current

The ring current is a major current system that encircles the Earth and lies primarily in the equatorial plane. This current is caused by magnetic field gradient drift and curvature drift, which cause positively charged particles to drift towards the West and negatively charged particles to the East. The direction of the circular flow of current is such that the $\mathbf{J} \times \mathbf{B}$ force of the ring current with the Earth's internal dipole field tends to hold the current close to the Earth. Thus, during times of ring current intensification, this current system moves Earthward. The magnetic field produced by this ring current is such that it opposes the internal magnetic field of the Earth. The primary

measure of the ring current is given by the DST index, which is an averaged value of the depression of the geomagnetic field.

The ring current stores a significant portion of the energy in the magnetosphere, and therefore the dynamics of this energy storage is important to the dynamics of the magnetosphere. In this section we show that the constant inductance approximation that allows the ring current, and thus the magnetic field at the surface of the Earth (as measured by the DST index), to be related to the stored magnetic energy is valid for the databases used in the early Tsyganenko models.

Tsyganenko's 1987 model gives an analytic expression for the ring current vector potential, A_ϕ, in cylindrical coordinates. In this cylindrical coordinate system the origin is at the center of the Earth, the z-axis is the same as in the GSM coordinate system, $\rho = \sqrt{X_{\rm GSM}^2 + Y_{\rm GSM}^2}$ is the radial distance, and ϕ is the angle about the z axis and corresponds to the longitude. This model for A_ϕ produces a well-localized current distribution centered at ρ_0 (a parameter of the model) and decreasing as $(\rho_0/\rho)^6$ for $\rho \gg \rho_0$. Clearly the model breaks down for $r = (\rho^2 + z^2)^{1/2} \leq R_E$ and it neglects the noon-midnight asymmetry. The model is useful, however, for certain calculations due to its simplicity. Tsyganenko's 1987 model of the ring current is given by

$$A_\phi = \frac{C\rho}{(\rho^2 + z^2 + 4\rho_0^2)^{\frac{3}{2}}}. \tag{1.4}$$

Tsyganenko's parameterization of the constants C and ρ_0 as a function of K_p are given in Table 1.1. In Eq. (1.10) below we show that the C and ρ_0 parame-

K_p	$C\ [T \cdot m^3]$	$\rho_0\ [m]$
0	$-2.9642 \cdot 10^{15}$	$3.3038 \cdot 10^7$
1	$-3.7375 \cdot 10^{15}$	$3.3210 \cdot 10^7$
2	$-3.7860 \cdot 10^{15}$	$3.1112 \cdot 10^7$
3	$-4.8507 \cdot 10^{15}$	$3.1265 \cdot 10^7$
4	$-4.1513 \cdot 10^{15}$	$2.8790 \cdot 10^7$
5	$-7.8066 \cdot 10^{15}$	$2.9709 \cdot 10^7$
6	$-6.4975 \cdot 10^{15}$	$2.8212 \cdot 10^7$
7	$-6.7040 \cdot 10^{15}$	$2.7362 \cdot 10^7$
8	$-6.8045 \cdot 10^{15}$	$2.6512 \cdot 10^7$
9	$-6.8111 \cdot 10^{15}$	$2.5662 \cdot 10^7$

Table 1.1: Values of constants relevant to the ring current, taken from Tsyganenko 1987 [184] and converted to the notation used in Tsyganenko 1982 [189]. For K_p greater than 5, the values of the constants were obtained through linear interpolation; these interpolated results are shown in italics.

ters determine the total ring current through $\mu_0 I_{RC} = C/\rho_0^2$. Parameter values were given through a maximum value of $K_p = 5$ in Tsyganenko 1987 [184]; for this work we extended these values using a linear fit through a maximum value of $K_p = 9$. In Table 1.1 the extrapolated parameter values are indicated by italics. From the definition of the vector potential, we can calculate the magnetic field according to $\mathbf{B} = \nabla \times A_\phi \hat{\boldsymbol{\phi}} = \nabla (\rho A_\phi) \times \nabla \phi$. Using Eq. (1.4) yields

$$B_\rho = -\frac{\partial A_\phi}{\partial z} = \frac{3C\rho z}{(\rho^2 + z^2 + 4\rho_0^2)^{\frac{5}{2}}} \tag{1.5}$$

$$B_z = \frac{1}{\rho}\frac{\partial}{\partial \rho}(\rho A_\phi) = \frac{C(-\rho^2 + 2z^2 + 8\rho_0^2)}{(\rho^2 + z^2 + 4\rho_0^2)^{\frac{5}{2}}}. \tag{1.6}$$

One can estimate what a measured DST might be by taking $B_z(\rho = 0, z = 0)$, or $B_z(\rho = 1R_E, z = 0)$. Figure 1.3 shows these fields as a function of

K_P. To within the difference shown in this figure, we see that an adequate approximation is DST$\simeq C/(4\rho_0^3)$.

The energy in the magnetic field is proportional to the volume integral of $\mathbf{B}^2$, where

$$\mathbf{B}^2 = \frac{C^2\rho^2 z^2 + C^2\left(-\rho^2 + 2z^2 + 8\rho_0^2\right)^2}{\left(\rho^2 + z^2 + 4\rho_0^2\right)^5}. \tag{1.7}$$

Figure 1.4 shows the magnetic energy density computed for the model ring current system for several K_p values, as well as a reference magnetic energy density typical for a magnetotail field. For large ρ the magnetic energy density of the ring current drops off as $(\rho_0/\rho)^6$, just as that for a dipole field would. For a typical geotail magnetic field value of $B = 10$ nT, the crossover point between the ring current and geotail current-dominated fields is at $x = -5\ R_E$ to -9 R_E, which can be seen in Fig. 1.4. For quiet times the ring current appears almost indistinguishable from the magnetotail current since the energy densities are comparable. Note that for the purposes of computing inductances, we are only interested in the energy density of the current systems in the magnetosphere; thus it is appropriate here to ignore the energy density of the Earth's dipole field.

The current distribution of the ring current may be obtained from the vector potential of Eq. (1.4), by $\mathbf{J} = -\frac{1}{\mu_0}\nabla^2\mathbf{A} + \frac{1}{\mu_0}\nabla(\nabla\cdot\mathbf{A})$. The ring current vector potential is divergence free, $\nabla\cdot\mathbf{A} = 0$, and moreover $\mathbf{A} = A_\phi(\rho, z)\hat{\phi}$, so the current density is

$$J_\phi = -\frac{1}{\mu_0}\left[\frac{1}{\rho}\frac{\partial}{\partial\rho}\left(\rho\frac{\partial A_\phi}{\partial\rho}\right) + \frac{\partial^2 A_\phi}{\partial z^2}\right] \tag{1.8}$$

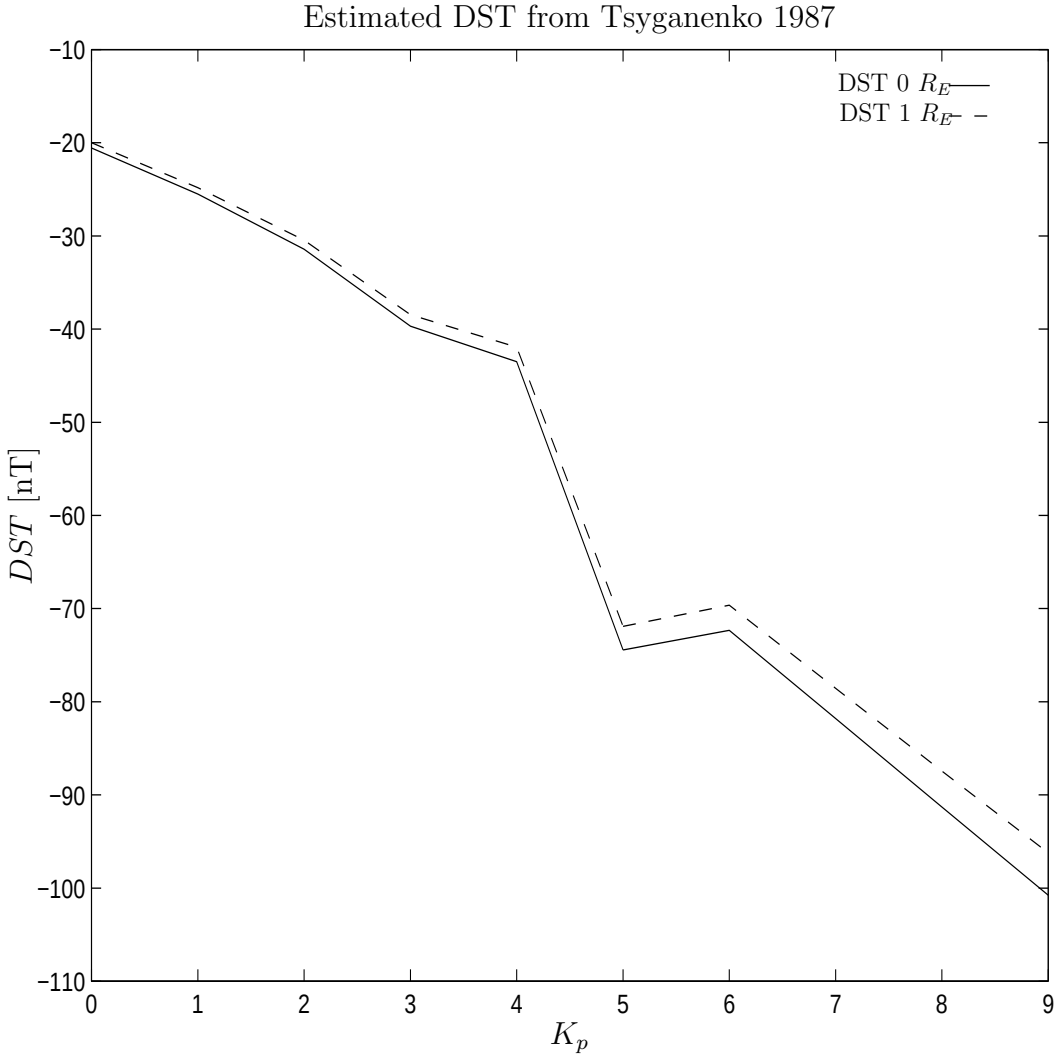

Figure 1.3: The DST index estimated from Tsyganenko's 1987 [184] model by computing the magnetic field at the center of the Earth, DST $= C/(4\rho_0^3)$ (solid line) and at the surface of the Earth (dashed line). For $K_p > 5$ the interpolated model parameters were used.

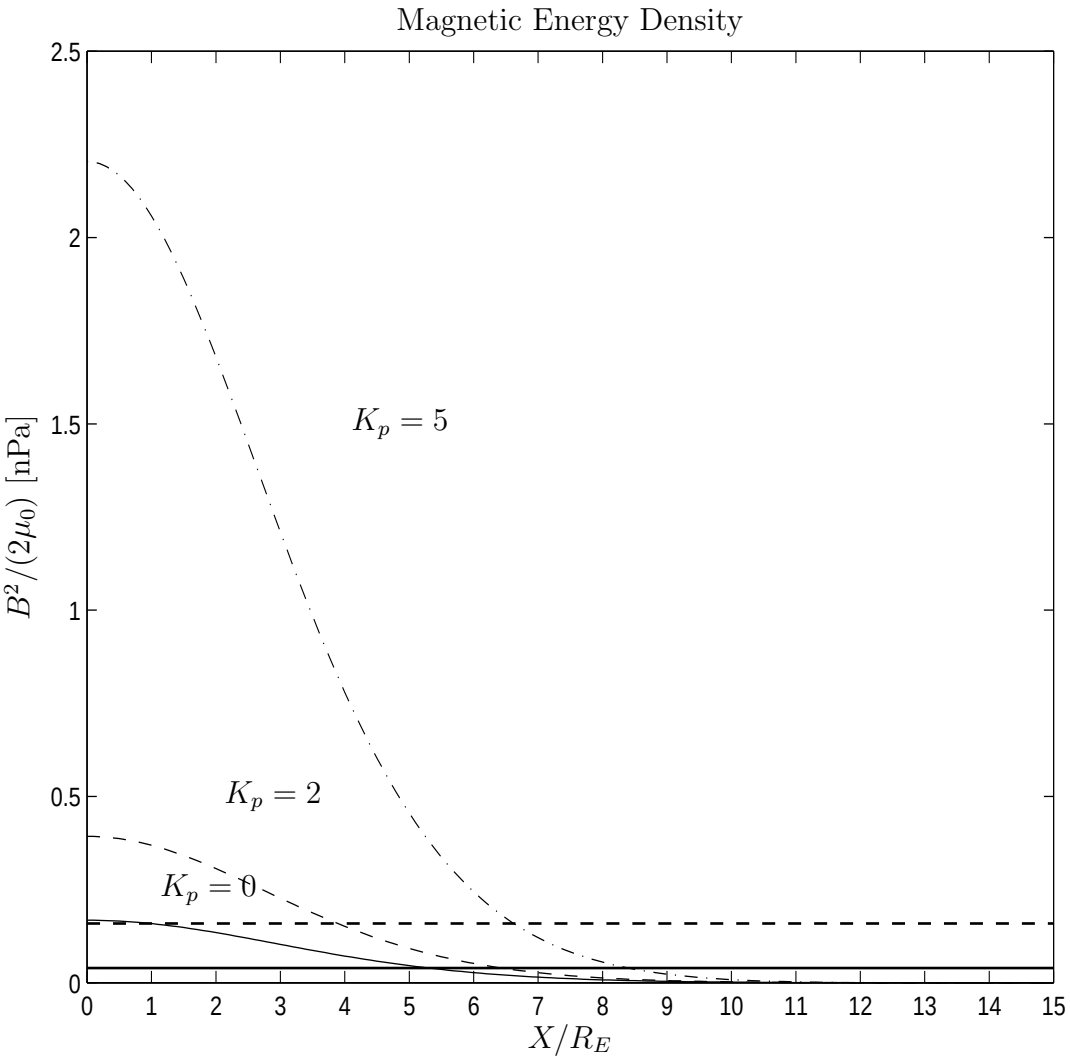

Figure 1.4: Magnetic energy density as a function of distance from the Earth. Note that the magnetic energy density falls off to negligible values by $10R_E$. Values for C and ρ_0 were taken from Tsyganenko's 1987 paper. The solid horizontal line shows the energy density for a 10 nT field (typical of the distant geotail), and the dashed horizontal line shows the energy density for a 20 nT field (typical of the inner geotail).

For Tsyganenko's vector potential of Eq. (1.4), the current density is

$$J_\phi = \frac{60 \cdot C\rho_0^2}{\mu_0} \frac{\rho}{(\rho^2 + z^2 + 4\rho_0^2)^{\frac{7}{2}}} \tag{1.9}$$

The maximum of the current density in the equatorial plane, $z = 0$, is located at $\rho = \sqrt{\frac{2}{3}}\rho_0$, which occurs at about $4.2\,R_e$ for $K_p = 0$ and $z = 0$. Figure 1.5 shows a contour plot of the current density, J_ϕ, in the x-z plane for $K_p = 0$; note that the maximum is near $4\,R_e$. Figure 1.6 shows a plot of the value of ρ at the maximum value of the current density for $z = 0$ as a function of K_p. As seen in the figure, the ring current, as the particles are energized, moves Earthward due to the enhanced $\mathbf{v} \times \mathbf{B}$ forces, where $\mathbf{v}$ is the velocity of the drifting particles.

The total ring current, I_{RC}, for this model can be found by integrating the current density over the noon-midnight meridian and is given by

$$\begin{aligned} I_{RC} &= \int \mathbf{J} \cdot d\mathbf{A} = \frac{60C\rho_0^2}{\mu_0} \int_0^\infty d\rho \int_{-\infty}^\infty dz \frac{\rho}{(\rho^2 + z^2 + 4\rho_0^2)^{7/2}} \\ &= \frac{C}{\mu_0 \rho_0^2}. \end{aligned} \tag{1.10}$$

Figure 1.6 shows the total current contained in the ring current as a function of K_p. From the value for B_z evaluated at 1 R_E as given by Eq. (1.6), we see that the relationship between the current and the DST index is $\mathrm{DST} = \mu_0 \mathrm{I_{RC}}/(4\rho_0)$. For the reference values of $I_{RC} = 4$ MA and $\rho_0 = 4.9\,R_E$ this gives DST=-40 nT.

The magnetic energy, W_{RC}, stored in the ring current is given by $W_{\mathrm{RC}} =$

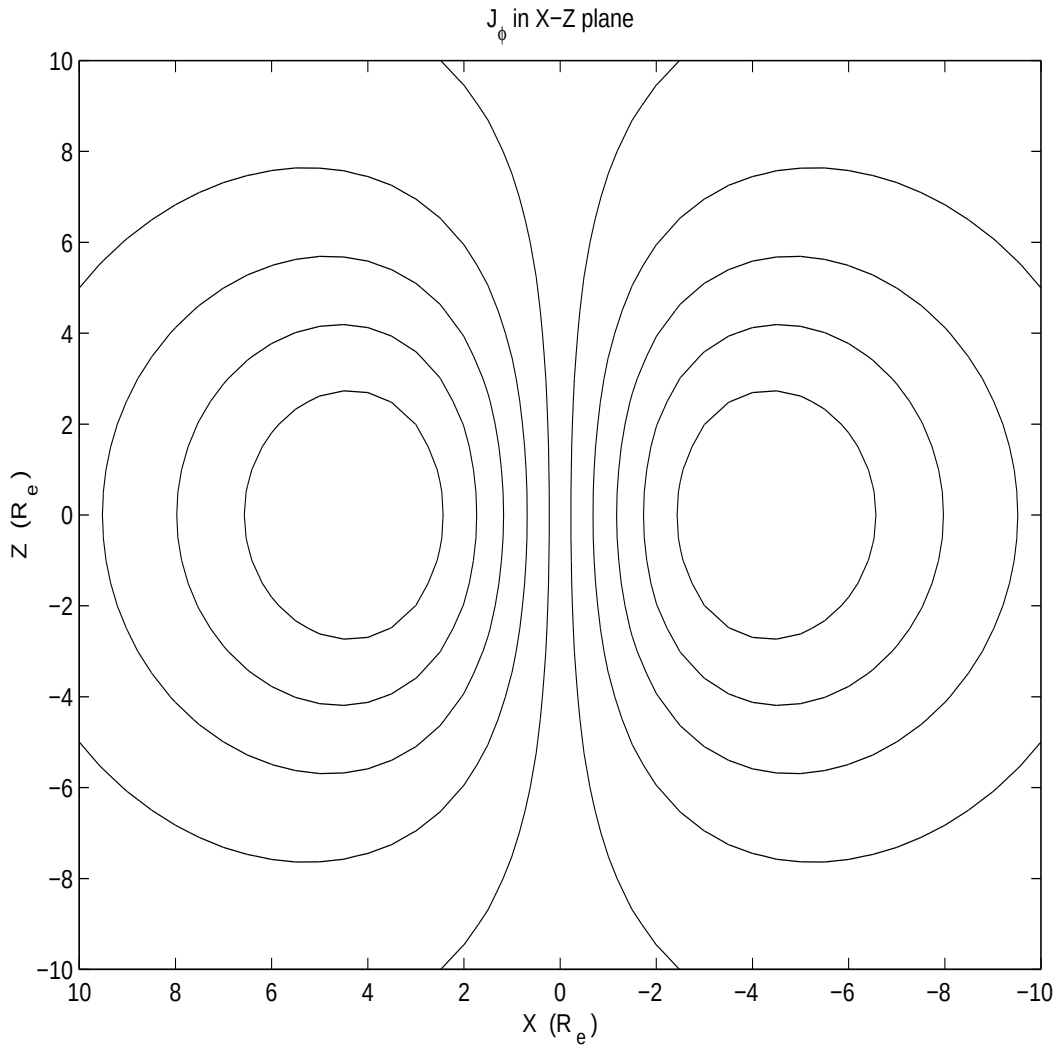

Figure 1.5: Contour plot of J_ϕ in the x-z plane for the model ring current given by Eq. (1.4) with parameters valid for $K_p = 0$. The maximum current density of approximately 10 nA/m^2 occurs near $\pm 4\, R_E$.

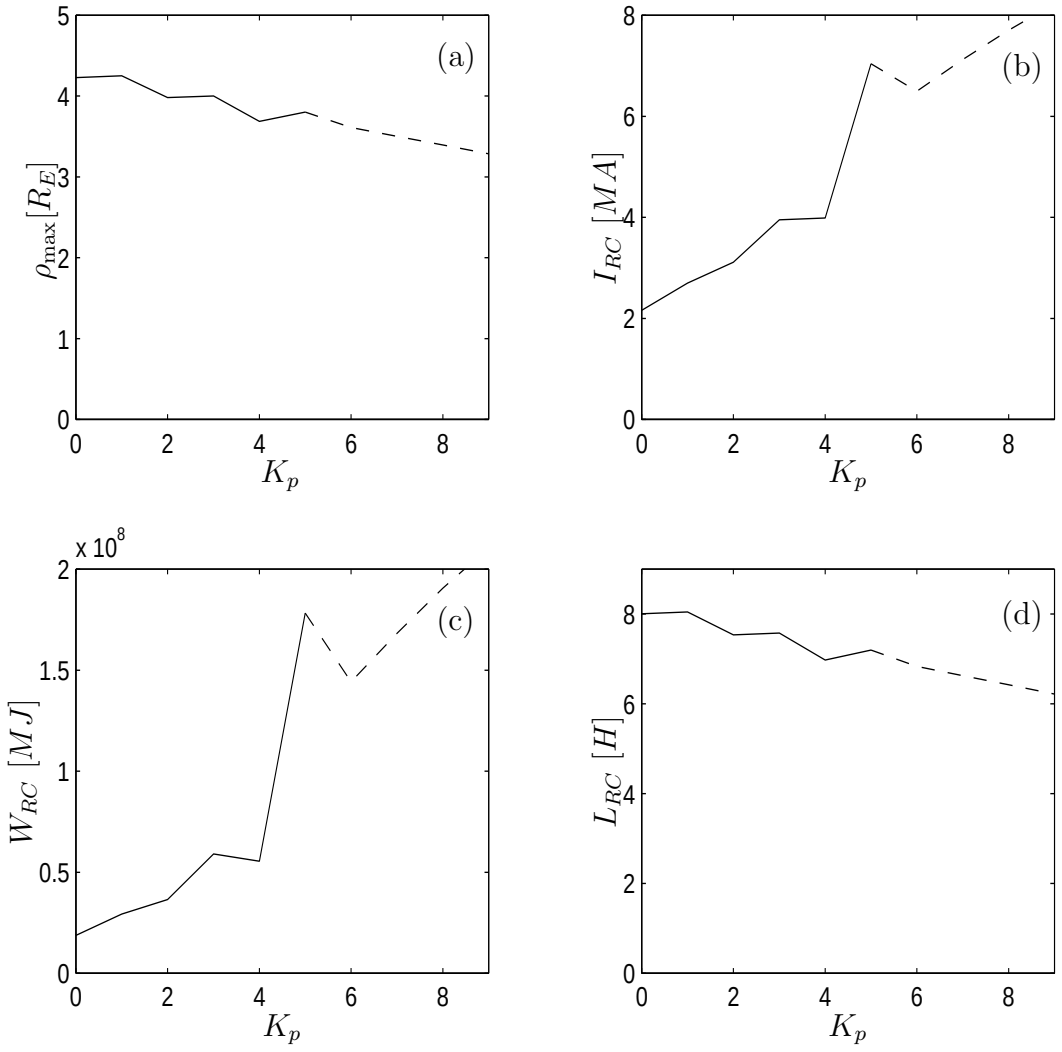

Figure 1.6: Physical quantities computed from Tsyganenko's 1987 [184] magnetic field model as a function of K_p. For K_p greater than 5, the field model parameters were obtained through linear interpolation. The quantities computed with these interpolated parameters are plotted with a dashed line. All quantities were computed analytically with the use of the vector potential given in Eq. (1.4) [189]. Panel (a) shows the radius in units of R_E for which the maximum value of the current density occurs, which is found to be $\sqrt{2/3}\rho_0$. Panel (b) shows the total current in the ring current in units of MA. Panel (c) shows the total energy in units of MJ. Panel (d) shows the self inductance of the ring current in units of H.

$1/2 \int \mathbf{J} \cdot \mathbf{A}$. Using Eqs. (1.9) and (1.4), we obtain

$$\begin{aligned} W &= \frac{30C^2\rho_0^2}{\mu_0} \int_{-\infty}^{\infty} dz \int_0^{\infty} d\rho \int_0^{2\pi} d\theta \frac{\rho^3}{\left(\rho^2 + z^2 + 4\rho_0^2\right)^5} \\ &= \frac{5}{512} \frac{\pi^2 C^2}{\mu_0 \rho_0^3}. \end{aligned} \tag{1.11}$$

Figure 1.6 shows the total energy contained in the ring current as a function of K_p. The rise of stored magnetic energy at $K_p = 5$ is particularly sharp, increasing by a factor of three going from $K_p = 4$ to $K_p = 5$. From the value of B_z at 1 R_E in Eq. (1.6) we now see that the relationship between the magnetic energy and the DST index is $DST = (512\mu_0/20\pi^2 C)W$.

It is interesting to compare this calculation with the Dessler-Parker-Sckopke relationship [167],

$$\frac{\Delta B_{\text{particles}}}{B_0} = -\frac{2}{3} \frac{W_{\text{particles}}}{W_{\text{mag}}} \hat{\mathbf{e}}_z, \tag{1.12}$$

which relates an estimate of the DST index to the ratio of the energy contained in the particles in the ring current to the energy contained in the vacuum dipole field. In Eq. (1.12), $B_0 = 3.1 \cdot 10^{-5}\, T$ is the magnetic field strength of the Earth's internal dipole field at the Earth's surface on the equator and W_{mag} is the total energy in the Earth's dipole field above the Earth's surface, $W_{\text{mag}} = 4\pi/3\mu_0 B_0^2 R_E^3 = 8.2 \cdot 10^{11}$ MJ. Rewriting Eq. (1.12) by recognizing that the dipole moment of the Earth is $M = B_0 R_E^3 = 8 \cdot 10^{15}\text{T}\cdot\text{m}^3$, we obtain

$$\text{DST} = -\frac{\mu_0}{2\pi} \frac{W_{\text{particles}}}{M}. \tag{1.13}$$

From this equation and the relationship $DST = (512\mu_0/20\pi^2 C)W$ we can relate the estimated DST from Tsyganenko's parameterization to the estimated kinetic energy of the trapped particles in the radiation belts.

The self inductance of the ring current is given by $L_{RC} = 2W/I_{RC}^2$. Using Eqs. (1.10) and (1.11), we find that the inductance is

$$L_{RC} = \frac{5\pi^2}{256}\mu_0\rho_0 \tag{1.14}$$

For $L_{RC} = 8H$ the relationship of Eq. (1.14) gives $\rho_{\max} = 4.2$. Figure 1.6 shows the self inductance of the ring current as a function of K_p. The inductance is approximately constant and equal to 8 H over the whole K_p range. This can be understood from the geometrical meaning of the inductance and from the fact that the effective radius of the ring current, ρ_0, changes little Tsyganenko's 1987 model. In the tokamak literature, it is common to use a large-aspect-ratio approximation from which we can estimate the inductance of a tokamak according to the formula

$$L = \mu_0 R\left[\log\left(\frac{R}{a}\right) + \frac{1}{4}\right], \tag{1.15}$$

where R is the major radius and a is the minor radius. Taking $R = 4R_E$ and $a = 2R_E$ this gives an approximation for the inductance of the ring current of about $L_{RC} = 8H$. The effect of the large aspect ratio approximation is that the inductance scales logarithmically with respect to the radius, where as in the previous calculation of the ring current it scales linearly with the radius.

These calculations show that the stored magnetic energy in the ring current component of the magnetic field varies as $L_{RC}I_{RC}^2/2$, with $L_{RC} \simeq 8$ H

a constant. The mutual inductance of the near geotail current loop through the night side part of the ring current system has been estimated as $M_{GT,RC} \simeq 5$H. Thus a change of $dI/dt = 1$ MA/min would induce a typical voltage of 8 kilovolts in the ring current. We know that during a typical storm the DST index varies in value from nearly zero to -100 nT in 3 hours (see Fig. 1.7 which shows the DST index during the GEM storm of May 1997). This implies that the ring current changes by about 0.04 MA/min giving an induced electromotive potential from the time derivative of the ring current, $\mathrm{d}I_{RC}/\mathrm{d}t$, of $\mathcal{E} = L\mathrm{d}I_{RC}/\mathrm{d}t = 4.5$ kV or an electric field of about 0.03 mV/m in the Dusk-to-Dawn direction.

In this section we have demonstrated some simple calculations that can be made using a simplified Tsyganenko magnetic field model (simplified in the sense that we only included the ring current). These calculations are useful in showing the relationship between the DST index, a commonly reported index of geomagnetic activity, and important physical quantities such as the current and the magnetic field energy. Also, we demonstrated the role of the ring current as an inductor in a simplified description of the dynamics of the magnetosphere.

1.2.2 Tail Current

The magnetotail current system is the primary energy storage mechanism of the magnetosphere. The distinguishing feature of this current system is that it consists of a thin current sheet in the equatorial plane, with current

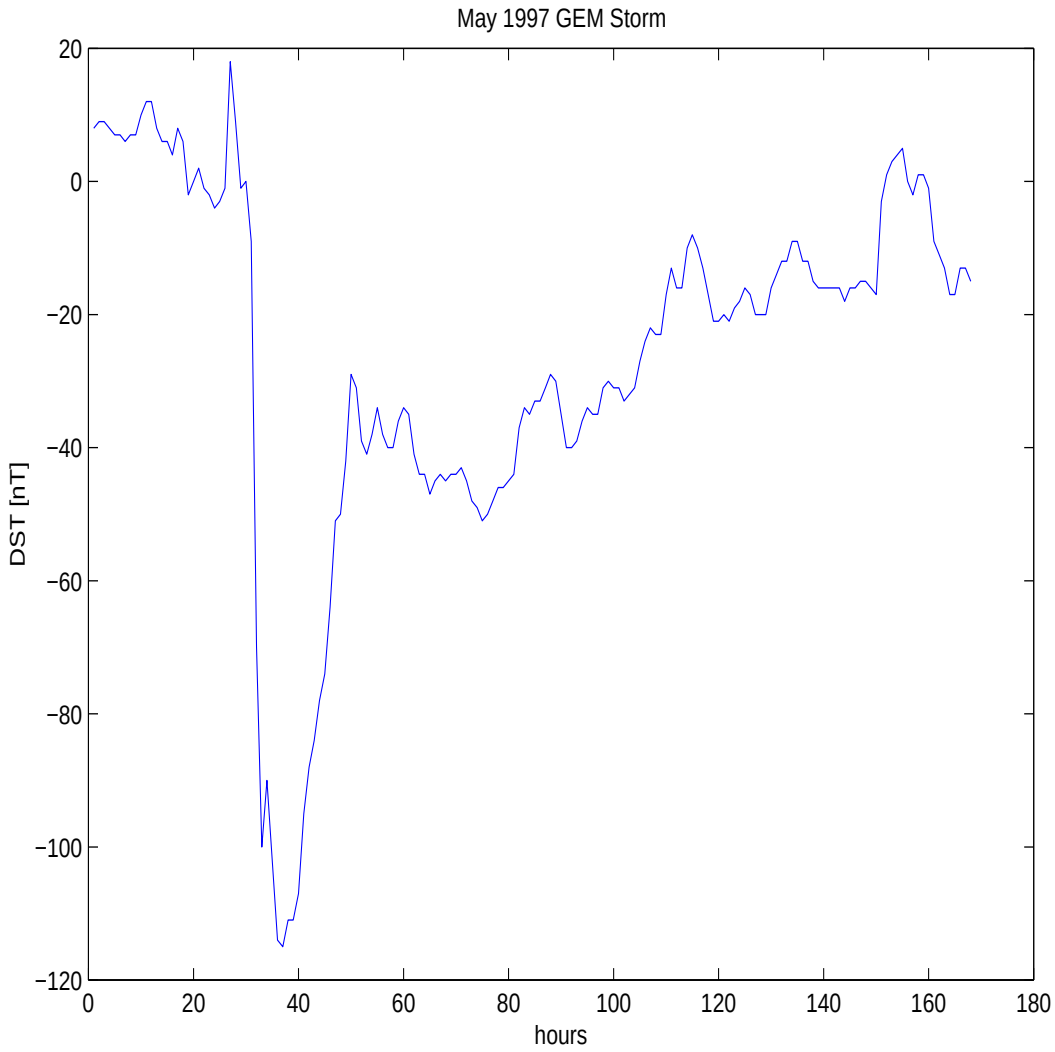

Figure 1.7: DST as a function of time for the GEM storm of May 1997.

flowing from East (dawn) to West (dusk). This thin current sheet is often referred to as the central plasma sheet. At or near the magnetopause, this current closes by diverting both North and South, forming a theta structure, as depicted in Fig. 1.8. The Earthward edge of the central plasma sheet is typically located near geosynchronous orbit, between -5 and -10 R_E. The tail-ward edge of the central plasma sheet can extend hundreds of R_E, but because of sparse satellite coverage out this far, nothing precise can be said about the tail-ward boundary. The thickness of the current sheet varies depending on geomagnetic activity, thinning before substorm onsets, which causes very stretched field lines in the magnetotail. At times the current sheet can be thinner than 1 R_E. Figure 1.9 shows the current density in the $\hat{\mathbf{y}} - \hat{\mathbf{z}}$ plane computed from the Tsyganenko 1996 magnetic field model. The bottom panel shows the extent of bins in the $\hat{\mathbf{x}}$-direction for which 1 MA of current flows in the $\hat{\mathbf{y}}$ direction. Between $X = -5\,R_E$ and $X = -60\,R_E$, approximately 15 MA of current flows in the $\hat{\mathbf{y}}$ direction.

Tsyganenko and coworkers model the magnetotail current by superimposing current filaments along the $\hat{\mathbf{x}}$ axis. Each filament has a radial current distribution flowing in the $\hat{\mathbf{y}}$ direction. Then the current density $I(x)$ per unit length (A/m) along the tail is approximated as

$$I(x) = \frac{2}{\mu_0} B_T(x), \tag{1.16}$$

where

$$B_T(x) = B_0 + \frac{B_1}{x - x_1} + \frac{B_2}{(x - x_2)^2}. \tag{1.17}$$

Then, to determine the magnetic field components due to the central plasma sheet, the following integrals are performed,

$$B_x^{\text{tail}} = \frac{z}{\pi}\int_{-\infty}^{x_N} B_T(x_0)\frac{\mathrm{d}x_0}{(x_0-x)^2+z^2+D^2} \tag{1.18}$$

$$B_z^{\text{tail}} = \frac{1}{\pi}\int_{-\infty}^{x_N} B_T(x_0)\frac{\mathrm{d}x_0(x_0-x)}{(x_0-x)^2+z^2+D^2}, \tag{1.19}$$

where x_N is the inner edge of the current sheet and D is its half-thickness scale-length. To account for the θ structure of the magnetotail current system, two similar sheets located at $z = \pm R_T$ are added to the representation of Eqs. (1.18) and (1.19), each carrying a current of $-1/2I(x)$. To close the currents in the flanks, an even parity function of y is multiplied by these three current sheets, giving the magnetotail its three-dimensional structure.

1.2.3 Magnetopause and Birkeland Currents

Birkeland currents are primarily field-aligned currents that intersect the ionosphere. These currents are named after the Norwegian scientist Kristian Birkeland who, before the advent of satellites, postulated the existence of electrical currents connecting the Earth to the Sun. These currents are divided into two categories: Region 1 currents and Region 2 currents. Region 1 current systems flow into the ionosphere on the morning side and out of the ionosphere on the dusk-side. These current systems are connected to the solar wind and are driven by the dynamo action of the solar wind blowing over the Earth's poles. Region 2 current systems flow in the opposite direction, *i.e.*, out of the ionosphere on the morning side and into the ionosphere on the dusk-side.

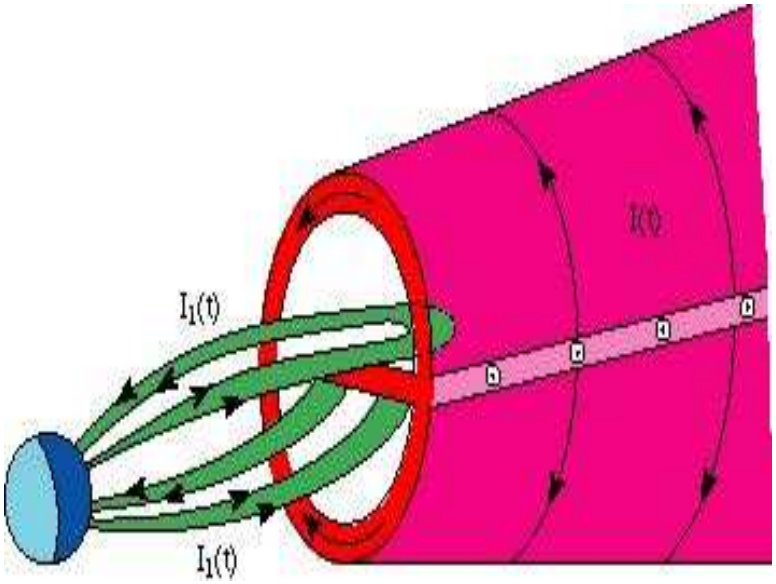

Figure 1.8: Cartoon illustrating the tail current system and the Region 2 current system. The tail current has a θ structure in the $y-z$ plane, with the current in the central plasma sheet flowing from East to West. The Region 2 current system connects the Earthward portion of the tail current with the ionosphere. The ionospheric foot-print of the Region 2 currents is illustrated in Fig. 1.10.

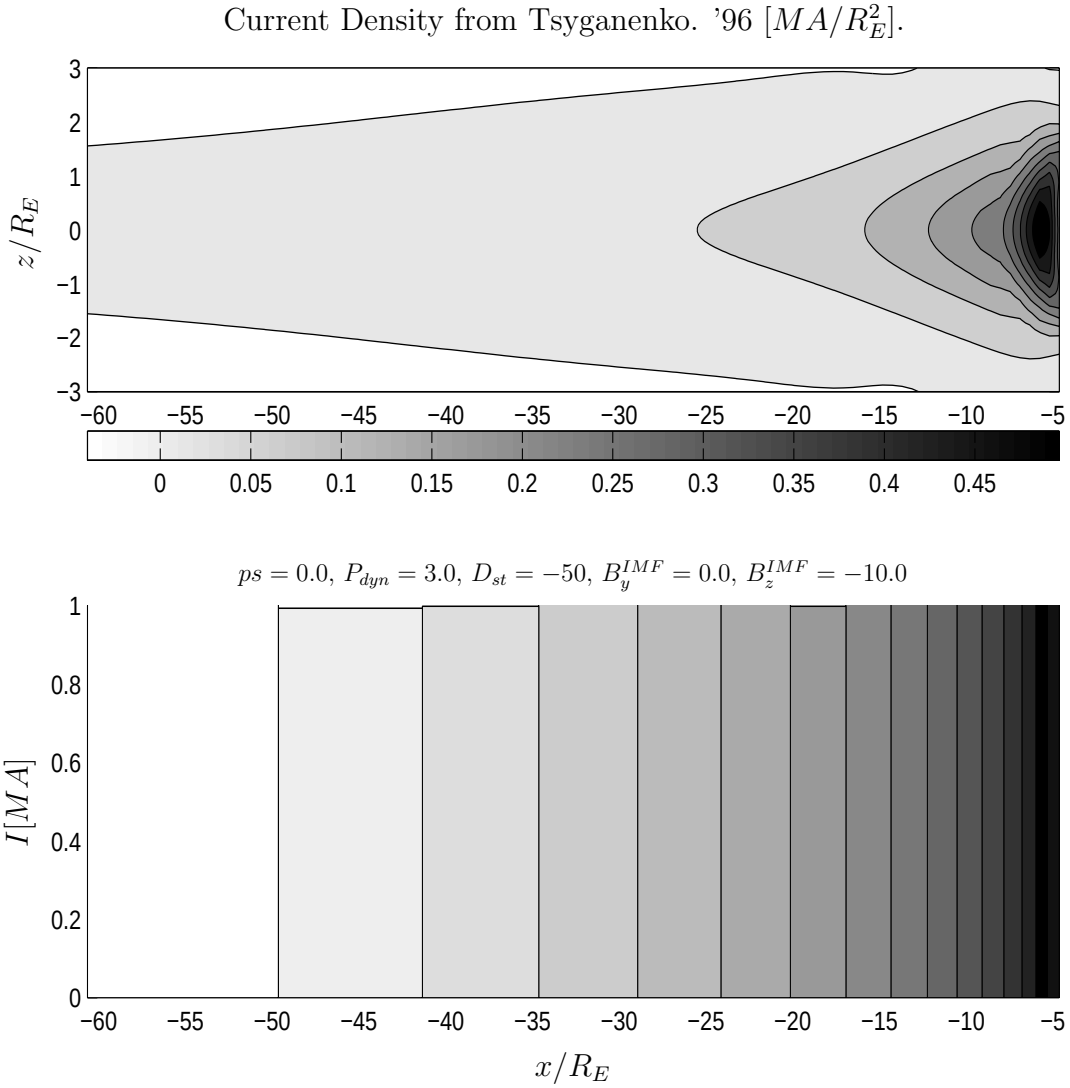

Figure 1.9: Contour plot of the current density in units of MA/R_E^2 (top panel). The total current computed flowing through a region extending 1 R_E in the x direction, and 3 R_E above and below the equatorial plane in units of MA. All quantities are computed numerically from Tsyganenko's 1996 magnetic field model with the parameters $ps = 0.0$, $P_{dyn} = 3.0$ nPa, $D_{st} = -150$ nT, $B_y^{IMF} = 0.0$, and $B_z^{IMF} = -10.0$ nT.

Region 2 currents are closed in the magnetosphere, specifically through the inner tail and ring current, and are thus significantly different from Region 1 currents.

In Tsyganenko's early models [184, 189] the field-aligned currents, along with the magnetopause currents, were modeled with a fit to a finite polynomial expansion. The number of terms used in the polynomial expansion was not adequate to model the spatial sharpness of the real field-aligned currents. The Tsyganenko 1996 model [185, 188] included specific modeling of these current systems.

Magnetopause currents flow along the boundary between the interplanetary magnetic field and the magnetosphere. The general function of these currents is to shield the inner current systems. As mentioned earlier, the early models by Tsyganenko *et al.* did not provide these shielding currents explicitly. Instead, they used a simple polynomial expansion and fit these parameters to the data. Starting with the 1996 model, the magnetopause boundary and model shielding currents along this boundary are explicitly specified by means of an expansion in a suitable set of harmonic functions to represent the internal scalar potential. The explicit form of the magnetopause was taken to be a prolate hemi-ellipsoid of revolution at the nose (up to a tail-ward distance of 60-70 R_E), smoothly continued in the far tail by a cylindrical surface [185].

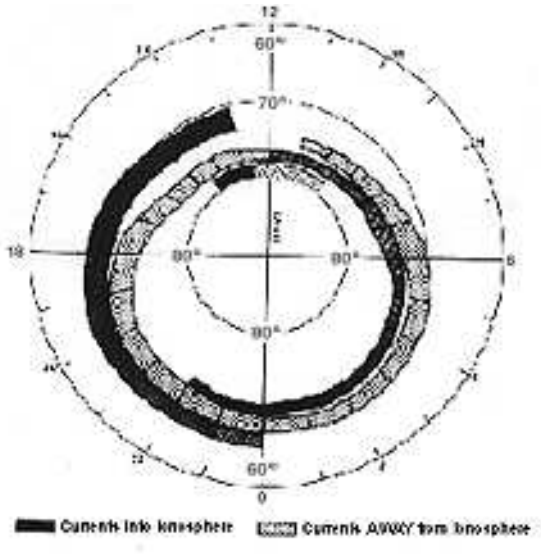

Figure 1.10: Adaptation from Kivelson and Russell [5] of the region 1 and Region 2 Birkeland current systems in the ionosphere. In this figure the Region 1 currents flow into the ionosphere (Black Region) on the morning side (right) and out of the ionosphere (Grey Region) on the evening side (left). Region 2 currents flow out of the ionosphere (Grey Region) on the morning side (right) and into the ionosphere (Black Region) on the evening side (left).

1.3 Equilibrium Considerations

Not all magnetic field models discussed in our work will necessarily be in equilibrium since some do not take into account both the pressure and the magnetic field. However, all of the two-dimensional reduced magnetic field models that we discuss will be in equilibrium. An equilibrium must be in force balance, and for a scalar pressure it must satisfy the following equation:

$$\nabla p = \mathbf{J} \times \mathbf{B}. \tag{1.20}$$

A consequence of Eq. (1.20) is that the pressure is constant along a field line, $\mathbf{B} \cdot \nabla P = 0$. For the two-dimensional simple equilibriums in which we are interested, we choose the magnetic vector potential to have only a component in the ignorable direction ($\hat{\mathbf{y}}$) and to be only a function of (x, z). Thus, from $\mathbf{B} = \nabla \times \mathbf{A}$, the magnetic field can be written as

$$\mathbf{B} = \nabla A_y(x, z) \times \hat{\mathbf{y}}. \tag{1.21}$$

A consequence of Eq. (1.21) is that $A_y(x, z)$ is a constant along a field line, so that contours of constant $A_y(x, z)$ correspond to magnetic field lines. Furthermore, because $A_y(x, z)$ is constant along a field line and p is constant along a field line, we can express the pressure p as a function only of A_y. Writing the current in terms of A_y, we find that the current is consequently only in the $\hat{\mathbf{y}}$ direction:

$$\mathbf{J} = \frac{1}{\mu_0} \nabla \times \mathbf{B} = -\frac{1}{\mu_0} \hat{\mathbf{y}} \nabla^2 A_y(x, z). \tag{1.22}$$

Since the pressure is a function of A_y and since A_y satisfies the equilibrium relation then $\mathrm{d}P/\mathrm{d}A_y = J_y$, and we obtain

$$\begin{aligned} \nabla P &= \mathbf{J} \times \mathbf{B} \\ \frac{\mathrm{d}P}{\mathrm{d}A_y}\nabla A_y &= J_y \hat{\mathbf{y}} \times (\nabla A_y \times \hat{\mathbf{y}}) = J_y \nabla A_y \\ \frac{\mathrm{d}P}{\mathrm{d}A_y} &= J_y \end{aligned}$$

consequently the Grad-Shafranov equation can be written as

$$-\frac{1}{\mu_0}\nabla^2 A_y = \frac{\mathrm{d}P}{\mathrm{d}A_y}. \tag{1.23}$$

By making the *ansatz* that $P = kA_y^2/2$, we can convert Eq. (1.23) into a linear partial differential equation:

$$\nabla^2 A_y = -\mu_0 k^2 A_y. \tag{1.24}$$

The Tsyganenko series of empirical models only supply a model for the structure of the magnetic field; they do not supply any information about the plasma, such as its density, temperature, or pressure. However, if one assumes that the model is in force balance, one can estimate the pressure. For example, the pressure along the $\hat{\mathbf{x}}$ axis in the magnetotail is a crucial quantity for stability. To obtain an estimate of the pressure from a model that only takes into account the magnetic field, one can compute the current density $\mathbf{J} = \nabla \times \mathbf{B}/\mu_0$ numerically and then integrate along the magnetotail:

$$P(x) = P_T + \int_{x_T}^{x} (J_y B_z - B_y J_z)\,\mathrm{d}x, \tag{1.25}$$

where x_T is a point at which we know the plasma pressure from other sources, and P_T is the plasma pressure at x_T. Figure 1.11 shows the results of such a calculation, using the Tsyganenko 1996 magnetic field model along with data taken from the AMPTE/CCE satellite [172, 173]. For these calculations we used $x_T = -34\,R_E$ and $P_T = 0.06$ nPa (values which was taken from the satellite data). Note that the pressure computed from the Tsyganenko magnetic field models tends to exceed the observed value of the pressure. The high pressure values computed from the Tsyganenko 1996 model are thought to be due to an overestimate of the $\hat{\mathbf{z}}$ component of the magnetic field, B_z, in the magnetotail. The amount of current computed by the model, J_y, is thought to be more accurate.

1.4 Constant Current Model

A simple magnetic field model equilibrium that has some of the features of the geotail is the Constant Current Model (CCM). The geotail is a simple reversed magnetic field; hence, if we require B_x to reverse sign at $z = 0$ and B_z to be non-zero, then A_y must be even in z. A simple function that satisfies this condition is $A_y(x, z) = 1/2\,B'_x z^2 + B_n x$, which is exactly the Constant Current Model. Notice that for this model, the current is indeed constant $J_y = B'_x/\mu_0$, and therefore $P(A_y) \propto A_y$. The parameter B'_x parameterizes the current, and the parameter B_n represents the magnetic field component produced by currents outside of our system of interest.

For this model the magnetic field line curvature, $\boldsymbol{\kappa}$ and gradient are as

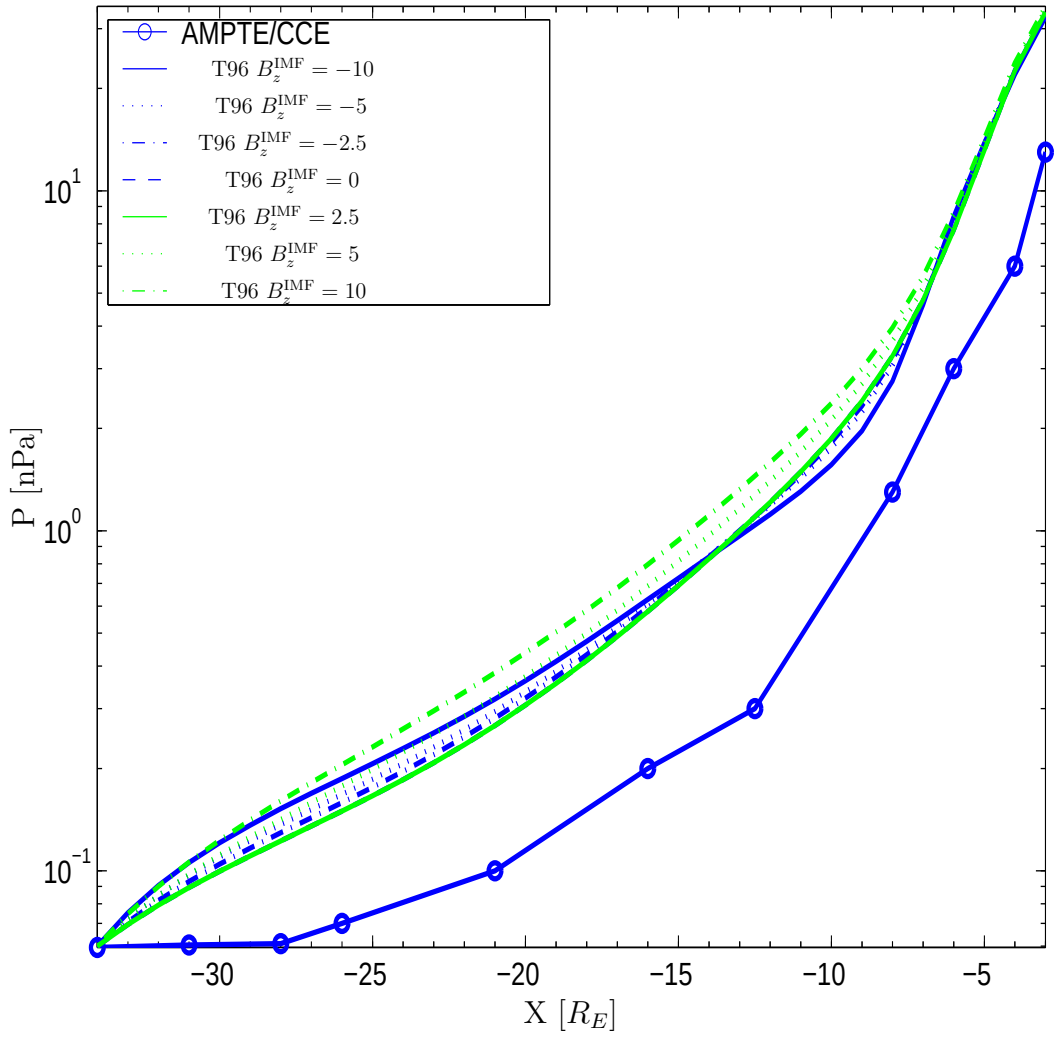

Figure 1.11: Pressure computed from Tsyganenko 1996 field model with the assumption of force balance. The line with circles at the data points was made using satellite data from AMPTE/CCE, the rest of the curves were computed using Tsyganenko 1996.

follows:

$$\boldsymbol{\kappa} = \frac{B_n^2 B_x'}{B^4} \nabla A_y \tag{1.26}$$

$$\nabla B = \frac{(B_x')^2}{B} z\hat{\mathbf{z}}. \tag{1.27}$$

A property of this model is that the bounce-averaged total drift velocity is precisely zero.

It is often useful to add a two-dimensional dipole to this model. The two-dimensional dipole will maintain translational symmetry in the $\hat{\mathbf{y}}$ direction, while also causing the field lines to bend in towards the Earth, rather than going off to infinity. The y-component of the magnetic vector potential for a 2D dipole can be written,

$$A_y^{2D} = -\frac{B_0 r_0^2 x}{x^2 + z^2} \tag{1.28}$$

1.4.1 Useful analytical relations

As discussed previously, the Constant Current Model is a very useful model for the geomagnetic tail system, quantitatively valid out to geosynchronous orbit. It consists of the linear superposition of the two-dimensional dipole and a uniform current sheet ($J_y = const$). Since the model is translationally invariant in y, the eigenmodes are strictly sinusoidal in the y-direction, which greatly simplifies the stability analysis. The parameters of the 2D model are $B_0 r_0^2$, B_x' and B_n and they will be optimized with respect to a given space region $\Omega = L_x L_y L_z$ for the best representation of the three-dimensional fields. The analytical and numerical advantages of the two-dimensional model are

clear. The particle simulations of Pritchett *et al.*[148] were performed in such a two-dimensional system with compression of the space and time scales by the use of a small ion-to-electron mass ratio. In this section we will perform some useful analytical operations with the model.

The two-dimensional magnetotail model is derived from $\mathbf{B} = \nabla \times (A_y \hat{y}) = \nabla A_y \times \hat{y}$ with

$$A_y(x,z) = -\frac{B_0 r_0^2 x}{x^2+z^2} - \frac{1}{2}B'_x z^2 + B_n x. \tag{1.29}$$

This gives

$$B_z(x,z) = B_n + \frac{B_0 r_0^2 (x^2-z^2)^2}{x^2+z^2} \tag{1.30}$$

$$B_x(x,z) = B'_x z - \frac{B_0 r_0^2 xz}{(x^2+z^2)^2}, \tag{1.31}$$

with

$$B^2 = B_n^2 + {B'_x}^2 z^2 + \frac{B_0 r_0^2 \left[B_n(x^2-z^2) - 2B'_x x z^2\right]}{(x^2+z^2)}. \tag{1.32}$$

The shear matrix, $\mathrm{d}B_i/\mathrm{d}x_j$ of the magnetic field has components

$$B_{x,x} = \frac{2B_0 r_0^2 z(3x^2-z^2)}{(x^2+z^2)^3} \tag{1.33}$$

$$B_{x,z} = B'_x - \frac{2B_0 r_0^2 x(x^2-3z^2)}{(x^2+z^2)^3} \tag{1.34}$$

$$B_{z,x} = -\frac{2B_0 r_0^2 x(x^2-3z^2)}{(x^2+z^2)^3} \tag{1.35}$$

$$B_{z,z} = \frac{2B_0 r_0^2 z(z^2-3x^2)}{(x^2+z^2)^3} \tag{1.36}$$

From Eqs. (1.33)-(1.36) we see that $\nabla \cdot \mathbf{B} = 0$ and that $\mu_0 j_y = B_{x,z} - Bz, x = B'_x$.

In the region $x^2 >> z^2$ of the deep tail model, the effect of the two-dimensional dipole on the constant current sheet is

$$B'_x \rightarrow B'_x - \frac{2B_0 r_0^2}{x^3} \tag{1.37}$$

$$B_n \rightarrow B_n + \frac{B_0 r_0^2}{x^2} \tag{1.38}$$

where we note that x is negative in the night-side region of interest.

Notice that this model is valid for $\beta \gg 1$. For smaller values of β we can see the most important corrections through the equilibrium equation $\nabla p = \mathbf{J} \times \mathbf{B}$, which can be written as

$$\frac{\partial p}{\partial x} = j_y B_z = \frac{B_z}{\mu_0} \frac{\partial B_x}{\partial z} \left(1 - R\right), \tag{1.39}$$

where $R = \partial B_z / \partial x / \partial B_x / \partial z \simeq 1/(1+\beta)$. For $\beta \gg 1$ we see that $\partial P / \partial x$ comes from the variation of B_z with respect to z, but for lower values of β the quantity R involving the variation of B_x with respect to z becomes important.

Figure 1.12 shows some simple computations with the Tsyganenko 1996 magnetic field model and the simple two-dimensional CCM model. One can see from this figure that the gross features of a particular flux-tube are represented fairly well by the CCM model, except that the CCM model has a shallow B profile due to the use of a two-dimensional dipole rather than a three-dimensional dipole. We will use these models throughout the dissertation to investigate the stability of the night-side magnetosphere.

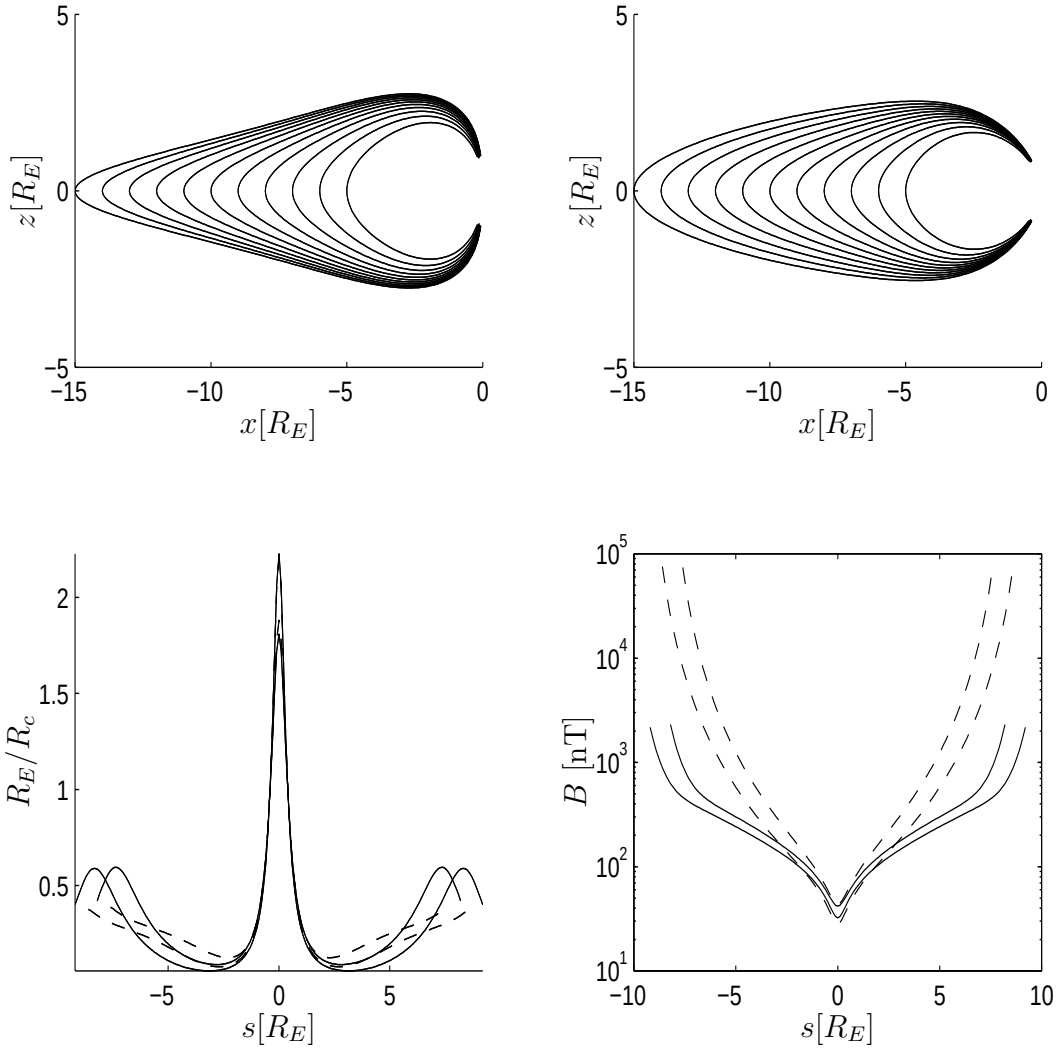

Figure 1.12: Magnetic field lines computed from the CCM model with $B'_x = 64\text{nT}/R_E$, $B_n = 1.0\text{nT}$, $B_0 r_0^2 = 4000\text{nT}\, R_E^2$ (top left panel). Magnetic field lines computed from Tsyganenko's 1996 model with $PS = 0$, $P_{\text{dyn}} = 3.0\text{nPa}$, $\text{DST} = -50\text{nT}$, $B_y^{\text{IMF}} = 0$, and $B_z^{\text{IMF}} = 5.0\text{nT}$ (top right panel). The inverse of the radius of curvature and the magnitude of the magnetic field B are plotted as functions of s, the distance along a field line (bottom panels). Values on two different field lines are shown, one with equatorial plane crossing at $-9R_E$ and the other at $-10R_E$. Results with Tsyganenko's model are shown in the dashed curves, and with the CCM model in solid curves.

1.5 Outline of Dissertation

In Chapter 1 we have given an introduction to the structure of the magnetosphere and we have discussed in some detail how the major current systems are modeled. These magnetic field models will be used throughout the dissertation to assess the stability of the magnetosphere. The stability of these models is important for understanding the nature of the onset of magnetospheric substorms. In Chapter 2 the most important properties of magnetospheric substorms will be reviewed, as well as the competing phenomenological views for understanding the various observations of substorms. In Chapter 3 we will consider the problem of the ideal MHD ballooning stability of our model magnetic fields using a Fast-MHD $\delta W_p^{\mathrm{MHD}}$ formulation that does not violate the assumptions of MHD. We will determine when these models can exhibit fast unstable motions and also where these motions are most likely to occur. In Chapter 4 we will develop a gyrokinetic dispersion relation valid for electromagnetic perturbations in high-β plasmas. We will then use this dispersion relation to examine the stability of magnetospheric plasmas under the assumption that the eigenmode structure along the flux-tube is concentrated at the equatorial plane. The gyrokinetic approximation will allow us to determine whether wave-particle resonances or finite gyroradius effects modify the stability limits obtained in the Fast-MHD approximation. In Chapter 5 we will relax the assumption of locality, used in Chapter 4, by introducing numerical methods to solve for the bounce-averaged eigenmode structure along the magnetic field. We will then use these methods to investigate non-local ki-

netic electrostatic modes in magnetotail flux-tubes. In Chapter 6 the non-local approximation will be applied to a new series of modes, called compressional drift waves, whose primary component is the parallel perturbation of the magnetic field. We obtain the conditions under which these waves might become unstable, and we discuss their role in substorms.

Chapter 2

Characteristics of Substorms

A substorm is an ordered sequence of events that results in a global magnetospheric reconfiguration and energy release [13]. Substorms are observed in both auroral and magnetic activity. Substorms have a lifetime of one to three hours and are divided into two phases: (1) an expansion phase, lasting 10-30 minutes, and (2) a recovery phase, lasting between one to two and a half hours. Akasofu [7] was the first to develop a global picture of a substorm, and his basic picture has not changed significantly. Akasofu's global picture was obtained without the aid of satellites. To construct his model, he used all-sky camera images across Alaska, Canada, and Siberia of the auroral forms. Since his first characterization, there have been many more detailed observations of the various substorm stages, which have led to a divergence in the interpretation of the data. In this chapter the basic phenomenonology of a substorm and some of the most popular explanations will be discussed.

During the course of a substorm, the magnetosphere extracts energy from the solar wind, stores this energy in the magnetotail, forms an extremely thin current sheet within the tail plasma sheet, and then explosively disrupts this thin current sheet.

For decades, the detailed observational data from both ground-based magnetometer stations and nightside spacecraft measurements of plasma particles and fields have been analyzed for the purpose of understanding substorm dynamics. While many mechanisms have been proposed and investigated over the years, processes in two distinct regions now seem to be intimately linked to substorms. The first, historically, is the formation of a neutral line by a $B_n + \delta B_z < 0$ perturbation in the mid-tail region at $X \simeq -25\,R_E$, called the Near Earth Neutral Line (NENL) model. Here $B_n(X)$ is the northward ambient field on the axis of the geomagnetic tail, and δB_z is a southward perturbation which, when larger than $B_n(x)$, forms the neutral line. The second mechanism, for which there is growing observational evidence [60, 131], is characterized by the onset of low-frequency precursor pulsations in the Pi2 frequency band (Pi2 waves are Irregular pulsations with frequencies between 2 and 24 mHz [5]) and the sudden brightening of auroral arcs associated with flux tubes that map to equatorial crossing points in the region between $X = -6R_E$ and $-12R_E$, dependent on the state of the magnetosphere. Substorms with these onset characteristics have been named NGO (near geosynchronous orbit) events, although the Keplerian orbits with a twenty-four hour period play no role in the plasma electrodynamics. The large number of geosynchronous spacecraft provide excellent data coverage of this region.

In this chapter we will discuss the important features and characteristics of magnetospheric substorms. In Section 2.1 we will go through the details of the different stages of a magnetospheric substorm. In Section 2.2 we will

explain the Near Earth Neutral Line (NENL) model for understanding substorm dynamics and describe how this model was obtained from observations. In Section 2.3 we will explain the Near Geosynchronous Orbit (NGO) model of substorm dynamics and the observations that support this viewpoint. In Section 2.4 we will explain recent attempts to combine these two viewpoints in order to account for all of the observations. In Section 2.5 we will focus on the observations of compressional Pi2 oscillations since the work done in Chapter 6 is particularly relevant to these observations. Finally, in Section 2.6 we offer some concluding remarks on substorm observational characteristics.

2.1 Substorm stages

2.1.1 Growth phase

The aurora, which is constant and usually stable, occurs around each of the poles. Typically the quiet aurora occurs between a geomagnetic latitude of 60 to 65 degrees. These aurora consist of long arcs roughly parallel to lines of constant geomagnetic latitude. During quiet times there are also polar features of auroral activity that align themselves between the Sun and Earth. Figure 2.1 is a cartoon adapted from Akasofu [7] that shows the auroral activity during the different stages of a substorm. In panel (a) of Fig. 2.1 a depiction of quiet auroral arcs can be seen. Usually for the aurora to be considered quiet, the region must be free from activity for about 3 hours.

During the growth phase, the magnetosphere extracts energy from the solar wind, and stores it in the magnetotail, to be later explosively released at

the onset of expansion.

The canonical substorm is typically observed after the interplanetary magnetic field (IMF) has been directed steadily southward (anti-parallel to the Earth's internal dipole field) for about one hour [16].

During the growth phase, the near-Earth current sheet becomes thinner and more intense, causing the magnetic field lines to be very stretched [15]. The strength of the magnetic field in the equatorial plane becomes very weak [109]. Particles whose pitch angles are close to 90 degrees move closer to the Earth, causing pitch angle distributions to become highly elongated [14].

Typically, during the growth phase a small net westward electric field can be observed. This indicates an Earthward convection due to $\mathbf{E} \times \mathbf{B}$ drift. Importantly, growth phase oscillations of the electric field with 60 to 90 second periods are observed at geosynchronous orbit [60]. In the late growth phase (Step 2 of Erickson's 7 steps of a substorm), trigger waves grow in the inner magnetotail. These are indicated by the quiet oscillations of the electric field with periods of 60 to 90 seconds, whose amplitudes grow large enough to reverse the direction of the total electric field. During the reversal, the electric field is in the eastward direction and $\mathbf{j} \cdot \mathbf{E} < 0$. Erickson *et al.* [60] report that during these Eastward excursions of the electric field, the wave power is predominately directed along the magnetic field toward the ionosphere.

There is evidence that before substorm onset, when energy is being extracted from the plasma and put into the oscillating electric field, the cross-tail

current is reduced, giving rise to a dipolarization of the magnetic field and the formation of the Substorm Current Wedge (SCW) [60]. During the dipolarization, an oscillation of the magnetic field with a 30 second period is observed at geosynchronous orbit, while the electric field continues its oscillation with a period of 60 to 90 seconds.

2.1.2 Triggering Phase

The triggering phase is also called substorm onset or stage I of the expansive phase [7]. This stage is characterized by a very sudden brightening of a single auroral arc, approximately centered on the noon midnight meridian at the Equatorward edge of the auroral zone (≈ 62 deg magnetic latitude). These field lines typically map to near geosynchronous orbit. Frank and Sigwarth [66] used high-resolution global images of the visible emissions of atomic oxygen at 557.7 nm on board the Polar spacecraft to determine the magnetic latitude and local time of the auroral arc that participates in the initial brightening. They provided a case study of six isolated substorms and found a minimum magnetic latitude of 59.9 degrees and a maximum of 66.8 degrees. They then used Tsyganenko's 1989 empirical magnetic field model to map these positions into the equatorial plane. The results of their study are summarized in Table 2.1. They also independently verified the mapping location of the onset field lines by observing the atmospheric footprint of protons originating in the ring current. The footprint was observed in the emissions through the Hα line at 656.3 nm. The radial distances of the maximum intensities in the ring current

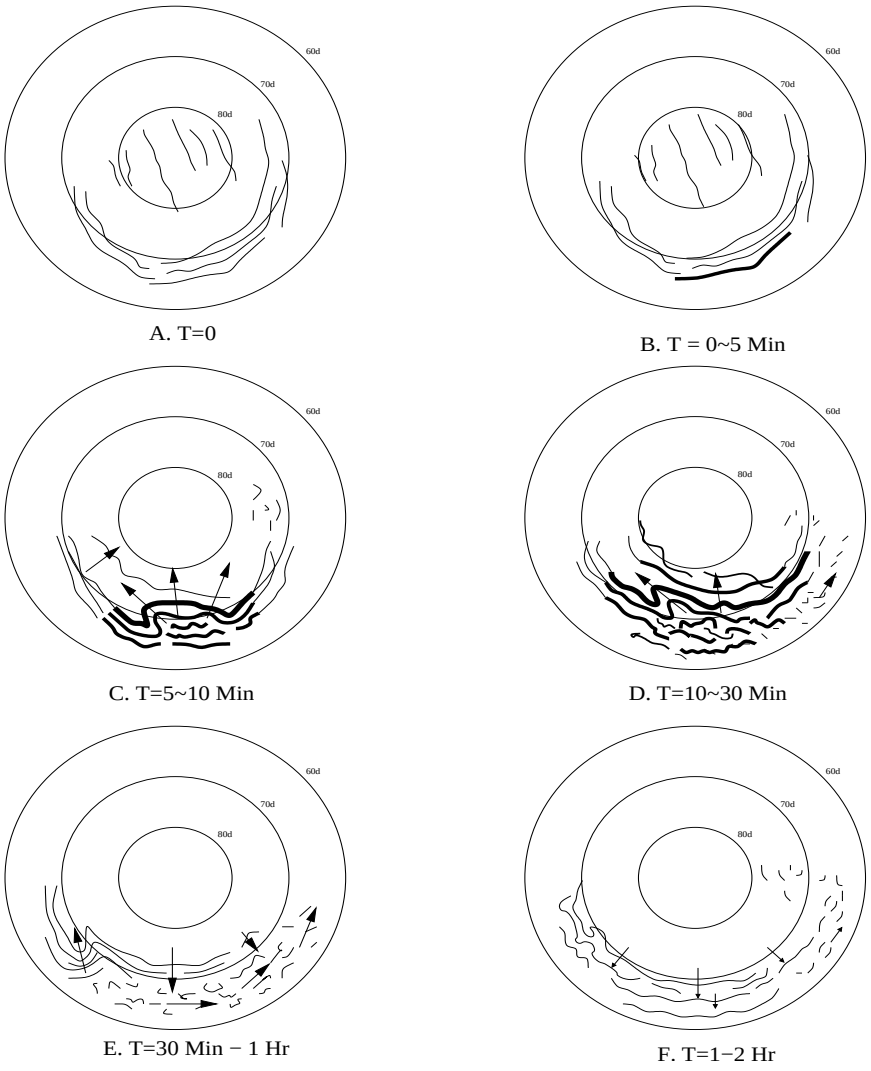

Figure 2.1: Depiction of the stages of an auroral substorm. Each panel shows the auroral arc formations observed in the ionosphere during different stages as described by Akasofu [7]. The various stages depicted in the panels are: A) Quiet phase B) Triggering Phase (Expansive Phase Stage I) C) Expansive Phase Stage II D) Expansive Phase Stage III E) Recovery Phase Stage I F) Recovery Phase Stage II. The magnetic North pole is at the center of the lines of constant geomagnetic latitude.

Date	Time, UT	Latitude	Longitude	K_p
Dec. 17, 1997	2051:33	66.8 deg	109.6 deg	1^-
Dec. 17, 1997	2221:54	66.2 deg	73.5 deg	2^+
Jan. 6, 1998	1618:53	62.1 deg	171.2 deg	4^+
Jan. 6, 1998	1843:49	62.9 deg	147.9 deg	4
Jan. 6, 1998	2341:29	60.8 deg	83.9 deg	4^-
Mar. 1, 1999	2119:07	59.9 deg	120.1 deg	4^+

Table 2.1: Table (From Frank and Sigwarth [66]) showing the location, date, and time of six different substorm onsets and the general geomagnetic disturbance level as determined by K_p.

are in the range of -3 to -8 R_E.

Figure 2.2 shows the equatorial crossing point ($z_{\rm GSM} = 0$) for field lines that map from 60 to 65 deg, for various geomagnetic indices computed with Tsyganenko and Stern's 1996 magnetic field model [188]. This range of magnetic latitude corresponds to the study by Elphinstone *et al.* [62], who found that, for 80 onset brightenings seen in the Viking far-ultraviolet images, the average magnetic latitude was 62.9±3.5 degrees. This mapping is important because it is believed that the substorm process is a consequence of dynamics in the magnetotail. Panel B of Figure 2.1 depicts the triggering phase and the sudden brightening of the equatorward auroral arc.

At geosynchronous orbit, there is evidence [60] that the oscillating electric field with 60 to 90 second period undergoes explosive growth within two periods following the onset of dipolarization. This explosive growth of wave power is termed Local Explosive Onset (LEXO) and is often observed to precede the sudden brightening of the auroral arc that is typically used to des-

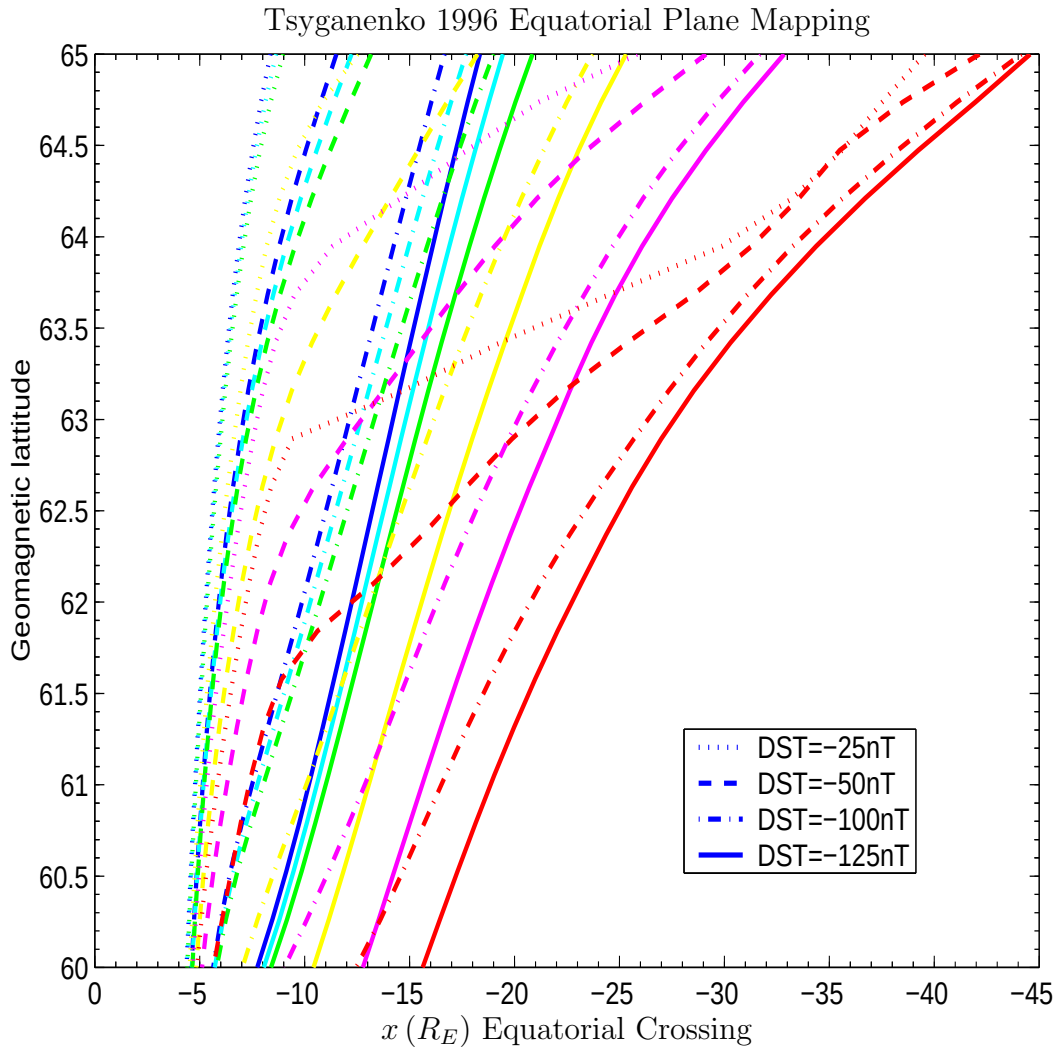

Figure 2.2: Map of Equatorial plane crossings in the noon-midnight meridian for the auroral region for many different geomagnetic conditions. Blue is for $B_z^{\rm IMF} = 10nT$, cyan is for $B_z^{\rm IMF} = 5nT$, green is for $B_z^{\rm IMF} = 0nT$, yellow is for $B_z^{\rm IMF} = -5nT$, magenta is for $B_z^{\rm IMF} = -10nT$, and red is for $B_z^{\rm IMF} = -15nT$. In all of these figures the solarwind dynamic pressure was 3 nPa, and the $B_y^{\rm IMF}$ was 0 nT. The legend shows the dot pattern for different values of the DST index. Substorm onset typically occurs at a magnetic latitude of $\approx$ 62 deg.

ignate substorm onset. This wave power is primarily directed, as the trigger waves are, toward the ionosphere. Large field-aligned currents (FAC) and energetic particles are typically observed to coincide with this explosive growth phase.

2.1.3 The Expansive Phase

Akasofu's Expansive stage II occurs approximately five minutes after the initial onset of the substorm and lasts for approximately five minutes. During this stage, the auroral arcs that brightened during the triggering phase develop a poleward motion as depicted in panel C of Figure 2.1. The speed of the poleward motion is usually on the order of 20 to 200 km/min.

Akasofu's Expansive stage III occurs approximately ten minutes after the initial onset of the substorm and lasts for approximately twenty minutes. During this stage, the poleward motion of the auroral arc reaches its northernmost point, between 75 and 80 degrees latitude. A fold develops in the arc and a westward travelling surge develops, as depicted in panel D of Figure 2.1. The speed of the surge is on the order of 10 to 100 km/min.

2.1.4 The Recovery Phase

Typically the recovery phase begins 30 minutes after the substorm onset. Akasofu [7] breaks this stage into three parts. The first, stage I, lasts about 30 minutes and is depicted in panel E of Figure 2.1. As soon as the poleward motion reaches its highest latitude, the arc begins to return to lower latitudes.

Typically the return motion is slower than the original poleward motion, but can be as fast as 50 km/min. The speed and intensity of the westward surge is also reduced during this stage. The westward travelling surges eventually break up and dissipate, with some of them forming irregular arcs that then drift back eastwards at about 30 km/min. During stage II (panel F of Figure 2.1), the equatorward motion of the arcs continue. New arcs can form near the polar cap, and the irregular arcs of the previous stage become longer but still irregular. Stage III, the final one, is characterized by equatorward motion of quiet arcs. Usually after an hour, the quiet phase returns.

2.2 Near Earth Neutral-Line Model

The Near Earth Neutral-Line (NENL) model was the first phenomenological model that attempted to provide a picture of the entire substorm process throughout the magnetosphere. It was proposed by Russell and McPherron *et al.* in 1973 [159] and has continued to be developed since that time [16, 133]. Most recently, Baker *et al.* in 1996 reviewed all the issues involved, including criticisms of this phenomenological framework.

This model begins with a growth phase that is initiated by a southward turning of the IMF. Before the southward turning there is a distant X-line that separates the magnetic field lines that close in the ionosphere (the auroral oval) from those that are connected to the interplanetary magnetic field (the polar cap). This is considered the ground state and is pictured in panel (a) of Figure 2.3.

At the initiation of the growth phase by the southward turning of the IMF, an X-line is formed at the day-side magnetopause. Figure 2.4 depicts the formation of this X-line and the creation of the associated flows. This figure is a view of what happens in the noon-midnight meridian. Reconnected magnetic flux from the day-side closed magnetic field lines is transported to the open magnetotail lobe fields by the solar wind. A flow is set up, flowing Sunward from the Earth, to feed the reconnection site. This convective flow is retarded by the finite conductivity and self inductance of the ionosphere. The retarded flow is not enough to balance the rate at which magnetic flux reconnects; thus the day-side magnetopause erodes Earthward. The Earthward flow into the reconnection site initiates a rarefaction wave, traveling around the Earth (out of the plane of Figure 2.4) and initiating Earthward flow in the magnetotail.

The erosion of the day-side magnetopause causes flaring and an increase in the dynamic pressure at the magnetopause. This pressure causes the flaring angle to reduce, squeezing the tail. The requirement that the total pressure be balanced on either side of the magnetopause means that the plasma sheet current becomes thin. This is the main result of the NENL model during the growth phase. The end of the growth phase in the NENL model is depicted in panel (b) of Figure 2.3.

At some point the magnetotail current becomes sufficiently thin that magnetic reconnection occurs. The magnetic topology is such that a plasmoid is formed between the new X-line closer to the Earth and the distant X-line. There is strong evidence for the existence of such an X-point in the mid-tail

(X =-20 R_E to -30 R_E) region [13, 138]. The onset of reconnection is depicted in panel (c) of Figure 2.3.

Once this plasmoid is formed, the combination of plasma pressure and magnetic tension causes it to accelerate tailward, taking with it a significant portion of the energy stored in the magnetotail.

2.3 Near Geosynchronous Orbit Model

The difference between the Near Geosynchronous Orbit model (NGO) and the Near Earth Neutral-Line model (NENL) is to be found in the causal nature of the onset of the substorm expansion phase. In the NGO model the substorm is triggered by a plasma instability near geosynchronous orbit (usually between $X = -6$ R_E and -10 R_E). The instability invoked to explain substorm onset in the NGO model is not reconnection. In most NGO models, magnetic reconnection occurs after substorm onset and deeper in the tail. In the NENL model, substorm onset is caused by onset of magnetic reconnection at $X = -20$ R_E to -30 R_E.

The primary evidence for the initiation of substorm onset not being due to the formation of a NENL is that ground-based auroral observations show that the arc brightening at the expansion onset is on field lines that map to $\sim -10R_E$ [64, 66, 67, 122, 162], rather than to the mid-tail region where X-points have been observed. In Section 2.1.2 this evidence was discussed in detail.

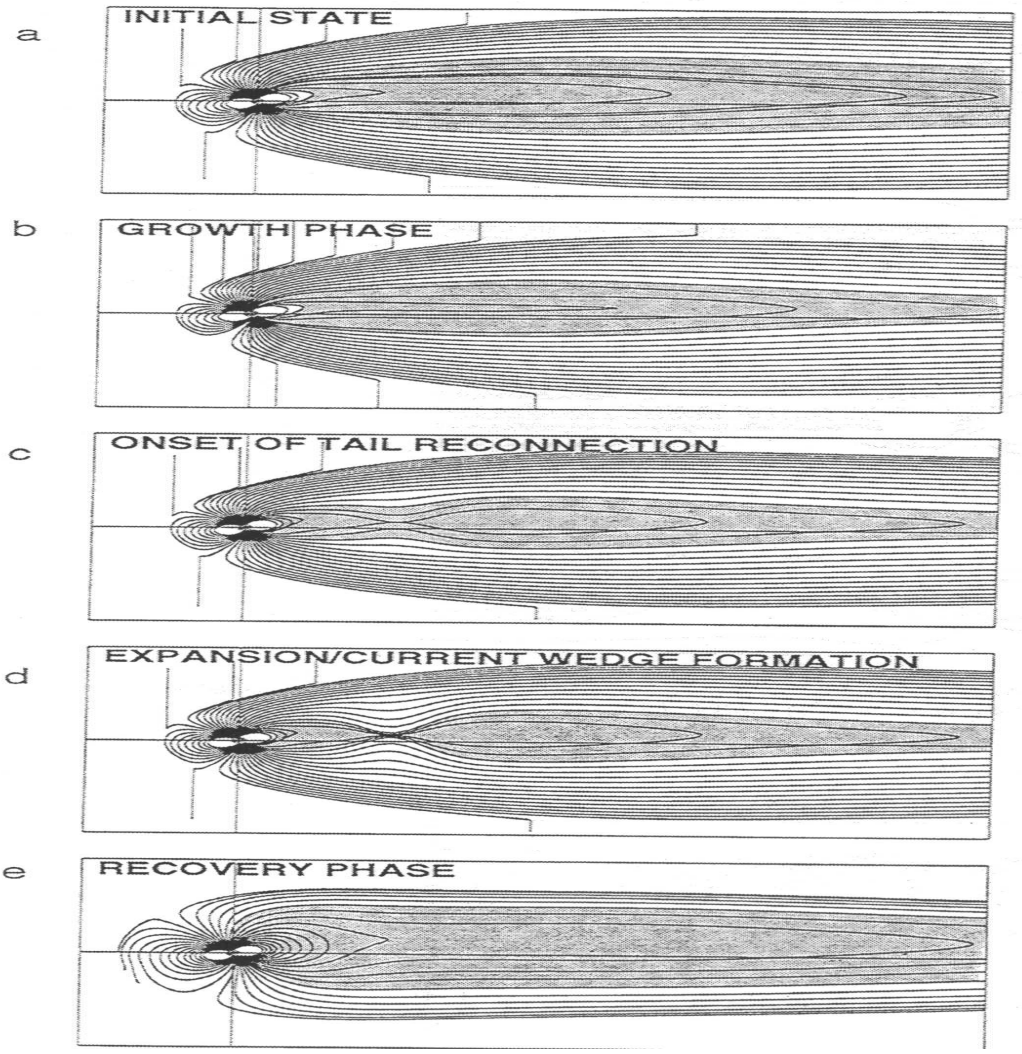

Figure 2.3: Near Earth Neutral Line (NENL) view of substorm sequence of events. Adapted from Baker *et al.* (1996) [16]

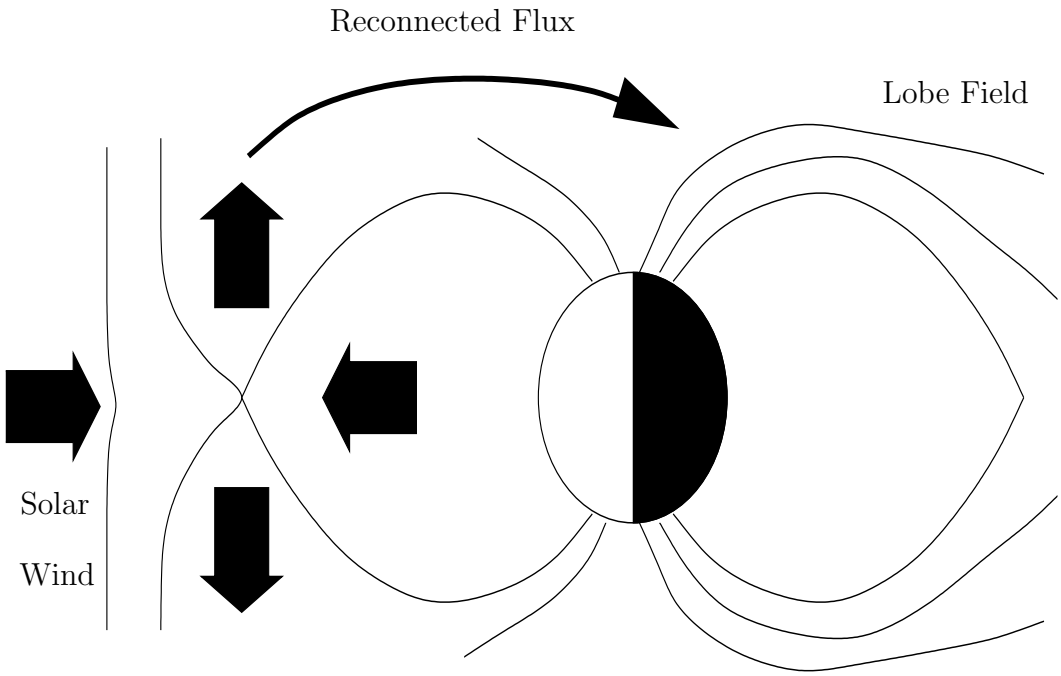

Figure 2.4: Near Earth Neutral Line (NENL) model of flows at initiation of southward IMF

2.4 Synthesis Models

Whether the formation of a near-Earth neutral line is the trigger mechanism for substorm onset or whether it occurs after substorm onset is an open issue. Nagai *et al.* [138], using Pi2 oscillations to define substorm onset, argued that the timing evidence supports the NENL model for substorm onset. In contrast, Lui *et al.* (1998) [125] used data from POLAR and GEOTAIL and came to a different conclusion. They stated that the overall plasma flow pattern during the course of substorms remains ill defined. They showed the details of one event (April 28, 1996) and constructed synoptic charts for both the total flow velocities and the perpendicular flow velocities in the equatorial plane for the relevant space-time domain for 102 events with good geotail coverage. They concluded that strong flows do not necessarily precede substorm onset. Thus, the formation of the NENL may not be the trigger for substorm onset.

Lui *et al.* (1991) introduced a synthesis model to combine the observational evidence for both the formation of a near-Earth neutral-line and an instability at near geosynchronous orbit. In their model a configurational instability occurs at the inner edge of the plasma sheet. This instability generates a finite amplitude compressional/rarefraction wave that travels to the mid-tail region, where the amplitude is large enough for the fluctuating $\delta B_{\|}$ to produce the negative $B_z = \langle B_z \rangle + \delta B_{\|}$ that is necessary to initiate magnetic reconnection and the global reconfiguration of the magnetosphere that is associated with substorms.

Pu *et al.* (1999) [150] proposed an alternative synthesis of the NENL substorm model and the cross-field current disruption model. They observed that the fast Earthward plasma flow produced by magnetic reconnection in the midtail can be abruptly decelerated at the inner edge of the plasma sheet, compressing the plasma and creating the large pressure gradients necessary to drive a ballooning instability. In Chapter 6, we use a one-dimensional transport equation to further investigate the process of pressure gradient steepening due to braking of the Earthward flows.

2.5 Compressional Pulsations

Kepko and Kivelson [101, 102] showed that low-frequency magnetic fluctuations in the Pi2 frequency band (2-25 mHz) [5] that precede substorm onset are associated with increased Earthward $\mathbf{E} \times \mathbf{B}$ flows of greater than 100 km/s. They determined three different classes of Pi2 fluctuations. The first class consists of compressional pulsations with waveforms that have one-to-one correspondence with the waveforms of the flow bursts. These compressional pulses propagate from the near-Earth tail region as fast-mode wave fronts. The second form of compressional Pi2 pulsations are created by the breaking of fast Earthward flows. The compressional waves are generated by inertial currents generated by the breaking flow. These compressional waveforms also have a one-to-one correlation with the variability of the Earthward flow. The final class of Pi2 oscillations are transient response Pi2 oscillations that are driven by pressure gradients and flow shears and whose wave forms are independent

of the variations in the Earthward flow.

Sigsbee *et al.* [169] also reported Pi2 pulsations (2-25 mHz compressional magnetic fluctuations) but observed these oscillations before the initiation of the strongest Earthward flow. In contrast to Kepko and Kivelson [101, 102], they did not determine that the variations in the Earthward flow were correlated with the fluctuations in the magnetic field data. In fact, they found that the time scales of the flow variations were shorter than the time scales of the magnetic field fluctuations associated with Pi2 pulsations. They did, however, agree that the signature of the magnetic oscillations was observed on the ground 1 to 2 minutes after the signature was observed in the near-tail region of the magnetosphere.

Figure 2.5 shows 20 minutes of actual magnetic field data from magnetic field experiment aboard the Wind spacecraft, recorded on October 10, 1996, from 14:00 UT to 14:20 UT. Because the time resolution was 3 seconds the data array for each component of the magnetic field has 400 elements. During the recording of this data the spacecraft was at Geocentric Solar Ecliptic (GSE) (X,Y,Z)=(-8,-1,-0.5) R_E. To create Figure 2.5, the quiet-time magnetic field was computed from an average of the vector components over the first 360 seconds of data. This quiet-time magnetic field was then used to compute the oscillating parallel magnetic field (the compressive component) which is plotted in the figure. In this data one can see low-frequency compressional Pi2 oscillations with period of approximately 25 seconds.

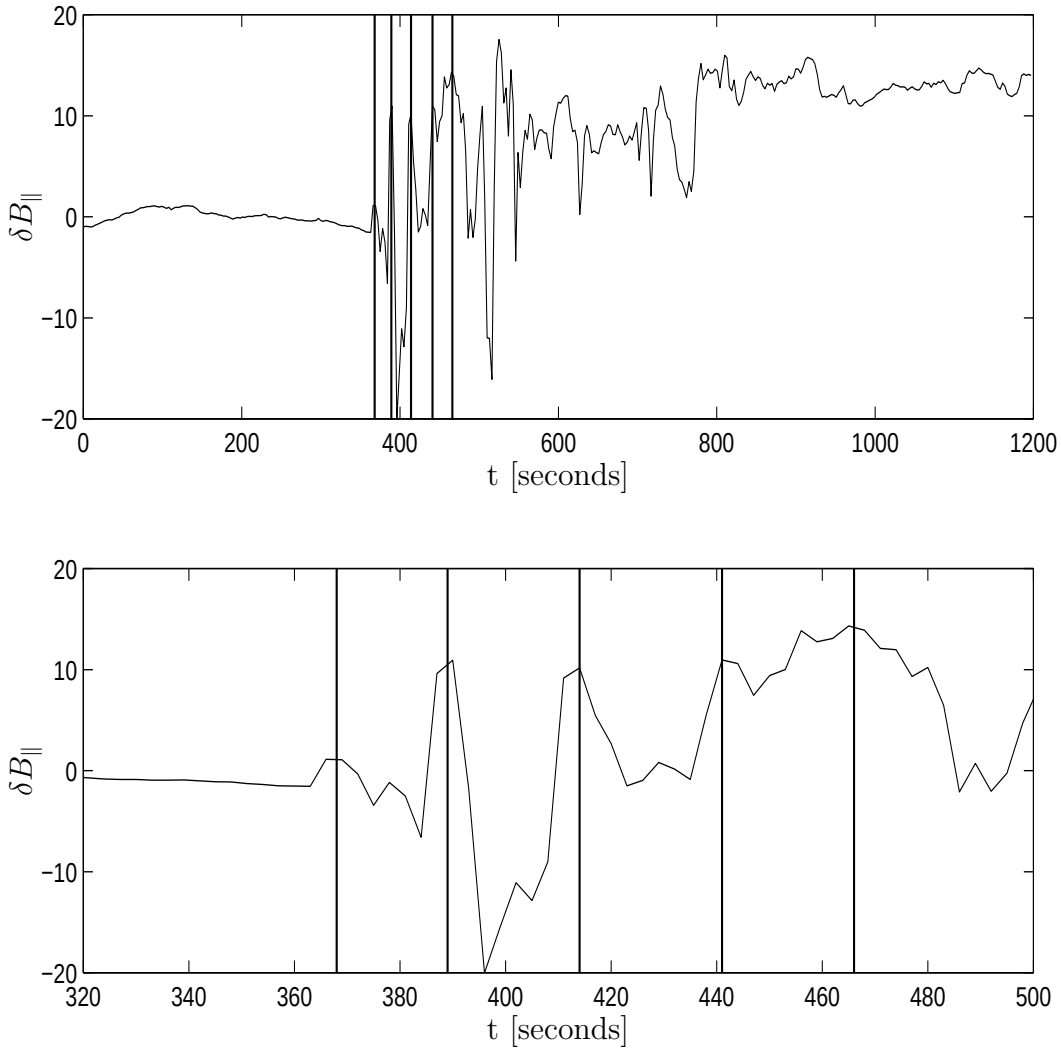

Figure 2.5: Measurements from the magnetic field experiment aboard the Wind spacecraft of Low-Frequency compressional oscillations taken in the equatorial plane at (X,Y,Z)=(-8,-1,-0.5) on October 10, 1996, from 14:00 UT to 14:20 UT. The vertical lines represent the peaks of the oscillation with a period of approximately 25 seconds.

2.6 Conclusions

In this chapter we reviewed the most important features of magnetospheric substorms stage by stage. The remainder of this dissertation explores the stability of magnetic field models, in order to investigate whether plasma instabilities can cause substorm expansion onset. For this reason, the most important observations are the timing and duration of substorm onset events and the observed electric field and magnetic field oscillations observed in the region of the magnetosphere at which substorm onset is observed.

Chapter 3

Ideal Magnetohydrodynamic Stability

Ideal Fast-MHD unstable modes are the most important instabilities to consider in the substorm process since they are the most violent and release the most energy–due to their fast growth rate ($\gamma \gg v_{ti}/L_n$)–over large space scales ($L_\perp \gg \rho_i$). In the near tail of the magnetosphere, there are strongly curved field lines containing a high pressure plasma. For example, Fig. 1.12 shows the sharp curvature of the extended night-side field lines. Since the curvature of the field lines is such that the high pressure is on the concave side (as one sees in Fig. 1.11), one expects ideal MHD ballooning or interchange modes to be unstable. The plasma energy released by these instabilities must, however, overcome the energy required to bend the magnetic field lines and compress the plasma. We determine the stability boundaries for ideal Fast-MHD instabilities. For slower modes we use kinetic theory to determine stability (Chapters 4-6).

Many authors have studied the ideal MHD stability of magnetospheric flux tubes. In particular, Lee and Wolf (1992) [116], used the ideal MHD energy principle $\delta W_p^{\rm MHD}$ of Bernstein *et al.* 1957 [22] and trial functions to investigate the stability of symmetric ballooning modes for various equilibria

numerically. They found no reasonable magnetotail configuration that was unstable to compressible symmetric ballooning modes and stable against interchange modes. All of the equilibria they looked at were stable with respect to interchange. They used "hard" boundary conditions at the ionosphere, taking the ionosphere to be a perfect conductor. Instead of solving an eigenvalue equation, they used trial functions as approximations to the eigenfunctions and simply monitored the sign of $\delta W_p^{\mathrm{MHD}}$. Also, they minimize $\delta W_p^{\mathrm{MHD}}$ with respect to the parallel displacement $\xi_\parallel$. In this case any slightly unstable state violates the criteria under which MHD is valid.

In this chapter we use standard models of the Earth's magnetic field to investigate the night-side region of the magnetosphere for flux tubes that might be unstable to Fast-MHD ballooning-interchange modes. In Section 3.1 the assumptions used in the MHD approximation are stated and statements on the violation of these conditions in the Earth's magnetosphere are made. In Section 3.2 the Tsyganenko magnetic field model is used to determine if the interchange of night-side flux tubes with equal magnetic flux is energetically favorable. In Section 3.3 the equations of Ideal MHD are linearized about an equilibrium and the change in the potential energy $\delta W_p^{\mathrm{MHD}}$ is derived in terms of the plasma displacement vector $\boldsymbol{\xi}$. In Section 3.4 the different ways in which $\delta W_p^{\mathrm{MHD}}$ may be reduced to a tractable form are discussed. Specifically in Section 3.4.1 $\delta W_p^{\mathrm{MHD}}$ is minimized with respect to the parallel component of the plasma displacement $\xi_\parallel$, and the formulation of Lee and Wolf [116] is recovered. In Section 3.4.2 the equation of motion for the parallel plasma

displacement is derived. From this equation it is shown that the classical minimization procedure of Section 3.4.1 is inappropriate and a new condition called Fast-MHD is derived that respects the validity criteria of MHD. In Section 3.4.3 the Fast-MHD minimizing condition is used to derived the Fast-MHD $\delta W_p^{\mathrm{MHD}}$, from which eigenmode equations are derived in Section 3.5. The method for solving the resulting eigenmode equations are also discussed. In Section 3.6 the Fast-MHD eigenmode equation is solved using the Constant Current Model (CCM). Conditions under which the this model are unstable are found and discussed. In Section 3.7 the Fast-MHD eigenmode equation is solved using the Tsyganenko 1996 magnetic field model. Growth rates, eigenmode structures, and stability criteria are found and discussed. Finally, in Section 3.8 conclusions and summary are given of the results of this chapter.

3.1 Limits of MHD

It is important to keep in mind the criteria under which MHD is valid. Typically, MHD is valid for frequencies that are greater than the ion bounce frequency, ω_{bi}, for the mirror motion between the North and South poles and that are less than the ion gyrofrequency: $\omega_{bi} \ll |\omega| \ll \omega_{ci}$. Also, MHD requires that for hot ion plasmas, like that found in the magnetosphere, the perpendicular wavelengths $\lambda_\perp$ be greater than the ion gyroradius: $\lambda_\perp \gg \rho_i$. Drift waves are not treated correctly in the MHD picture because of this approximation and also because the parallel electric fields are neglected. Also, motion parallel to the magnetic field lines is not treated correctly in MHD because the

parallel heat flux is neglected in the pressure equation. The full equation for the pressure is

$$\frac{3}{2}\frac{\partial}{\partial t}\left(nT\right) + \nabla \cdot \left(\frac{3}{2}nT\mathbf{v} + \mathbf{q}\right) + nT\nabla \cdot \mathbf{v} = 0, \tag{3.1}$$

Where $\mathbf{q}$ is the heat flux. For MHD to be valid, the term $\nabla \cdot \mathbf{q}$ must be negligible compared with the terms $\partial_t(3/2nT)$ and $nT\nabla \cdot \mathbf{v}$. The heat flux fluctuation, $\delta\mathbf{q}$, is driven by the temperature fluctuation, δT, according to

$$\delta\mathbf{q} = -C_T n v_t \delta T\, \hat{\mathbf{b}}, \tag{3.2}$$

where C_T is a closure constant of order unity [178]. Now we compare the fluctuations

$$-i\frac{3}{2}\omega n\delta T \tag{3.3}$$

and

$$\nabla \cdot \delta\mathbf{q} = ik_\parallel C_T n v_t \delta T. \tag{3.4}$$

Comparing Eq. (3.3) with Eq. (3.4), we find that there are two regimes depending on the ratio $\omega/k_\parallel v_t$. For negligible heat flux contribution, the motion must be adiabatic, meaning $\omega \gg k_\parallel v_t$. For the slow motions observed in the magnetosphere, the ions are in the regime $\omega \ll k_\parallel v_{ti}$ and thus the heat flux contribution is not negligible. In contrast, the electrons are usually in the isothermal regime with $\omega \ll k_\parallel v_{te}$. For a detailed theory of collisionless closure, see Sugama *et al.* [178].

For waves $(\omega, k_\parallel)$ and fluctuations that are smoothly varying over the mirror field, the parallel motion frequency $k_\parallel v_{tj}$ is comparable to the bounce

frequency ω_{bj}. Therefore the regime $k_\parallel v_{tj} > \omega$ implies the regime $\omega < \omega_{bj}$, in which regime the bounce average of fields must be used. Subsequent chapters deal with the bounce averaged fields and kinetic effects; here we develop the fluid picture.

3.2 Interchange Stability

In this section we will consider whether the interchange of two flux tubes in the dipole-tail transition region of the Earth's magnetosphere is energetically favorable. Thermodynamics is used to calculate the change in pressure with volume during adiabatic and isothermal motions. The Carnot cycle limits the amount of work done by the system. We will follow closely the treatment of Rosenbluth and Longmire in 1957 [156]. If the potential energy of the final state, upon interchange, is lower than the energy of the initial state then it may be assumed that a suitable motion exists to enable the interchange. In MHD it is easy to justify that such a motion exists because the equations of motion follow from minimizing the potential energy, as in mechanics.

The potential energy is the sum of the magnetic field energy $B^2/2\mu_0$ and the internal energy of the plasma $p/(\Gamma - 1)$. Here Γ is the adiabatic gas constant, which varies between 5/3 and 3 for various types of plasma dynamics. The internal plasma energy in a flux tube is given by

$$E_p = \int \frac{p}{\Gamma - 1} \mathrm{d}V = \int \frac{P}{\Gamma - 1} \mathrm{d}s \mathrm{d}A = \int \frac{p}{\Gamma - 1} \Phi \frac{\mathrm{d}s}{B} = \frac{p\Phi}{\Gamma - 1} \int \frac{\mathrm{d}s}{B} \qquad (3.5)$$

where s is the length along the flux tube, $\mathrm{d}A$ is the cross sectional area of

the flux tube, and $\Phi = B\mathrm{d}A$ is the magnetic flux, which is constant along a flux tube. The internal plasma energy in a flux tube can be well estimated by noting that $\mathrm{d}A$ is approximately the typical size of an MHD convection cell, i.e. $\mathrm{d}A \sim 1/k_x k_y$. Recall that the MHD ballooning limit implies $k_x \ll k_y \ll 1/\rho_i$. For a typical ion gyroradius of 300 km this leads to estimates for the wavenumber in the y-direction of $k_y \sim 1/R_E$ and in the x-direction of $k_x \sim 0.1/R_E$. Thus the area of a typical convection cell is $\mathrm{d}A \sim 10\, R_E^2$. For a typical geotail magnetic field intensity of 10 nT, the magnetic flux is $\Phi = 4 \cdot 10^6$ Wb and the flux tube volume V is about $V \sim 10^{22}\,\mathrm{m}^3$. For a typical energy density of 10 nPa, this gives an estimate for the total energy in a flux tube of about $E_p \simeq 10^7$ MJ. A typical interchange/ballooning time scale is $\tau = R_c/v_i = 1R_E/(300\mathrm{km/s}) = 20\mathrm{s}$ so that the power released is of the order 10^6 MW=1 TW.

In any adiabatic motion we have $P \sim V^{-\Gamma}$ so that on interchange of flux tubes labeled 1 and 2, we have

$$P_1' = P_2 \left(\frac{V_2}{V_1}\right)^{\Gamma} \quad \text{and} \quad P_2' = P_1 \left(\frac{V_1}{V_2}\right)^{\Gamma} \tag{3.6}$$

where the prime signifies the final state. Thus the change in internal plasma energy due to the interchange of two flux tubes is given by

$$\Delta E_p = \frac{1}{\Gamma - 1}\left[\left\{P_1 \frac{V_1^{\Gamma}}{V_2^{\Gamma}} V_2 + P_2 \frac{V_2^{\Gamma}}{V_1^{\Gamma}} V_1\right\}_{\text{final}} - \{P_1 V_1 + P_2 V_2\}_{\text{init}}\right]. \tag{3.7}$$

The magnetic energy in a flux tube is

$$E_{\mathrm{M}} = \int \frac{B^2}{2\mu_0} \mathrm{d}V = \frac{\Phi^2}{2\mu_0} \int \frac{\mathrm{d}s}{\mathrm{d}A}. \tag{3.8}$$

When two flux tubes labeled 1 and 2 are interchanged, the change in the magnetic energy is given by

$$\Delta E_{\rm M} = \frac{1}{2\mu_0}\left[\left\{\Phi_1^2\int_2\frac{{\rm d}s}{{\rm d}A}+\Phi_2^2\int_1\frac{{\rm d}s}{{\rm d}A}\right\}_{\rm final}-\left\{\Phi_1^2\int_1\frac{{\rm d}s}{{\rm d}A}+\Phi_2^2\int_2\frac{{\rm d}s}{{\rm d}A}\right\}_{\rm init}\right]. \tag{3.9}$$

Thus, if we exchange two flux tubes that have the same amount of magnetic flux, *i.e.*, $\Phi_1 = \Phi_2$, then $\Delta E_{\rm M} = 0$ and there is no change in the magnetic energy [156].

Figure 3.1 shows the pressure, flux tube volume, and plasma energy as a function of $X\,[R_E]$ for different z-components of the IMF. In this and the following figures the center of the Earth is off scale to the right at $X = 0$ and $X = -1[R_E]$ is the midnight surface of the Earth. Figure 3.2 shows the change in plasma energy, computed from Eq. (3.7), as a function of $X\,[R_E]$ for different z-components of the IMF. The first thing to notice is that for all positions in the magnetotail and for all values of the northward component of the IMF, there is no unstable interchange of flux tubes. However, Figure 3.2 clearly shows that the system is most nearly unstable to interchange motion in the region between $X = -5\,[R_E]$ and $X = -7\,[R_E]$. We know, from Chapter 2, that this region in the near tail maps to the auroral oval. Also, as expected, the most nearly unstable cases occur for the most highly disturbed magnetospheric configurations. As discussed earlier, a good estimate for the wavenumber in the x-direction is $k_x \sim 1/R_E$. The non-linear limit of MHD motion is $k_x\xi^{\rm max} = 1$, which, along with the MHD ordering, implies that a typical interchange motion will be $0.05\,R_E < \xi < 1R_E$. Thus, in all of the interchange calculations in this

chapter, the distance between the two flux tubes for which we are considering an interchange is $\xi^{\text{interchange}} = 0.5R_E$. As discussed in the estimate of the internal energy of the flux tube, all fluxes are taken to be $\Phi_1 = \Phi_2 = 4{\cdot}10^6$ Wb.

3.3 MHD Linear Stability

In this section the linear stability of ideal MHD plasmas is considered. The equations of ideal MHD are linearized about an equilibrium state (*i.e.*, a state in which all of the forces are balanced) and the resulting equations of motion are found in terms of a single field variable, $\boldsymbol{\xi}$, describing the displacement of the plasma from the initial state. The potential energy of the perturbed state is calculated and, as in the interchange problem of Section 3.2, perturbations are sought that reduce the potential energy of the equilibrium and are thus unstable.

For the equilibriums considered here, there is no equilibrium plasma flow or electric field: $\mathbf{u}_0 = \mathbf{E}_0 = 0$. The steady-state magnetosphere actually has a non-zero electric field, $\mathbf{E}_0 \not\simeq 0$, driven by the solar wind; however this complication must be neglected in order to make the analysis tractable. In the geotail, the quiet-time ambient electric field is roughly $\mathbf{E}_0 \simeq 0.1$ mV/m $\hat{\mathbf{e}}_y$, which drives an Earth ward flow of order $\mathbf{u}_0 = u_x \simeq 0.1\text{mV/m}/10\text{nT} \simeq 10$ km/s. The associated cross tail potential is $E_y L_y \simeq 10$ kV.

The linearized MHD description to first order is given in terms of the

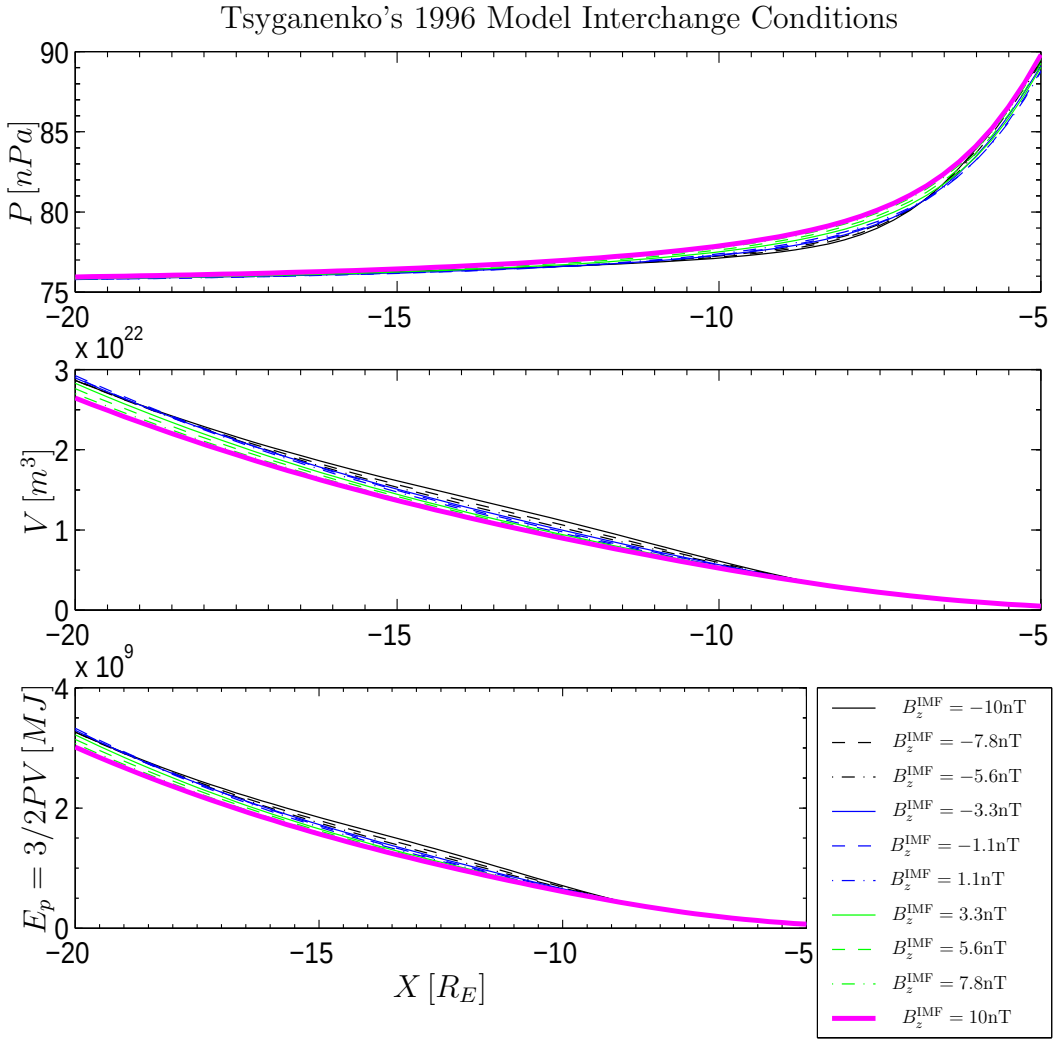

Figure 3.1: The top panel shows the pressure in nPa computed from equilibrium assumptions using $\nabla P = \mathbf{J} \times \mathbf{B}$, the middle panel shows the flux tube volume $V = \int \mathrm{d}s/B$, and the bottom panel shows the plasma energy. Calculation performed with Tsyganenko's 1996 magnetic field model with parameters $PS = 0$, $DST = -50$nT, $B_y^{\rm IMF} = 0.0$, $P_{\rm dyn} = 3.0$nPa. The ten different curves represent different values of the northward component of the IMF field. Flux tubes separated by $0.5\,R_E$ were exchanged.

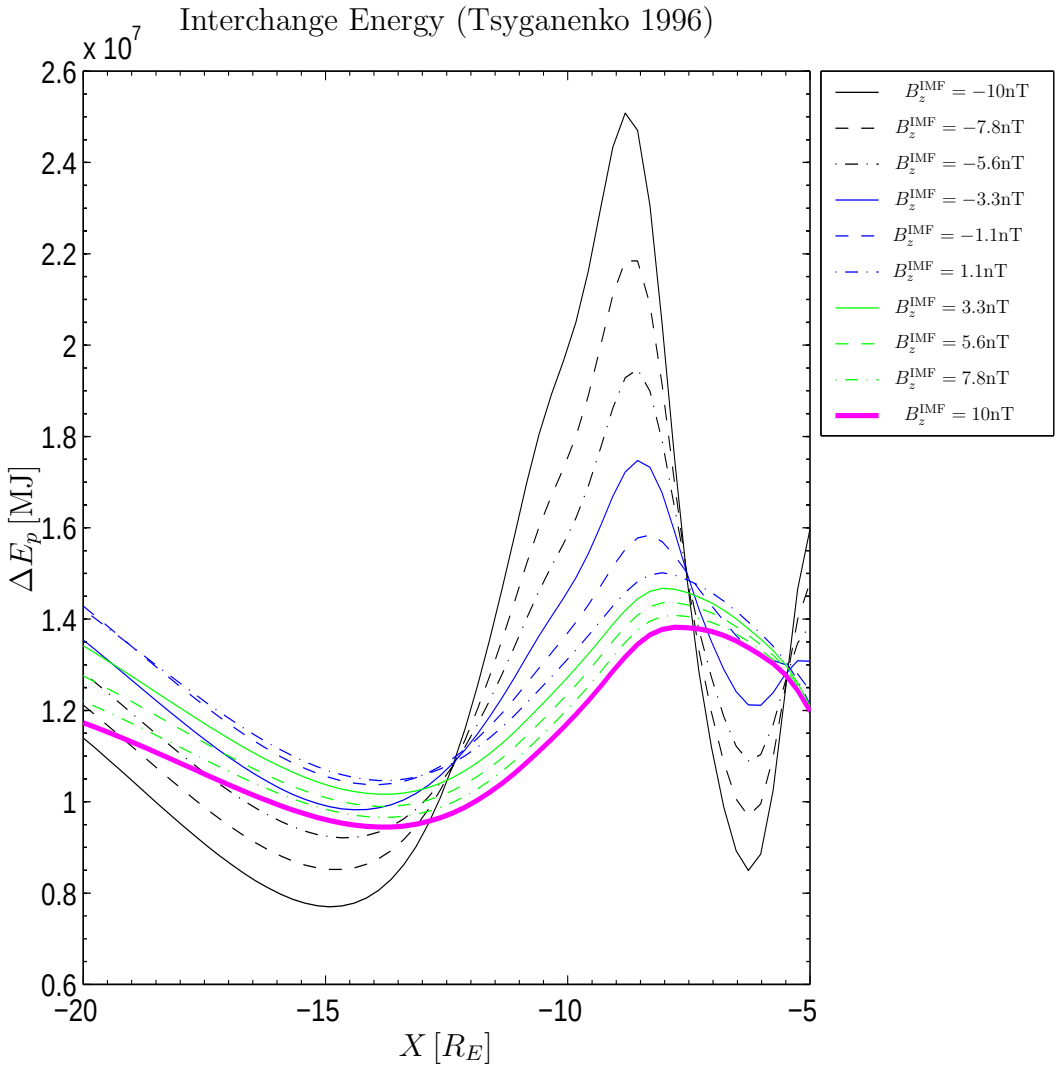

Figure 3.2: Change in energy of the system from interchange of two flux tubes with equal magnetic flux using Eq. (3.7). A positive energy change means it requires energy to undergo the interchange. Calculation performed with Tsyganenko's 1996 magnetic field model with parameters $PS = 0$, $DST = -50$nT, $B_y^{\rm IMF} = 0.0$, $P_{\rm dyn} = 3.0$nPa. The ten different curves represent different values of the northward component of the IMF field. Flux tubes separated by $0.5\,R_E$ were exchanged.

following field variables:

$$\rho(\mathbf{r},t) = \rho_0(\mathbf{r}) + \delta\rho(\mathbf{r},t) \tag{3.10}$$

$$\mathbf{u}(\mathbf{r},t) = \delta\mathbf{u}(\mathbf{r},t) \tag{3.11}$$

$$p(\mathbf{r},t) = p_0(\mathbf{r}) + \delta p(\mathbf{r},t) \tag{3.12}$$

$$\mathbf{J}(\mathbf{r},t) = \mathbf{J}_0(\mathbf{r}) + \delta\mathbf{J}(\mathbf{r},t) \tag{3.13}$$

$$\mathbf{E}(\mathbf{r},t) = \delta\mathbf{E}(\mathbf{r},t) \tag{3.14}$$

$$\mathbf{B}(\mathbf{r},t) = \mathbf{B}_0(\mathbf{r}) + \delta\mathbf{B}(\mathbf{r},t). \tag{3.15}$$

Here, equilibrium quantities are labeled by a subscript 0, and first order quantities are labeled by a preceding δ. Also, $\rho(\mathbf{r},t)$ is the mass per unit volume, $\mathbf{u}(\mathbf{r},t)$ the fluid velocity, $p(\mathbf{r},t)$ the plasma pressure, $\mathbf{J}(\mathbf{r},t)$ the current density, $\mathbf{E}(\mathbf{r},t)$ the electric field, and $\mathbf{B}(\mathbf{r},t)$ the magnetic field. The explicit dependence on space and time will now be assumed in the notation. Ignoring all second-order terms the linearized ideal MHD equations are as follows:

$$\frac{\partial}{\partial t}\delta\rho = -\nabla\cdot(\rho_0\delta\mathbf{u}) \tag{3.16}$$

$$\rho_0\frac{\partial}{\partial t}\delta\mathbf{u} = -\nabla\delta p + \mathbf{J}_0\times\delta\mathbf{B} + \delta\mathbf{J}\times\mathbf{B}_0 \tag{3.17}$$

$$\frac{\partial}{\partial t}\delta p = -\delta\mathbf{u}\cdot\nabla p_0 - \Gamma p_0\nabla\cdot\delta\mathbf{u} \tag{3.18}$$

$$\nabla\cdot\delta\mathbf{B} = 0 \tag{3.19}$$

$$\mu_0\delta\mathbf{J} = \nabla\times\delta\mathbf{B} \tag{3.20}$$

$$\frac{\partial}{\partial t}\delta\mathbf{B} = -\nabla\times\delta\mathbf{E} \tag{3.21}$$

$$\delta\mathbf{E} = -\delta\mathbf{u}\times\mathbf{B}_0 \tag{3.22}$$

Let $\boldsymbol{\xi}$ be the displacement vector of a fluid element from its equilibrium position ($\mathbf{r}_0$), so that $\mathbf{r} = \mathbf{r}_0 + \boldsymbol{\xi}(\mathbf{r}_0, t)$, and

$$\mathbf{u}(\mathbf{r}, t) = \frac{\mathrm{d}}{\mathrm{d}t}\boldsymbol{\xi}(\mathbf{r}_0, t) \simeq \frac{\partial}{\partial t}\boldsymbol{\xi}(\mathbf{r}, t) + O(\delta^2) \tag{3.23}$$

The strategy now is to write all perturbed quantities in terms of the fluid displacement $\boldsymbol{\xi}$. The change in mass density due to motion of the fluid element can be related to the the displacement through mass continuity, Eq. (3.16), as

$$\delta\rho = -\boldsymbol{\xi} \cdot \nabla\rho_0 - \rho_0 \nabla \cdot \boldsymbol{\xi}. \tag{3.24}$$

The change in plasma pressure due to motion of the fluid element can be related to the displacement through the adiabatic equation of state, Eq. (3.18), as

$$\delta p = -\Gamma p_0 \nabla \cdot \boldsymbol{\xi} - \boldsymbol{\xi} \cdot \nabla p_0. \tag{3.25}$$

Inserting Ohm's law, Eq. (3.22), into Faraday's law, Eq. (3.21), yields the usual compact formalism:

$$\frac{\partial}{\partial t}\delta\mathbf{B} = \nabla \times (\delta\mathbf{u} \times \mathbf{B}_0). \tag{3.26}$$

Removing the time derivatives and using the definition of the plasma displacement we can rewrite Faraday's law to show how the magnetic field is perturbed due to motion of the plasma fluid element:

$$\begin{aligned} \delta\mathbf{B} &= \nabla \times (\boldsymbol{\xi} \times \mathbf{B}_0) \\ &= -\boldsymbol{\xi} \cdot \nabla\mathbf{B}_0 + \mathbf{B}_0 \cdot \nabla\boldsymbol{\xi} + \mathbf{B}_0 \nabla \cdot \boldsymbol{\xi}. \end{aligned} \tag{3.27}$$

Often in MHD linear stability analysis, the perturbed magnetic field is called $\mathbf{Q} = \delta\mathbf{B}$, and the magnitude of the perturbed magnetic field as seen in the frame of the moving plasma is written as

$$Q_L = -B\left(\nabla \cdot \boldsymbol{\xi}_\perp + 2\boldsymbol{\xi} \cdot \boldsymbol{\kappa}\right), \tag{3.28}$$

where $\boldsymbol{\kappa} = \hat{\mathbf{b}} \cdot \nabla\hat{\mathbf{b}}$ is the curvature vector and $\hat{\mathbf{b}} = \mathbf{B_0}/B_0$ is the unit vector in the direction of the equilibrium magnetic field. Another important quantity is the perturbed parallel magnetic field $Q_\parallel$, which can be computed using the important identity $\boldsymbol{\kappa} = -\hat{\mathbf{b}} \times (\nabla \times \hat{\mathbf{b}})$:

$$Q_\parallel = Q_L - \boldsymbol{\xi}_\perp \cdot \nabla B_0 + B_0 \boldsymbol{\xi} \cdot \boldsymbol{\kappa}. \tag{3.29}$$

Finally, the momentum equation, Eq. (3.17) can be written in terms of $\boldsymbol{\xi}$ as

$$\begin{aligned}
\rho_0 \frac{\partial^2 \boldsymbol{\xi}}{\partial t^2} &= \nabla\left(\Gamma p_0 \nabla \cdot \boldsymbol{\xi} + \boldsymbol{\xi} \cdot \nabla p_0\right) + \mathbf{J}_0 \times \delta\mathbf{B} + \delta\mathbf{J} \times \mathbf{B}_0 \\
&= \nabla\left(\Gamma p_0 \nabla \cdot \boldsymbol{\xi} + \boldsymbol{\xi} \cdot \nabla p_0\right) + \frac{1}{\mu_0}(\nabla \times \mathbf{B}_0) \times \delta\mathbf{B} \qquad (3.30) \\
&\quad + \frac{1}{\mu_0}(\nabla \times \delta\mathbf{B}) \times \mathbf{B}_0. \qquad (3.31) \\
&\equiv \mathbf{F}(\boldsymbol{\xi})
\end{aligned}$$

The operator $\mathbf{F}$ is the force acting on a fluid element. It is a linear self-adjoint operator, as shown in Friedberg [2], which means that

$$\int \mathrm{d}^3 r \boldsymbol{\eta} \cdot \mathbf{F}(\boldsymbol{\xi}) = \int \mathrm{d}^3 r \boldsymbol{\xi} \cdot \mathbf{F}(\boldsymbol{\eta}). \tag{3.32}$$

The kinetic energy of the perturbation is defined as

$$K = \frac{1}{2}\int \mathrm{d}r^3 \frac{\partial \boldsymbol{\xi}^\dagger}{\partial t} \cdot \frac{\partial \boldsymbol{\xi}}{\partial t}, \tag{3.33}$$

and the potential energy is

$$\delta W = -\frac{1}{2}\int \mathrm{d}^3 r \boldsymbol{\xi}^\dagger \cdot \mathbf{F}(\boldsymbol{\xi}). \tag{3.34}$$

It is straightforward to show that the total energy is conserved, *i.e.*, $H = K + \delta W$ is constant:

$$\frac{\partial}{\partial t}H = \frac{\partial}{\partial t}(K + \delta W) = \frac{1}{2}\int \mathrm{d}^3 r \rho_0 \frac{\partial \boldsymbol{\xi}}{\partial t} \cdot \frac{\partial^2 \boldsymbol{\xi}}{\partial t^2} - \frac{1}{2}\frac{\partial}{\partial t}\int \mathrm{d}^3 r \boldsymbol{\xi} \cdot \mathbf{F}(\boldsymbol{\xi}) \tag{3.35}$$

We can use the momentum equation, Eq. (3.17), and the self-adjoint property of the operator $\mathbf{F}(\boldsymbol{\xi})$ to show that

$$\begin{aligned} \frac{\partial}{\partial t}K = \int \mathrm{d}^3 r \rho_0 \frac{\partial \boldsymbol{\xi}}{\partial t} \cdot \frac{\partial^2 \boldsymbol{\xi}}{\partial t^2} &= \int \mathrm{d}^3 r \frac{\partial \boldsymbol{\xi}}{\partial t} \cdot \mathbf{F}(\boldsymbol{\xi}) \\ &= \frac{1}{2}\int \mathrm{d}^3 r \frac{\partial \boldsymbol{\xi}}{\partial t} \cdot \mathbf{F}(\boldsymbol{\xi}) + \frac{1}{2}\int \mathrm{d}^3 r \boldsymbol{\xi} \cdot \mathbf{F}(\frac{\partial \boldsymbol{\xi}}{\partial t}). \end{aligned}$$

The time derivative of the potential energy is

$$\frac{\partial}{\partial t}K = -\frac{1}{2}\int \mathrm{d}^3 r \frac{\partial \boldsymbol{\xi}}{\partial t} \cdot \mathbf{F}(\boldsymbol{\xi}) - \frac{1}{2}\int \mathrm{d}^3 r \boldsymbol{\xi} \cdot \mathbf{F}(\frac{\partial \boldsymbol{\xi}}{\partial t}) \tag{3.36}$$

so that

$$\frac{\partial}{\partial t}\left(K + \delta W\right) = 0 \tag{3.37}$$

or $K(\boldsymbol{\xi}, \boldsymbol{\xi}) + \delta W(\boldsymbol{\xi}, \boldsymbol{\xi})$ =constant. If $\delta W > 0$ for all allowable $\boldsymbol{\xi}$, then one sees that unbounded growth of the kinetic energy, corresponding to exponential instability violates energy conservation. Thus $\delta W > 0$ is sufficient for stability. It can also be shown that $\delta W < 0$ implies instability [2]. Note that δW and K are second-order quantities in $\boldsymbol{\xi}$.

Using the definition of the force operator in Eq. (3.31) we can write δW in an intuitive form [2]. Switching the volume integration to our local flux tube variables (Ψ, y, s) we write the MHD plasma energy functional as

$$\delta W_p^{\mathrm{MHD}} = \frac{1}{2}\int \frac{\mathrm{d}\Psi \mathrm{d}y \mathrm{d}s}{B}\left[\Gamma p(\nabla\cdot\boldsymbol{\xi})^2 + \mathbf{Q}_\perp{}^2 + Q_L^2 - 2\boldsymbol{\xi}\cdot\boldsymbol{\kappa}\boldsymbol{\xi}\cdot\nabla p\right]. \quad (3.38)$$

The first term on the right-hand side of Eq. (3.38) represents plasma compression, with Γ the adiabatic index. The second and third terms represent field line bending and magnetic field compression, respectively, and the fourth term is the destabilizing term due to the pressure gradient. Note the subscript on equilibrium quantities is now dropped.

It is important to understand the physical mechanism behind the destabilizing term and the source of the instability. Figure 3.3 depicts the instability. The radial plasma displacement vector ξ_r has a sinusoidal component in the $\hat{\mathbf{y}}$-direction. Thus, as the eigenfunction balloons in the equatorial plane due to a random perturbation, fingers are formed in the $x-y$ plane and charge separation occurs. This charge separation causes an electric field, which leads to an $\mathbf{E}\times\mathbf{B}$ drift that pushes the plasma in the same direction as the initial perturbation. Thus a positive feedback system is set up and the instability grows exponentially.

3.4 Minimizing $\delta W_p^{\mathrm{MHD}}$

To determine the stability of a system using Eq. (3.38), it is advantageous first to perform as many analytical operations as possible to minimize

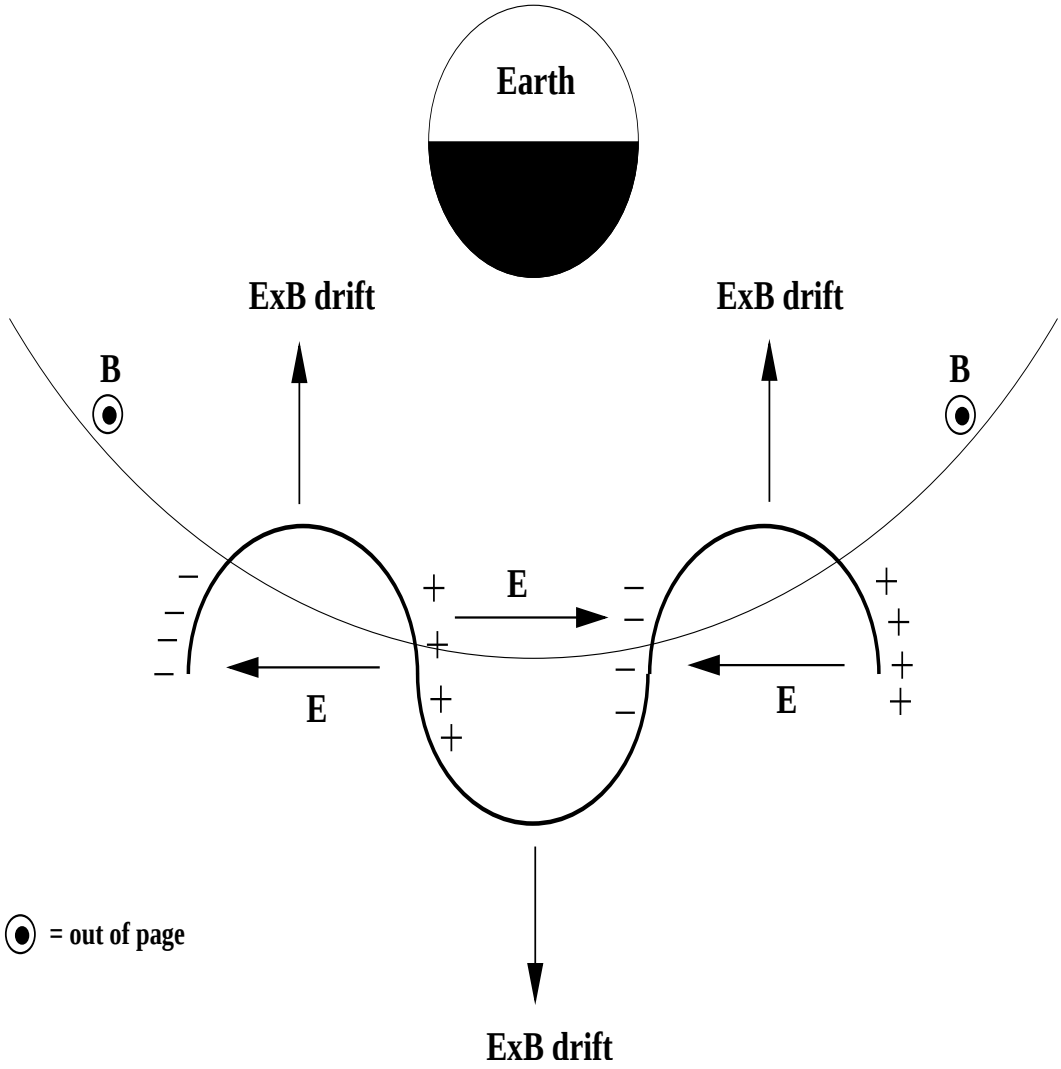

Figure 3.3: Diagram of the ballooning-interchange dynamics in the equatorial plane. Perturbation generates charge separation in the $\hat{\mathbf{y}}$ direction, the resulting electric field creates an $\mathbf{E} \times \mathbf{B}$ drift motion that drives Ballooning/Interchange instability exponentially.

the potential energy. However, we must do so in a way that maintains the level of description implied by the MHD approximation. In this section we will perform the analytic minimizations and explore their validity. The most crucial minimization is to note that $\xi_\parallel$ occurs in $\delta W_p^{\rm MHD}$ only in the plasma compression term, $\nabla \cdot \boldsymbol{\xi}$. Thus we can take the first variation of $\delta W_p^{\rm MHD}$ with respect to the field variable $\xi_\parallel$, find the form of $\xi_\parallel$ that minimizes $\delta W_p^{\rm MHD}$, and use this form to construct a new $\delta W_p^{\rm MHD}$ that has one less field component and is thus more tractable to stability analysis. This is the procedure followed in the classical minimization procedure described in Friedberg [2] and followed by most authors in the space physics literature [113–116].

3.4.1 Classical minimization procedure

The first variation of $\delta W_p^{\rm MHD}$, Eq. (3.38), with respect to $\xi_\parallel$ can be written as

$$\delta(\delta W_p^{\rm MHD})_{\xi_\parallel} = \frac{1}{2}\int \frac{{\rm d}\Psi {\rm d}y{\rm d}s}{B}\Gamma p(\nabla\cdot\boldsymbol{\xi})\left(\nabla\cdot\xi_\parallel\frac{\mathbf{B}}{B}\right) \tag{3.39}$$

where $\delta\xi_\parallel$ is the formal variable used in computing the first variation of $\delta W_p^{\rm MHD}$ with respect to $\xi_\parallel$. We integrate by parts, noting that the boundary term vanishes due to $\boldsymbol{\xi} = 0$ at the boundaries and $\mathbf{n}\cdot\mathbf{B} = 0$ at the volume boundaries of the plasma, *i.e.* in the $\hat{\mathbf{y}}$ and $\nabla\Psi$ directions; also, we make use of the equilibrium relation $\mathbf{b}\cdot\nabla p = 0$ to rewrite Eq. (3.39) as

$$\delta(\delta W_p^{\rm MHD})_{\xi_\parallel} = \frac{1}{2}\int \frac{{\rm d}\Psi {\rm d}y{\rm d}s}{B}\Gamma p\hat{\mathbf{b}}\cdot\nabla(\nabla\cdot\delta\boldsymbol{\xi})\delta\xi_\parallel = 0 \tag{3.40}$$

If the variation with respect to $\xi_\parallel$ is to vanish for arbitrary $\delta\xi_\parallel$, we must have

$$\mathbf{b}\cdot\nabla(\nabla\cdot\boldsymbol{\xi})=0, \tag{3.41}$$

which means that the plasma compression is constant along the flux tube. Since $\nabla\cdot\boldsymbol{\xi}$ is independent of distance along the magnetic field line, s, if we rewrite the compression as

$$\nabla\cdot\boldsymbol{\xi}=\nabla\cdot\boldsymbol{\xi}_\perp+\mathbf{B}\cdot\nabla\left(\frac{\xi_\parallel}{B}\right) \tag{3.42}$$

and integrate along a magnetic field line with $\int \mathrm{d}s/B$, we find

$$\nabla\cdot\boldsymbol{\xi}=\frac{\int\frac{\mathrm{d}s}{B}\nabla\cdot\boldsymbol{\xi}_\perp}{\int\frac{\mathrm{d}s}{B}}=\langle\nabla\cdot\boldsymbol{\xi}_\perp\rangle\,. \tag{3.43}$$

Here the angle brackets $\langle\,\rangle$ refer to the flux tube volume averaging operation defined in Eq. (3.43). Using this new minimized value of $\nabla\cdot\boldsymbol{\xi}$, we can rewrite the ideal MHD plasma functional as

$$\delta W_p^{\mathrm{MHD}}=\frac{1}{2}\int\frac{\mathrm{d}\Psi\mathrm{d}y\mathrm{d}s}{B}\left[\Gamma p\,\langle\nabla\cdot\boldsymbol{\xi}_\perp\rangle^2+\mathbf{Q}_\perp{}^2+Q_L^2-2\boldsymbol{\xi}\cdot\boldsymbol{\kappa}\boldsymbol{\xi}\cdot\nabla p\right]. \tag{3.44}$$

Next note that we can treat $\nabla\cdot\boldsymbol{\xi}_\perp$ as a field variable and perform a minimization with respect to this variable. The first variation with respect to $\nabla\cdot\boldsymbol{\xi}_\perp$ can be written as

$$\delta(\delta W_p^{\mathrm{MHD}})_{\nabla\cdot\boldsymbol{\xi}_\perp}=\int\frac{\mathrm{d}\Psi\mathrm{d}y\mathrm{d}s}{B}\left[\Gamma p\,\langle\nabla\cdot\boldsymbol{\xi}_\perp\rangle+B^2(\nabla\cdot\boldsymbol{\xi}_\perp+2\xi_\perp\cdot\kappa)\right]\delta(\nabla\cdot\boldsymbol{\xi}_\perp). \tag{3.45}$$

For this variation to vanish requires

$$\Gamma p\,\langle\nabla\cdot\boldsymbol{\xi}_\perp\rangle+B^2(\nabla\cdot\boldsymbol{\xi}_\perp+2\boldsymbol{\xi}_\perp\cdot\boldsymbol{\kappa})=0. \tag{3.46}$$

Performing a line average, we can rewrite the requirement of Eq. (3.46) as

$$\langle \nabla \cdot \boldsymbol{\xi}_\perp \rangle = \frac{-2 \int \frac{\mathrm{d}s}{B} \boldsymbol{\xi}_\perp \cdot \boldsymbol{\kappa}}{\int \frac{\mathrm{d}s}{B} \left(1 + \frac{\Gamma p_0}{B^2}\right)}. \tag{3.47}$$

Substituting Eqs. (3.47) and (3.46) into Eq. (3.44), we find

$$\delta W_p^{\mathrm{MHD}} = \int \frac{\mathrm{d}\Psi \mathrm{d}y \mathrm{d}s}{B} \left[\mathbf{Q}_\perp^2 - 2\boldsymbol{\xi} \cdot \boldsymbol{\kappa} \boldsymbol{\xi} \cdot \nabla p\right] + \int \mathrm{d}\Psi \mathrm{d}y \frac{4\Gamma p \left| \int \frac{\mathrm{d}s}{B} \boldsymbol{\xi} \cdot \boldsymbol{\kappa} \right|^2}{\int \frac{\mathrm{d}s}{B} \left(1 + \frac{\mu_0 \Gamma p}{B^2}\right)} \tag{3.48}$$

Our final simplification is achieved by making the ballooning approximation, *i.e.*, $k_y \to \infty$. First, the perturbed magnetic field is written in terms of our local flux tube variables (Ψ, y, s):

$$\begin{aligned} \mathbf{Q} &= \nabla \times (\boldsymbol{\xi} \times \mathbf{B}_0) = \nabla \times (\xi^\Psi \hat{\mathbf{y}} - \xi^y \nabla \Psi) \\ &= \nabla \xi^\Psi \times \hat{\mathbf{y}} - \nabla \xi^y \times \nabla \Psi. \end{aligned} \tag{3.49}$$

where the equilibrium magnetic field has the representation $\mathbf{B}_0 = \hat{\mathbf{y}} \times \nabla \Psi$. Then the perpendicular component is found to be

$$\mathbf{Q}_\perp = \frac{1}{B_0} (\hat{\mathbf{b}} \cdot \nabla \xi^\Psi) \nabla \Psi - (\hat{\mathbf{b}} \cdot \nabla \xi^y) B_0 \hat{\mathbf{y}} \tag{3.50}$$

By taking the divergence of $\mathbf{Q}$ and using Maxwell's equation that prohibits magnetic monopoles we find that Eq. (3.50) shows that the ballooning requirement of $k_y \to \infty$ implies that ξ^y plays no role in the perturbed magnetic field:

$$\mathbf{Q}_\perp = \frac{1}{B_0} \frac{\partial \xi^\Psi}{\partial s} \nabla \Psi. \tag{3.51}$$

Hence the magnetic field perturbation will be confined to a particular meridian in the magnetosphere. Using the ballooning approximation and considering

only a single flux tube at a time, we recover Lee and Wolf's $\delta W_p^{\rm MHD}$ formulation [116]:

$$\delta W_p^{\rm MHD} = \int \frac{\mathrm{d}s}{B}\left[\left(\frac{\partial \xi^\Psi}{\partial s}\right)^2 - 2\boldsymbol{\xi}\cdot\boldsymbol{\kappa}\boldsymbol{\xi}\cdot\nabla p\right] + \frac{4\Gamma p\left|\int \frac{\mathrm{d}s}{B}\boldsymbol{\xi}\cdot\boldsymbol{\kappa}\right|^2}{\int \frac{\mathrm{d}s}{B}\left(1+\frac{\mu_0\Gamma p}{B^2}\right)} \tag{3.52}$$

Notice that this final form of $\delta W_p^{\rm MHD}$ has only one field variable $\xi^\Psi(s)$ which Lee and Wolf [116] call X(s). This field variable is dependent only on the distance along the equilibrium magnetic field, s.

3.4.2 Parallel Displacement

We now consider parallel motion, represented by $\xi_\parallel$, and examine whether the minimization condition of the previous section is appropriate under the MHD approximation. Define the unit vector $\mathbf{b}(\mathbf{r}) = \mathbf{B}_0/\|\mathbf{B}_0\|$ parallel to the unperturbed magnetic field. Then the parallel component of the fluid displacement is $\xi_\parallel = \mathbf{b}\cdot\boldsymbol{\xi}$, and the parallel component of the momentum equation is

$$\begin{aligned}\rho_0\frac{\partial^2}{\partial t^2}\xi_\parallel &= \mathbf{b}\cdot\mathbf{F}(\boldsymbol{\xi}) \\ &= \mathbf{b}\cdot\nabla\left(\Gamma p_0\nabla\cdot\boldsymbol{\xi} + \boldsymbol{\xi}\cdot\nabla p_0\right) + \frac{1}{\mu_0}\mathbf{b}\cdot(\nabla\times\mathbf{B}_0)\times\delta\mathbf{B}\end{aligned} \tag{3.53}$$

Using the definition of $\mathbf{b}$ and the commutativity of the vector triple product, we obtain

$$\mathbf{b}\cdot\mathbf{J}_0\times\delta\mathbf{B} = \frac{1}{B_0}(\mathbf{B}_0\times\mathbf{J}_0)\cdot\delta\mathbf{B}. \tag{3.54}$$

From the equilibrium relation $\mathbf{J}\times\mathbf{B}_0 = \nabla p_0$, we have

$$\mathbf{b}\cdot\mathbf{J}_0\times\delta\mathbf{B} = -\frac{1}{B_0}\nabla p_0\cdot\delta\mathbf{B}. \tag{3.55}$$

Inserting the definition of $\delta\mathbf{B}$, we rewrite Eq. (3.55) as

$$\mathbf{b}\cdot\mathbf{J}_0\times\delta\mathbf{B}=-\frac{1}{B_0}\nabla p_0\cdot\nabla\times(\boldsymbol{\xi}\times\mathbf{B}_0). \tag{3.56}$$

With the vector identity $\nabla\cdot(\mathbf{A}\times\mathbf{B})=\mathbf{B}\cdot\nabla\times\mathbf{A}-\mathbf{A}\cdot\nabla\times\mathbf{B}$, this becomes

$$\mathbf{b}\cdot\mathbf{J}_0\times\delta\mathbf{B}=\frac{1}{B_0}\nabla\cdot(\nabla p_0\times(\boldsymbol{\xi}\times\mathbf{B}_0)). \tag{3.57}$$

The vector identity $\mathbf{A}\times(\mathbf{B}\times\mathbf{C})=(\mathbf{A}\cdot\mathbf{C})\mathbf{B}-(\mathbf{A}\cdot\mathbf{B})\mathbf{C}$ gives

$$\mathbf{b}\cdot\mathbf{J}_0\times\delta\mathbf{B}=\frac{1}{B_0}\nabla\cdot(\mathbf{B}_0\cdot\nabla p_0\boldsymbol{\xi}-\mathbf{B}_0\boldsymbol{\xi}\cdot\nabla p_0). \tag{3.58}$$

Using the fact that the pressure is constant along a flux surface, $\mathbf{b}\cdot\nabla p_0=0$, we obtain

$$\mathbf{b}\cdot\mathbf{J}_0\times\delta\mathbf{B}=-\frac{1}{B_0}\nabla\cdot(\mathbf{B}_0(\boldsymbol{\xi}\cdot\nabla p_0)). \tag{3.59}$$

Finally, using the vector identity $\nabla\cdot(f\mathbf{A})=f\nabla\cdot\mathbf{A}+\mathbf{A}\cdot\nabla f$ and Maxwell's equation for the divergence of a magnetic field $\nabla\cdot\mathbf{B}_0=0$, we derive

$$\mathbf{b}\cdot\mathbf{J}_0\times\delta\mathbf{B}=-\mathbf{b}\cdot\nabla(\boldsymbol{\xi}\cdot\nabla p_0). \tag{3.60}$$

Therefore, the parallel equation of motion is

$$\rho_0\frac{\partial^2\xi_\parallel}{\partial t^2}=\mathbf{b}\cdot\nabla(\Gamma p_0\nabla\cdot\boldsymbol{\xi}). \tag{3.61}$$

Decompose the plasma displacement vector $\boldsymbol{\xi}=\boldsymbol{\xi}_\perp+\xi_\parallel\mathbf{b}$, so that

$$\nabla\cdot\boldsymbol{\xi}=\nabla\cdot\boldsymbol{\xi}_\perp+\mathbf{B}_0\cdot\nabla\frac{\xi_\parallel}{B_0}. \tag{3.62}$$

Equation (3.61) becomes

$$\rho_0\frac{\partial^2\xi_\parallel}{\partial t^2}=\mathbf{b}\cdot\nabla(\Gamma p_0\nabla\cdot\boldsymbol{\xi}_\perp)+\Gamma p_0\mathbf{b}\cdot\nabla(B_0\mathbf{b}\cdot\nabla\frac{\xi_\parallel}{B_0}). \tag{3.63}$$

Let $\partial/\partial t \rightarrow -i\omega$ and $\mathbf{b}\cdot\nabla \rightarrow ik_{\parallel}$, then Eq. (3.63) is

$$-\rho_0\omega^2\xi_{\parallel} \simeq -k_{\parallel}^2\Gamma p_0\xi_{\parallel} + \Gamma p_o \mathbf{b}\cdot\nabla\nabla\cdot\boldsymbol{\xi}_{\perp} \tag{3.64}$$

, from which we obtain the parallel displacement:

$$\xi_{\parallel} = \frac{-\mathbf{b}\cdot\nabla(\Gamma p_0\nabla\cdot\boldsymbol{\xi}_{\perp})}{\rho_0\omega^2 - k_{\parallel}^2\Gamma p_0}. \tag{3.65}$$

Taking the limit $\rho_0\omega^2 \ll k_{\parallel}^2\Gamma p_0$, which corresponds to taking $\omega \ll k_{\parallel}v_{ti}$, we have

$$\xi_{\parallel} = \frac{1}{k_{\parallel}^2}\mathbf{b}\cdot\nabla(\nabla\cdot\boldsymbol{\xi}_{\perp}). \tag{3.66}$$

The expression for $\xi_{\parallel}$ in Eq. (3.66) is precisely the same as that obtained in Eqs. (3.41) and (3.42), for which $\delta W_p^{\mathrm{MHD}}$ is minimized with respect to $\xi_{\parallel}$ perturbations. In Section 3.1 it was stated that the limit $\omega \ll k_{\parallel}v_{ti}$ is not appropriately treated by ideal MHD, because in this limit the equations should be bounce-averaged over the mirroring motion of the particles. For this reason, the classical minimization procedure is not appropriate for magnetotail plasmas.

Now, taking the limit $\rho_0\omega^2 \gg k_{\parallel}^2\Gamma p_0$ in Eq. (3.65), which limit corresponds to taking $\omega \gg k_{\parallel}v_{ti}$, we obtain

$$\xi_{\parallel} = 0 \tag{3.67}$$

from Eq. (3.65). In Section 3.1 it was stated that the limit $\omega \gg k_{\parallel}v_{ti}$ is appropriately treated by the MHD approximation. Thus, taking $\xi_{\parallel} = 0$ rather than the expression in Eq. (3.66), is justified and will allow $\delta W_p^{\mathrm{MHD}}$ to be simplified

by removing its dependence on $\xi_\parallel$. The condition $\xi_\parallel = 0$ is called Fast-MHD. The Fast-MHD condition is not the absolute minimization of $\delta W_p^{\mathrm{MHD}}$. Thus Fast-MHD solutions may predict stability for cases where slow MHD solutions predict a slowly growing instability. In order to investigate the more slowly growing solutions, we will use kinetic theory in later chapters.

3.4.3 Fast-MHD

As mentioned in the previous section we are primarily interested in the fast-growing instabilities for which MHD is valid. In particular, this requires that $|\omega| \gg \omega_{bi} \sim k_\parallel v_{ti}$, as stated in Section (3.1). This implies that we are not looking for a minimizing condition like that of Lee and Wolf [116]. Instead, we want the Fast-MHD condition given by $\xi_\parallel = 0$.

With $\xi_\parallel = 0$, the displacement can be written as

$$\boldsymbol{\xi} = \frac{\hat{\mathbf{b}} \times \mathbf{A}_\perp}{B} \tag{3.68}$$

where $\mathbf{A}_\perp$ is the perpendicular component of the perturbed magnetic vector potential:

$$\mathbf{A}_\perp = A_\Psi \nabla\Psi + B\nabla_\perp \frac{\phi}{B}. \tag{3.69}$$

Thus, we have

$$\boldsymbol{\xi} = -\hat{\mathbf{y}} A_\Psi + \hat{\mathbf{b}} \times \nabla_\perp \frac{\phi}{B}. \tag{3.70}$$

Recall that $\boldsymbol{\xi}$ is an infinitesimal motion of the plasma. The representation of Eq. (3.70) shows that the dominant contribution to this motion comes from

the $\mathbf{E} \times \mathbf{B}$ drift:

$$\frac{\mathbf{E} \times \mathbf{B}}{B^2} = i\omega \left[-A_\Psi \hat{\mathbf{y}} + \hat{\mathbf{b}} \times \nabla_\perp \frac{\phi}{B} \right] \tag{3.71}$$

where we used

$$\mathbf{E}_\perp = -\frac{\partial \mathbf{A}_\perp}{\partial t} = i\omega \mathbf{A}_\perp \tag{3.72}$$

Thus ϕ represents the field line displacement through the frozen-in condition and the $\mathbf{E}\times\mathbf{B}$ drift velocity, and A_Ψ represents the magnetic field compression. The perpendicular component of the perturbed magnetic field, $\mathbf{Q}_\perp$, is then found to be

$$\mathbf{Q}_\perp = ik_y \frac{\partial \phi}{\partial s} \mathbf{b} \times \mathbf{y} + O\left(\frac{\kappa}{k_y}\right) \tag{3.73}$$

In the ballooning limit, $k_y \to \infty$, terms of order κ/k_y are neglected. This ballooning limit was also used in the classical minimization procedure presented in Section 3.4.1 and the results are equivalent when one considers that $\xi^\Psi = ik_y\phi$. The following identities are useful in expressing the $\delta W_p^{\mathrm{MHD}}$ in terms of the two field variables ϕ and A_Ψ:

$$Q_L = -\frac{\boldsymbol{\kappa} \cdot \nabla \Psi}{B} \xi^\Psi + ik_y B A_\Psi \tag{3.74}$$

$$\xi^\Psi = \boldsymbol{\xi} \cdot \nabla \Psi = \hat{\mathbf{b}} \times \nabla_\perp \frac{\phi}{B} \cdot \nabla \Psi = ik_y \phi \tag{3.75}$$

$$\boldsymbol{\xi} \cdot \boldsymbol{\kappa} = \frac{\boldsymbol{\kappa} \cdot \nabla \Psi}{B^2} \xi^\Psi \tag{3.76}$$

$$\nabla \cdot \boldsymbol{\xi} = -\boldsymbol{\xi} \cdot \boldsymbol{\kappa} - ik_y A_\Psi \tag{3.77}$$

$$\boldsymbol{\xi} \cdot \nabla p = \xi^\Psi \frac{\partial p}{\partial \Psi}. \tag{3.78}$$

Recall that $\boldsymbol{\xi}$ is the displacement vector, measured in meters, describing the motion of the flux tube, and $|\xi^\Psi| = B\xi$ is the displacement in flux (Wb/m=T·m).

Note that, it is ξ^{Ψ} that is constant along a field-line for a flute-type interchange motion. Thus, for flute-type interchange motions, $\boldsymbol{\xi}$ decreases strongly from the equatorial plane approaching the Earth due to the increase in the magnitude of the magnetic field. This notion applies to Equations (3.76) through (3.78) as well, demonstrating the importance of the deep magnetic well.

Expressing $\delta W_p^{\mathrm{MHD}}$ in terms of the field variables ϕ and A_Ψ, we can then minimize with respect to A_Ψ and find the polarization of the most unstable perturbations:

$$A_\Psi = \frac{2-\Gamma\beta}{2+\Gamma\beta}\frac{\boldsymbol{\kappa}\cdot\nabla\Psi}{B^2}\phi. \tag{3.79}$$

Using Eq. (3.79), we find the Fast-MHD change in potential energy:

$$\delta W_p^{\mathrm{MHD}} = k_y^2 \int \frac{\mathrm{d}\Psi \mathrm{d}y \mathrm{d}s}{B}\left[\left(\frac{\partial\phi}{\partial s}\right)^2 + \frac{4\Gamma\beta}{2+\Gamma\beta}\frac{(\boldsymbol{\kappa}\cdot\nabla\psi)^2}{B^2}\phi^2 - 2\frac{\boldsymbol{\kappa}\cdot\nabla\Psi}{B^2}\frac{\partial p}{\partial\Psi}\phi^2\right]. \tag{3.80}$$

The first term on the right-hand side is the change in potential energy due to the bending of the magnetic field line:

$$\delta W_{\mathrm{Bend}}^{\mathrm{FMHD}} = k_y^2 \int \frac{\mathrm{d}\Psi \mathrm{d}y \mathrm{d}s}{B}\left(\frac{\partial\phi}{\partial s}\right)^2. \tag{3.81}$$

The second term is the change in potential energy due to compression:

$$\delta W_{\mathrm{Comp}}^{\mathrm{FMHD}} = k_y^2 \int \frac{\mathrm{d}\Psi \mathrm{d}y \mathrm{d}s}{B}\frac{4\Gamma\beta}{2+\Gamma\beta}\frac{(\kappa\cdot\nabla\psi)^2}{B^2}\phi^2. \tag{3.82}$$

The final term is the driving energy released in the ballooning-interchange motion

$$\delta W_{\mathrm{Drive}}^{\mathrm{FMHD}} = -2k_y^2 \int \frac{\mathrm{d}\Psi \mathrm{d}y \mathrm{d}s}{B}\frac{\kappa\cdot\nabla\Psi}{B^2}\frac{\partial p}{\partial\Psi}\phi^2. \tag{3.83}$$

3.5 Fast-MHD eigenvalue equation

The eigenmode equation for Fast MHD may be obtained by forming a Lagrangian with the kinetic energy due to the plasma displacement and the minimized potential energy due to the plasma displacement. The resulting Euler-Lagrange equation is the eigenvalue equation presented in this section. Notice that we follow the notation of Lee and Wolf [116] here by calling $X(s) = ik_y\phi = \xi^{\Psi}$ the eigenmode. The Fast-MHD eigenvalue equation is thus given by

$$\frac{\mathrm{d}}{\mathrm{d}s}\left(\frac{1}{B}\frac{\mathrm{d}X}{\mathrm{d}s}\right) + \left[2\mu_0\frac{\kappa_c}{B^2}\frac{\partial p}{\partial \Psi} - \frac{4\mu_0\Gamma p}{B}\left(\frac{\kappa_c}{B}\right)^2\frac{1}{1+\frac{\mu_0\Gamma p}{B^2}}\right]X + \frac{\mu_0\rho}{B^3}\omega^2 X = 0, \tag{3.84}$$

with

$$\kappa_c = \frac{\boldsymbol{\kappa}\cdot\nabla\Psi}{B} \tag{3.85}$$

$$\frac{\partial p}{\partial \Psi} = -\frac{1}{\mu_0}\left[\frac{\partial B_x}{\partial z} - \frac{\partial B_z}{\partial x}\right]. \tag{3.86}$$

If define,

$$P(s) = \frac{1}{B(s)} \tag{3.87}$$

$$Q(s) = -2\mu_0\frac{\kappa_c}{B^2}\frac{\partial p}{\partial \Psi} + \frac{4\mu_0\Gamma p}{B}\left(\frac{\kappa_c}{B}\right)^2\frac{1}{1+\frac{\mu_0\Gamma p}{B^2}} \tag{3.88}$$

$$R(s) = \frac{\mu_0\rho}{B^3}, \tag{3.89}$$

then Eq. (3.84) can be rewritten as

$$\frac{\mathrm{d}}{\mathrm{d}s}\left(P(s)\frac{\mathrm{d}X}{\mathrm{d}s}\right) - Q(s)X + \omega^2 R(s)X = 0. \tag{3.90}$$

In order to solve Eq. (3.90) numerically we discretize it using

$$\frac{\mathrm{d}}{\mathrm{d}s}\left(P(s)\frac{\mathrm{d}X}{\mathrm{d}s}\right) \rightarrow \frac{1}{h}\left[P_{i+1/2}\left(\frac{X_{i+1}-X_i}{h}\right) - P_{i-1/2}\left(\frac{X_i - X_{i-1}}{h}\right)\right], \quad (3.91)$$

where

$$\begin{aligned} s_i &= a + ih & (3.92)\\ s_{i\pm 1/2} &= s_i \pm \frac{h}{2} & (3.93)\\ h &= \frac{b-a}{N-1}. & (3.94)\\ & & (3.95) \end{aligned}$$

The differential eigenvalue equation can now be posed as a standard matrix eigenvalue problem,

$$\sum_{j=1}^{N}\left[a_i\delta_{i-1,j} + b_i\delta_{i,j} + c_i\delta_{i+1,j}\right]X_j = -\omega^2 X_i, \quad (3.96)$$

where the matrix elements are given by

$$\begin{aligned} a_i &= \frac{P_{i-1/2}}{R_i h^2} & (3.97)\\ b_i &= -\left(a_i + c_i + \frac{Q_i}{R_i}\right) & (3.98)\\ c_i &= \frac{P_{i+1/2}}{R_i h^2}. & (3.99) \end{aligned}$$

Matrix elements can be computed by using a magnetic field model from Chapter 1 to compute the field lines and associated quantities. Once a matrix is formed, the LAPACK library is used to compute the eigenvalues and eigenvectors of the matrix. The eigenvector is then identified with the discretized eigenfunction. It is found that excellent convergence may be obtained by considering 100 points along the magnetic field line.

3.6 MHD Stability of the Constant Current Model

3.6.1 Without 2D Dipole Field

In this section we set the two-dimensional dipole field to zero. This approximation is valid if we are primarily interested in solutions that are confined to the magnetotail. Thus the boundary, of perfect conductivity, is at the edge of the central plasma sheet rather than at the ionosphere Without the two-dimensional dipole field we find that the equations greatly simplify. In this limit the magnetic field only depends on the z coordinate, and derivatives with respect to s, the distance along the field line, can be written in terms of the z coordinate. The bending term can be rewritten:

$$B\frac{\mathrm{d}}{\mathrm{d}s}\left(\frac{1}{B}\frac{\mathrm{d}X}{\mathrm{d}s}\right) = B_n^2\frac{\mathrm{d}}{\mathrm{d}z}\left(\frac{1}{B^2}\frac{\mathrm{d}X}{\mathrm{d}z}\right). \tag{3.100}$$

The inertia term remains the same:

$$\frac{\omega^2}{V_A^2} = \frac{\mu_0\rho\omega^2}{B^2} \tag{3.101}$$

The term involving the pressure gradient and the curvature that drives the instability can be rewritten:

$$2\mu_0\frac{\kappa_c}{B}\frac{\partial p}{\partial\Psi} = 2\left(\frac{B_nB_x'}{B^2}\right)^2. \tag{3.102}$$

The stabilizing term representing the energy required to compress the plasma becomes:

$$4\mu_0\Gamma p\left(\frac{\kappa_c}{B}\right)^2\frac{1}{1+\frac{\mu_0\Gamma p}{B^2}} = 4\mu_0\Gamma p\left(\frac{B_n^2B_x'}{B^4}\right)^2\frac{1}{1+\frac{\mu_0\Gamma p}{B^2}}. \tag{3.103}$$

Putting all the terms together, the Fast-MHD eigenvalue equation of Eq. (3.84) can be written as

$$B_n^2 \frac{\mathrm{d}}{\mathrm{d}z}\left(\frac{1}{B^2}\frac{\mathrm{d}X}{\mathrm{d}z}\right) + \left(\frac{\mu_0\rho\omega^2}{B^2} + 2\left(\frac{B_n B_x'}{B^2}\right)^2\right) X = 4\mu_0\Gamma p \left(\frac{B_n^2 B_x'}{B^4}\right)^2 \frac{X}{1+\frac{\mu_0\Gamma p}{B^2}}. \tag{3.104}$$

We can make this equation non-dimensional by introducing a distance unit $L = B_n/B_x'$. Then the magnetic field magnitude is simply $B(z) = B_n(1 + z^2/L^2)^{1/2}$. Using the definition $\beta_0 = 2\mu_0 p/B_n^2$, identifying $\lambda = \mu_0\rho\omega^2 L^2/B_n^2$, and measuring z in units of L, *i.e.*, $\zeta = z/L$ we can write the differential eigenvalue equation in terms of the single parameter $\Gamma\beta_0$ as follows:

$$(1+\zeta^2)\frac{\mathrm{d}}{\mathrm{d}\zeta}\left[\frac{1}{1+\zeta^2}\frac{\mathrm{d}X}{\mathrm{d}\zeta}\right] + \left[\lambda + \frac{2}{1+\zeta^2}\right] X = \frac{2\Gamma\beta_0}{(1+\zeta^2)^2}\frac{X}{1+\zeta^2+\Gamma\beta_0/2} \tag{3.105}$$

Making the identifications

$$\begin{aligned} P(\zeta) &= \frac{1}{1+\zeta^2} \\ Q(\zeta) &= \frac{-2}{(1+\zeta^2)^2} + \frac{2\Gamma\beta_0}{(1+\zeta^2)^3}\frac{1}{1+\zeta^2+\Gamma\beta_0/2} \\ R(\zeta) &= \frac{1}{1+\zeta^2}, \end{aligned}$$

we can use our numerical technique from the previous section to compute growth rates and eigenfunctions.

Figure 3.4 shows the eigenvalues $\lambda = \mu_0\rho\omega^2 L^2/B_n^2$ in the top panel as a function of β. We find that for $\beta \lesssim 4.24$, this equilibrium model is unstable to Fast-MHD perturbations. For $\beta \gtrsim 4.24$, this equilibrium model is stable to Fast-MHD perturbations. The bottom panel of Figure 3.4 shows three

eigenfunctions for three different values of β. The most unstable eigenfunctions are very peaked near the equatorial plane ($\zeta = 0$). As β increases to the critical β value, the eigenfunctions develop symmetrical maximum that are slightly displaced from the equatorial plane. Completely stable eigenfunctions have maxima clearly away from $\zeta = 0$.

Figure 3.5 shows the absolute magnitude of the different components of the Fast-MHD $\delta W_p^{\rm MHD}$, these components being given by Eqs. (3.81), (3.82), and (3.83). Two different calculations are presented Figure 3.5. The top panel shows the different components of $\delta W_p^{\rm MHD}$ computed with the CCM model under the assumption that the perturbation is a flute-mode, *i.e.* $X(s) = 1$. Here one clearly sees that the stabilization at high β occurs due to the increasing amount of energy required to compress the plasma. This high-β stabilization due to compressibility was first pointed out by Horton *et al.* [93]. They defined two critical β values, between which, $\beta_1 < \beta < \beta_2$ the magnetotail was defined to be unstable to Fast-MHD ballooning-interchange motions. For magnetotail equilibria with a plasma β below β_1 the fast ballooning-interchange motions are stabilized by the energy required to bend the magnetic field. The bottom panel of Figure 3.5 shows evidence for the increasing role of bending at small β values. For $\beta > \beta_2$, the fast ballooning-interchange motions are stabilized due to the energy required to compress the plasma. For the CCM model Horton *et al.* [93] estimated $\beta_2 \sim 2 - 3$, and we clearly reproduce this result.

In the bottom panel of Fig. 3.5 the same $\delta W_p^{\rm MHD}$ components are computed, this time using the actual eigenfunctions shown in Fig. 3.4. Now we

find that the CCM model is not stabilized at low β by the energy required to bend the magnetic field; instead for $\beta \lesssim 4.24$, this model is always unstable. In addition, as β becomes larger, the energy required to compress the plasma is reduced although it remains the dominant stabilizing factor. These more unstable eigenfunctions minimize the role that compression plays, while maximizing the destabilizing influence of the driving term.

3.6.2 With 2D dipole field

With the addition of the 2D dipole field to the constant current model, we can no longer make the transformation in the eigenmode equation to z. Computations must be performed along the magnetic field line, and the real variable s must be used. Nevertheless, the same numerical procedure can be used as presented in Section 3.5. For these computations the parameters used in the model were taken to match closely the parameters of particular flux tubes found from the Tsyganenko 1996 magnetic field model.

In Fig. 3.6 the properties of one particular flux tube are shown. In Fig. 3.7 the solution of the Fast-MHD eigenmode equation is shown for different values of β imposed on the flux tube. For this CCM model one sees that the bending energy never totally compensates the interchange drive term since unstable eigenmodes exist even at $\beta = 0$. However, as the plasma pressure increases, the flux tube is again stabilized by the compressional energy. For the CCM model with a 2D dipole field, we reproduce the upper critical β_2. We find this value to be approximately $\beta_2 = 2.9$, which is less than the critical β found

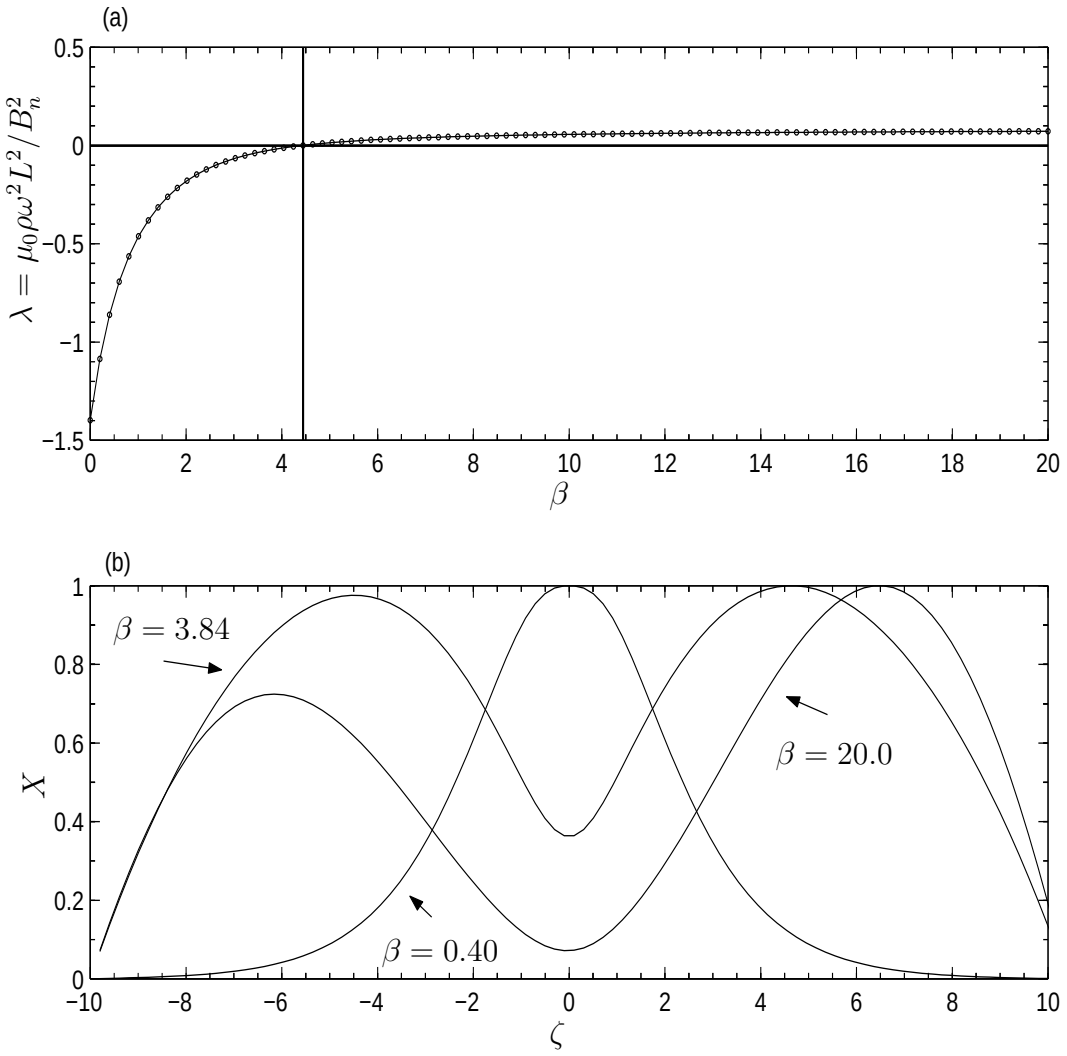

Figure 3.4: a.) The top panel shows the eigenvalues of the Fast-MHD differential eigenvalue equation with the CCM model and no dipole field as a function of β. The vertical line denotes the β value ($\beta \simeq 4.24$) for which higher β values yield a positive eigenvalue. Positive eigenvalues represent stable equilibriums. b.) The bottom panel shows three eigenfunctions X as a function of the dimensionless variable ζ along the field line for the β values corresponding to 0.40, 3.84, and 20.0. For this figure 100 values of β were considered, $\Gamma = 5/3$ and there were 100 grid points along the field line.

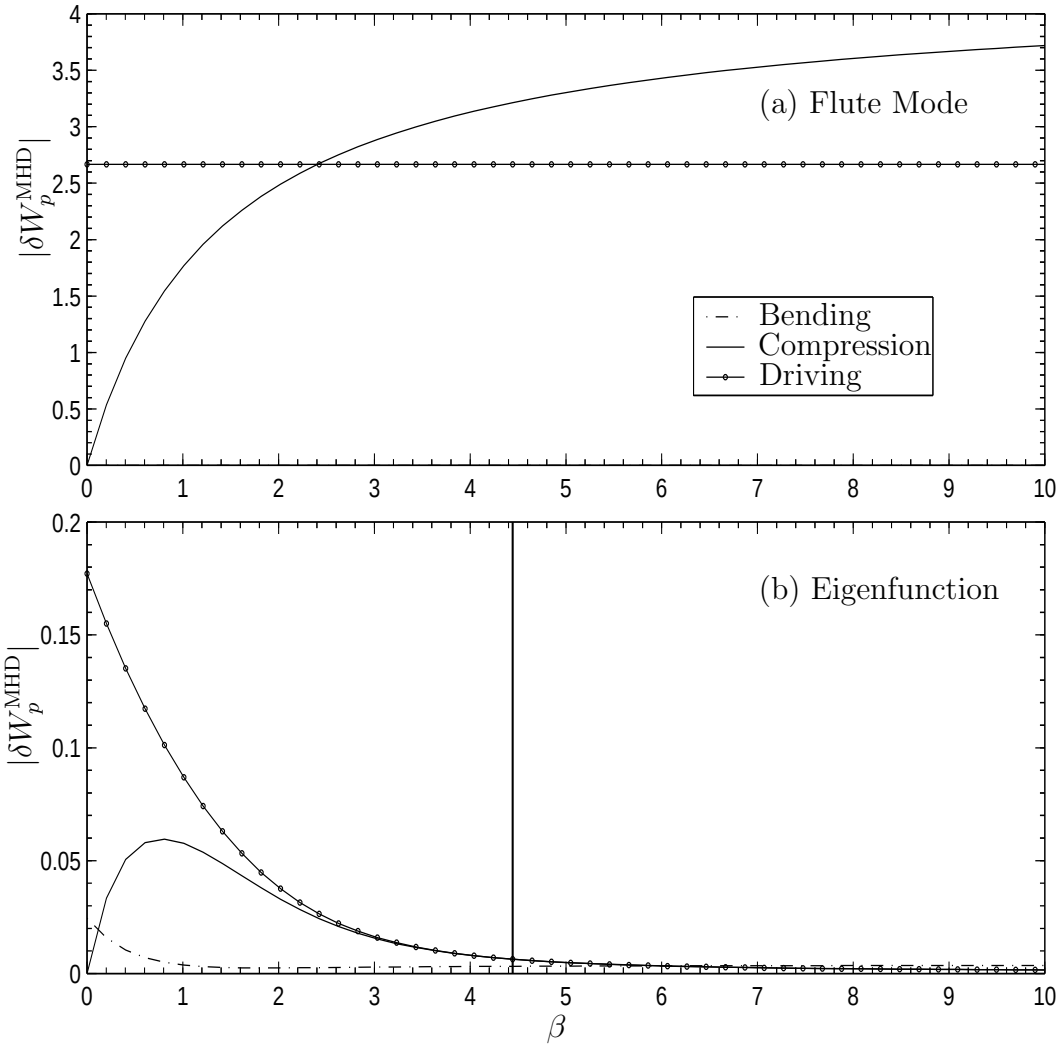

Figure 3.5: a.) The top panel shows the absolute magnitude of the different components of $\delta W_p^{\rm MHD}$ computed using a flute mode $\phi = 1$. b.) The bottom panel shows the absolute magnitude of the different components of $\delta W_p^{\rm MHD}$ computed using the actual eigenfunctions computed in Fig. 3.4. The vertical line denotes the β value ($\beta \simeq 4.24$) for which higher β values yield a positive eigenvalue. For this figure 100 values of β were considered, $\Gamma = 5/3$ and there were 100 grid points along the field line.

without the dipole field. Another feature of note is the highly ballooning character of the unstable eigenfunctions. They are strongly peaked in the equatorial plane, which is the region of maximum curvature, whereas the stable eigenfunctions have their maximum located near the ionosphere.

3.7 MHD Stability of the Tsyganenko 1996 Magnetic Field

To compute the MHD stability of Tsyganenko's 1996 empirical magnetic field model, it is necessary to make the assumption that this model is in an equilibrium state. There have been several efforts to verify that this model is in an approximate equilibrium state, notably Horton *et al.* 1993 [86] and Zaharia *et al.* 2002 [193]. The conclusion is that, to a fair approximation, one may assume that computing the plasma pressure by integrating the equilibrium relation $\mathbf{J} \times \mathbf{B} = \nabla p$ along the axis of the magnetotail gives a pressure that is in good agreement with an equilibrium, however, as seen in Chapter 1 this pressure tends to overestimate pressures observed in the magnetosphere.

Figure 3.8 shows the properties of a single flux tube in the Noon-Midnight meridian with an equatorial foot-point of -8 R_E. Note that the magnetic well, is very deep, so deep that we expect all of the particles to be confined. The other extremely important feature to notice is the magnitude of the curvature vector $\boldsymbol{\kappa} = \hat{\mathbf{b}} \cdot \nabla \hat{\mathbf{b}}$ as a function of the distance along the field line. The curvature is extremely peaked at the equatorial plane. The pressure assigned to this flux tube is 2.7 nPa, computed with the use of ISEE data of

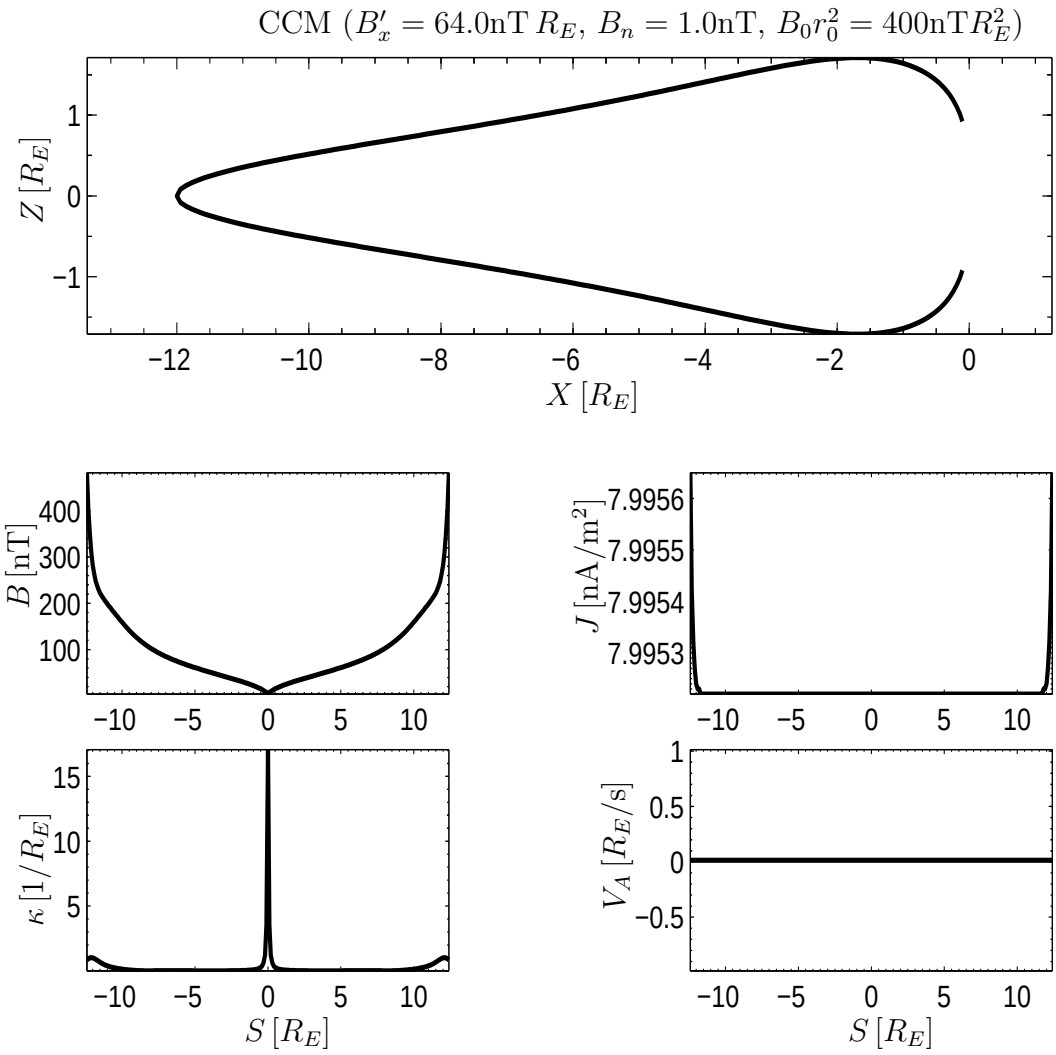

Figure 3.6: Properties of a single flux tube computed using the CCM magnetic field model. This flux tube was used in solving the Fast-MHD eigenmode equation shown in Fig. 3.7. The top panel shows the magnetic field line defining the flux tube. The bottom four panels show the magnitude of the magnetic field, the inverse of the radius of curvature κ, the current density and the Alfvén velocity all a function of the distance along the field line.

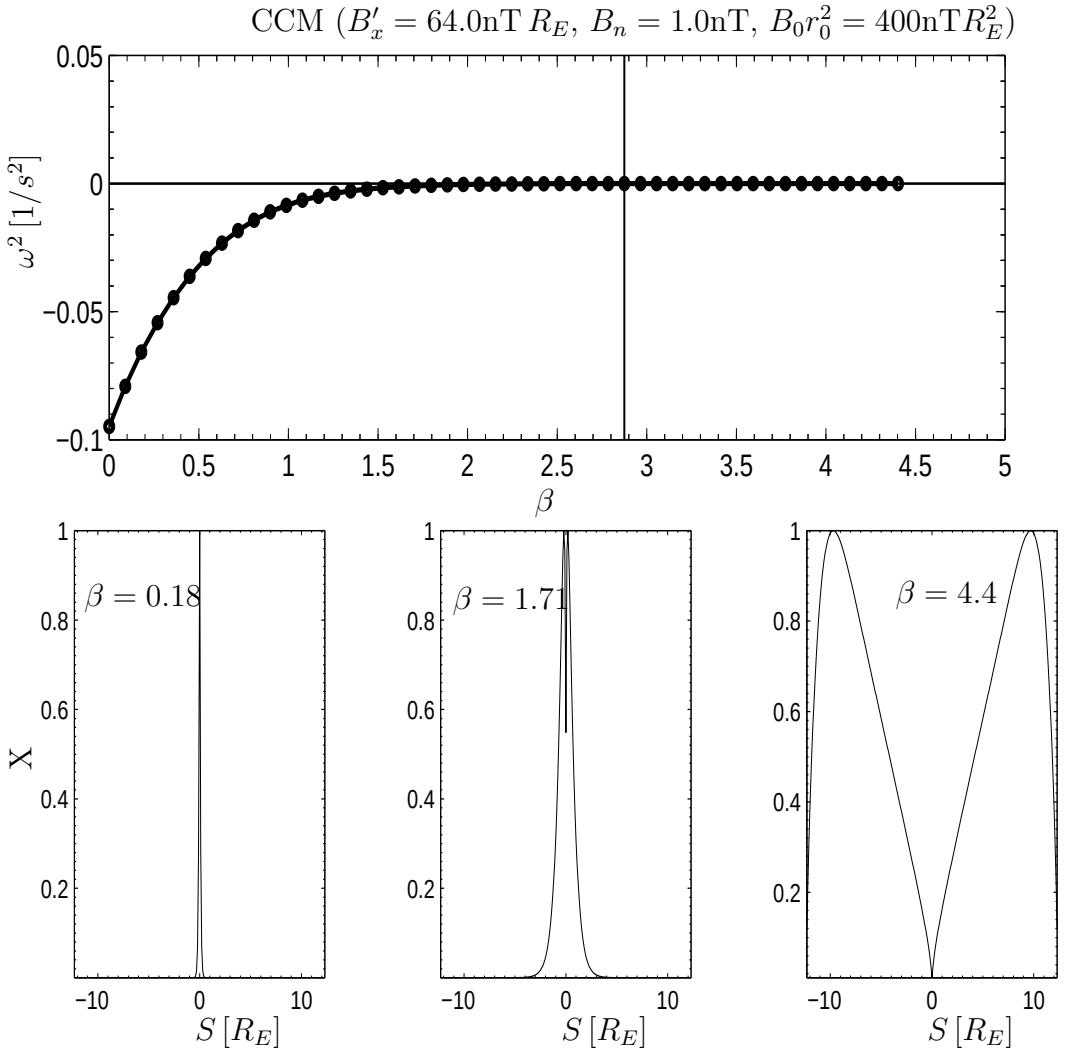

Figure 3.7: Solution of the Fast-MHD eigenmode equation as a function of β for the flux tube explored in Fig. 3.6. In the top panel the eigenvalue ω^2 is plotted as a function of β. The critical $\beta_2 \simeq 2.9$ is represented by the solid vertical line. In the bottom three panels the eigenfunctions for different β values are plotted as a function of s the distance along the field line.

0.06 nPa at -30 R_E and integrating $\mathbf{J} \times \mathbf{B}$ along the magnetotail. Figure 3.9 shows the eigenvalues and four of the most unstable eigenfunctions computed from the Fast-MHD eigenmode equation. We see that this flux tube is completely stable to Fast-MHD ballooning perturbations at a plasma pressure of 2.7 nPa. For this computation we used Lysak's model for the mass density [127, 128].

Figure 3.10 also shows the eigenvalues and four of the most unstable eigenfunctions computed from the Fast-MHD eigenmode equation. The difference between Fig. 3.10 and 3.9 is that the former takes the Alfvén velocity to be constant along the field line. The value taken for the constant value is computed at the equatorial plane. All authors that have previously reported linear ideal MHD stability results have assumed that the Alfvén velocity velocity is constant. We note however that the magnitude of the magnetic field is strongly varying along the flux tubes, and therefore the Alfvén velocity is also strongly varying. We find that accounting for the variation of the Alfvén velocity along the flux tube is a stabilizing influence and modifies the structure of the eigenmodes.

In Figure 3.11 the Fast MHD eigenmode equation is solved as a function of X in units of R_E with Tsyganenko's 1996 model for the magnetic field. In this calculation we computed the plasma pressure by assuming that the magnetic field model was in equilibrium and then integrating $\nabla P = \mathbf{J} \times \mathbf{B}$ along the magnetotail from $X = -30\,[R_E]$, where satellite data suggest the plasma pressure should be $P = 0.06$ nPa. Figure 3.11 shows the plasma β,

as well as the inverse radius of curvature and the magnitude of the magnetic field, as a function of the equatorial crossing point of the flux tube. We clearly see that ballooning-interchange motion is stable throughout the entire magnetotail. The flux tubes further away from the Earth are closer to marginal stability, which is due to a reduction in the energy required to bend the magnetic field further away from the Earth and a corresponding increase in the magnitude of the curvature vector. All of the calculations so far have assumed the model to be in force-balance, and as seen in Chapter 1, this tends to overestimate the plasma pressure.

Figure 3.12 shows the critical β_2 value computed as a function of the equatorial crossing point. To obtain this critical β_2 along the magnetotail, we computed the properties of the flux tube for each equatorial crossing point. Then a plasma pressure starting with $\beta = 0$ was assigned to the flux tubes and the Fast-MHD eigenmode equation was solved. The plasma pressure was increased until the solution of the eigenmode equation became stable. In the top panel, the critical value β_2 is plotted; note that for flux tubes further from the Earth the value of β_2 is higher than near the Earth. Just Earthward of $X = -5R_E$ there is no critical β_2 because the driving energy is insufficient to overcome the bending energy. The bottom panel displays the ratio of the critical value β_2 to the β value computed from the Tsyganenko model under the assumption of force balance. We clearly see that the plasma pressure computed from the equilibrium assumption gives a value that is too high to allow Ideal Fast-MHD ballooning-interchange motions. However, in the region

near geosynchronous orbit ($X \simeq -6R_E$) the plasma pressure is the very close to this critical β_2 requirement. This is precisely the region that maps to the bottom of the auroral oval where substorm onsets are first seen (see Chapter 2). It is also important to point out here that the plasma pressure computed under the assumption of force balance is approximately five times the value of the observed pressure near geosynchronous orbit as seen in Figure 1.11. With the ratio of the critical β_2 to the β computed from Tsyganenko reaching nearly 0.25 near geosynchronous orbit, it is reasonable that that this region is unstable in the magnetosphere.

3.8 Conclusions

In this chapter we have investigated the linear stability of different magnetospheric magnetic field models with respect to MHD ballooning-interchange modes. First, it was shown that the Tsyganenko 1996 magnetic field model was stable to the interchange of two flux tubes with equal magnetic flux. The calculations showed however that the flux tubes near geosynchronous orbit were close to marginal stability compared with flux tubes in other regions of the magnetotail.

Next, the conditions under which the MHD description is valid were stated; namely, that the frequency of the wave considered must be larger than the ion thermal velocity divided by the parallel wavelength ($\omega \gg k_\parallel v_{ti}$). Next the MHD energy principle was discussed and the change in potential energy $\delta W_p^{\mathrm{MHD}}$ was derived in terms of the plasma displacement vector ξ.

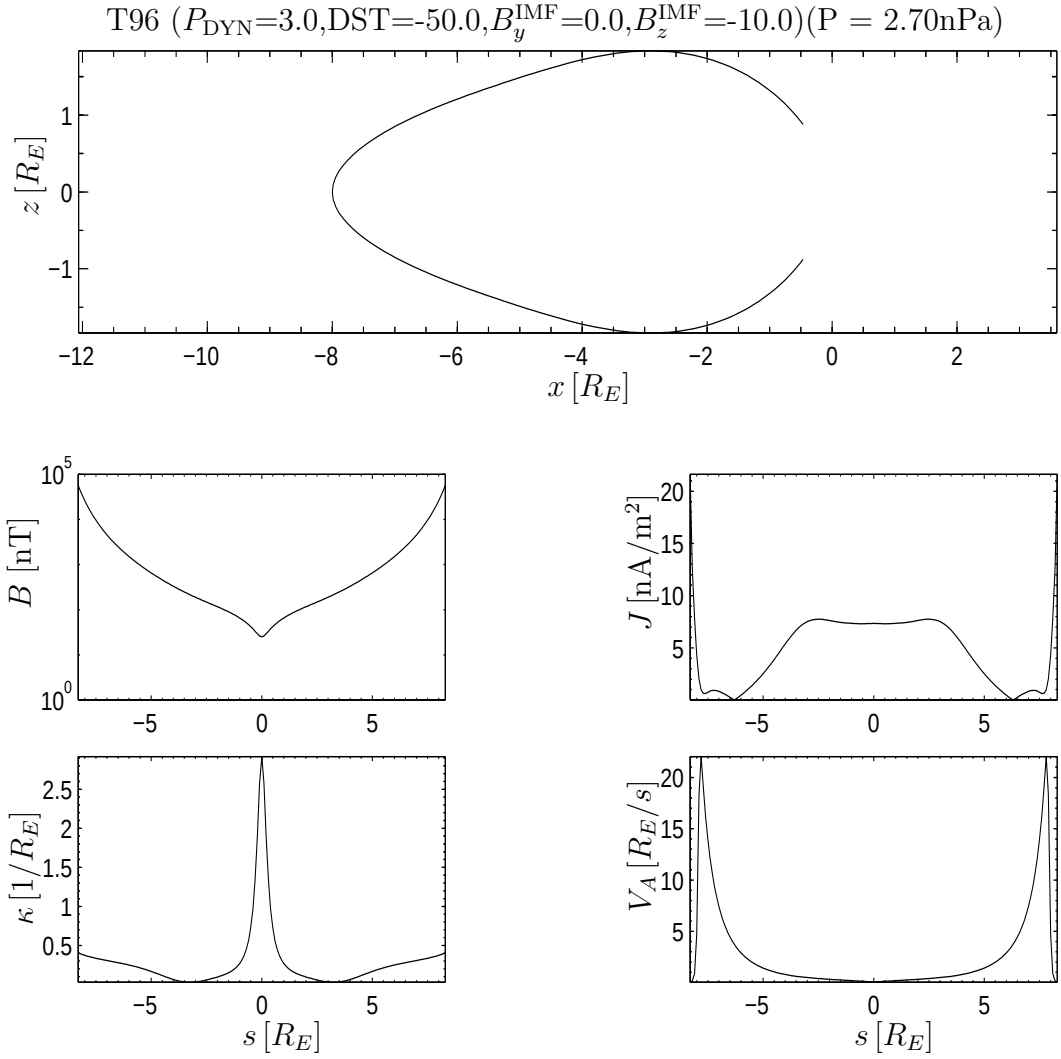

Figure 3.8: The top panel shows a single magnetic field line computed using Tsyganenko's 1996 magnetic field model. This field line punctures the equatorial plane at $X = -8R_E$. The pressure along this flux tube is 2.7 nPa computed by integrating the $\mathbf{J} \times \mathbf{B}$ force from the distant tail. In the bottom four panels profiles of the magnetic field magnitude, current density magnitude, radius of curvature, and Alfvén velocity are plotted as a function of sR_E (the distance along the field line). This particular flux tube was used to solve the Fast-MHD linear eigenmode equation in Fig. 3.9.

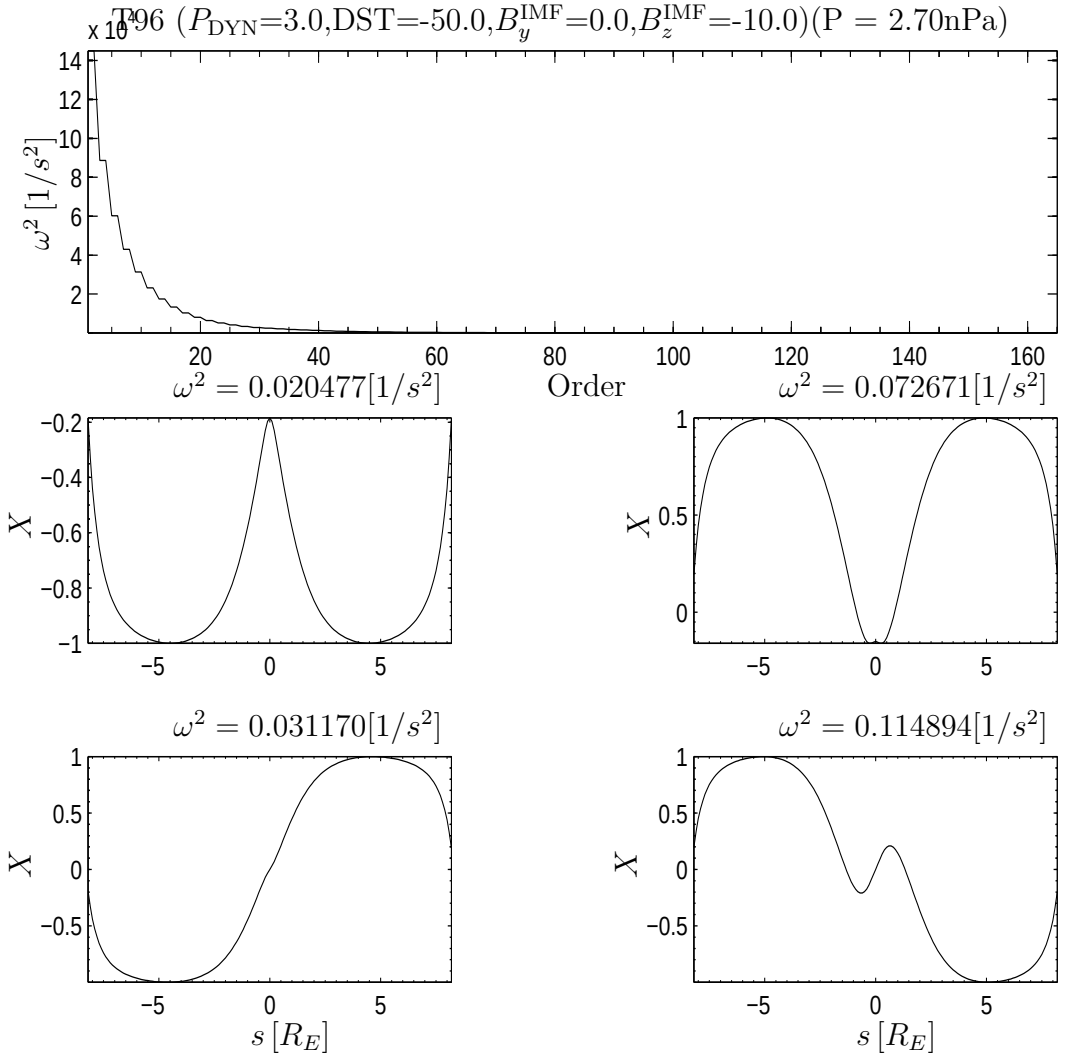

Figure 3.9: The top panel shows all of the eigenvalues of the Fast-MHD linear eigenmode equation, ω^2, computed from the flux tube whose properties are shown in Fig. 3.8. One can see that this flux tube is stable to ballooning-interchange motions, $\omega^2 > 0$, for the assigned plasma pressure. In the bottom four panels different stable eigenfunctions are shown as function of s/R_E, the distance along the flux tube. In this figure the Alfvén velocity was taken to vary as a function of the distance along the field line s. The density was computed from Lysak's model.

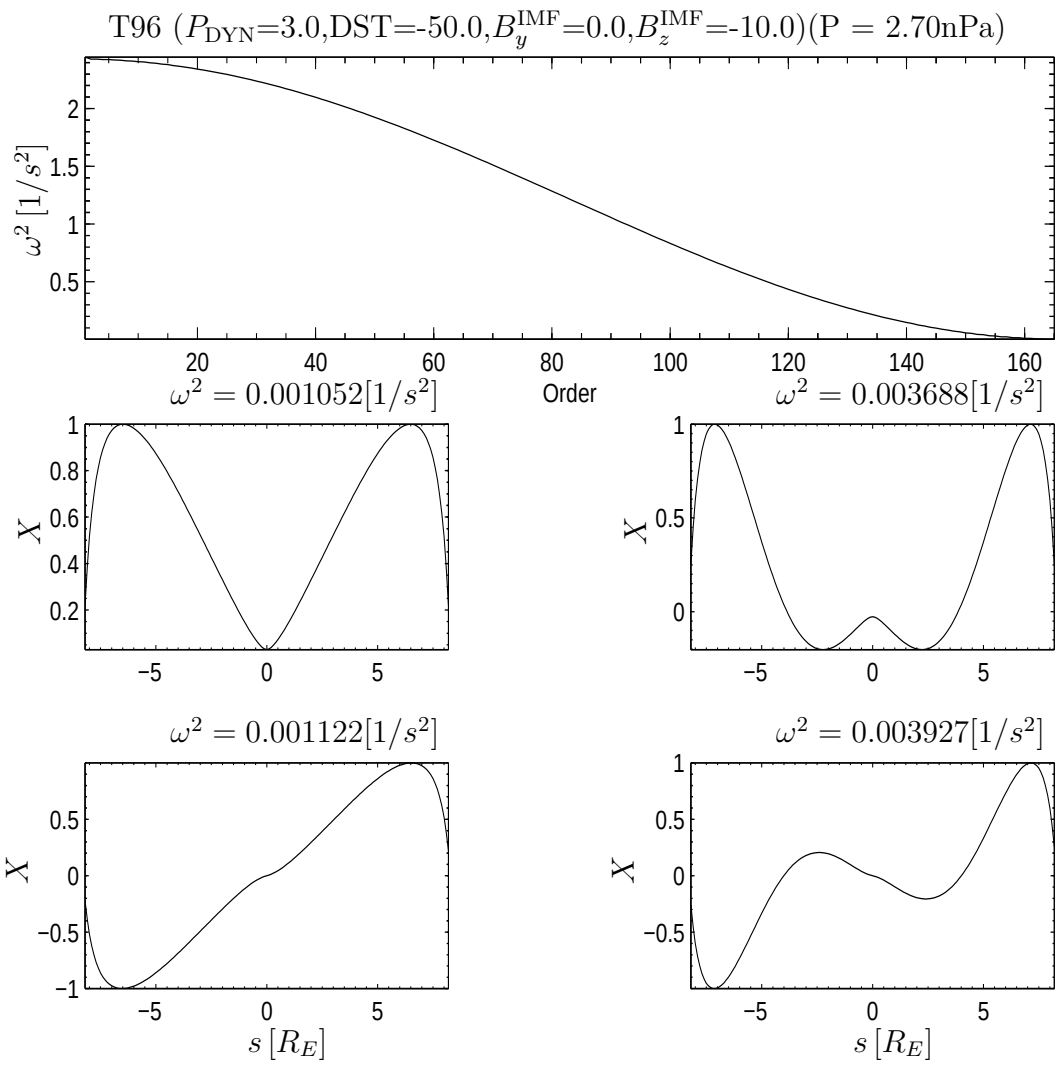

Figure 3.10: The top panel shows all of the eigenvalues of the Fast-MHD linear eigenmode equation, ω^2, computed from the flux tube whose properties are shown in Fig. 3.8. One can see that this flux tube is stable to ballooning-interchange motions, $\omega^2 > 0$, for the assigned plasma pressure. In the bottom four panels different stable eigenfunctions are shown as function of s/R_E, the distance along the flux tube. In this figure the Alfvén velocity V_A is taken to be constant and taken to be the Alfvén velocity at the equatorial plane.

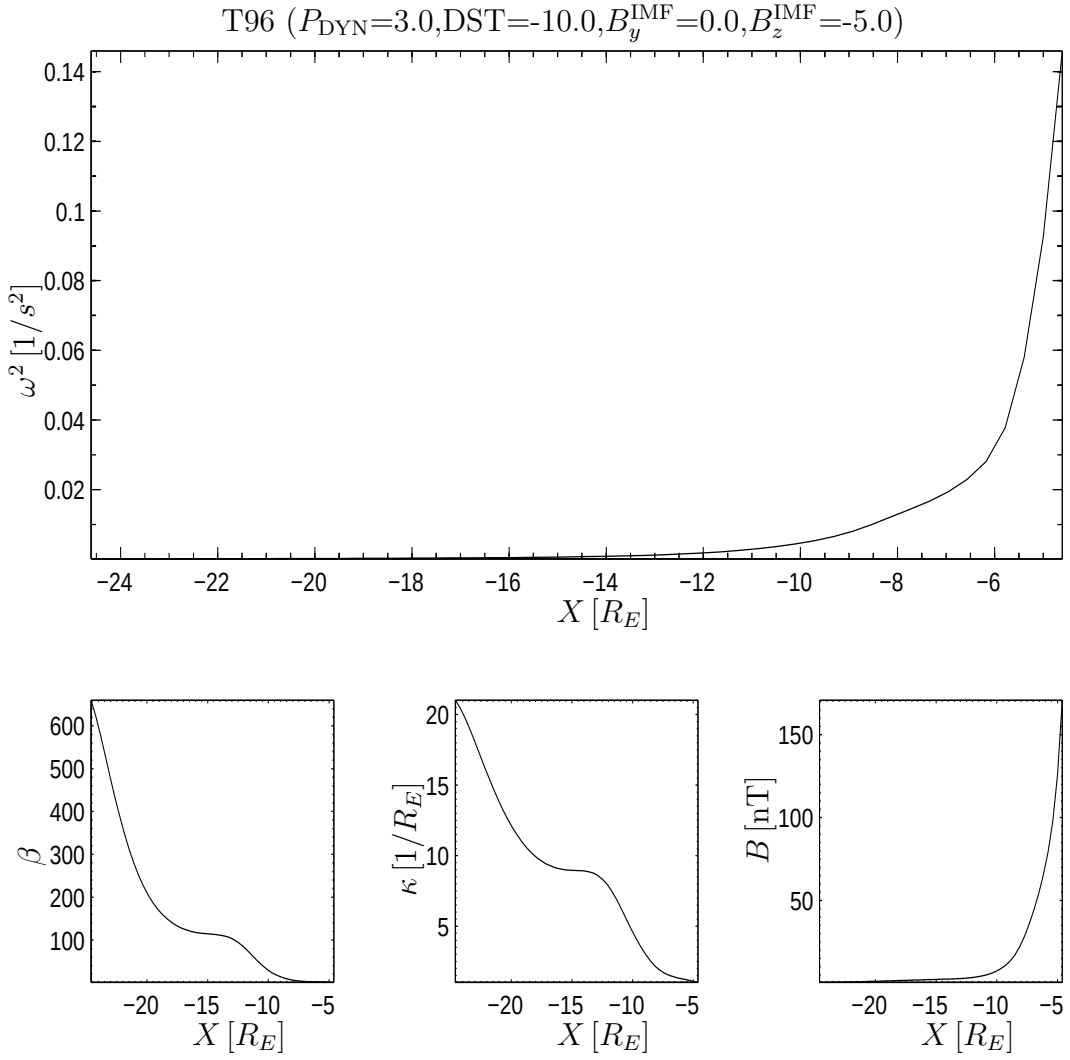

Figure 3.11: Solutions to the Fast-MHD eigenmode equation for different equatorial crossing points using the Tsyganenko 1996 magnetic field model. The top panel shows the smallest eigenvalue, ω^2, as a function of the equatorial crossing point. For this computation the pressure was computed by integrating $\mathbf{J} \times \mathbf{B}$ force along the magnetotail. In the bottom left panel the computed β value is shown along the magnetotail. In the middle panel the inverse of the radius of curvature (the magnitude of the curvature vector) is plotted as a function of $X\,R_E$. In the bottom right panel the magnitude of the magnetic field in the equatorial plane is plotted as a function of $X\,R_E$. In this computation the Alfvén velocity was computed using Lysak's density model and took different values along the flux tube.

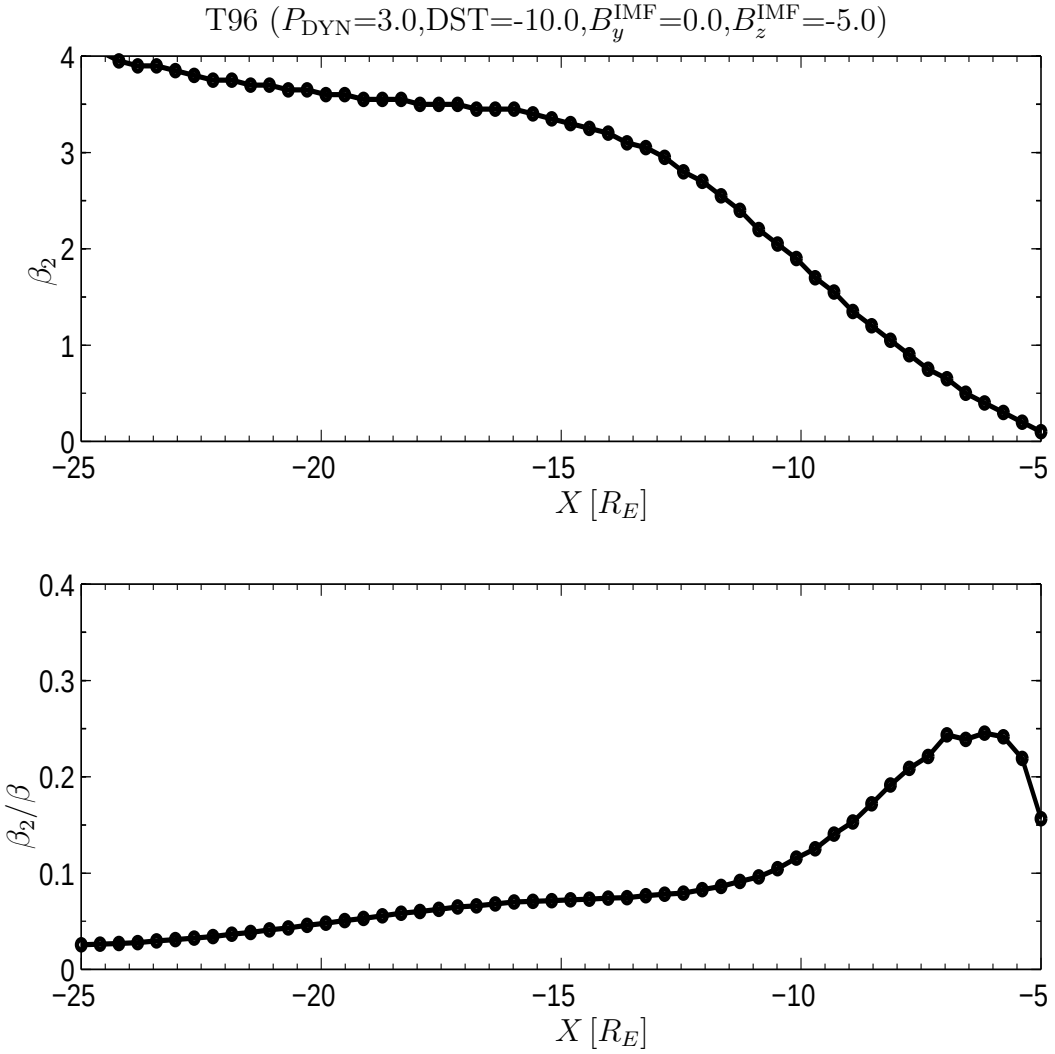

Figure 3.12: Computing the β_2 value as a function of the equatorial crossing point using the Tsyganenko 1996 magnetic field model. The top panel shows the value of β_2, the critical β value for which $\beta < \beta_2$ the flux tubes are unstable to Fast-MHD ballooning-interchange motions. The bottom panel shows the ratio of the computed β_2 value to the β value computed by assuming the Tsyganenko 1996 magnetic field model is in equilibrium and integrating the $\mathbf{J} \times \mathbf{B}$ force along the magnetotail.

The $\delta W_p^{\mathrm{MHD}}$ was then minimized with respect to $\xi_\parallel$, and it was shown that ensuring the plasma pressure to be constant along the flux tube was equivalent to minimizing $\delta W_p^{\mathrm{MHD}}$ with respect to $\xi_\parallel$. The parallel equation of motion was then derived and it was shown that in order to minimize $\delta W_p^{\mathrm{MHD}}$ absolutely with respect to $\xi_\parallel$ the MHD approximation that $\omega \gg k_\parallel v_{ti}$ was violated. The Fast-MHD approximation was introduced by noting that taking $\xi_\parallel = 0$ was more appropriate under the MHD approximation $\omega \ll k_\parallel v_{ti}$. The Fast-MHD approximation is more stringent on instability criteria. Thus slow growing modes found using the classical ideal MHD minimization will be considered stable with respect to Fast-MHD calculations.

By comparing the different terms in the Fast MHD δW it was shown that there were two key stabilizing influences on ballooning-interchange modes: 1) field-line bending and 2) plasma compression. The Fast-MHD linear eigenmode equations were then solved for different models of the magnetospheric magnetic field. These solutions were then used to show that there are two critical plasma β values: β_1 and β_2. An equilibrium with a plasma β value between these two critical values is unstable. An equilibrium with $\beta > \beta_2$ is stabilized by the energy required to compress the plasma. An equilibrium with $\beta < \beta_1$ is stabilized by the energy required to bend the magnetic field lines.

The database derived empirical magnetic field model of Tsyganenko was found to be stable for plasma pressures computed under the assumption of force balance. However, for externally imposed plasma pressures, more like those measured in the magnetotail ($\beta \lesssim 4$), flux tubes in the Tsyganenko

magnetic field model were found to be unstable. Finally, it was demonstrated that in the region near geosynchronous orbit, which maps to the equator-ward edge of the auroral oval, the critical plasma β was closest to the critical β_2 value, below which flux tubes are unstable.

Chapter 4

Gyrokinetic equations

In this chapter, we consider how the MHD stability pictured, developed in the previous chapter, is modified by non-ideal MHD effects such as finite parallel electric field, wave-particle resonance, and finite gyroradius. There is considerable observational evidence to suggest that in the early stages of substorm development there are westward propagating magnetic oscillations on auroral field lines [60, 131, 158] in the transitional region between the dipole-dominated field region and the high β geotail plasma near geosynchronous orbit. The wave-particle resonance is expected to be important because these westward traveling modes propagate at speeds near the gyrokinetic drift velocity of ions. As discussed in Chapter 3, the slow growth rates typically found from ideal MHD is not sufficiently fast to justify the MHD description. This fact has been pointed out in the space physics literature as well [44, 93, 94]. Thus kinetic theory is needed for a more accurate description. It is expected that as the growth rate is decreased from values that are valid in the MHD approximation the mode will continuously deform into a kinetic version of the ballooning-interchange mode with a small but finite parallel electric field.

In this chapter we develop the linear stability of magnetospheric plas-

mas using the gyrokinetic approximation. In Section 4.1 we introduce the different electromagnetic gauges used in this dissertation and give the equations used to transform from one description to the other. In Section 4.2 we give the perturbed distribution function found by solving the linearized gyrokinetic equation. In Section 4.3 we use this perturbed distribution function in the quasineutrality condition and find an equation for the three components of the electromagnetic field. In Section 4.4 the perturbed distribution is used to find the perturbed parallel current which is then used in the parallel component of Ampere's law. This provides a second equation for the electromagnetic field. Then in Section 4.5 the perturbed distribution function is used to find the perturbed radial current which is then used in the radial component of Ampere's law. This third and final equation allows us to solve a system of equations giving the three components of the electromagnetic field. In Section 4.6 the three mode equations are combined into a matrix form and a local approximation is made. The local approximation is made by assuming the response of the fields along the flux-tube will be confined to the equatorial plane where the curvature is a maximum and the magnetic field is a minimum. The determinant of the three by three matrix gives us a dispersion relation from which we can find roots and thus the complex frequency of the electromagnetic fields. A positive imaginary frequency indicates the wave is unstable. In this section the MHD limit of the dispersion relation is also taken and discussed. In Section 4.6.1 the electrostatic limit that is often taken in tokamak plasmas is taken and discussed in the context of magnetospheric

plasmas. In Section 4.7 a reduced two by two matrix dispersion relation is found and the compressional effects are discussed. The full gyrokinetic local dispersion relation is solved and stability limits on the plasma β are found. In Section 4.8 a different way of describing the kinetic stability is presented that is useful because of its similarity to the MHD $\delta W_p^{\rm MHD}$ formulation. Finally in Section 4.9 conclusions and a summary is presented.

4.1 Electromagnetic Gauges

There are two primary gauges that are used in the kinetic stability analysis of high-β plasmas. The first is the Kadomtsev gauge. In this gauge the perturbed electric field is given by

$$\mathbf{E} = -\nabla\varphi - \nabla \times (a\hat{\mathbf{b}}) - \frac{\partial A_\parallel}{\partial t}\hat{\mathbf{b}}. \tag{4.1}$$

where $\hat{\mathbf{b}} = \mathbf{B}/B$ is the unit vector in the direction of the magnetic field. The time dependence of all perturbation quantities is $\exp(-i\omega t)$. Then from Faraday's law we can determine the perturbed magnetic field

$$\delta\mathbf{B} = \hat{\mathbf{b}}(\frac{1}{i\omega})\nabla_\perp^2 a + \nabla A_\parallel \times \hat{\mathbf{b}} = \delta B_\parallel \hat{\mathbf{b}} + \delta\mathbf{B}_\perp, \tag{4.2}$$

and we can identify $\delta B_\parallel = (1/i\omega)\nabla_\perp^2 a$. Note that in the following all quantities (unless noted otherwise) refer to perturbed quantities. Following Horton *et al.* (1985) [91] we note that it is convenient to introduce the field ψ such that

$$\frac{\partial\psi}{\partial s} = i\omega A_\parallel \tag{4.3}$$

where s is the coordinate that measures distance along a magnetic field line. Note that by computing $E_\parallel = \hat{\mathbf{b}} \cdot \mathbf{E}$ from Equation (4.1), and using the field variable ψ we find

$$E_\parallel = -\frac{\partial}{\partial s}\left(\varphi - \psi\right). \tag{4.4}$$

From Ampere's law we can express the parallel current in terms of the parallel vector potential,

$$\mu_0 \delta J_\parallel = -\nabla_\perp^2 A_\parallel \tag{4.5}$$

and the perpendicular current in terms of the parallel perturbation of the magnetic field $\delta B_\parallel$

$$\mu_0 \delta \mathbf{J}_\perp = \nabla \delta B_\parallel \times \hat{\mathbf{b}}. \tag{4.6}$$

With this representation in this gauge our final set of field variables that we will use are $(\varphi, \psi, \delta B_\parallel)$. Using these field variables we can find a dispersion relation from Equations (4.5), (4.6), and the quasineutrality condition. Using $\mathbf{B} = \hat{\mathbf{y}} \times \nabla\Psi$, we can write the vector potential as

$$\mathbf{A} = -\frac{i}{k_y}\frac{\delta B_\parallel}{B}\nabla\Psi + \frac{1}{i\omega}\hat{\mathbf{b}}\hat{\mathbf{b}} \cdot \nabla\psi. \tag{4.7}$$

The second gauge is the MHD gauge, which has the representation (ϕ, ξ^Ψ, Q_L). In the MHD gauge, the parallel component of the magnetic vector potential is zero ($A_\parallel = 0$), leaving the electrostatic potential $\phi = \phi \exp(ik_y y - i\omega t)$, which is absent in the MHD description, and the two components of the perpendicular vector potential $\mathbf{A}_\perp = \boldsymbol{\xi} \times \mathbf{B}$. The plasma displacement is

written as

$$\boldsymbol{\xi} = \nabla y \left[\frac{i}{k_y B} \left(Q_L + \kappa \xi^{\Psi} \right) \exp(i k_y y - i\omega t) \right] - \hat{\mathbf{b}} \times \nabla \left[\frac{i}{k_y B} \xi_{\Psi} \exp(i k_y y - i\omega t) \right], \tag{4.8}$$

Where $\kappa = \boldsymbol{\kappa} \cdot \nabla \Psi / B$. Note that as in the MHD description the magnitude of the perturbed magnetic field in the Lagrangian frame is given by

$$Q_L = Q_{\parallel} + \boldsymbol{\xi} \cdot \nabla \mathbf{B} - B \boldsymbol{\xi} \cdot \boldsymbol{\kappa} = -\mathbf{B} \left(\nabla \cdot \boldsymbol{\xi} + 2 \boldsymbol{\xi} \cdot \boldsymbol{\kappa} \right) \tag{4.9}$$

and the plasma displacement vector is given by magnetic vector potential as

$$\boldsymbol{\xi} = \frac{\hat{\mathbf{b}} \times \mathbf{A}}{B}. \tag{4.10}$$

Notice that the Kadomtsev gauge and the MHD gauge differ by a gauge transformation. Defining a gauge transformation [6] as

$$\mathbf{A} \rightarrow \mathbf{A} + \nabla \Lambda \tag{4.11}$$

$$\phi \rightarrow \phi - \frac{\partial \Lambda}{\partial t}. \tag{4.12}$$

For the specific gauge transformation between the Kadomtsev gauge and the MHD gauge, the function Λ is given by

$$\Lambda = -\frac{1}{i\omega} \psi. \tag{4.13}$$

The following matrix operation gives explicitly the operations required to carry one from the Kadomtsev gauge to the MHD gauge:

$$\begin{pmatrix} \phi \\ \xi^{\Psi} \\ Q_L \end{pmatrix} = \begin{pmatrix} 1 & -1 & 0 \\ 0 & -\frac{k_y}{\omega} & 0 \\ 0 & -\frac{k_y}{\omega} \kappa & 1 \end{pmatrix} \begin{pmatrix} \varphi \\ \psi \\ \delta B_{\parallel} \end{pmatrix} \tag{4.14}$$

and the inverse transformation can be made by using

$$\begin{pmatrix} \varphi \\ \psi \\ \delta B_{\parallel} \end{pmatrix} = \begin{pmatrix} 1 & -\frac{\omega}{k_y} & 0 \\ 0 & -\frac{\omega}{k_y} & 0 \\ 0 & -\kappa & 1 \end{pmatrix} \begin{pmatrix} \phi \\ \xi^{\Psi} \\ Q_L \end{pmatrix}. \tag{4.15}$$

4.2 Solution to Gyrokinetic Equation

The solution to the Gyrokinetic equation and the resulting perturbed electromagnetic fields closely follows the results of Antonsen *et al.* [8] and Horton *et al.* [91]. The solution of the gyrokinetic equation f_j can be written as

$$f_j = -(q_j/T_j)\varphi F_j + g_j \exp(iL_j) \tag{4.16}$$

where

$$L_j = \mathbf{k} \cdot \mathbf{v} \times \hat{\mathbf{b}}/\Omega_j \tag{4.17}$$

and $\Omega_j = q_j B/m_j$ is the gyrofrequency for particle species j. In Eq. (4.16), F_j represents the adiabatic part of the perturbed distribution function and g_j represents the non-adiabatic part and may be determined by solving the following equation

$$\left(v_{\parallel}\frac{\partial}{\partial s} - i(\omega - \omega_{Dj})\right) g_j = -iF_j(\omega - \omega_{*tj}) \left[\frac{q_j}{T_j}\left(\varphi - v_{\parallel}A_{\parallel}\right) J_0 + \frac{a_j}{b_j}\frac{\delta B_{\parallel}}{B} J_1\right]. \tag{4.18}$$

Here the diamagnetic drift frequency is given by

$$\omega_{*tj} = \omega_{*j}\left[1 - \frac{3}{2}\eta_j + \eta_j \frac{mv^2}{2T_j}\right] \tag{4.19}$$

where $\eta_j = (\mathrm{d}\log T_j)/(\mathrm{d}\log n_j)$ is the ratio of the density gradient scale length to the temperature gradient scale length, and

$$\omega_{*j} = \frac{T_j}{q_j B}\mathbf{k}_\perp \cdot \hat{\mathbf{b}} \times \nabla \log n. \tag{4.20}$$

The gyrokinetic drift frequency of species j is given by

$$\omega_{Dj} = \mathbf{k}\cdot\hat{\mathbf{b}} \times \left[\mu\nabla B + v_\parallel^2 \hat{\mathbf{b}}\cdot\nabla\hat{\mathbf{b}}\right]/\Omega_j \tag{4.21}$$

where $\mu = v_\perp^2/2B$ is the magnetic moment. In the above $a_j = k_\perp v_\perp/\Omega_j$, $b_j = k_\perp^2 T_j/m_j\Omega_j^2$ and $J_{0,1}$ are Bessel's functions of order 0 and 1 with arguments $k_\perp v_{tj}/\Omega_j$. In all of the following equations, the field variables φ and ψ will be normalized by the factor q/T_e. Taking all of the electrons to be trapped the solution to Eq. (4.18) for the electrons can be written as

$$\frac{1}{2}\left(g_+ + g_-\right) = -F_e\left[(1-\omega_{*te}/\omega)\psi + \frac{\omega-\omega_{*te}}{\omega-\overline{\omega}_{de}}\overline{X}\right] \tag{4.22}$$

where subscripts $\pm$ indicate the direction of the electrons along the magnetic field. Notice that the last term on the left hand side of Eq. (4.22) represents the effects of the trapped electrons. For now we are only interested in the local approximation and will ignore trapped particle effects. The over-line represents bounce-averaging

$$\overline{(\,\cdot\,)} = \left(\int \frac{\mathrm{d}s}{v_\parallel}\right)^{-1}\int\frac{\mathrm{d}s}{v_\parallel}(\,\cdot\,) \tag{4.23}$$

and X is given by

$$X = \left[\varphi - \left(1-\frac{\omega_{De}}{\omega}\right)\psi - \frac{v_\perp^2}{v_e^2}\frac{\delta B_\parallel}{B}\right]. \tag{4.24}$$

Next we must consider the passing ions. Expanding in powers of $v_i/\omega L_c$ one obtains,

$$\frac{1}{2}\left(g_+ + g_-\right) = F_i \left(\frac{\omega - \omega_{*ti}}{\omega - \omega_{Di}}\right)(1-\sigma^2)^{-1}\left[\tau\varphi J_0 + \frac{a_i}{b_i}\frac{\delta B_\parallel}{B}J_1 + \frac{J_0 v_\parallel^2}{\omega(\omega-\omega_{Di})}\frac{\partial^2}{\partial s^2}\tau\psi\right] \tag{4.25}$$

where $\tau = T_e/T_i$ and

$$\sigma = \frac{i|v_\parallel}{\omega - \omega_{Di}}\frac{\partial}{\partial s}. \tag{4.26}$$

4.3 Quasineutrality

For simplicity the effects of trapped particles will be ignored for now. Then the perturbed electron density can be written with the help of Eqs. (4.16) and (4.22) as

$$\frac{\delta n_e}{n_0} = \varphi - \left(1 - \frac{\omega_{*e}}{\omega}\right)\psi, \tag{4.27}$$

and the perturbed ion density can be written with the help of Eqs. (4.16) and (4.25) as

$$\frac{\delta n_i}{n_0} = \tau(P-1)\varphi + Q\frac{\delta B_\parallel}{B}. \tag{4.28}$$

The quasineutrality condition of $\delta n_e = \delta n_i$ can be used to obtain a single mode equation:

$$(-1 + \tau(P-1))\varphi + \left(1 - \frac{\omega_{*e}}{\omega}\right)\psi + Q\frac{\delta B_\parallel}{B} = 0, \tag{4.29}$$

where the kinetic response functions $P(\omega)$ and $Q(\omega)$ are given by

$$P = \left\langle \frac{\omega - \omega_{*ti}}{\omega - \omega_{Di}} J_0^2 \right\rangle \tag{4.30}$$

$$Q = \left\langle \frac{\omega - \omega_{*ti}}{\omega - \omega_{Di}} \left(\frac{1}{b_i}\frac{m_i}{T_i}\right)^{1/2} v_\perp J_0 J_1 \right\rangle \tag{4.31}$$

and the angle brackets represent an integral over the equilibrium distribution function which we take to be Maxwellian:

$$\langle (\cdot) \rangle = \frac{1}{n_0} \int \mathrm{d}\mathbf{v} F_i (\cdot). \tag{4.32}$$

The fluid limit of the kinetic response functions may be found by expanding the denominators in the limit $\omega/\omega_{Di} \gg 1$ and performing the integrals over velocity space. One then finds

$$P^f = \left(1 - \frac{\omega_{*i}}{\omega}\right) + \left(1 - \frac{\omega_{*i}(1+\eta_i)}{\omega}\right) \frac{\omega_{Di}}{\omega} \tag{4.33}$$

$$Q^f = 1 - \frac{\omega_{*i}(1+\eta_i)}{\omega}. \tag{4.34}$$

4.4 Parallel component of Ampere's law

The parallel component of Ampere's law can be written as

$$\delta J_\parallel = -\frac{1}{\mu_0} \nabla_\perp^2 A_\parallel = i \frac{1}{\omega} \nabla_\perp^2 \frac{\partial \psi}{\partial s}. \tag{4.35}$$

The parallel currents are prescribed through the solution to the gyrokinetic equation f_j by the equation

$$\delta J_{\parallel j} = \frac{1}{\mu_0} \int \mathrm{d}^3\mathbf{v}\, q_j v_\parallel f_j. \tag{4.36}$$

The parallel derivative of the perturbed parallel current can be conveniently computed directly from the kinetic equation (4.18) by integrating over velocity space with $q_j \int \mathrm{d}\mathbf{v} \exp(iL)$ obtaining:

$$\begin{aligned} \frac{\partial}{\partial s} \delta J_{\parallel j} &= i q_j \int \mathrm{d}\mathbf{v} J_0 \frac{1}{2} \left(g_+ + g_-\right)_j (\omega - \omega_{Dj}) \\ &\quad - i q_j \int \mathrm{d}\mathbf{v} F_j J_0 (\omega - \omega_{*tj}) \left[\varphi J_0 + \frac{a_j}{b_j} \frac{\delta B_\parallel}{B} J_1\right]. \end{aligned} \tag{4.37}$$

For the electron contribution to the parallel current, we obtain

$$\frac{\partial}{\partial s}\delta J_{\parallel e} = i\omega n_0 e\left\{-\left(1-\frac{\omega_*}{\omega}\right)\varphi+\left[\left(1-\frac{\omega_{*e}}{\omega}\right)-\left(\frac{\omega_{De}}{\omega}\right)\left(1-\frac{\omega_{*pe}}{\omega}\right)\right]\psi + \left(1-\frac{\omega_{*pe}}{\omega}\right)\frac{\delta B_\parallel}{B}\right\} \tag{4.38}$$

where $\omega_{*pj}=\omega_{*j}(1+\eta_j)$. At the level of description we are interested in the ions do not contribute to the perturbed parallel current. Taking the parallel derivative of the parallel component of Amperes law gives

$$\frac{\partial}{\partial s}\delta J_\parallel = -\frac{1}{\mu_0}\frac{\partial}{\partial s}\nabla_\perp^2 A_\parallel = i\frac{1}{\mu_0\omega}\frac{\partial}{\partial s}\nabla_\perp^2\frac{\partial}{\partial s}\psi. \tag{4.39}$$

Now, inserting the electron contribution to the parallel current yields a second mode equation given by

$$\frac{\rho^2 v_A^2}{\omega^2}\frac{\partial}{\partial s}\nabla_\perp^2\frac{\partial}{\partial s}\psi = -\left(1-\frac{\omega_{*e}}{\omega}\right)\varphi+\left[\left(1-\frac{\omega_{*e}}{\omega}\right)-\left(\frac{\omega_{De}}{\omega}\right)\left(1-\frac{\omega_{*pe}}{\omega}\right)\right]\psi + \left(1-\frac{\omega_{*pe}}{\omega}\right)\frac{\delta B_\parallel}{B}. \tag{4.40}$$

4.5 Radial component of Ampere's law

The radial component of the perturbed current δJ_Ψ can be computed by integrating over velocity space with the perturbed distribution function as given by

$$\delta J_\Psi = -i\frac{k_\Psi}{k_y}\sum_j q_j\int \mathrm{d}\mathbf{v}\frac{1}{2}(g_+ + g_-)_j v_\perp J_1. \tag{4.41}$$

The electron contribution is then given by

$$\delta J_\Psi^e = \frac{ik_\Psi n_0 q T_e}{m_e\Omega_e}\left(1-\frac{\omega_{*pe}}{\omega}\right)\psi \tag{4.42}$$

and the ion contribution to the perturbed radial current is given by

$$\delta J_\Psi^i = -\frac{ik_\Psi n_0 q T_i}{m_i \Omega_i}\left[\tau Q\varphi + R\frac{\delta B_\parallel}{B}\right]. \tag{4.43}$$

As discussed in Section 4.1 the radial component of Ampere's law is given by

$$\delta J_\Psi = \frac{1}{\mu_0}\hat{\mathbf{e}}_\Psi \cdot \nabla \delta B_\parallel. \tag{4.44}$$

Using Eqs. (4.42) and (4.43) in Amperes law (4.44) we obtain the third and final mode equation:

$$\frac{\delta B_\parallel}{B} = \frac{\beta_e}{2}\left(1 - \frac{\omega_{*pe}}{\omega}\right)\psi - \frac{\beta_i}{2}\tau Q\varphi + R\frac{\delta B_\parallel}{B} \tag{4.45}$$

where the final ion kinetic integral is

$$R = \left\langle \left(\frac{\omega - \omega_{*ti}}{\omega - \omega_{Di}}\right)\frac{1}{b}\frac{m_i}{T_i}v_\perp^2 J_1^2 \right\rangle. \tag{4.46}$$

The fluid limit of the kinetic response function $R(\omega)$ may be taken, as before, by expanding the denominators in the limit $\omega/\omega_{Di} \gg 1$ and performing the integrals over velocity space. One then finds

$$R^f = 2 - \frac{2\omega_{*i}}{\omega}(1 + 2\eta_i). \tag{4.47}$$

4.6 Matrix electromagnetic dispersion relation

The three mode equations derived from the linear solution to the gyrokinetic equation, as discussed in the previous three sections, can be written together in matrix form as

$$\begin{bmatrix} a & b & c \\ b & d & e \\ c & e & f \end{bmatrix}\begin{pmatrix} \varphi \\ \psi \\ \frac{\delta B_\parallel}{B} \end{pmatrix} = 0 \tag{4.48}$$

where

$$a = -1 + \tau(P(\omega) - 1) \tag{4.49}$$

$$b = 1 - \frac{\omega_{*e}}{\omega} \tag{4.50}$$

$$c = Q(\omega) \tag{4.51}$$

$$d = \frac{k_\perp^2 \rho^2 \omega_A^2}{\omega^2} - \left(1 - \frac{\omega_{*e}}{\omega}\right) + \left(1 - \frac{\omega_{*pe}}{\omega}\right)\left(\frac{\omega_{De}}{\omega}\right) \tag{4.52}$$

$$e = -\left(1 - \frac{\omega_{*pe}}{\omega}\right) \tag{4.53}$$

$$f = \frac{2}{\beta_e} + \frac{R(\omega)}{\tau}. \tag{4.54}$$

A dispersion relation may be formed by determining when the determinant of the matrix in Eq. (4.6) is zero for a given ω, or more explicitly

$$D(\omega) = adf - ae^2 - fb^2 - dc^2 + 2bec = 0. \tag{4.55}$$

Where following Horton *et al.* (1985) [91] all frequencies are measured in units of c_s/L_n and the cross field wavenumber $k_\perp$ in units of $\rho = (m_i T_e)^{1/2}/eB$. The

dimensionless frequencies are then given by

$$\begin{aligned}
\omega_{*e} &= k \\
\omega_{*i} &= -k/\tau \\
\omega_{*pe} &= k(1+\eta_e) \\
\omega_{*pi} &= -k(1+\eta_i)/\tau \\
\omega_A &= \sqrt{\frac{2}{\beta}}\frac{\epsilon_n}{q} \\
\omega_\kappa^e &= k\epsilon_n \\
\omega_\kappa^i &= -k\epsilon_n/\tau \\
\omega_{\nabla B}^e &= k\epsilon_n - (\beta/2)(k(1+\eta_e) + k(1+\eta_i)/\tau) \\
\omega_{\nabla B}^i &= -k\epsilon_n/\tau - (\beta/2)(k(1+\eta_e) + k(1+\eta_i)/\tau)/\tau \\
\omega_{De} &= \omega_\kappa^e + \omega_{\nabla B}^e \\
&= 2k\epsilon_n - (\beta/2)(k(1+\eta_e) + k(1+\eta_i)/\tau) \\
\omega_{Di} &= \omega_\kappa^i + \omega_{\nabla B}^i \\
&= -2k\epsilon_n/\tau + (\beta/2)(k(1+\eta_e) + k(1+\eta_i)/\tau)/\tau \\
b_i &= k^2/\tau.
\end{aligned}$$

Thus there is a seven dimensional parameter vector for this dispersion relation $P^{3\text{by}3} = (k, \eta_i, \eta_e, \epsilon_n, \beta_e, q, \tau)$ which is summarized in Table 4.1. There are some well known limits of this dispersion relation that should be pointed out here. The first is for a low β plasma, $\beta \ll 1$. In this limit f is dominated by the first term and the kinetic integral term accounting for the wave-particle resonance is unimportant. It can be quickly determined that for $\beta \ll 1$ one

Parameter	Definition	Description
k	$\frac{k_\perp c_s}{\Omega_i}$	Measure of $k_\perp$
ϵ_n	$\frac{L_n}{R_c}$	Density gradient scale length to radius of curvature
η_i	$\frac{d\ln T_i}{d\ln n_0}$	Ion Temperature gradient
η_e	$\frac{d\ln T_e}{d\ln n_0}$	Electron Temperature gradient
τ	$\frac{T_e}{T_i}$	Ratio of species temperatures
β_e	$\frac{8\pi n_0 T_e}{B^2}$	Ratio of electron energy density to magnetic energy density
q	$\frac{1}{R_c k_\|\|}$	Measure of parallel wavelength

Table 4.1: Parameter summary for local gyrokinetic dispersion relation

must have $f \gg 1$ and consequently a more simple dispersion relation may be used:

$$D_{\mathrm{low}\beta}(\omega) = (ad - b^2)f \simeq 0. \tag{4.56}$$

Using the fluid limits of the P function, and taking f to be large and not close to zero, one can arrive at a quadratic dispersion relation:

$$\omega^2 - \omega\omega_{*pi} + \gamma^2_{\mathrm{MHD}} = 0 \tag{4.57}$$

which gives the MHD limit of the full gyrokinetic dispersion relation.

A computer code called GKLDR (Gyro-Kinetic Local Dispersion Relation) was developed to evaluate the kinetic energy functions $P(\omega), Q(\omega), R(\omega)$ using a time-history method. This code also can find roots of various dispersion relations involving these functions and may numerically evaluate Nyquist diagrams. These kinetic integrals were explored by Similon *et al.* (1984) [170].

4.6.1 Electrostatic modes

The electrostatic modes are given by

$$a(\omega) = -1 - \tau + \tau P(\omega) = 0. \tag{4.58}$$

This mode was studied by Terry *et al.* [181] and Horton *et al.* [91]. These modes are found to require $\eta_i > 2/3$ for instability. For $\eta_i > 2$ all wave numbers are unstable with a peak in wave-number at approximately $k = 0.5$. For $2/3 < \eta_i < 2$ there is a range of unstable k values. Figure 4.1 shows solutions to the electrostatic dispersion relation of Eq. (4.58) as a function of the perpendicular wave number, for several different ratios of the ion density gradient to the ion temperature gradient (η_i) for a plasma with $\beta = 0$. This figure is identical to the figure in Horton *et al.* [91] and verifies that the new code for solving the complex ion velocity integrals agrees with the previous results.

Figure 4.2 shows the effect of finite β on the stability of electrostatic modes. The dependence of these growth rates on β arises solely in the effect that β has on the ∇B drift. One clearly sees that as β is increased from tokamak values, $\beta \sim 0.01$, to values more relevant to the magnetosphere, $\beta \sim O(1)$ the electrostatic modes are completely stabilized.

4.7 High β stabilization of Ballooning/Interchange Modes

Considering the mode equation resulting from the radial component of Amperes law we can relate the compressional change in the magnetic field

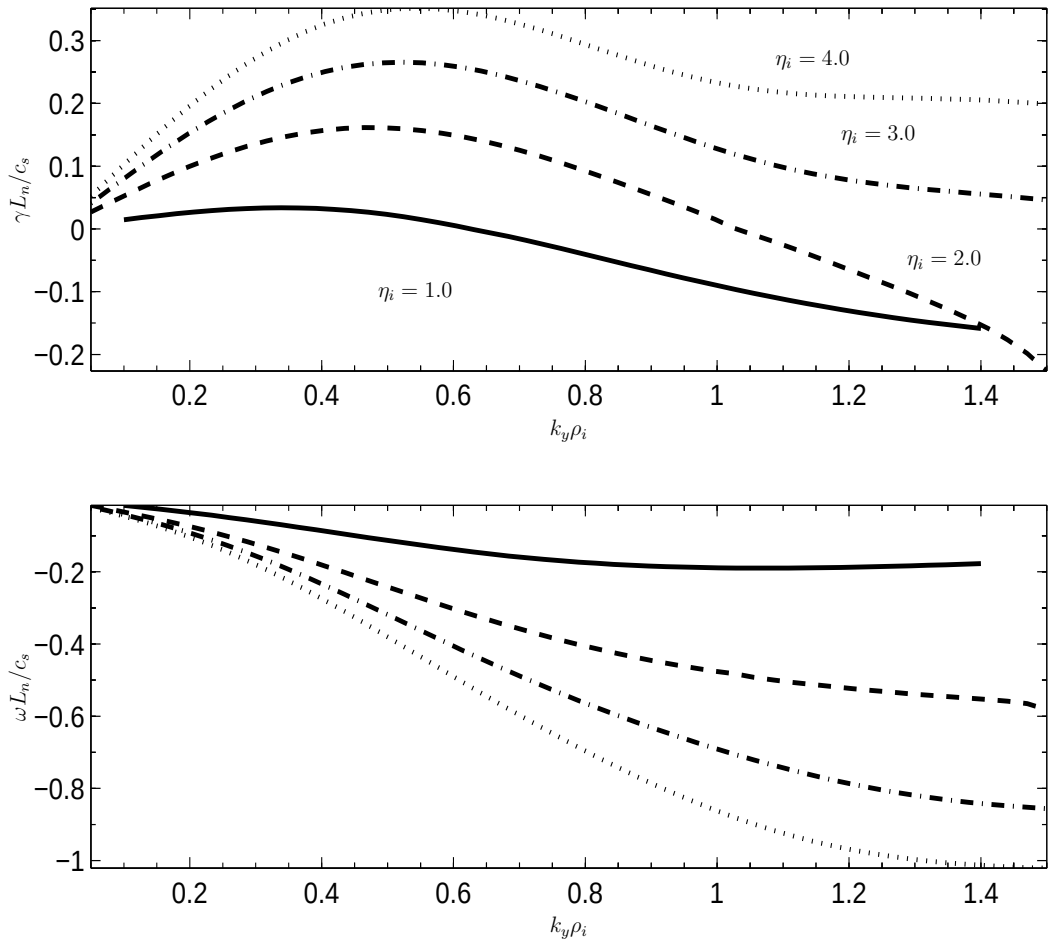

Figure 4.1: Roots of the electrostatic dispersion relation of Eq. (4.58) as a function of wave number k for different values of η_i. In this figure $\epsilon_n = 0.25$, $\tau = 1$ and $\beta = 0$.

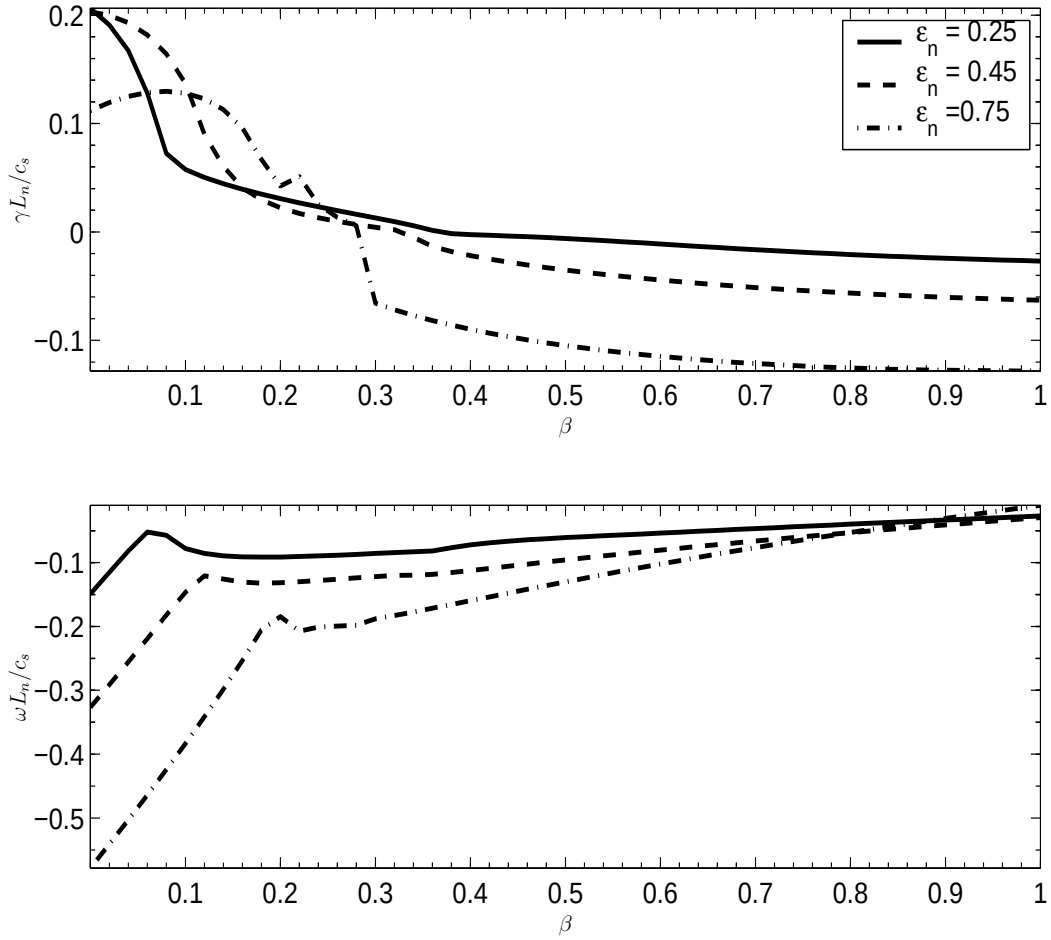

Figure 4.2: Roots of the electrostatic dispersion relation of Eq. (4.58) as a function of β for different values of ϵ_n. In this figure $\tau = 1$, $k = 0.29$, and $\eta_i = 3.0$, $\eta_e = 2.0$

given by $\delta B_\parallel/B$ to the electrostatic potential ϕ and the component of the vector potential given by ψ through

$$\frac{\delta B_\parallel}{B} = -\frac{1}{f}(c\phi + e\psi) \tag{4.59}$$

where we note that our local approximation does not allow for the true nature of the complex non-local operator $1/f$ which will be further studied in Chapter 6. Substituting Eq. (4.59) into the full matrix expression of Eq. (4.6) gives a reduced 2×2 symmetric matrix equation:

$$\begin{bmatrix} a - \frac{c^2}{f} & b - \frac{ce}{f} \\ b - \frac{ce}{f} & d - \frac{e^2}{f} \end{bmatrix} \begin{pmatrix} \varphi \\ \psi \end{pmatrix} = 0. \tag{4.60}$$

The dispersion relation is now given by

$$D_{2\text{by}2}(\omega) = ad - b^2 - \frac{1}{f}(c^2 d - 2bce + e^2 a) = 0. \tag{4.61}$$

The compressional MHD limit is $a \simeq -b \simeq d$, which reduces Eq. (4.61) to

$$ad - b^2 - \frac{d}{f}(c+e)^2 = 0. \tag{4.62}$$

To find analytically the kinetic ballooning-interchange drift mode and connect with the variational formulas, we take $\eta_e = 0$ and note $a \simeq -b \simeq d \simeq e$ for the dominant terms owing to the small $E_\parallel$. Then the full determinant D factors as

$$ad - b^2 + \frac{\tau(1-\omega_*/\omega)(Q-(1-\omega_*/\omega))^2}{\frac{2}{\beta_e} + \frac{T_i}{T_e}R} = 0 \tag{4.63}$$

as shown by Eq. (4.62). Here $\omega_{*e} = \omega_*$ for $\eta_e = 0$. The last term in Eq. (4.63) gives the kinetic compressional response. For the near-MHD regime, the response function ϕ reduces to

$$Q - 1 + \frac{\omega_*}{\omega} \simeq -\frac{\omega_{*pi} - \omega_*}{\omega} + i\Delta_Q = -\frac{\omega_{*p}}{\omega} + i\Delta_Q \tag{4.64}$$

with ω_{*p} having the total pressure gradient and a small resonant part $i\Delta_Q$ from wave-particle resonance. A reasonable approximation for R in the region $\omega\omega_{Di} > 0$ is

$$R \cong c_0 \frac{[\omega - \omega_{*i}(1 + 2\eta_i)]}{\omega - \omega_{Di} + ic_1|\omega_{Di}|} \tag{4.65}$$

where c_0 and c_1 are positive fitting parameters of order $c_0 \simeq 1, c_1 \simeq 0.1$. Here $\Delta_Q = \mathrm{Im}\, Q(\omega)$ and $\Delta_R = \mathrm{Im}\, R(\omega)$ are real numbers giving the resonant ion contributions.

The resonant modes in the high-β region have

$$\omega = \omega_0 + i\gamma_k \simeq \omega_{*i}(1 + \eta_i) + i\gamma_k \tag{4.66}$$

which is a westward propagating drift wave. (Here ω_0 and γ_k are real numbers.) A Taylor-series expansion of the dominant terms in Eq. (4.63) gives

$$\begin{aligned} ad - b^2 \;&\simeq\; \left(\frac{\omega_*}{\omega} - 1\right)\left[\frac{\omega_A^2}{\omega_0^2}\, b - b\left(1 - \frac{\omega_{*pi}}{\omega_0}\right) - \frac{\omega_*\omega_D}{\omega_0^2}\right] \\ &+\; \left(\frac{\omega_*}{\omega_0} - 1\right)\frac{i\gamma_k}{\omega_0}\left[\frac{-2\omega_A^2}{\omega_0^2}\, b - \frac{b\omega_{*pi}}{\omega_0} + \frac{2\omega_*\omega_D}{\omega_0^2}\right] \end{aligned} \tag{4.67}$$

for $\omega = \omega_0 + i\gamma_k$ with $|\gamma_k| \ll \omega_0$. Thus, the growth rate γ_k is determined by

$$\frac{i\gamma_k}{\omega_0}\left[\frac{2\omega_A^2}{\omega_0^2} + \frac{\omega_{*pi}}{\omega_0}\right] b + \frac{T_e}{T_i}\frac{(\omega_{*p}/\omega_0 - i\Delta_Q)^2}{c_0[1 - \frac{\omega_{*i}(1+2\eta_i)}{\omega_0} - i\Delta_R]} = 0 \tag{4.68}$$

for $\Delta_Q \sim \Delta_R \ll 1$. Since $\omega_{*p}/\omega_0 \gtrsim 1$ the significant resonant contribution comes from $i\Delta_R$ in the denominator. Thus, we obtain the growth rate formula

$$\frac{\gamma_k}{\omega_0}\left(\frac{2\omega_A^2}{\omega_{*p}^2}+1\right) b = -\frac{T_e}{T_i}\frac{(\omega_*/\omega_0)^2\Delta_R}{c_0\left[\left(\frac{\eta_i}{1+\eta_i}\right)^2+\Delta_R^2\right]} \tag{4.69}$$

with $\gamma_k > 0$ for $\Delta_R \equiv \mathrm{Im}\,(R(\omega_0)) < 0$.

In Figure 4.3 we give the stability results for the full 3×3 determinant, which shows the high-beta stabilization of the strongly ($\gamma_k/\omega_k \lesssim 1$) unstable modes for $\beta > \beta_2$ in frame (a). The high beta region in the full kinetic description has only a resonant ion-wave pressure gradient driven instability that produces anomalous transport rather than global MHD-like motions. Here $k_y\rho_i = 0.3$, $T_e/T_i = 1$ and $L_p/R_c = 1$ and the figure shows that the critical values β_1 and β_2 are still well defined. However, due to the ion kinetic resonances $\omega_\kappa = \omega_{Di}(\mathcal{E},\mu)$ there is a residual kinetic instability for $\beta > \beta_2$. The unstable mode has an MHD-like polarization (with $\psi/\phi = 0.9$) and is westward propagating. In the strongly unstable region the speed is $\omega/k_y = \frac{1}{2}\,v_{di} = \overline{v_i(\rho_i/2L_p)}$ and in the weakly unstable high beta region the speed is $\omega/k_y = v_{di}(x)$. These waves are in the 2 mHz-20 mHz (Pi 2 and Pc5) range and propagate westward with speeds of 5 to 10 km/s.

4.8 Full electromagnetic variational form

The most useful way to express the three coupled equations for the three electromagnetic field components is to use a variational functional $\mathcal{L}$ for field components that are analogous to those used in MHD calculations. The

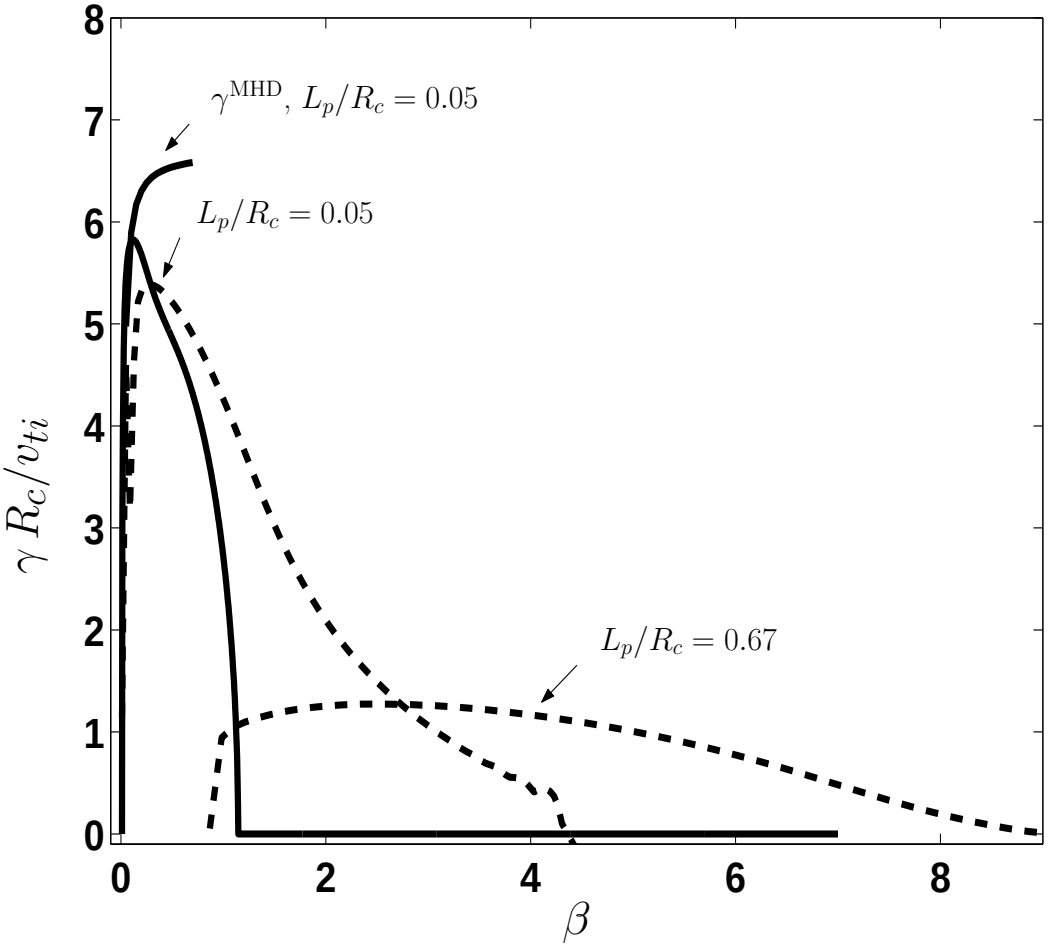

Figure 4.3: The local kinetic theory growth rate computed from the full 3×3 determinant in Eq. (12) as a function of β. Here $k_y\rho_i = 0.3$, $T_e/T_i = 1$ and $L_p/R_c = 1$ and the figure shows that the critical values β_1 and β_2 are still well defined. However, due to the ion kinetic resonances $\omega_\kappa = \omega_{Di}(\mathcal{E}, \mu)$ there is a residual kinetic instability for $\beta > \beta_2$. The unstable mode has an MHD-like polarization (with $\psi/\phi = 0.9$) and is westward propagating. In the strongly unstable region the speed is $\omega/k_y = \frac{1}{2}\, v_{di} = \overline{v_i(\rho_i/2L_p)}$ and in the weakly unstable high beta region the speed is $\omega/k_y = v_{di}(x)$. These waves are in the 2 mHz-20 mHz (Pi 2 and Pc5) range and propagate westward with speeds of 5 to 10 km/s.

variational form that describes stability of low-frequency waves in the limit is given by *Horton et al.* (2001) and is repeated here:

$$\mathcal{L}(\boldsymbol{\xi},\phi) = \int \frac{\mathrm{d}s}{B}\left[-\rho_m\omega^2\boldsymbol{\xi}\cdot\boldsymbol{\xi} + \frac{1}{\mu_0}\mathbf{Q}_\perp\cdot\mathbf{Q}_\perp + \frac{1}{\mu_0}Q_LQ_L - 2\boldsymbol{\xi}\cdot\nabla p(\Psi)\boldsymbol{\kappa}\cdot\boldsymbol{\xi}\right]$$
$$-\sum_a \int\frac{ds}{B}\int \mathrm{d}v^3\frac{F_a}{T_a}\left[q_a^2\phi\phi - \frac{\omega-\omega_*}{\omega-\overline{\omega}_D}\overline{\mathcal{K}}\,\overline{\mathcal{K}}\right] \tag{4.70}$$

where $\mathcal{K}$ is the perturbed particle energy,

$$\mathcal{K} = \epsilon T_a\left[\frac{q_a}{\epsilon T_a}\phi + \lambda\frac{Q_L}{B_{\min}} + (2-\lambda\frac{B}{B_{\min}})\boldsymbol{\kappa}\cdot\boldsymbol{\xi}\right] \tag{4.71}$$

and the over-line represents bounce averaging. Taking variations of this integral equation with respect to ϕ and the two components of $\boldsymbol{\xi}$, which in our case are only a function of s, the distance along the field line, yields the set of integral-differential eigenvalue equations to be solved. In Eq. (4.70)

$$\mathbf{Q} = \nabla\times(\boldsymbol{\xi}\times\mathbf{B}) \tag{4.72}$$

$$Q_L = \delta B_\parallel + \boldsymbol{\xi}\cdot\nabla B - B\boldsymbol{\xi}\cdot\boldsymbol{\kappa}. \tag{4.73}$$

4.9 Conclusions

In this chapter the gyrokinetic equation was used to provide a more detailed description of magnetospheric plasmas. This equation was linearized and solved under the condition of locality and without the effects of trapped particles. The effects of trapped particles is deferred to later chapters. The resulting perturbed distribution function was used to compute the perturbed densities and currents. Then using quasi-neutrality, the parallel component of

Amperes law and the radial component of Amperes law, three coupled mode equations were found. Combining these three equations resulted in a 3×3 matrix equation with the determinant of the operator providing a dispersion relation.

The elements of the 3×3 matrix contained complex integrals over the ion velocity distribution. These integrals account for the resonance of the oscillating electromagnetic fields with the ion gyrokinetic drift due to the ∇B and κ drifts. A method and computer program was developed to compute these integrals accurately for all values of the frequency including stable solutions. These integrals were then used to numerically evaluate the full electromagnetic dispersion relation.

The important result of this chapter is that plasmas that are MHD stable may still be unstable to a drift ballooning/interchange mode due to wave-particle resonances. In chapter 3, two critical β values were found in the Fast-MHD limit. Equilibrium plasmas with a β value in between these two critical values were found to be unstable. The lower bound β_1 value was set by the energy required to bend the magnetic field of the particular flux-tube. The upper bound β_2 value was set by the energy required to compress the magnetic field. In this chapter we found that plasmas with $\beta > \beta_2$ may still be unstable due to wave-particle resonances, but that eventually as one considers equilibria with higher and higher β values the plasma is again stabilized. These results can be summarized by the illustration in Figure 4.4.

Finally, a new variational form was presented that uses a convenient

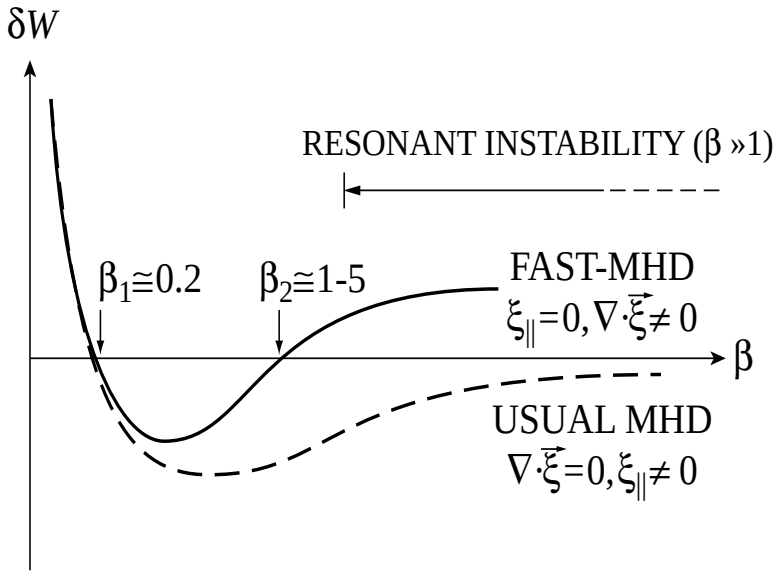

Figure 4.4: Illustration showing the relationship between the $\delta W_p^{\rm MHD}$ computed from the minimization of the ideal MHD model over all trial functions and the minimization δW (Fast) which takes into account the physical condition for applicability of MHD. The stabilization of Fast-MHD for $\beta > \beta_2^{\rm FMHD}$ is doe to compression of the plasma in the flux-tubes, which requires kinetic theory for a precise evaluation. A resonant instability is found for $\beta > \beta_2^{\rm FMHD}$ as a result of the 3×3 dispersion relation.

gauge and a convenient set of variables. In the fluid limit the variables used in this new variational form reduce to the variables used to describe plasmas in the MHD limit. This is important for many practical reasons such as comparing to MHD simulations and connecting to MHD δW calculations. This new variational form retains trapped particle effects for both the ions and the electrons and if solved would account for the non-local bounce-averaged effects.

Chapter 5

Bounce-Averaged Electrostatic Modes

As discussed in Chapters 3 and 4 the MHD approximation is not appropriate for dealing with slowly growing low frequency fluctuations. For these modes of oscillation the bounce frequency, the frequency at which particles mirror between the North and South poles, is high; thus the mirroring particles sample the entire field line. In Chapter 3 we saw that high-β plasmas were stabilized due to the energy required to compress the plasma, and then in Chapter 4 it was shown that resonant particles can destabilize this parameter regime. However, in Chapter 4 we took a local approximation, by assuming that the eigenmode structure was confined to the equatorial plane where the curvature of the magnetic field was the highest. In this chapter we discuss the bounce-averaged non-local effects and introduce methods for solving the resulting integro-differential non-linear eigenmode equations.

In Section 5.1 the numerical methods used in computing bounce-averages and bounce-averaged operators is described in some detail. In Section 5.2 the numerical methods used to compute the integrals over particle energy that describe the resonant response of the drifting particles to the waves is discussed. In Section 5.3 the electrostatic eigenmode equation is found from the

drift kinetic variation form presented in Chapter 4. In Section 5.4 we make the approximation that the frequency of the electrostatic oscillation is very much bigger than the diamagnetic drift frequency and the gradient curvature drift. In this approximation analytical solutions to the eigenmode equation are shown and compared to the numerical results. In Section 5.5 we make the approximation that the frequency of the electrostatic oscillation is very much less than the diamagnetic drift frequency and the gradient and curvature drift frequency. Then in Section 5.6 a Nyquist analysis is performed in the limit that the perturbation is confined to the equatorial plane. Finally, in Section 5.7 conclusions and a summary are given.

5.1 Bounce-Averaged Numerical Methods.

5.1.1 Bounce Averages

The bounce average of a function ϕ, that is a function of the distance along the field line s, is a function of $\lambda = \sin^2(\alpha)$ where α is the pitch angle at the equatorial plane. The bounce average is formally defined as

$$\overline{\phi}(\lambda) = \frac{1}{\tau(\lambda)} \int \frac{\mathrm{d}s}{u_{\parallel}(\lambda, s)} \phi(s) \quad \text{where} \quad \tau(\lambda) = \int \frac{\mathrm{d}s}{u_{\parallel}(\lambda, s)} \tag{5.1}$$

where the limits of the integrals are taken to be between the turning points for the particle. The parallel velocity used in Eq. 5.1 may be written with the help of the constancy of the magnetic moment and the fact that the bounce-average is independent of the particle energy as

$$u_{\parallel}(\lambda, s) = \sqrt{1 - \lambda B(s)/B_{\min}} \tag{5.2}$$

We take the field lines to be symmetric about the equatorial plane. We further label the field line coordinate $s = 0$ at the equatorial plane and only consider one half of the field line extending from the equatorial plane to the ionosphere. Thus the bounce average integrals over s will extend from $s = 0$ to $s = s_{\rm tp}(\lambda)$ where $s_{\rm tp}(\lambda)$ is the turning point for the particle with pitch angle coordinate given by λ.

To perform these kinds of integrals numerically the spaces (s, λ) are discretized such that one turning point occurs in between each s grid point. The bounce-time $\tau(\lambda)$ provides the simplest means of describing the numerical procedure. The bounce-time can be discretized as follows:

$$\begin{aligned} \tau(\lambda) &= \int \frac{{\rm d}s}{u_\parallel(\lambda, s)} \\ &= \sum_{i=0}^{l} \int_{s_i}^{s_l} \frac{{\rm d}s}{u_\parallel(\lambda, s)} \end{aligned}$$

where $s_l = s_{\rm tp}(\lambda)$ and $s_0 = 0$. Care must be taken with the interval s_{l-1} to s_l as $u_\parallel$ goes to zero. Now discretizing the λ space as well and labeling it with l the bounce-time may be written as

$$\tau(\lambda_l) \simeq \tau_l = \sum_{i=0}^{l} g_{i,l} \quad \text{where} \quad g_{i,l} = \int_{s_i}^{s_l} \frac{{\rm d}s}{u_\parallel(\lambda_l, s)} \tag{5.3}$$

where $g_{i,l}$ is a bounce matrix with interesting properties and features.

Now consider the actual bounce average of a quantity $\phi(s)$. This can be approximated by the following

$$\overline{\phi} \approx \phi_l = \frac{1}{2\tau_l} \sum_{i=0}^{l} (\phi_i + \phi_{i+1}) g_{i,l}. \tag{5.4}$$

For convenience one can define q_i^l such that

$$\bar{\phi} \approx \sum_{i=0}^{l+1} q_i^l \phi_i \tag{5.5}$$

where

$$q_i^l = \begin{cases} \frac{1}{2}\frac{g_{i,l}}{\tau_l} & \text{if} \quad i == 0 \\ \frac{1}{2}\frac{(g_{i,l}+g_{i-1,l})}{\tau_l} & \text{if} \quad 0 \leq i \leq l \\ \frac{1}{2}\frac{g_{l,l}}{\tau_l} & \text{if} \quad i == l+1 \end{cases} \tag{5.6}$$

Care must be taken in order to compute the $g_i(\lambda_l)$ as they have a square root singularity at the end-points. Their will be a sub-grid over which all physical variables are stored and the dynamic variables will be stored at the main-grid scale. Figure 5.1 depicts the two-scale discretization scheme.

For $i \neq l$ the $g_{i,l}$ can be approximated with two closed five-point quadrature formulas, the first covering the length from s_i to the turning point found at λ_i and the second length covering the length from the turning point at λ_i to s_{i+1}:

$$g_{i,l} \simeq \sum \left[\frac{14}{45}\frac{\delta s}{u_\parallel(\lambda_l, s_i)} + \frac{64}{45}\frac{\delta s}{u_\parallel(\lambda_l, s_{i+1})} + \frac{24}{45}\frac{\delta s}{u_\parallel(\lambda_l, s_{i+2})} + \frac{64}{45}\frac{\delta s}{u_\parallel(\lambda_l, s_{i+3})} + \frac{14}{45}\frac{\delta s}{u_\parallel(\lambda_l, s_{i+4})} \right]. \tag{5.7}$$

If $i = l$ then $g_{i,l}$ can be approximated with an open three-point quadrature rule, spanning the length of s beginning with s_l and ending with the turning point with λ_l:

$$g_{i,l} \simeq \left[\frac{3}{2}\frac{\delta s}{u_\parallel(\lambda_l, s_{i+1})} + \frac{\delta s}{u_\parallel(\lambda_l, s_{i+2})} + \frac{3}{2}\frac{\delta s}{u_\parallel(\lambda_l, s_{i+3})} \right] \tag{5.8}$$

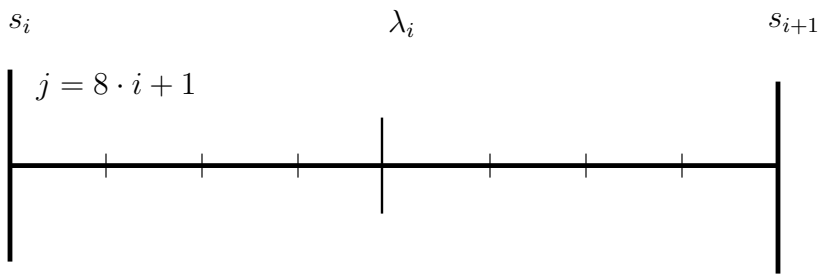

Figure 5.1: This figure shows one unit of the grid used for these calculations. The points s_i and s_{i+1} are the main grid level, where all dynamical variables are stored. The middle point labeled λ_i shows that there is one turning point for particles between each dynamical variable. The sub-grid scale shown is used to compute the $g_{i,l}$.

5.1.2 Bounce Time

$1 + s^2$ *Model.*

For the magnetic field model with $B(s) = 1 + s^2$, the bounce time can be computed analytically and provides a convenient means to check the accuracy of the numerical scheme. The bounce-time in the $1 + s^2$ model is given by

$$\tau(\lambda) = \int_0^{\sqrt{(1-\lambda)/\lambda}} \frac{ds}{\sqrt{1-\lambda b}} = \frac{\pi}{2\sqrt{\lambda}}. \tag{5.9}$$

Figure 5.2 compares the analytical solution given in Eq. (5.9) versus the numerical method presented in the previous section. As a measure of the accuracy of the method, the relative error was computed as

$$\epsilon_{\text{rel}} = \Sigma \frac{\left(\tau_{\text{num}} - \tau_{\text{ana}}\right)^2}{N \tau_{\text{num}}^{avg}}, \tag{5.10}$$

where $\tau_{\rm num}$ is computed numerically, $\tau_{\rm ana}$ is the exact result, N is the number of points used, and $\tau_{\rm num}^{avg}$ is the average of the numerically computed values for τ. Figure 5.3 shows the relative error versus the distance between grid points along the field line ds.

5.1.3 Bounce-Averaged Drifts

The magnetic guiding-center curvature and ∇B drift frequencies are given, respectively, by

$$\omega_{\boldsymbol{\kappa} j} = \frac{k_y T_j}{q_j B \min} 2\left(1 - \lambda \frac{B}{B_{\rm min}}\right) \frac{\widehat{\mathbf{y}} \cdot \mathbf{B} \times \boldsymbol{\kappa}}{B^2} B_{\rm min} \left(\frac{K}{T_j}\right) \tag{5.11}$$

$$\omega_{\nabla B j} = \frac{k_y T_j}{q_j B_{\rm min}} \lambda \frac{\widehat{\mathbf{y}} \cdot \mathbf{B} \times \nabla B}{B^2} \left(\frac{K}{T_j}\right) \tag{5.12}$$

Here $\lambda = \sin^2(\alpha) = \mu B_{\rm min}/K$ is the dimensionless pitch angle variable in the equatorial plane with the pitch angle given by α, $\boldsymbol{\kappa} = \hat{\mathbf{b}} \cdot \nabla \hat{\mathbf{b}}$ is the curvature vector, K is the kinetic energy of the particle, and $|\boldsymbol{\kappa}| = 1/R_c$ is the inverse of the radius of curvature $R_c(x)$ which is a function of position. For $\rho_i = 300$ km the wavelength is $2\pi/k_y = 20\rho_i = 6 \cdot 10^6 \text{m} \approx 1 R_E$, which is approximately the limit of the local approximation. Notice that $k_y T_j/(q_j B_{\rm min})$ can be rewritten as $k_y \rho_j v_{tj}$; with typical magnetospheric parameters of a 5 KeV proton (corresponding to a thermal velocity of $\simeq 2.7\, R_E/\text{min}$) and $k_y \rho_i = 0.5$ and a $0.2 R_E$ radius of curvature, this gives an estimate of 3 mHz for drift frequencies. In a vacuum field, the ∇B drift frequency reduces to $\omega_{\nabla B} \rightarrow (T_\perp/2T_\parallel)\omega_{\boldsymbol{\kappa}}$ [4]. Thus, near the Earth where the magnetic field is primarily due to the Earth's dipole field, the plasma current is small, and consequently

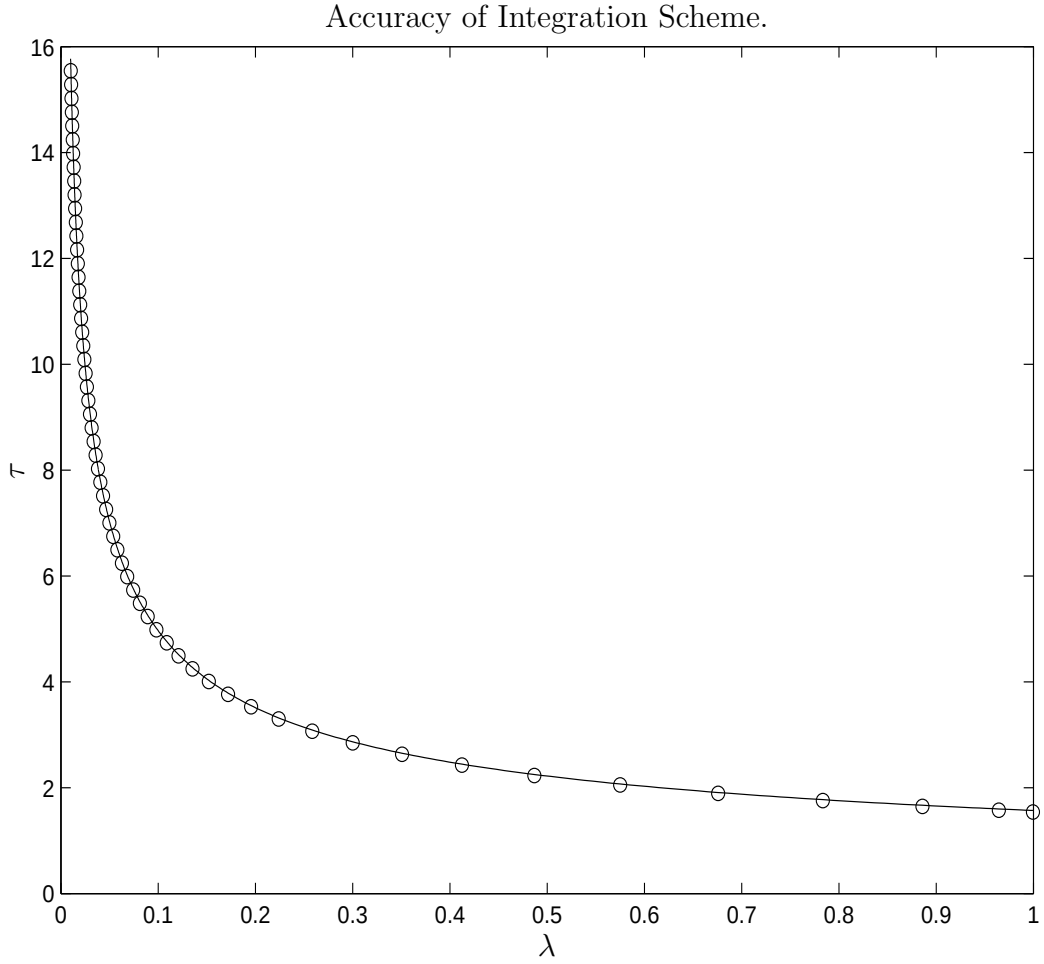

Figure 5.2: The bounce-time, τ is computed as a function of λ, a pitch angle variable, for the $B(s) = 1 + s^2$ magnetic field model. For the numerical computation 600 points were taken along the field line, and the field line had a length of 10. A relative error of 0.0525 was obtained for this configuration.

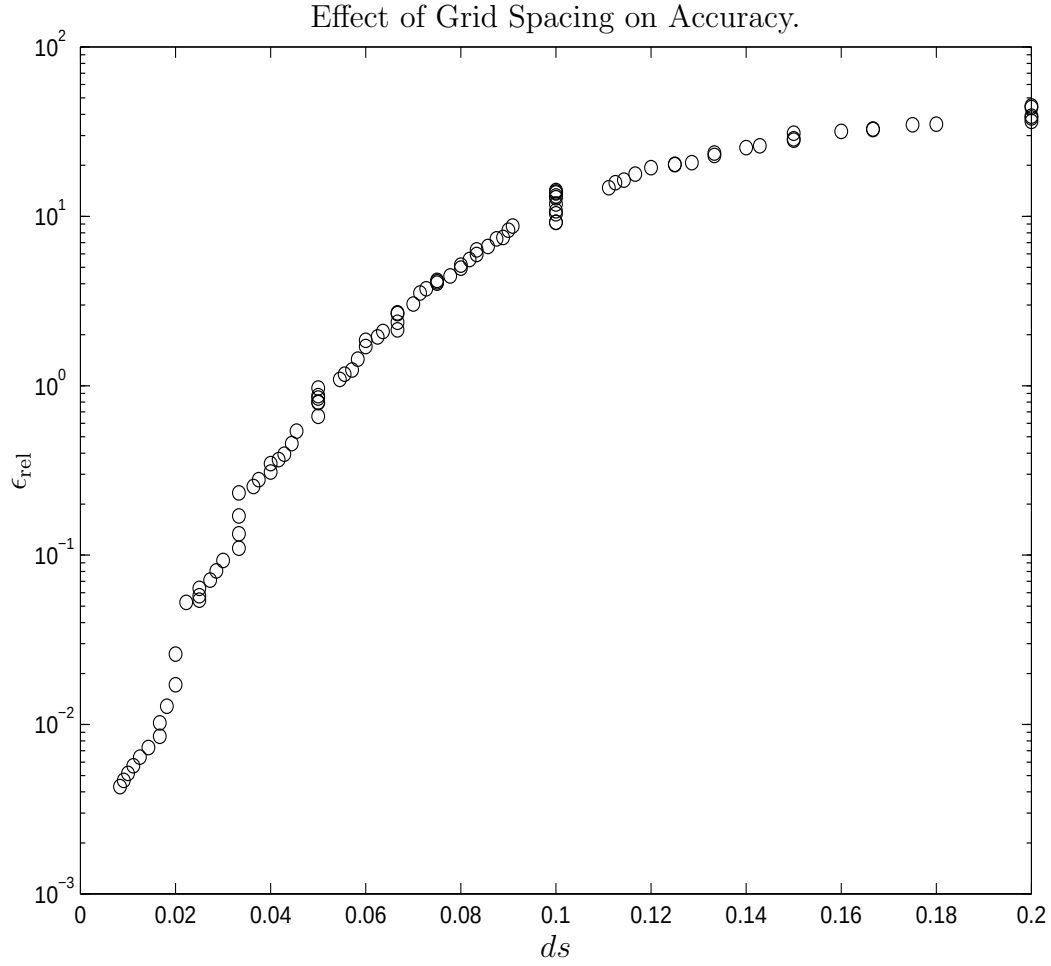

Figure 5.3: The bounce-time, τ is computed as a function of λ, a pitch angle variable, for the $B(s) = 1+s^2$ magnetic field model. The numerically computed value is compared with the exact answer for 120 different grid spacings, ds.

the pressure is low ($\beta \ll 1$) and the curvature and ∇B drift are in the same direction. However, at high beta one can use $\mathbf{B} \times (\mathbf{J} \times \mathbf{B} - \nabla p) = 0$ to derive

$$\frac{\mathbf{B} \times \nabla B}{B^2} = \frac{\mathbf{B} \times \boldsymbol{\kappa}}{B} - \frac{\mu_0 \mathbf{B} \times \nabla p}{B^3} \tag{5.13}$$

and thus

$$\omega_{\nabla Bj} = \frac{k_y T_j}{q_j B_{\min}} \lambda \widehat{\mathbf{y}} \cdot \left[\frac{\mathbf{B} \times \boldsymbol{\kappa}}{B} - \frac{\mu_0 \mathbf{B} \times \nabla p}{B^3} \right] \left(\frac{K}{T_j} \right) \tag{5.14}$$

so that reversal of the drift direction occurs for $\beta \gtrsim L_p/R_c$. Using this relation we can repartition the total magnetic drift ω_{Di} into one term that represents the vacuum effect on particles $\omega_{\kappa'}$ and another that is due to the pressure gradients. This separation gives $\omega_{Di} = \omega_{\kappa'} + \omega_{\nabla p}$ with

$$\omega_{\kappa'} = \frac{k_y T_i}{q B_{\min}} \left(2 - \lambda \frac{B}{B_{\min}} \right) \frac{\hat{\mathbf{y}} \cdot \mathbf{B} \times \kappa}{B^2} B_{\min} \left(\frac{K}{T_i} \right) \tag{5.15}$$

$$\omega_{\nabla p} = -\frac{k_y T_i}{q B_{\min}} \lambda \frac{\mu_0 \hat{\mathbf{y}} \cdot \hat{\mathbf{b}} \times \nabla p}{B^2} \left(\frac{K}{T_i} \right) \tag{5.16}$$

which is useful for the high-β stability formulas. The drift $\omega_{\kappa'}/k_y$ is Westward, and the drift $\omega_{\nabla p}/k_y$ is Eastward for Earthward increasing pressure profiles. For $\lambda B/B_{\min} = 1$ the opposing drifts cancel when $R_c \mu_0 \nabla p / B^2 \simeq 1$. In terms of the plasma pressure $\beta = 2\mu_0 p/B^2$, this drift reversal of the total guiding center drift velocity occurs for $\beta > 2L_p/R_c$ where L_p is the pressure gradient scale length. Generally the drift reverse β value $\beta_{\rm dr} = 2L_p/R_c$ is very high since $L_p \gg R_c$ except during transient periods.

The response of the plasma to a wave depends on the orbits of the particles over a wave period. For low frequencies, the bouncing motion of the particles due to the mirror force becomes important, and thus the bounce

average of the magnetic drift velocities arises. Figure 5.4 shows the bounce-averaged drifts as a function of λ for three different positions, computed from the Tsyganenko 1996 magnetic field model. The characteristic property of the NGO region to notice on these plots is that Earthward of the NGO region, the magnetic curvature drift and the magnetic ∇B drift are in the same direction, and tailward they are in the opposite direction, as is expected from Eq. (5.14). However, neither of these two models exhibit drift reversal as defined previously. Also shown in Fig. 5.4 is the stability parameter $R(\beta) = \int_0^{K/B_{\min}} \mathrm{d}\mu (B_{\min}/K)(\omega_{*i}/\overline{\omega}_{Di}(\beta))$ which is used for drift compressional modes investigated in Chapter 6. The minimum of R is found to be in the NGO region.

Figure 5.5 shows the relevant frequencies for the kinetic stability analysis as a function of x/R_E in the nightside equatorial plane, computed from Tsyganenko's 1996 model. Bounce-averaged magnetic drift components for particles with three different equatorial pitch angles are shown, along with the diamagnetic drift frequency for a pressure gradient scale length of $L_p = 2.0R_E$. It is seen that $\omega_{*i} \sim \overline{\omega}_{Di} \ll \omega_{bi}$. It can also be seen from these plots that the $\overline{\omega}_{\nabla Bi}$ component becomes negative tailward of the NGO region, where $\omega_{bi} = 2\pi v_{ti}/\tau(\lambda)$ is the bounce frequency and v_{ti} is the ion thermal velocity. The polarization of the fluctuations is $\delta B_\parallel \gg \delta B_\perp$, with a small $\delta E_\perp \sim v_{\mathrm{di}} \delta B_\parallel \ll v_{ti} \delta B_\parallel$ in the direction perpendicular to that of the wave propagation.

Here we took the particles to have a Maxwellian velocity distribution

$f_j(\mathbf{x},\mathbf{v}) = n_j(\mathbf{x})(m_j/2\pi T_j(\mathbf{x}))^{3/2}\exp(-K/T_j(\mathbf{x}))$. In a future work we will consider a kappa distribution. For the local Maxwellian, the diamagnetic drift frequency is

$$\omega_{*tj} = \frac{k_y T_j}{q_j B_{\min} L_n}\left(1 - \frac{3}{2}\eta_j + \eta_j \frac{K}{T_j}\right). \tag{5.17}$$

For an adiabatically compressed energy distribution, we have $f_j = f_j(KV^{2/3})$, where $V = \int ds/B$ is the flux-tube volume. Then the effective value of $\eta_j = L_n/L_{Tj}$ is $\eta_j = 2/3$.

5.2 Energy functions

In computing the response of the particles to the waves an integral over the distribution function is used. This integral can be done by integrating over the energy of the particles, the pitch angle of the particles and the gyrophase angle. They gyrophase angle is trivial while the remaining integrals are somewhat complicated. In this section we present the methods used to perform the integrals over the energy of the particles. First, we note that there is a class of integrals of the type found in these distribution averages and they are given by the function $F^n(\omega)$ which is defined as follows:

$$F^n(\omega) = \frac{2}{\sqrt{\pi}}\int_0^\infty d\epsilon\ \epsilon^{n+1/2}\, e^{-\epsilon}\frac{1}{\omega-\epsilon} \tag{5.18}$$

$$= \frac{2}{\sqrt{\pi}}\int_{-\infty}^\infty dx\ x^{2(n+1)} e^{-x^2}\frac{1}{\omega-x^2} \tag{5.19}$$

The limit $\omega \to 0$ is important because it occurs often in the following work. The resulting function will be labeled P^n, thus $F^n(\omega \to 0) = P^n$ and

$$P^n = -\frac{2}{\sqrt{\pi}}\int_{-\infty}^\infty dx\ x^{2n} e^{-x^2} \tag{5.20}$$

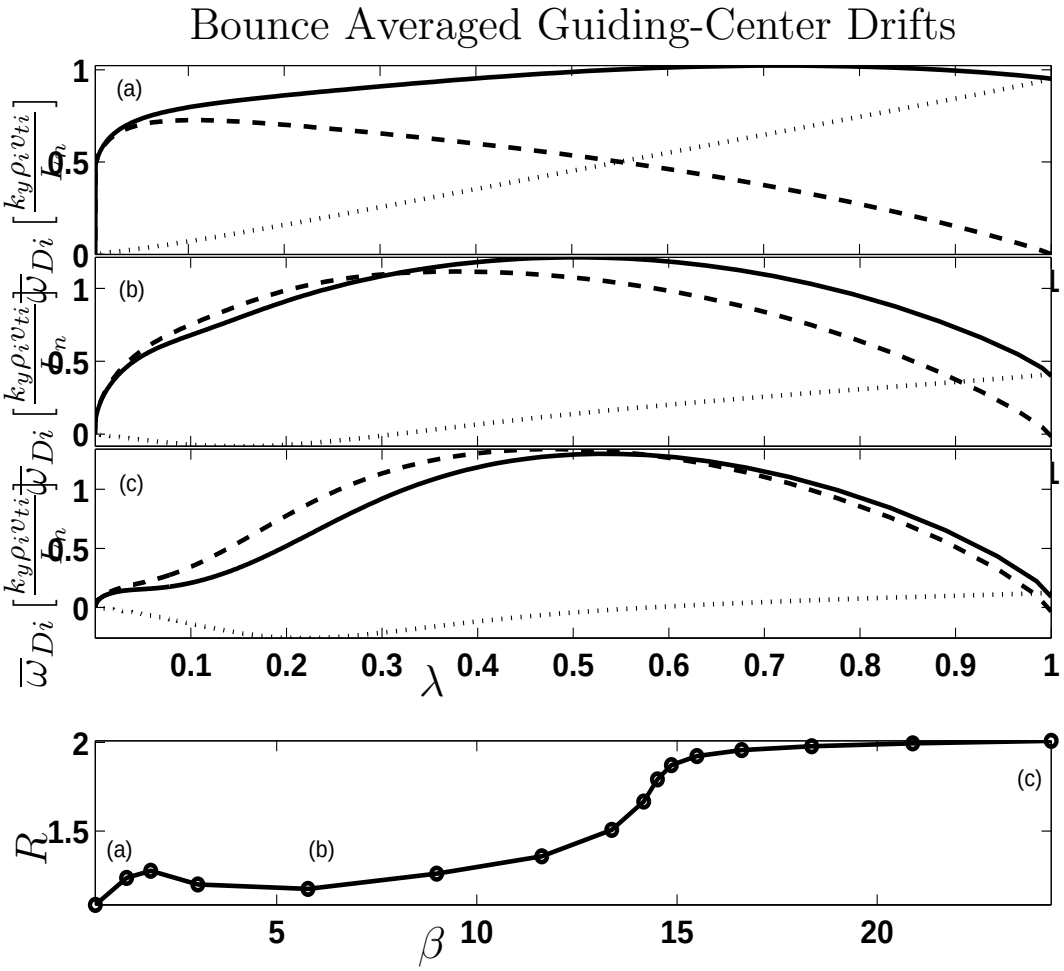

Figure 5.4: The pitch angle dependence of the bounce-averaged drifts of the Tsyganenko 1996 model. The $\overline{\omega}_{Di}$ frequency is shown in units of $k_y\rho_i v_{ti}/L_n$ with $L_n = 2R_E$. The heavy dashed lines shows the bounce-averaged curvature drift component $\overline{\omega}_{\kappa i}$, the dotted line shows $\overline{\omega}_{\nabla B\, i}$, and the solid line shows the total drift $\overline{\omega}_{Di} = \overline{\omega}_{\kappa i} + \overline{\omega}_{\nabla B\, i}$. The top three panels correspond to different flux tubes whose equatorial foot points correspond to the labels (a) at $x = -5R_E$ with $\beta = 0.5$, (b) at $x = -9R_E$ with $\beta = 5.8$, and (c) at $x = -20R_E$ with $\beta = 24.3$ found in the bottom panel, which shows the stability parameter $R(\beta)$.

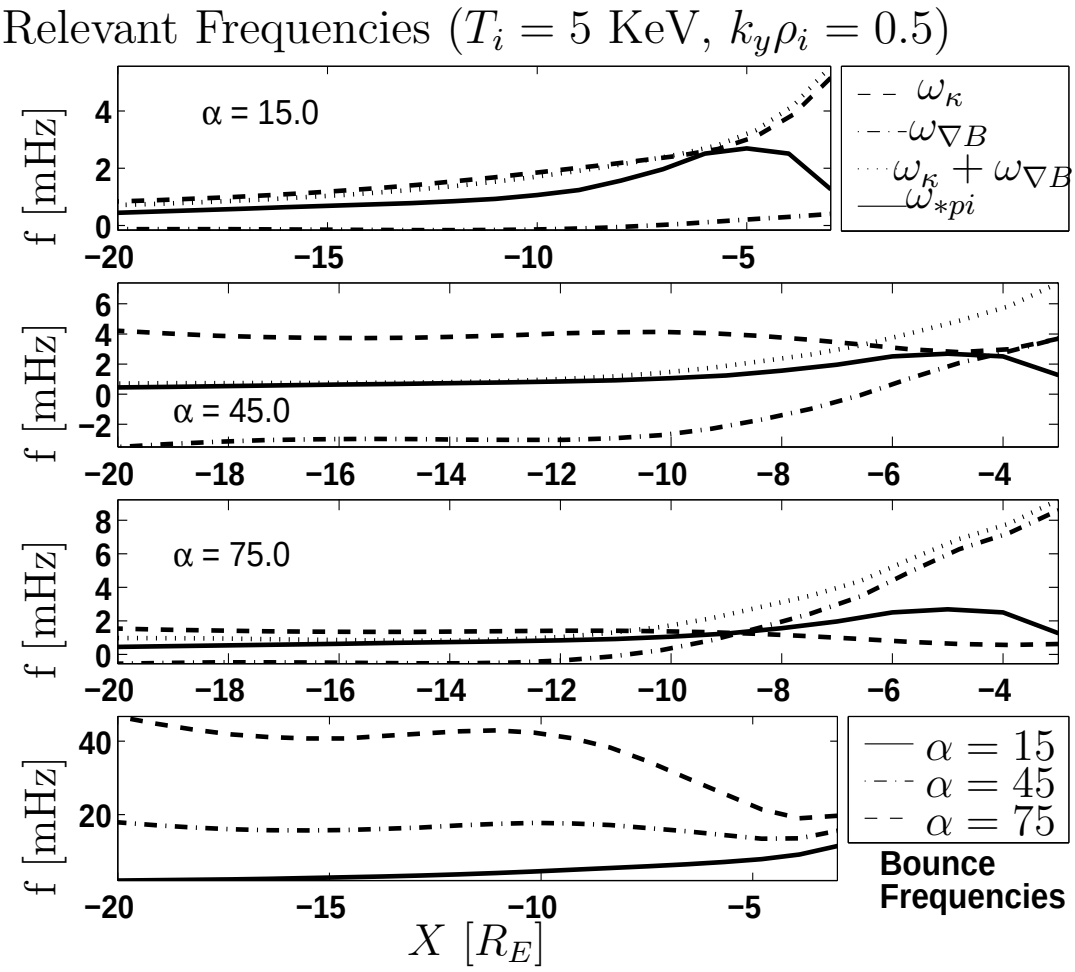

Figure 5.5: Relevant frequencies as a function of $x\,[R_E]$ through the inner edge of the plasma sheet. The top panel shows the frequencies for particles with a pitch angle of 15 degrees, the second for particles with a pitch angle of 45 degrees, and the third for 75 degrees. Tsyganenko's (1996) model was used with $PS = 0$, $P_{\rm dyn} = 3.0\,$nPa, DST $= -50nT$, $B_y^{\rm IMF} = 0$, and $B_z^{\rm IMF} = 5.0$nT to compute the properties of the flux tube, including the pressure gradient scale length (assuming force balance) used in ω_{*pi}. The bottom panel shows the bounce frequencies for particles with these three pitch angles.

where for $n < 0$,

$$P^n = 2\frac{(-2)^{|n|}}{(2|n|-1)!^{\text{odd}}}, \tag{5.21}$$

$P^0 = 2$, and for $n > 0$,

$$P^n = 2\frac{(2n-1)!^{\text{odd}}}{2^n}. \tag{5.22}$$

The factorials in the above equations refer to multiplying only the odd terms, i.e. $7!^{\text{odd}} = 7 \cdot 5 \cdot 3 \cdot 1$ The recurrence relation for the P^n's is given by $P^{n+1} = (n + 1/2)P^n$. So a power series representation of Eqs. (5.19) can be written in terms of the P^n as

$$F^n(\omega) = \sum_{k=0}^{\infty} P^{n-k}\omega^{\kappa} \tag{5.23}$$

Next the numerical method used to compute the functions $F^n(\omega)$ for arbitrary complex ω is discussed.

5.2.1 Sampling theorem method

The sampling theorem states that

$$g(x) = \sum_{l=-\infty}^{\infty} g(x_l)\frac{\sin(\frac{\pi}{h}(x - x_l))}{\frac{\pi}{h}(x - x_l)} + e(x) \tag{5.24}$$

where $e(x)$ is an error term that is small for $g(x)$'s that fall off fairly rapidly and whose Fourier transform falls off fairly rapidly as well. The uncertainty principle makes this a difficult feat to accomplish; thus functions like $g(x) \simeq e^{-x^2}$ have the smallest $e(x)$.

Notice that the energy integrals (5.19) can be made somewhat simple

using this theorem. By expressing $x^{1/2+n}\,e^{-x}$ using Eq. (5.24) we can write

$$F^n \simeq \sum_{l=-\infty}^{\infty} x_l^{2(n+1)} e^{-x_l^2} \int_{-\infty}^{\infty} dx \frac{\sin(\frac{\pi}{h}(x-x_l))}{\frac{\pi}{h}(x-x_l)(\omega-x^2)}. \tag{5.25}$$

Then expressing the sin function as complex exponentials we can write

$$F^n \simeq \sum_{l=-\infty}^{\infty} x_l^{2(n+1)} e^{-x_l^2} \frac{h}{2\pi i} \int_{-\infty}^{\infty} dx \frac{e^{\frac{i\pi}{h}(x-x_l)} - e^{-\frac{i\pi}{h}(x-x_l)}}{(x-x_l)(\omega-x^2)}. \tag{5.26}$$

In Eq. (5.26) there are two elementary contour integrals to perform. The first can be evaluated as follows:

$$\begin{aligned} \int_{-\infty}^{\infty} dx \frac{e^{\frac{i\pi}{h}(x-x_l)}}{(x-x_l)(\omega-x^2)} &= i\pi \left[\frac{1}{(\sqrt{\omega}-x_l)(\sqrt{\omega}+x_l)} + \right. \\ &\left. \frac{e^{i\frac{\pi}{h}(\sqrt{\omega}-x_l)}}{(\sqrt{\omega}-x_l)\sqrt{\omega}} - \frac{e^{-i\frac{\pi}{h}(\sqrt{\omega}+x_l)}}{(\sqrt{\omega}+x_l)\sqrt{\omega}} \right]. \end{aligned} \tag{5.27}$$

Similarly, the second integral is found to be

$$\int_{-\infty}^{\infty} dx \frac{e^{-\frac{i\pi}{h}(x-x_l)}}{(x-x_l)(\omega-x^2)} = \frac{-i\pi}{(\sqrt{\omega}-x_l)(\sqrt{\omega}+x_l)}. \tag{5.28}$$

Finally using the expressions for the integrals of Eqs. (5.27) and (5.28) we can compute the value of the energy function as

$$F^n \simeq \sum_{l=-\infty}^{\infty} x_l^{2(n+1)} e^{-x_l^2} \frac{h}{2} \frac{2 + e^{i\frac{\pi}{h}(\sqrt{\omega}-x_l)}(1+x_l/\sqrt{\omega}) - e^{-i\frac{\pi}{h}(\sqrt{\omega}+x_l)}(1-x_l/\sqrt{\omega})}{(\omega-x_l^2)} \tag{5.29}$$

Numerically we find these summations to converge rapidly by keeping 30 terms in the summation. Note that in the numerical implementation when $\omega \simeq \pm x_l$ the denominators in the summations must be handled carefully. In all of the following numerical considerations of the wave-particle resonance the sampling theorem is used as presented here to evaluate the integrals over particle energy.

5.3 Electrostatic Eigenmode Equation

As discussed in Chapter 4 the variational form that describes the stability of low-frequency electromagnetic drift modes is conveniently given by,

$$\mathcal{L}(\boldsymbol{\xi},\phi) = \int \frac{\mathrm{d}s}{B}\left[-\rho_m\omega^2\boldsymbol{\xi}\cdot\boldsymbol{\xi} + \frac{1}{\mu_0}\mathbf{Q}_\perp\cdot\mathbf{Q}_\perp + \frac{1}{\mu_0}Q_LQ_L - 2\boldsymbol{\xi}\cdot\nabla p(\Psi)\boldsymbol{\kappa}\cdot\boldsymbol{\xi}\right]$$
$$-\sum_a \int\frac{ds}{B}\int \mathrm{d}v^3\frac{F_a}{T_a}\left[q_a^2\phi\phi - \frac{\omega-\omega_*}{\omega-\overline{\omega}_D}\overline{\mathcal{K}}\,\overline{\mathcal{K}}\right] \tag{5.30}$$

Uncoupled electrostatic oscillations may be discussed by taking the limit $\phi \gg Q_l,\, \xi^\Psi$, this is related to the dispersion relation discussed in Section 4.6.1, in which one component of the 3by3 dispersion relation was used, namely $a(\omega) = 0$. Thus, the variational form that describes the stability of a flux-tube to large k_y electrostatic perturbations in the $\omega \gg \omega_b$ limit is given by

$$\mathcal{L}(\phi) = \sum_j \int \frac{\mathrm{d}s}{B_{\min}}\int_0^{B_{\min}/B}\frac{\mathrm{d}\lambda}{\sqrt{1-\lambda\frac{B}{B_{\min}}}}\left[\phi^2(s) - H^j(\omega,\lambda)\overline{\phi}^2\right] \tag{5.31}$$

where,

$$H^j(\omega,\lambda) = \frac{2}{\sqrt{\pi}}\int_0^\infty \mathrm{d}\epsilon\exp(-\epsilon)\frac{\omega-\omega_{*ti}(\epsilon)}{\omega-\overline{\omega}_{Dj}(\epsilon,\lambda)} \tag{5.32}$$

represents the dielectric response of particles with a particular pitch angle given by $\lambda = \sin^2(\alpha)$. Note that here we have replaced the velocity integral by an integral over the dimensionless energy $\epsilon = E/T_a$ and the pitch angle λ. Taking the variation of $\mathcal{L}(\phi)$ in Eq. (5.31) we arrive at a bounce-averaged integral eigenvalue equation, which can be written,

$$\phi(s) = \sum_j \widehat{\Gamma}_j^{\mathrm{Es}}\phi(s') \tag{5.33}$$

where $\widehat{\Gamma}_j^{\mathrm{Es}}$ is the bounce-averaging operator

$$\widehat{\Gamma}_j^{\mathrm{Es}} = \frac{B}{B_{\min}} \int_0^L \mathrm{d}s' \int_0^{B_{\min}/B_0} \frac{\mathrm{d}\lambda}{\tau(\lambda)} \frac{H^j(\omega,\lambda)}{u_\parallel(\lambda,s)u_\parallel(\lambda,s')} \tag{5.34}$$

that describes the response of the field to the mirroring particles and acts to the write in Eq. (5.33). To solve Equation (5.33) the field variable $\phi(s)$ is discretized along the flux-tube as well as the space over pitch angles λ as discussed in the previous section. This discretization results in reducing Eq. (5.33) to a matrix eigenvalue problem. In this discrete representation the bounce-averaging operator of Eq. (5.34) is a matrix operator acting on the electrostatic oscillations,

$$M_{i,j}(\omega)\phi_j = \phi_j \tag{5.35}$$

where the operator depends on the frequency ω. An iteration scheme must be used to numerically solve this problem. First, an initial frequency is chosen $\omega^{(0)}$, and the eigenvalues and eigenvectors of $M_{i,j}(\omega)$ are computed, $\Lambda(\omega^{(0)})$ and $\phi^{(0)}$. Then the eigenvectors at this order are used to form a dispersion relation,

$$\phi_j^{(0)\dagger} M_{i,j}(\omega)\phi_j^{(0)} - \phi_j^{(0)\dagger}\phi_j^{(0)} = 0 \tag{5.36}$$

where we allow ω to take on any value but fix the electrostatic perturbation mode structure to be the eigenvectors of the zeroth order matrix operator. The root of this dispersion relation may then be found using standard numerical procedures such as Muller's method which works well for complex analytic functions. The root of this dispersion relation $\omega^{(1)}$, Eq. (5.36), is then used to compute the eigenvectors of the second order matrix operator $M_{i,j}(\omega^1)$. This

iteration procedure terminates when the frequency $\omega^{(n)}$ is a solution to the dispersion relation at order n.

5.4 Mode frequencies above the guiding center drift frequency

The high-frequency approximation is $\omega \gg \overline{\omega}_D$, which yields $H^j(\omega, \lambda) = 1 - \omega_{*j}/\omega$, so that the high-frequency eigenmode equation becomes

$$\phi(s) = \sum_j \left(1 - \frac{\omega_{*j}}{\omega}\right) \widehat{\Gamma}^{\mathrm{HFEs}} \phi(s') \tag{5.37}$$

where $\widehat{\Gamma}^{\mathrm{HFEs}}$ is the operator

$$\widehat{\Gamma}^{\mathrm{HFEs}} = \frac{B}{B_{\min}} \int_0^L \mathrm{d}s' \int_0^{B_{\min}/B_0} \frac{\mathrm{d}\lambda}{\tau(\lambda)} \frac{1}{u_\parallel(\lambda, s) u_\parallel(\lambda, s')} \tag{5.38}$$

Note that we can reduce the eigenmode equation to a simple dispersion relation by introducing the eigenvalues of the integral operator $\widehat{\Gamma}^{\mathrm{HFEs}}$ given by the variable Γ^{HFEs}.

$$\omega = \frac{\Gamma^{\mathrm{HFEs}}(\omega_{*i} + \omega_{*e})}{2\Gamma^{\mathrm{HFEs}} - 1} \tag{5.39}$$

The integral operator given in Eq. (5.38) is not only interesting physically, but is also convenient in verifying the numerical procedure because the highest eigenmode is easily found analytically. Consider $\phi(s') = 1$, then swapping the order of integration in the integral operator one finds,

$$\widehat{\Gamma}^{\mathrm{HFEs}} \phi(s') = \frac{B}{B_{\min}} \int_0^1 \frac{\mathrm{d}\lambda}{\tau(\lambda)} \frac{1}{u_\parallel(\lambda, s)} \int_0^{s_{\mathrm{tp}}} \frac{1}{u_\parallel(\lambda, s')}, \tag{5.40}$$

and then one notices that the integral over s' is simply the definition of $\tau(\lambda)$ so that,

$$\begin{aligned} \widehat{\Gamma}^{\text{HFEs}}\phi(s') &= \frac{B}{B_{\min}}\int_0^1 \frac{\mathrm{d}\lambda}{u)\|(\lambda,s)} \\ &= 2 \end{aligned} \tag{5.41}$$

Thus an eigenvalue of the operator $\widehat{\Gamma}^{\text{HFEs}}$ is 2 and the eigenvector is 1. With this result we see that the solution to the high-frequency dispersion relation is a purely oscillating solution with $\omega = \frac{2}{3}(\omega_{*i} + \omega_{*e})$. There are a few things to point out here. Recall that the field variable $\phi(s)$ was scaled with $\sqrt{B_0/B(s)}$ so that physically the eigenmode structure is still expected to be ballooning and not flute-like, with the exact form of $\phi(s) = \sqrt{B_0}B(s)$. Another crucial feature is that in performing the final integral in Eq. (5.41) it was assumed that all particles were trapped or equivalently that the mirror ratio $B_{\min}/B_{\max} = 0$. In the Earth's magnetosphere the mirror ratio is very small but not quite zero. Figure 5.6 shows some sample eigenfunctions computed from the discrete representation of $\widehat{\Gamma}^{\text{HFEs}}$ for different flux-tubes in the magnetotail. One sees from this figure that for flux-tubes deep in the tail the mirror ratio is very small so that the error in the computation is not from the untrapped particles but in fact is due to the steepness of the well and the finite number of points used in the discretization. For flux-tubes closer to the Earth the difference between the computed solution and the analytic solution is due to the untrapped particles. In this computation $\Delta s = 0.005R_E$ for the sub-grid scale, yielding on average 2000 points for integration and about 250 for the large grid scale. The eigenvalue was seen to be about five percent of the analytic solution of $\Lambda = 2$.

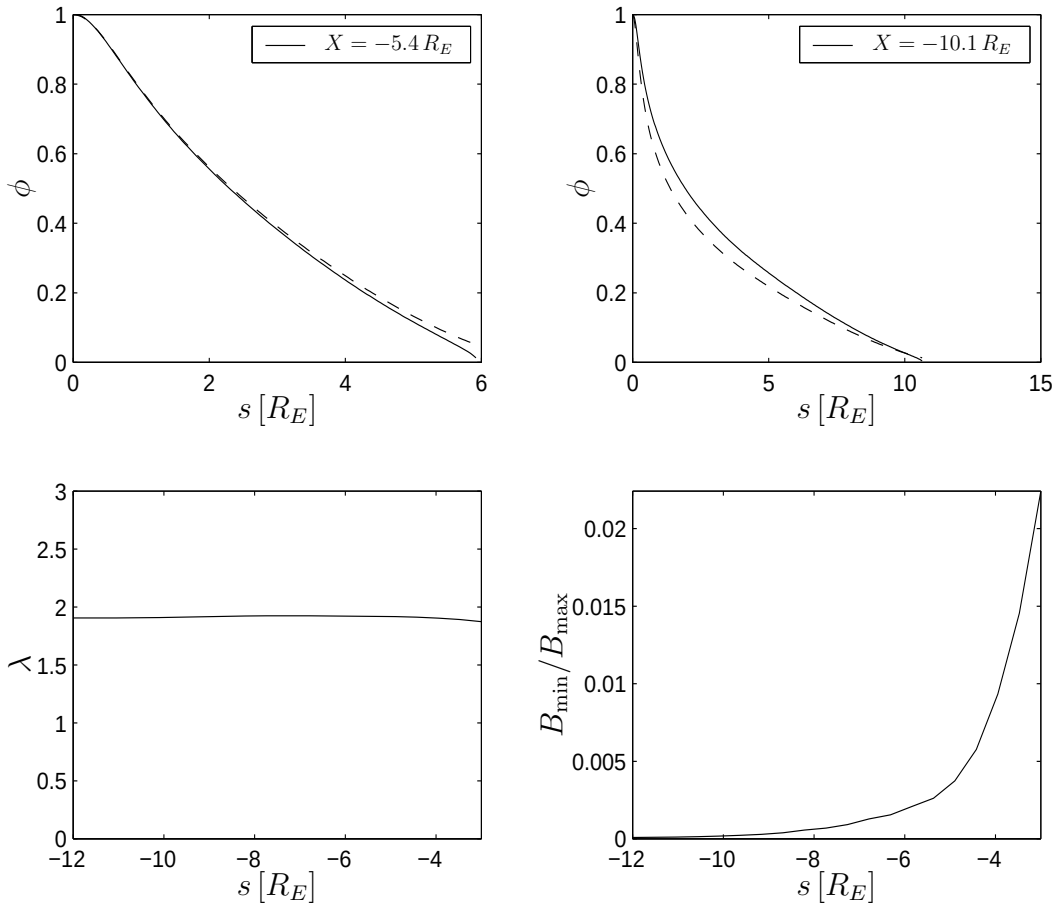

Figure 5.6: Eigenvalues and Eigenvectors of the high frequency electrostatic operator $\widehat{\Gamma}^{\mathrm{HFEs}}$ for different flux-tubes along the magnetotail

5.5 Mode frequencies below the guiding center drift frequency

The low-frequency approximation is $\omega \ll \overline{\omega}_D$, which yields $H^j(\omega,\lambda) = (\omega_{*j}/\widehat{\omega}_{Dj})(\eta_j - 1 - 2\omega/\omega_{*j})$, so that the low-frequency eigenmode equation becomes

$$\phi(s) = \sum_j (\eta_j - 1 - 2\omega/\omega_{*j})\widehat{\Gamma}^{\mathrm{LFEs}}\phi(s') \tag{5.42}$$

where $\widehat{\Gamma}^{\mathrm{LFEs}}$ is the operator given by

$$\widehat{\Gamma}^{\mathrm{LFEs}} = \frac{B}{B_{\min}} \int_0^L \mathrm{d}s' \int_0^{B_{\min}/B_0} \frac{\mathrm{d}\lambda}{\tau(\lambda)} \frac{1}{u_\parallel(\lambda,s)u_\parallel(\lambda,s')} \frac{\omega_*}{\widehat{\omega}_D}. \tag{5.43}$$

This eigenmode equation also reduces to a simple dispersion relation by introducing the eigenvalues of the integral operator $\widehat{\Gamma}^{\mathrm{LFEs}}$ given by the variable Γ^{LFEs}. The dispersion relation in the low-frequency approximation is given by

$$\omega = \frac{\omega_{*i}\omega_{*e}}{2}\left(\frac{\eta_i + \eta_e - 2 - \frac{1}{\Gamma^{LFEs}}}{\omega_{*i} + \omega_{*e}}\right). \tag{5.44}$$

Figure 5.7 shows the eigenvalues of the low-frequency electrostatic operator given in Eq. (5.43) for different flux-tubes in the magnetotail computed using the Tsyganenko model. We find that for flux-tubes far from the Earth the eigenvalues become very large and thus the term proportional to inverse of the eigenvalue in Eq. (5.44) becomes very small. For these flux-tubes deep in the magnetotail there exist a few particles with small pitch angles that exhibit drift reversal ($\omega_*/\omega_D < 0$). Consequently the eigenfunctions along these flux tubes develop a sharp structure approximately 1 R_E away from the equatorial plane (as shown in the second panel of Figure 5.7). For flux tubes closer to the

Earth the eigenvalues become smaller and thus the contribution to Eq. (5.44) becomes more important. The eigenfunctions also become more flute-like as they were in the high-frequency electrostatic case.

5.6 Nyquist analysis of the variational form dispersion relation

To analytically perform the Nyquist analysis on the variational form given in Eq. (5.33), we ignore the inertial term, considering , take the perturbing field to be flute-like $\phi(s) = \text{const.}$, and ignore the pitch angle dependence of the bounce averaged guiding center drift. Taking the temperature of the electrons and ions to be equal ($T_i = T_e$), the local dispersion relation for electrostatic modes is given by

$$C(\omega) = 2 - \frac{2}{\sqrt{\pi}} \int_0^\infty \mathrm{d}\epsilon \exp(-\epsilon)\epsilon^{1/2} \frac{\omega - \omega_{*i}(1 - \frac{3}{2}\eta + \eta\epsilon)}{\omega - \epsilon\omega_D} \tag{5.45}$$

One can rearrange this equation to make explicit the points at which $C(\omega)$ goes to zero.

$$C(\omega) = 2 - \frac{\omega_*\eta}{\omega_D} - \left(1 - \frac{\omega_*\eta}{\omega_D}\right)\left(\frac{\omega - \omega_I}{\omega_D}\right) \frac{2}{\sqrt{\pi}} \int_0^\infty \mathrm{d}\epsilon \exp(-\epsilon)\epsilon^{1/2} \frac{1}{\frac{\omega}{\omega_D} - \epsilon} \tag{5.46}$$

We can now evaluate the imaginary part of the integral and find,

$$\mathrm{Im}(C(\omega)) = -2\sqrt{\pi}\left(1 - \frac{\omega_*\eta}{\omega_D}\right)\left(\frac{\omega - \omega_I}{\omega_D}\right) \mathrm{sign}(\omega_D) \left(\frac{\omega}{\omega_D}\right)^{1/2} \exp(-\omega/\omega_D)\theta\left(\frac{\omega}{\omega_D}\right) \tag{5.47}$$

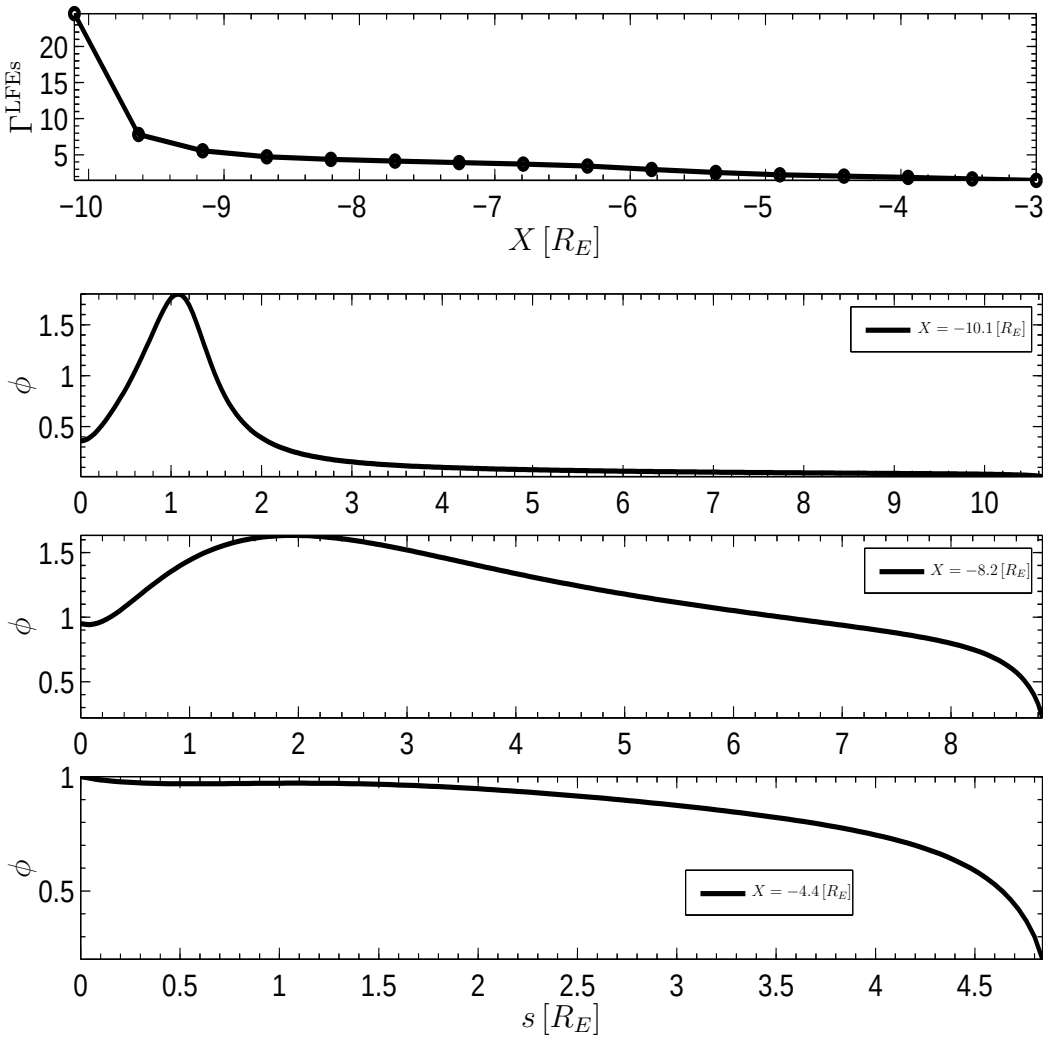

Figure 5.7: Eigenvalues and Eigenvectors of the low frequency electrostatic operator $\widehat{\Gamma}^{\mathrm{HFEs}}$ for different flux-tubes along the magnetotail.

From this equation it is clear that the imaginary part of $C(\omega)$ goes to zero at $\omega = \pm\infty, 0, \omega_I$, where,

$$\omega_I = \frac{\omega_* \left(1 - \frac{3}{2}\eta\right)}{1 - \frac{\omega_* \eta}{\omega_D}} \tag{5.48}$$

We can now evaluate the real part of $C(\omega)$ at the frequencies for which the imaginary part is zero and we find,

$$C(\pm\infty) = 1 \tag{5.49}$$

$$C(\omega = 0) = 2 - \frac{\omega_* \eta}{\omega_D} \tag{5.50}$$

$$C(\omega = \omega_I) = 2 - \frac{\omega_*}{\omega_D}\left(\frac{\eta}{4} + \frac{1}{2}\right) \tag{5.51}$$

We can now see that the two important stability parameters are η and ω_*/ω_D. For the electrostatic mode to be unstable we see that $C(\omega = 0)$ and $C(\omega = \omega_I)$ must have opposite signs and the imaginary part of $C(\omega)$ between these frequencies must not be zero. These conditions can be determined for each point in the parameter space of η and ω_*/ω_D. Figure 5.8 shows just such a computation over a wide region of parameter space. In this figure the dark regions represent parameters that yield unstable electrostatic oscillations and the empty regions represent stable or marginally stable conditions. We find that there are many regions of parameter space that are unstable to electrostatic trapped particle modes. In the drift reversed case, *i.e.* when $\omega_*/\omega_D < 0$, the absolute magnitude of η can not be too small for instability. It is interesting to note that even for $\eta = 0$, if $\omega_*/\omega D$ is large enough, an instability exists which is driven by wave-particle resonance.

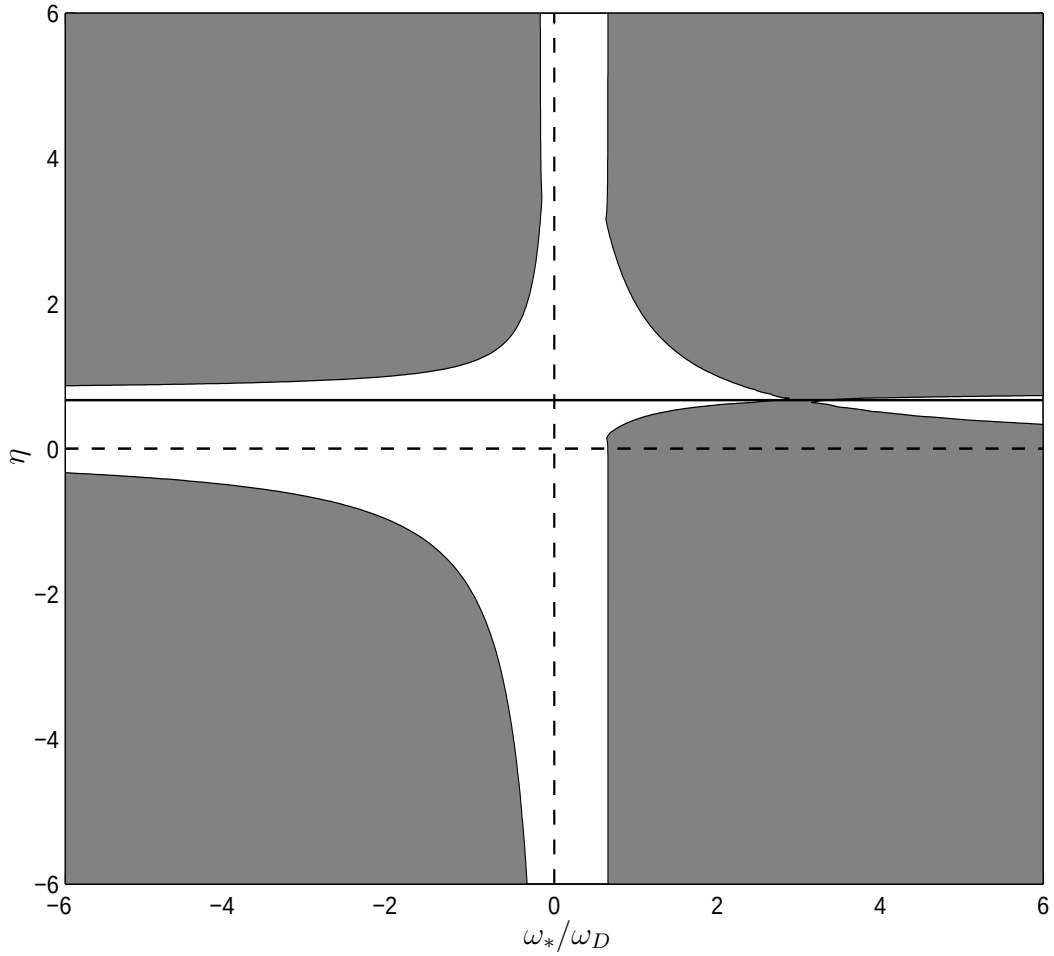

Figure 5.8: Stability diagram for electrostatic trapped particle modes. The shaded region represents parameters that are unstable to electrostatic trapped particle modes.

5.7 Conclusions

In this section we have introduced some of the details for a new method for solving bounce-averaged drift kinetic equations. The methods were applied to computing the bounce-averaged gradient and curvature drifts in the night-side region of the magnetosphere. Flux tubes further from the Earth with higher plasma pressure were found to have gradient drifts in the opposite direction to the curvature drift. However, the averaged drift (over pitch angles) was still always in the westward direction, and thus no drift-reversed configurations were found. There were however, certain pitch-angles, for which the total gradient and curvature drift velocity was eastward.

These bounce-averaging methods were then applied to the well known problem of high-frequency electrostatic modes. For these modes analytical solutions for the eigenvalues and eigenmode structure are known. The numerical results compared favorably to the analytical solutions.

The bounce-averaging methods were then applied to low-frequency electrostatic modes. It was found that drift-reversal, even for just a small range of pitch-angles, had a strong effect on the structure of the eigenmode. However, no unstable modes exist in this approximation.

Finally, a local approximation was made and a Nyquist stability analysis was performed on the resulting dispersion relation. Two regions of parameter space were identified for which instability may occur. The full non-local computation of the resonant eigenmodes was deferred to a later study.

Chapter 6

Bounce-Averaged Compressional Modes

As discussed in Chapter 2 there are observations of low-frequency compressional pulsations near geosynchronous orbit during substorms that are often related to bursty Earthward flows. For example, Kepko and Kivelson [101, 102] looked at correlations of Pi2 waves and variable Earthward flows. They found that the wave forms were correlated and defined a class of Pi2 waves that are directly driven by variable Earthward flow. Sigsbee *et al.* (2002) [169] showed that low-frequency magnetic fluctuations in the Pi2 frequency band (2-25 mHz) [5] preceded substorm onset and were associated with increased Earthward $\mathbf{E} \times \mathbf{B}$ flows greater than 100 km/s. They reported that the Pi2 pulsations are observed before the initiation of strong Earthward flow, but also that the largest flows were observed after substorm onset, finding a large class of Pi2 oscillations that were not directly driven. In this chapter we investigate the stability of purely magnetic compressional oscillations using the standard magnetic field models.

To evaluate the frequency of such modes, the long orbits of the mirroring ions in a flux tube must be considered. The MHD model is not generally valid for low frequencies $\omega < |\omega_{*pi}|, \omega_{bi}$, where ω_{p*i} is the diamagnetic

drift frequency formed by a pressure gradient and $\omega_{bi} = v_{ti}/L_{\parallel}^{\text{eff}} \approx 20\,\text{mHz}$ is the frequency of the ion bounce motion between the Southern and Northern ionosphere, with $L_{\parallel}$ being the approximate length of the field line. Thus a bounce-averaged eigenmode equation must be solved [94]. The stability analysis is local to the flux tube, and we investigate which flux tubes tend to be the first to go unstable. In our earlier analysis using the Fast-MHD energy principle principle of Chapter 3 and the local gyrokinetic dispersion relation of Chapter 4, the answer was found that the transitional region $\beta \sim 1$ to 10 was first to go unstable with respect to kinetic interchange modes. We now investigate which flux tubes are the first to go unstable with respect to drift-kinetic compressional waves.

Another related candidate for these observed magnetic oscillations is the drift mirror mode [37, 79] in which an instability due to the temperature anisotropy ($T_{\perp} > T_{\parallel}$) drives the unstable mode. The classical mirror mode instability has serious problems with self-consistency, as explained by Hasegawa (1969) [79] due to its derivation from double adiabatic MHD, which neglects the parallel heat flux; nevertheless this is an important mode. Here in this work we do not focus on the temperature anisotropy to drive the instability, but rather include the resonant effects that the waves have on the particles to drive a high-β mode that is analogous to the typical electrostatic drift-waves.

Rosenbluth (1981) [155] pointed out that for compressional modes, the role of magnetic drift reversal of the guiding center flux is important for high-β plasma stability. Drift reversal can occur when the ∇B drift is large and

opposite to the curvature drift, which occurs for high-β equilibria as discussed in Chapter 5. A Nyquist analysis will show that the dimensionless stability parameter is

$$R(\beta) = \int_0^{E/B_{\min}} \mathrm{d}\mu \frac{B_{\min}}{E} \frac{\omega_{*i}}{\overline{\omega}_D(\mu,\beta)} \simeq \frac{R_c}{L_{Ti}} \log(\frac{\overline{\omega}_{D\max}}{\overline{\omega}_{D\min}})$$

where ω_{*i} is the pitch angle-independent diamagnetic drift frequency from the density gradient, and $\overline{\omega}_{Di}(\mu,\beta)$ is the bounce-averaged magnetic guiding center drift frequency. The relevant dimensionless factor $R(\beta)$ as a function of β is an important quantity in determining stability. For the Tsyganenko (1996) [188] magnetic field model we report the dimensionless value of $R(\beta)$ as a function of both $X[R_E]$, between the NGO region and the NENL region, and $\beta_{\min} = 2\mu_0 p/B_{\min}^2$ the ratio of plasma kinetic energy density to magnetic field energy density, where $B_{\min}$ is the magnitude of the magnetic field at the equatorial plane, which is the minimum value of B for that flux-tube.

In Section 6.1 a simple fluid picture of magnetic drift compressional modes is developed in order to develop an intuition about the instability mechanism. In Sections 6.2 through 6.4 the variational form used to describe stability is presented, and its solution is discussed in two limits: (i) the limit that the frequency of the compressional wave is higher than the bounce-averaged drift frequency, $\omega \gg \overline{\omega}_D$ and (ii) the limit that the frequency of the wave is lower than the bounce-averaged drift frequency, $\omega \ll \overline{\omega}_D$. In Section 6.5 the $\omega = \overline{\omega}_D$ resonance is then introduced and estimates are made of the growth rate. These estimates are then compared to results of the eigenmode calculation in Section 6.6. In Section 6.7 a one-dimensional transport equation for

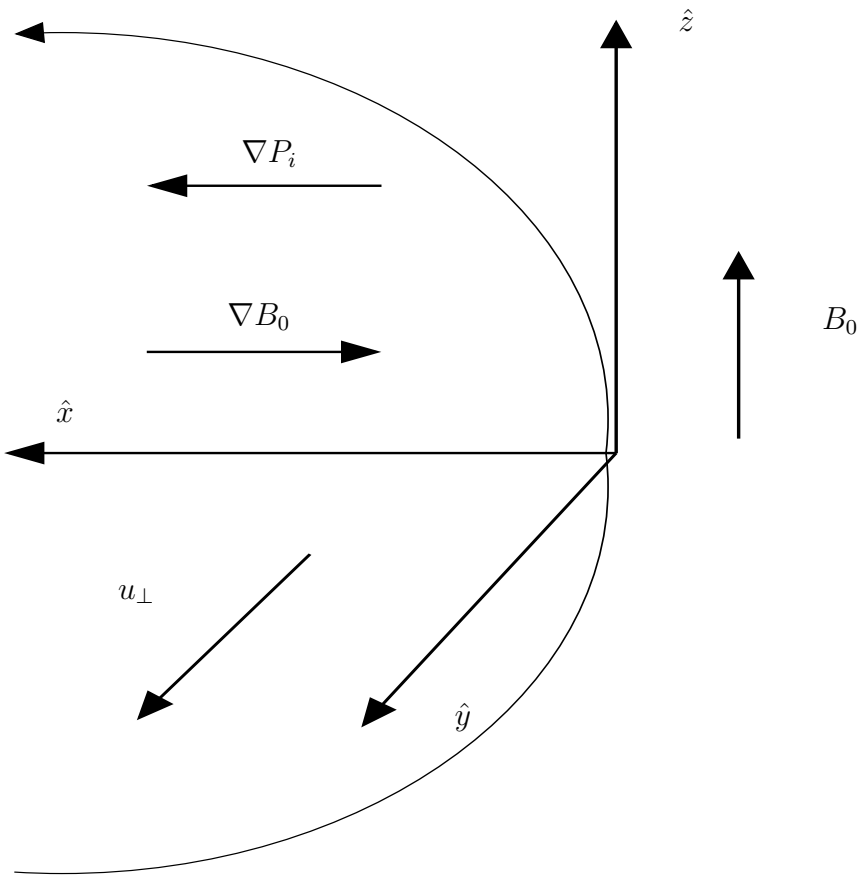

Figure 6.1: Geometry involved in deriving the fluid picture of compressional drift waves

the particle pressure is given. Solutions are shown for which large pressure gradients are observed in the NGO region due to flow braking, and the impact of these steep gradients on the stability of NGO flux tubes is discussed. In Section 6.8 the conclusions and summary are given.

6.1 Fluid Picture

In order to derive a simple fluid picture of an instability involving only the perturbed parallel magnetic field, $\delta B_{\|}$, consider an equilibrium situation like that shown in Figure 6.1. In this picture, the equilibrium magnetic field is in the $\hat{\mathbf{z}}$ direction, its gradient is in the negative $\hat{\mathbf{x}}$ direction, and for the sake of clarity we will ignore the curvature of the magnetic field lines. Because the curvature is very important more about this will be said later. In this simple equilibrium situation we have:

$$\begin{aligned} \mathbf{B}_0 &= B_0(x)\hat{\mathbf{z}} \\ \nabla B_0 &= -\left|\frac{\mathrm{d}B_0}{\mathrm{d}x}\right|\hat{\mathbf{x}}. \end{aligned}$$

The pressure, primarily due to the ions, is increasing towards the Earth such that the pressure gradient is in the positive $\hat{\mathbf{x}}$ direction

$$\nabla P_i = \frac{\mathrm{d}P_i}{\mathrm{d}x}\hat{\mathbf{x}}.$$

The perturbations of the parallel magnetic field can be written in terms of a vector potential; thus, one sees that there must be an oscillating component of the inductive electric field

$$\delta B_{\|} = \hat{z}\cdot\nabla\times\delta\mathbf{A} \qquad \delta\mathbf{E} = -\frac{\partial\delta\mathbf{A}}{\partial t}. \tag{6.1}$$

For low frequencies the fluid velocity, $\mathbf{u}$, is a combination of the $\mathbf{E}\times\mathbf{B}$ velocity and the Hall term which is a diamagnetic fluid drift:

$$\mathbf{u}_{\perp} = \frac{\mathbf{E}\times\mathbf{B}}{B^2} + \frac{\mathbf{B}\times\nabla P_i}{neB^2}. \tag{6.2}$$

Notice that for a small perturbation the reciprocal of the magnitude of the magnetic field may be expanded:

$$\frac{1}{B} = \frac{1}{B_0 + \delta B_\parallel} \simeq \frac{1}{B_0}\left[1 - \frac{\delta B_\parallel}{B_0}\right] + O(\delta B_\parallel^2), \tag{6.3}$$

so that the fluid velocity can be written explicitly as

$$\mathbf{u}_\perp = \frac{\delta \mathbf{E} \times \hat{\mathbf{z}}}{B_0} + \frac{1}{neB_0(x)}\frac{\mathrm{d}P_0}{\mathrm{d}x}\left[1 - \frac{\delta B_\parallel}{B_0}\right]\hat{\mathbf{y}} + (ik_x\hat{\mathbf{y}} - ik_y\hat{\mathbf{x}})\frac{\delta P}{neB_0(x)}. \tag{6.4}$$

Computing the divergence of the fluid velocity we can compute the plasma compression to first order:

$$\begin{aligned} \nabla \cdot \mathbf{u}_\perp &= \frac{-ik_y\delta E_x}{B} - \frac{ik_y}{enB}\frac{\mathrm{d}p_i}{\mathrm{d}x}\frac{\delta B_\parallel}{B} + \frac{ik_y\delta P}{neB^2}\frac{\mathrm{d}B_0}{\mathrm{d}x} - \frac{ik_y\delta P}{neB^2}\left|\frac{\mathrm{d}B_0}{\mathrm{d}x}\right| \\ &= i(\omega - \omega_{*pi})\frac{\delta B_\parallel}{B} - \frac{ik_y\delta P}{neB^2}\left|\frac{\mathrm{d}B_0}{\mathrm{d}x}\right|. \end{aligned} \tag{6.5}$$

Notice that here we have dropped a term $-1/B_0^2\left|\mathrm{d}B_0/\mathrm{d}x\right|\left(\partial A_y/\partial t\right)$. Using the MHD adiabatic equation of state to relate the change in plasma pressure to the compression we can write

$$i\omega\delta P_i = -P\Gamma\nabla\cdot\mathbf{u}_\perp = i(\omega - \omega_{*pi})\frac{\delta B_\parallel}{B} + i\omega_{\nabla B}\delta P \tag{6.6}$$

where we have introduced the definition of the ∇B drift frequency

$$\omega_{\nabla B} = \frac{k_y P_0 \Gamma}{neB_0^2}\frac{\mathrm{d}B_0}{\mathrm{d}x}. \tag{6.7}$$

Solving for the pressure perturbation this can be written as

$$\delta P = -P_0\Gamma\frac{(\omega - \omega_{*pi})}{(\omega - \omega_{\nabla B})}\frac{\delta B_\parallel}{B_0}. \tag{6.8}$$

Then using the equation of motion in the $\hat{\mathbf{y}}$ direction:

$$\rho\omega^2\xi_y = \frac{ik_y}{\mu_0}\delta B_\parallel B_0 - ik_y\delta P \tag{6.9}$$

and Faraday's Law with the frozen-in condition:

$$\xi_y = \frac{i}{k_y}\frac{\delta B_\parallel}{B_0} \tag{6.10}$$

a low-frequency drift-compressional dispersion relation can be written

$$\frac{\omega^2}{k_y^2 V_A^2} = 1 + \Gamma\frac{\beta}{2}\left(\frac{\omega - \omega_{*pi}}{\omega - \omega_{\nabla B}}\right). \tag{6.11}$$

The first thing we notice from this dispersion relation is that it can be unstable for $\omega < \omega_{*pi}, \omega_{\nabla B}$ when β is large and we have drift reversal ($\omega_{*pi}/\omega_{\nabla B} < 0$). Notice, that if we had accounted for the curvature of the magnetic field line the $\omega_{\nabla B}$ drift frequency would be replaced by the total magnetic drift frequency. This is important, because $\omega_{\nabla B}$ is proportional to the plasma β. Thus in the limit $\omega \ll |\omega_{*pi}|, |\omega_{\nabla B}|$ the dispersion relation in Eq. (6.11) becomes

$$\frac{\omega^2}{k_y^2 V_A^2} = 1 + \Gamma\frac{\beta}{2}\left(\frac{\omega_{*pi}}{\omega_{\nabla B}}\right), \tag{6.12}$$

where we see that with $\omega_{\nabla B}$ proportional to β the dispersion relation becomes independent of β.

Next, using the tools developed in Chapter 5, we consider these same compressional $\delta B_\parallel$ modes using a bounce-averaged drift-kinetic variational form (and retaining the important curvature terms in the magnetic drift velocity). We find a dispersion relation similar to the simple fluid dispersion

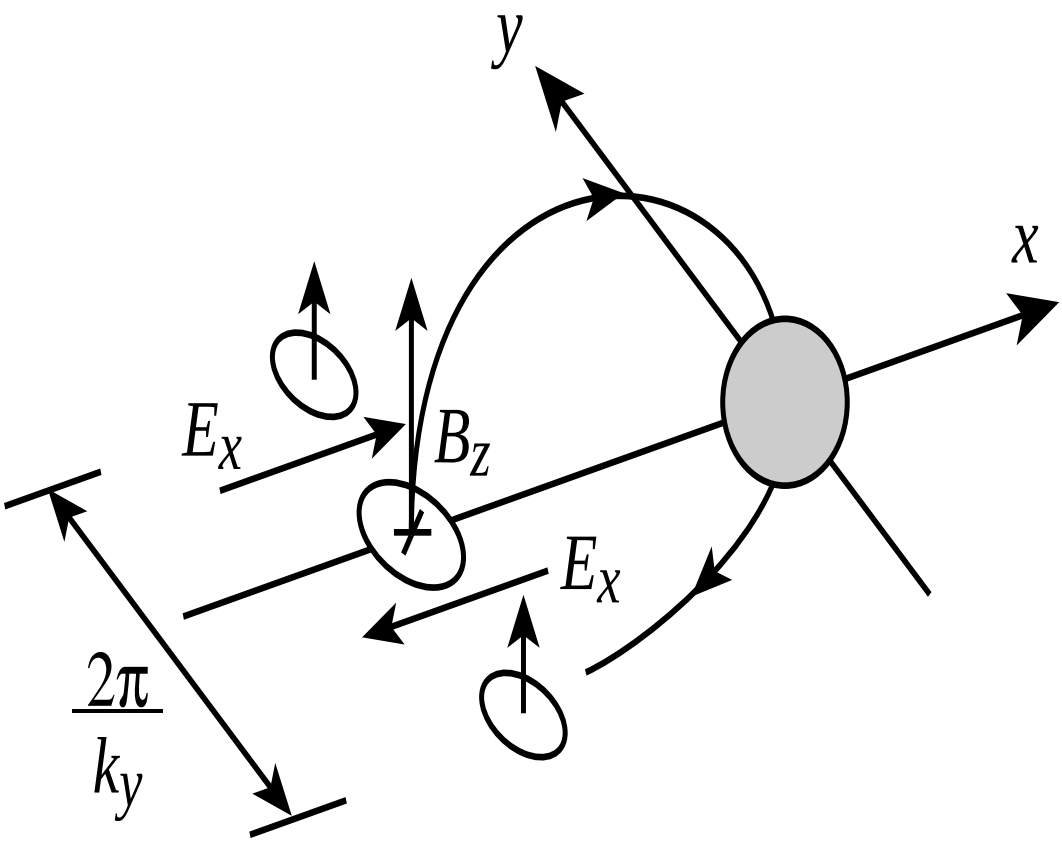

Figure 6.2: Fluid picture of compressional drift waves.

relation in Eq. (6.11). One difference is that the adiabatic gas constant in MHD, Γ, is replaced in the kinetic treatment with a bounce-averaging operator. Also, the fraction $(\omega - \omega_{*pi})/(\omega - \overline{\omega}_{Di})$ is integrated over the equilibrium phase space distribution function.

6.2 Reduction to Compressional Variational Form

In this chapter we we consider modes dominated by $\delta B_\parallel$, which implies $Q_L \simeq \delta B_\parallel \simeq -B\nabla\cdot\boldsymbol{\xi}_\perp$ [155], from the converging/diverging cross field flows that compress and expand the magnetic field. The kinetic energy from the flows is $T = \frac{1}{2}\int \rho_m u_\perp^2 \mathrm{d}^3x = \frac{1}{2}\omega^2 \int \rho_m \xi_y \xi_y \,\mathrm{d}\Psi dy ds/B$. From Faraday's law for the frozen-in flux equation $\delta\mathbf{B} = \nabla\times(\boldsymbol{\xi}\times\mathbf{B})$, we get $\delta B_\parallel = -iBk_y\xi_y$ for the most unstable displacements with $k_y \gg k_x$. To maintain $\nabla\cdot\mathbf{B} = 0$, especially for the modes that we find which are so strongly localized in the equatorial plane, there must be a small $\delta\mathbf{B}_\perp$ perturbation. Noting that $\partial\delta B_\parallel/\partial s \sim \partial\delta B_z/\partial z \sim -ik_y\delta B_y$, we find that in the large k_y limit only a small perpendicular perturbation, δB_y is necessary to satisfy $\nabla\cdot\mathbf{B} = 0$.

For these modes the perturbed particle energy is $K = \mu\delta B_\parallel$, and the Lagrangian component of the magnetic field is $Q_L = \delta B_\parallel$, and as mentioned before the plasma displacement in the y direction can be written as $\xi_y = ik_y^{-1}\delta B_\parallel/B$. Neglecting all other terms with ϕ or ξ^ψ, the variational form of Eq. (4.70) reduces to

$$\begin{aligned}\mathfrak{L} \;=\; & \int \frac{\mathrm{d}s}{B}\Big[-\frac{1}{2}\left(\frac{\omega}{k_y}\right)^2\frac{\rho_m}{B^2}\delta B_\parallel^2 + \frac{\delta B_\parallel^2}{2\mu_0} + \sum_j \frac{\beta_{\min}}{2\mu_0}\frac{B(s)}{B_{\min}}\sqrt{\frac{2}{\pi}} \\ & \times \int_0^\infty \mathrm{d}\epsilon\, \epsilon^{5/2}e^{-\epsilon}\int_0^1 \frac{\mathrm{d}\lambda\,\lambda^2}{u_\parallel(\lambda,s)}\frac{\omega-\omega_{*j}(\epsilon)}{\omega-\overline{\omega}_{Dj}(\lambda,\epsilon)}\left(\overline{\delta B_\parallel}\right)^2\Big] \qquad (6.13)\end{aligned}$$

for compressional drift modes. Here we have replaced the velocity integral by an integral over the dimensionless energy $\epsilon = E/T_i$ and the pitch angle variable $\lambda = \sin^2(\alpha)$.

For modes with odd symmetry $\delta B_\parallel(-s) = -\delta B_\parallel(s)$, the bounce integral vanishes and the waves are given by $\omega^2 = k_y^2 B^2/\rho_m\mu_0 \sim k_y^2 v_i^2/\beta_i$. In the absence of density and temperature gradients, Chen and Hasegawa (1991) [37] used the principal value of the integral $\int \mathrm{d}\lambda \overline{\delta B_\parallel}^2$ and the limit $|\gamma/\omega| < 1$ to show that the bounce-averaged terms in Eq. (6.13) are all stabilizing, and thus modes with odd symmetry are the most unstable. They relied on pressure anisotropy to drive a drift mirror instability. Here, we do not consider the pressure anisotropy but rely on the wave-particle resonance to drive an instability. In this case modes with odd symmetry are all stable oscillations, making the modes with even symmetry the most unstable.

Taking the variation of $\mathcal{L}$ in Eq. (6.13) we arrive at an integral eigenvalue equation, which can be written as

$$\frac{\omega^2}{k_y^2}\frac{\mu_0\rho_m}{B^2}\delta B_\parallel(s) = \delta B_\parallel(s) + \sum_j \beta_{\min}^j \,\widehat{\Gamma}_j\, \delta B_\parallel(s'), \tag{6.14}$$

where the operator on the right-hand side,

$$\widehat{\Gamma}_j = \frac{B(s)}{B_{\min}} \int_0^L \mathrm{d}s' \int_0^{B_{\min}/B} \frac{\mathrm{d}\lambda}{\tau(\lambda)} \frac{\lambda^2 G^j(\omega,\lambda)}{u_\parallel(\lambda,s)u_\parallel(\lambda,s')}, \tag{6.15}$$

is the bounce-averaging operator that describes the response of the plasma pressure of the mirroring particles to the parallel magnetic field perturbation $\delta B_\parallel$. The frequency response of the pressure fluctuation is governed by

$$G^j(\omega,\lambda) = \frac{2}{\sqrt{\pi}} \int_0^\infty \mathrm{d}\epsilon\, \epsilon^{5/2}\, e^{-\epsilon} \frac{\omega - \omega_{*j}(\epsilon)}{\omega - \overline{\omega}_{Dj}(\lambda,\epsilon)}. \tag{6.16}$$

Equation (6.16) is the response of the particle species j with a particular pitch angle given by λ. To solve the integral Eq. (6.14), the field variables are discretized along a particular flux tube, using the methods presented in Chapter 5, which creates a matrix eigenvalue problem. In this discrete representation the bounce-averaging operation is a matrix multiplication on the discretized magnetic fluctuations,

$$M_{i,j}(\omega)\delta B_{\parallel j} = \Lambda(\omega)\,\delta B_{\parallel j}, \tag{6.17}$$

where both the matrix $M_{i,j}(\omega)$ and the eigenvalue $\Lambda(\omega)$ are dependent on the frequency ω. The matrix operator is dependent on the frequency through the magnetic response accounted for in $G^j(\omega, \lambda)$. Thus the eigenvalue problem to be solved is a nonlinear transcendental function of the eigenfrequency ω that requires an iterative procedure to find the complex ω. An initial frequency $\omega^{(0)}$ is assumed, and the eigenvalues and eigenvectors of $M_{i,j}(\omega^{(0)})$ are computed, $\Lambda^{(0)}$ and $\delta B_{\parallel}^{(0)}$. Then the eigenvectors at this order are used to form a dispersion relation

$$\delta B_{\parallel}^{(0)\dagger} M(\omega)\delta B_{\parallel}^{(0)} - \delta B_{\parallel}^{(0)\dagger}\frac{\omega^2}{k_y^2 V_A^2}\delta B_{\parallel}^{(0)} = 0, \tag{6.18}$$

from which the next-order frequency $\omega^{(1)}$ can be found from the root of the dispersion relation. Next, we can again find the eigenvectors and eigenvalues of $M_{i,j}(\omega^{(1)})$, namely, $\Lambda^{(1)}$ and $\delta B_{\parallel}^{(1)}$, and form a new dispersion relation. This iteration procedure terminates when the frequency $\omega^{(n)}$ is a solution to the dispersion relation to the desired accuracy.

The parameter vector used to specify the problem is given by $P^{\rm L} = (k_y\rho_i, \eta_i, \eta_e, T_e/T_i, L_n/R_c, R_c/L_B, \beta_{\rm min})$, plus the parameters needed to specify the magnetic field model from which we compute such quantities as R_c/L_B, $\beta_{\rm min}$, and the details of the flux-tube. Here $\eta_{i,e} = L_n/L_{Ti,Te}$ is the ratio of the density gradient scale length to the temperature gradient scale length for each species. For the Tsyganenko (1996) model the parameters are $P^{\rm T96} = (P_{\rm dyn}, DST, B_y^{\rm IMF}, B_z^{\rm IMF})$, and for the constant current model the parameters are $P^{\rm CCM} = (B_0 r_0^2, B_x', B_n)$. The final parameters that need to be specified are the (x, y) coordinates (in units of R_E) in the equatorial plane for the flux tube.

In terms of the normalized drift wave units $\omega \rightarrow \omega\,[c_s/L_n]$, and $k_y \rightarrow k_y\left[\rho_i^{-1}\right]$, the left-hand side of Eq. (6.14) is small compared to $\delta B_\parallel$, namely,

$$\frac{\omega_{*i}^2}{k_y^2 V_A^2} = \frac{c_s^2}{L_n^2}\frac{\rho_i^2}{V_A^2} = \left(\frac{\rho_i}{L_n}\right)^2 \frac{\beta_i}{2} \ll 1,$$

and thus it does not appear in the 3×3 drift kinetic matrix formulation of low-frequency drift stability theory given in Chapter 4 [91].

6.3 Mode frequencies above the guiding center drift frequency

The high-frequency approximation is $\omega \gg \overline{\omega}_D$, which yields $G^j(\omega, \lambda) = (15/4)(1 - \omega_{*j}(1 + 2\eta_j)/\omega)$. In this limit only purely oscillating modes exist, related to the familiar magneto-acoustic mode with the dispersion relation

$$\frac{\omega^2}{k_y^2 V_A^2} = 1 + \frac{15}{4}\sum_j \beta_{\rm min}^j (1 - \frac{\omega_{*j}}{\omega}(1 + 2\eta_j))\Gamma^{\rm HF}, \tag{6.19}$$

where $V_A = B/\sqrt{\mu_0 \rho_m}$ and $\Gamma^{\rm HF}$ is given by the eigenvalues of the integral operator

$$\widehat{\Gamma}^{\rm HF} = \frac{1}{2}\frac{B(s)}{B_{\rm min}} \int_0^L {\rm d}s' \int_0^{B_{\rm min}/B} \frac{{\rm d}\lambda}{\tau(\lambda)} \frac{\lambda^2}{u_\parallel(\lambda, s) u_\parallel(\lambda, s')}. \tag{6.20}$$

Notice that in this high-frequency limit, the quantity $\overline{\omega}_{Dj}$ does not appear, so that the integral operator in Eq. (6.20) does not have any species-dependent quantities. The β_j and ω_{*j} absorb all of the species dependence. The difference between this mode and the usual magneto-acoustic mode is that in Eq. (6.19), the adiabatic index is given by the eigenvalues Γ^{HF} of the bounce-averaging integral operator. In the high $\beta \gg 1$ limit and taking ω to be large compared with ω_{*j}, we find the approximate solution to Eq. (6.19) to be given by

$$\omega \simeq 2 k_y V_A \sqrt{\beta}. \tag{6.21}$$

Figure 6.3 shows ω for the magnetoacoustic mode computed from Eq. (6.19), compared with the approximate formula of Eq. (6.21). The agreement is found to be good between Eq. (6.21) and the numerical solution of Eq. (6.19). Also shown in Fig. (6.3) are the eigenvalues $\Gamma^{\rm HF}$ of the integral operator of Eq. (6.20) as a function of β. The β dependence is found to be relatively weak, varying approximately 20% as β varies over an order of magnitude. Also shown are the eigenfunctions of the integral operator as a function of s, the distance along the field line. The eigenfunctions on flux tubes closest to the Earth (lowest β) tend to vary approximately as $(B_{\rm min}/B(s))^{3/2}$, and the eigenfunctions on flux tubes at higher β tend to vary more as $(B_{\rm min}/B(s))^{5/2}$. These eigenfunctions and eigenvalues are computed with both Tsyganenko's

1996 model through the tail/dipole transition region as a function of β. The value of β is computed from equilibrium assumptions with the magnetic field models. In this case we used the Lysak model [128] for the density profile $n(s)$ in order to compute the Alfvén velocity.

6.4 Mode frequencies below the guiding center drift frequency

The low-frequency modes occur for $\omega \ll \overline{\omega}_D$, which yields $G^j(\omega,\lambda) = (3/2)(\omega_{*j}/\overline{\omega}_{Dj})((1+\eta_j) - \omega/\omega_{*j})$ to first order. Unlike the high-frequency limit in Eq. (6.19), in the low-frequency limit the left-hand side $\omega^2/k_y^2 V_A^2$ is negligible. The dispersion relation is given by

$$0 = 1 + \frac{3}{4}\sum_j \beta^j_{\rm min}\left((1+\eta_j) - \frac{\omega}{\omega_{*j}}\right)\Gamma^{\rm LF}. \tag{6.22}$$

Here $\Gamma^{\rm LF}$ are the eigenvalues of the integral operator

$$\widehat{\Gamma}^{\rm LF} = \frac{1}{2}\frac{B(s)}{B_{\rm min}}\int_0^L {\rm d}s' \int_0^{B_{\rm min}/B} \frac{{\rm d}\lambda}{\tau(\lambda)}\frac{\lambda^2}{u_\parallel(\lambda,s)u_\parallel(\lambda,s')}\frac{\omega_{*j}}{\overline{\omega}_{Dj}(\lambda)}\,(\cdot) \tag{6.23}$$

The integral operator is again independent of species since $\omega_{*i} = -\omega_{*e}T_i/T_e$ and $\overline{\omega}_{Di} = -\overline{\omega}_{De}T_i/T_e$. Notice that if $T_e = T_i$, then the terms dependent on ω in Eq. (6.22) exactly cancel and it is necessary to take the $\omega/\overline{\omega}_D \ll 1$ expansion to next order.

Figure 6.4 shows the eigenvalues and eigenvectors of the low-frequency bounce-averaged operator of Eq. (6.23), as well as the shifted frequency computed from Eq. (6.22). Tsyganenko's 1996 magnetic field model was used

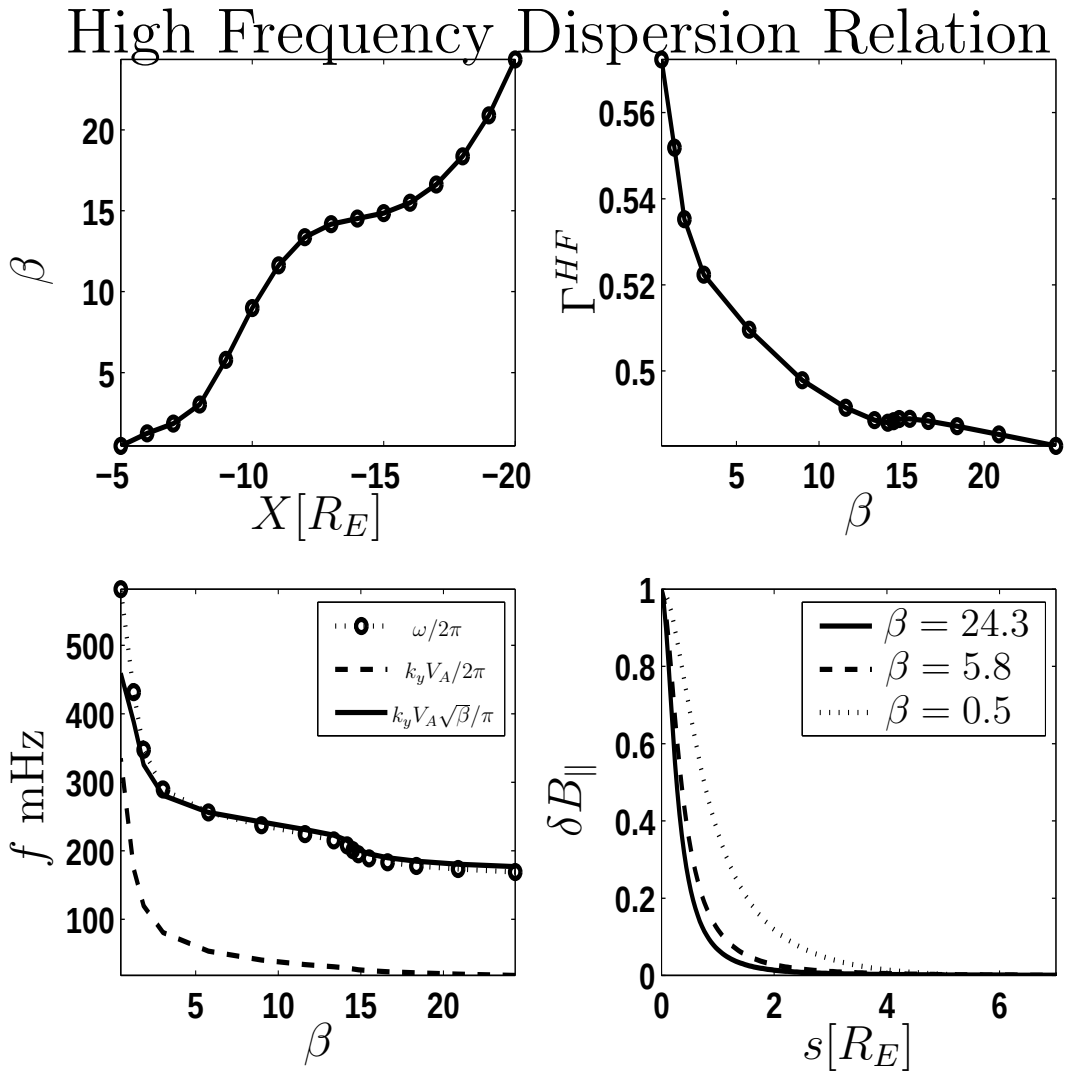

Figure 6.3: Calculation of the high frequency ($\omega \gg \omega_D$) dispersion relation. The upper left panel shows the value of β as a function of X/R_E. The upper right panel shows the eigenvalues of the high-frequency bounce-average operator of Eq. (6.20) as a function of β. The lower left panel shows the frequency in mHz computed with the dispersion relation in Eq. (6.19). The lower right panel shows three different eigenfunctions for three different β values as a function of s/R_E, the distance along the field; the eigenfunctions for the higher β cases were truncated to help visualize the data.

to compute all quantities, and T_e was taken to be negligible to prevent the previously mentioned cancellation. The computed frequency shift which is a rearrangement of the terms in Eq. (6.22) taking $T_e = 0$,

$$\omega_k = \omega_{*i}(1 + \eta_i) + \frac{4}{3\beta_i \Gamma^{\mathrm{LF}}}\omega_{*i}, \tag{6.24}$$

is seen to increase at lower β. The frequency ω_k is closest to the diamagnetic drift frequency ω_{*pi} and well below the bounce-averaged guiding center drift frequency. The eigenfunctions are seen to be strongly ballooning, meaning the perturbation is very strongly peaked at the equatorial plane. The eigenvalues of the the operator $\widehat{\Gamma}^{\mathrm{LF}}$ are seen to follow the general form of the computed stability parameter $R(\beta)$, and the approximation $R(\beta) \simeq 2\Gamma^{\mathrm{LF}}(\beta)$ is reasonable, as can be seen by comparing $R(\beta)$ from Figure 5.4 with $\Gamma^{\mathrm{LF}}(\beta)$ from Figure 6.4.

6.5 The ∇B and curvature drift resonance response

The stability of compressional modes for wave frequencies near the magnetic bounce-averaged guiding-center drift frequency ($\omega \sim \overline{\omega}_{Di}$) depends on the value of the complex integral as a function of frequency over the drift resonance between the particles and the waves. We now turn to the evaluation of the $\omega = \epsilon\overline{\omega}_{Di}(\lambda)$ resonance, so the iteration procedure discussed must be employed to solve the problem. Figure 5.4 shows $\overline{\omega}_{Di}$ computed with the Tsyganenko 1996 model. It is seen that through the transition region between the dipole-dominated magnetic field and the current sheet-dominated magnetic

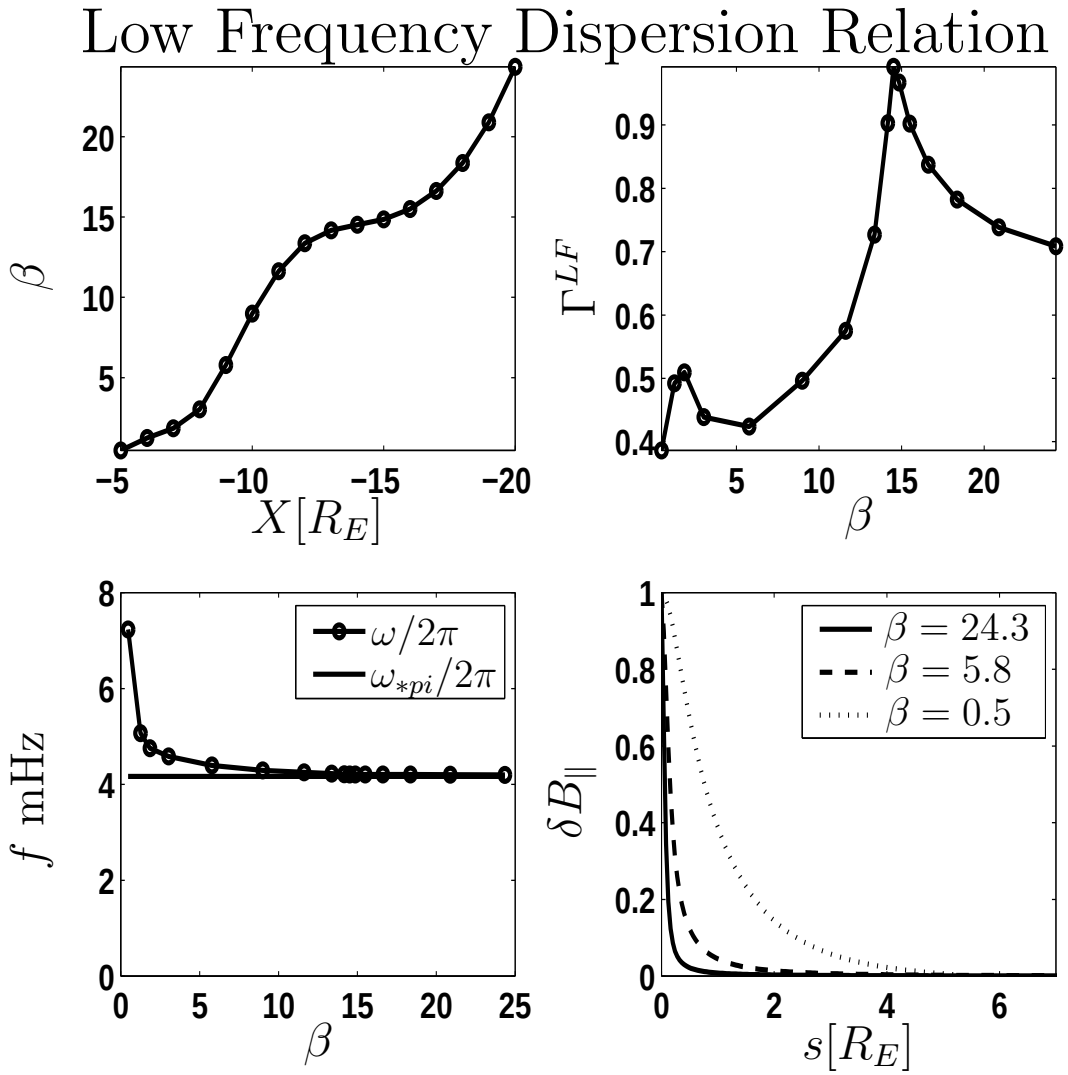

Figure 6.4: Calculation of the low frequency ($\omega \ll \omega_D$) dispersion relation. The upper left panel shows the value of β as a function of X/R_E. The upper right panel shows the eigenvalues of the low-frequency bounce-average operator of Eq. (6.23) as a function of β. The lower left panel shows the frequency in mHz computed with the dispersion relation in Eq. (6.22). The lower right panel shows three different eigenfunctions for three different β values as a function of s/R_E, the distance along the field; the eigenfunctions for the higher β cases were truncated to help visualize the data.

field, the ∇B drift reverses direction and becomes stronger, so that eventually it almost cancels the curvature drift. For most cases the variation of the total bounce-averaged drift frequency $\overline{\omega}_D(\lambda)$ with pitch angle λ is weak.

6.5.1 Nyquist analysis of the variational form dispersion relation

To analytically perform the Nyquist analysis on the variational form given in Eq. (6.14), we ignore the inertial term, considering $\omega \ll k_y V_A$, take the perturbing field to be flute-like $\delta B_\parallel(s) = \text{const.}$, ignore the pitch angle dependence of the bounce averaged guiding center drift, and consider only the ions by taking the limit $T_e/T_i \ll 1$. Then we obtain the complex dispersion relation

$$C = 1 + \sum_j \frac{\beta_j}{2} G^j(\omega) = 0 \tag{6.25}$$

for the compressional mode. In this limit $G^j(\omega) = G(\omega)$ can be written as

$$G(\omega) = \frac{2}{\sqrt{\pi}} \int_0^\infty \mathrm{d}\epsilon \epsilon^{5/2} e^{-\epsilon} \left[\frac{\omega_{*i}\eta_i}{\overline{\omega}_{Di}} + \left(1 - \frac{\omega_{*i}\eta_i}{\overline{\omega}_{Di}}\right) \frac{\omega - \omega_I}{\omega - \overline{\omega}_{Di}\epsilon} \right] \tag{6.26}$$

in order to make clear the four frequencies for which $\mathrm{Im}(C) = 0$, namely, $\omega = 0, \omega_I, \pm\infty$, where

$$\omega_I = \omega_{*i} \frac{1 - \frac{3}{2}\eta_i}{1 - \frac{\omega_{*i}\eta_i}{\overline{\omega}_{Di}}} = \frac{k_y \rho_i v_i}{L_{ni}} \frac{1 - \frac{3}{2}\frac{L_{ni}}{L_{Ti}}}{1 - \frac{R_c}{L_{Ti}}}. \tag{6.27}$$

Here $R_c = R_c(\beta)$ and using the constant current model deep in the tail we have $R_c^{-1} \simeq B_x'/B_n$ when $\mathrm{d}B_x/\mathrm{d}z \gg \mathrm{d}B_n/\mathrm{d}x$ from $\nabla B/B$. This gives roughly $R_c(\beta)^{-1} = (1 - R_c\beta')R_c^{-1} = R_c^{-1}(1 - R_c\beta/L_p)$. For $\beta > L_p/R_c$, the $\nabla B/B$

drift overcomes the curvature drift. Correspondingly, the real part of C at each of these critical frequencies is given by

$$C(\omega = \omega_I) = 1 + R(\beta)\eta_i \tag{6.28}$$

$$C(\omega = 0) = 1 + \frac{2}{5}R(\beta)(\eta_i + 1) \tag{6.29}$$

$$C(\omega = \pm\infty) = 1 + \frac{15}{8}\beta \tag{6.30}$$

where $R(\beta) \sim (15/8)\beta\omega_{*i}/\overline{\omega}_{Di}(\beta) \sim (15/8)\beta R_c/L_n$. The imaginary part of $C(\omega)$ for real ω can be written by distorting the ϵ integration contour below the singularity at $\overline{\omega}_{Di}$:

$$\begin{aligned} \mathrm{Im}[C(\omega)] &= -\sqrt{\pi}\frac{\beta_i}{\overline{\omega}_{Di}}\left[\omega\left(1 - \frac{\omega_{*i}\eta_i}{\overline{\omega}_{Di}}\right) - \omega_{*i}\left(1 - \frac{3}{2}\eta_i\right)\right] \\ &\quad \Theta\left(\frac{\omega}{\overline{\omega}_{Di}}\right)\left(\frac{\omega}{\overline{\omega}_{Di}}\right)^{5/2}\exp(-\frac{\omega}{\overline{\omega}_{Di}}). \end{aligned} \tag{6.31}$$

Here $\Theta(\omega/\overline{\omega}_{Di})$ is the step function, such that when ω and $\overline{\omega}_{Di}$ have the same sign the function has the value unity and otherwise is zero. An instability exists when $C(\omega = 0)$ and $C(\omega = \omega_I)$ have opposite signs and $C(\omega)$ between these two frequencies is imaginary, so that a contour enclosing the upper half plane in the complex ω plane corresponds to a contour that encircles the origin in the complex C plane. The system is marginally stable when the two values of $C(\omega)$ are both zero or when $C(\omega)$ between these two frequencies is purely real. In this analysis there are three stability parameters: β, $\omega_{*i}/\overline{\omega}_{Di}$, and η_i. By combining β and $\omega_{*i}/\overline{\omega}_{Di}$ to form the parameter $R(\beta)$ we can construct a simple picture.

From Eqs. (6.28)-(6.30) it can be seen that an instability exists when $R(\beta) < 0$, which is in the region of drift reversal, for a particular small range of η_i values. Another instability region exists for $\eta_i < 0$, or when the temperature gradient is opposite to the density gradient. For $\eta_i = -1$ it is clear that $C(\omega = 0) > 0$, so that for $R(\beta) > 1$ we find $C(\omega = \omega_I) < 0$ and the flux tube is unstable. There is some evidence [72] based on data published in [144], for such a negative η_i to exist.

To determine whether or not $\mathrm{Im}C(\omega) > 0$ for these regions we must determine if $\overline{\omega}_{Di}$ and ω_I have the same sign, which would imply

$$\frac{\omega_I}{\overline{\omega}_{Di}} = \frac{\omega_{*i}}{\overline{\omega}_{Di}} \frac{(1 - \frac{3}{2}\eta_i)}{(1 - \frac{\omega_{*i}\eta_i}{\overline{\omega}_{Di}})} > 0. \tag{6.32}$$

Thus if we are considering $\eta_i < 0$ then the above condition holds true as long as $\omega_{*i}/\overline{\omega}_{Di} > 0$ (which is true for the unstable region we are considering). If we are considering $\omega_{*i}/\overline{\omega}_{Di} < 0$ then it is easy to see that we must have $\eta_i > 2/3$.

Figure (6.5) shows the boundary between instability and stability as a function of η_i and $R(\beta)$ in two different regions: panel (a) shows the stability boundaries in the drift reversal region, and panel (b) shows the stability boundaries in the negative η_i region. It is interesting to point out here that this analysis differs from the electrostatic mode Nyquist analysis (performed in Chapter 5) due to the factor of β occurring here.

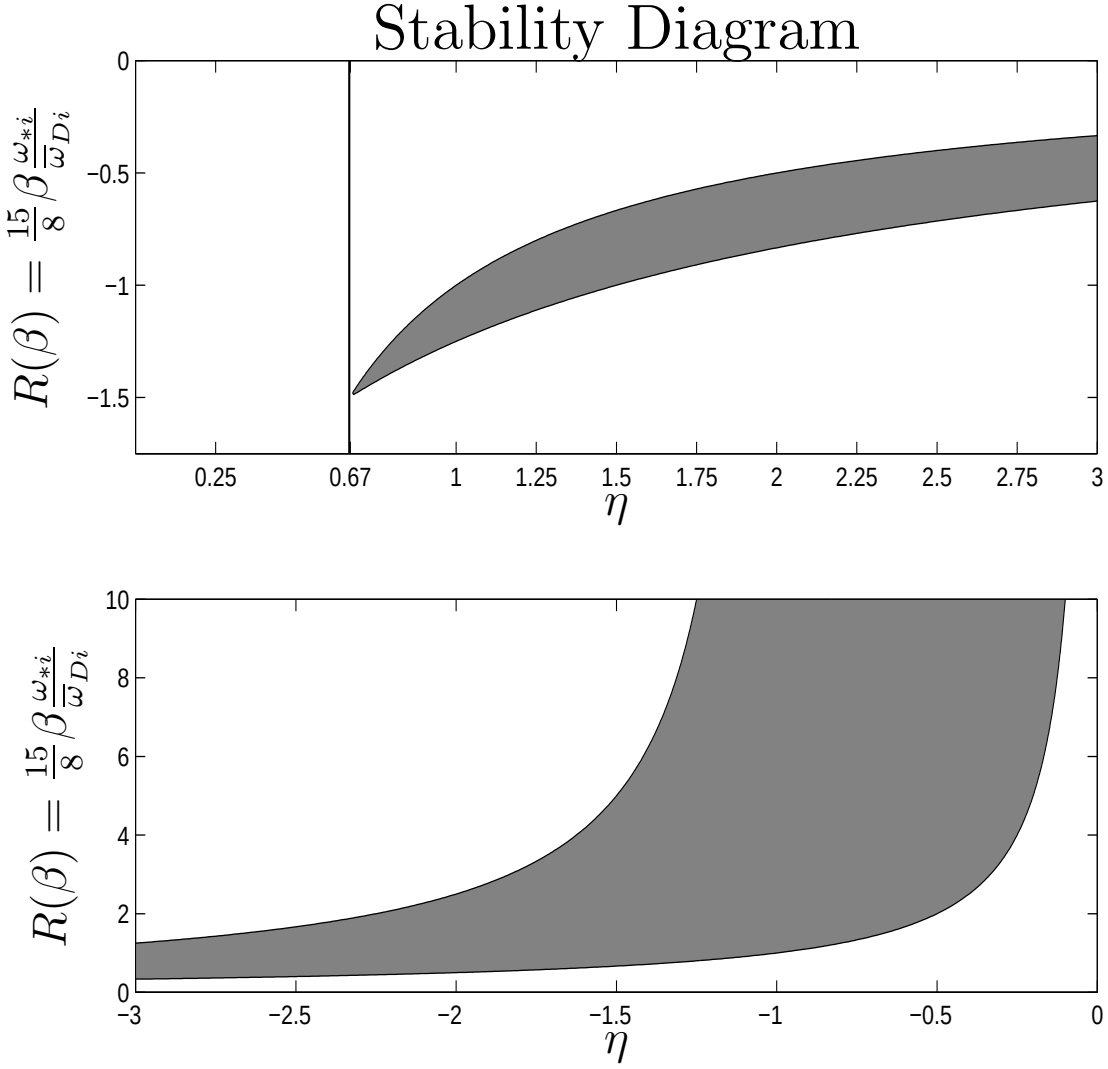

Figure 6.5: Stability diagram for compressional modes as a function of the stability parameters η and $R(\beta) = (15/8)\beta\omega_{*i}/\overline{\omega}_{Di}$. Panel (a) shows the region in parameter space of drift reversal, when $\overline{\omega}_{Di}$ is in the direction of the gradient drift. Panel (b) shows the region in parameter space where the temperature gradient and the density gradient are in opposite directions. In both panels the darker region in parameter space represents instability, while the white region represents at least marginal stability. For drift-reversal, an instability cannot exist unless $\eta_i > 2/3$. These parameters are similar to the standard electrostatic stability diagram except for the explicit presence of β.

6.5.2 Growth rate estimates

From Eq. (6.13) we now estimate, by making a local approximation, that the compressional drift waves have

$$\frac{\omega^2}{k_y^2 V_A^2} = C(\omega, k_y, \eta_i, \beta) \tag{6.33}$$

with

$$C \simeq 1 + \beta_i \Gamma \frac{\omega - \omega_{*i}(1 + \frac{3}{2}\eta_i)}{\omega - \overline{\omega}_{Di}} \tag{6.34}$$

where $C = 1 + \mu_0 \delta P_\perp / B \delta B_\parallel$ is the complex response function considered in detail in the previous section. Notice that in Eq. (6.34) we have used a mean value of $\epsilon = 3$; this value is near the maximum contribution from the integral $\int \mathrm{d}\epsilon\, \epsilon^{5/2} exp(-\epsilon)$, and agreement with actual results was quite good. Instability occurs from $\omega_0 \mathrm{Im}(C(\omega_0)) > 0$ for $\mathrm{Re}C(\omega_0) > 0$ and from new low frequency roots of $C(\omega) = 0$. The approximate roots of $C(\omega) = 0$ are

$$\omega_k \simeq \omega_{*i} \frac{\frac{\overline{\omega}_{Di}}{\omega_{*i}} + \beta_i \Gamma (1 + \frac{3}{2}\eta_i)}{\Gamma \beta_i + 1} < \omega_{bi}. \tag{6.35}$$

In the limit $\beta_i \gg \overline{\omega}_{Di}/\omega_{*i}$, then $\omega_k \sim \omega_{*i}(1 + 3\eta_i/2)$; and in the opposite limit $\beta \ll \overline{\omega}_{Di}/\omega_{*i}$, then $\omega_k \sim \omega_{Di}$. Figure 5.5 shows the relevant frequencies used in this estimation as a function of $X[R_E]$ at the edge of the plasma sheet. The magnetic drift frequencies were obtained by bounce averaging Eqs. (5.11)-(5.12) with the use of the Tsyganenko (1996) [188] magnetic field model. For example, for $x = -10R_E$, $L_{pi} = 2R_E$ and $k_y \rho_i = 0.5$, we find that 5 KeV particles have $\omega_{*i} = 5 k_y \rho_i v_i / (3 L_{pi}) = 3$mHz, $\omega_{bi} = 16$mHz, and $\overline{\omega}_{Di} = 3$mHz. For $\rho_i = 300$ km the wavelength is $2\pi/k_y = 20\rho_i = 6 \cdot 10^6$m $\approx 1 R_E$, which is

approximately the limit of the local approximation. Thus, since $\overline{\omega}_{Di} \simeq \omega_{*i}$, we approximate $\omega \simeq \omega_{*i} \simeq 3\text{mHz}$.

For these modes $\delta E = \delta E_x = (\omega/k_y)\delta B_\parallel = v_{Di}\delta B_\parallel$, so for $\delta B_\parallel = 10$ nT we find $\delta E_x \sim 10^{-4}$ V/m $\sim 100\mu$V/m. The Poynting flux is $\mathbf{S} = \delta\mathbf{E}\times\delta\mathbf{B}/\mu_0 = (\omega/k_y)\delta B_\parallel^2\widehat{\mathbf{y}}/\mu_0 = 1\mu\text{W/m}^2$. The displacement vector is then $\xi \approx (1/6)R_E$. The non-linear limit is reached when $\delta B_\parallel/B \sim k_y\xi_y \sim 1$.

Using Eq. (6.35) as the real part of the true root, we can then make the approximation that $\gamma/\omega \ll 1$ and obtain an approximate formula for the growth rate as

$$\begin{aligned}\gamma_k &\simeq -\frac{\text{Im}C(\omega)}{\frac{\partial C(\omega)}{\partial\omega}} \\ &\simeq \sqrt{\pi}\frac{(\omega_k-\overline{\omega}_{Di})^2}{\omega_{*i}-\overline{\omega}_{Di}}\left[\frac{\omega_k}{\overline{\omega}_{Di}}\left(1-\frac{\omega_{*i}\eta_i}{\overline{\omega}_{Di}}\right)-\frac{\omega_{*i}}{\overline{\omega}_{Di}}\left(1-\frac{3}{2}\eta_i\right)\right] \\ &\quad\times\left(\frac{\omega_k}{\overline{\omega}_{Di}}\right)^{5/2}e^{-\frac{\omega_k}{\overline{\omega}_{Di}}}. \end{aligned} \tag{6.36}$$

Here ω_k is the solution to $C(\omega_k) = 0$ given by Eq. (6.35). Figure 6.8 shows the growth rates and real parts of the frequencies of the full solution to the non-local dispersion relation, compared with the approximate formulas given by Eqs. (6.35) and (6.36) for a flux tube that exhibits drift reversal ($\overline{\omega}_{Di} < 0$). The agreement is quite good for this case and is seen to be only slightly worse for cases with larger growth rates.

The energy associated with the compressional drift wave is

$$\delta W^{\text{comp}} = \int\left(\frac{\delta B_\parallel^2}{2\mu_0}+\frac{1}{2}\rho v_y^2+\frac{1}{2}\delta p_\perp\frac{\delta B_\parallel}{B}\right)\frac{\text{d}s}{B}\text{d}\Psi, \tag{6.37}$$

where

$$v_y = \frac{E_x}{B} = \left(\frac{\omega}{k_y}\right)\frac{\delta B_\parallel}{B} \tag{6.38}$$

with energy released for $C(\omega) < 0$ due to the spatial gradients rather than the anisotropy as in a mirror mode. The energy release is not as large as a typical ballooning/interchange event. For example, for $\delta B_\parallel = 1\text{nT}$ over a region of volume R_E^3, there is $\delta W^{\text{comp}} = 2 \times 10^8 J$. The waves are most dangerous when they induce a local neutral line due to $\delta B_z(x,y) + B_n(x) < 0$.

These modes have $|\gamma_k/\omega_k| < 1$ and can produce local mirror trapping of ions at finite amplitude. These modes are due to the $\omega = \overline{\omega}_{Di}\epsilon$ resonance and do not require temperature anisotropy, as do the drift-mirror modes. The drift-mirror mode [1, 37] goes unstable when $1 + \beta_\perp - \beta_\perp^2/\beta_{||} < 0$, and its growth rate is given by

$$\omega^2 \simeq k_y^2 V_A^2 \left[1 + \beta_\perp \left(1 - \frac{\beta_\perp}{\beta_\parallel}\right)\right]. \tag{6.39}$$

Here one can see again that for $T_\perp = T_\parallel$ the familiar magneto-acoustic mode is obtained.

6.6 Numerical growth rates

Figure 6.6 shows the real and imaginary parts of the solutions, ω, to the dispersion relation given in Eq. (6.14), for different positions and different values of η_i, in the region of parameter space where $\eta_i < 0$. Comparing the growth rates in Fig. 6.6 to the marginal stability conditions in Fig. 6.5, one sees that for $X = -5R_E$ we have $R(\beta) \simeq 1.0$ and the compressional mode

is unstable for $-4 < \eta_i < -1$. As we consider flux-tubes farther in the tail, the value of $R(\beta)$ increases so that smaller values of negative η_i will lead to instability over a smaller region of η_i space, as seen in both by the marginal stability conditions shown in Fig. 6.5 and the actual growth rates shown in Fig. 6.6. The results of the local Nyquist analysis accurately predict the boundaries of marginal stability for this region of parameter space. The growth rates are not large ($\gamma/\omega < 1$), and the direction that these waves travel is from dawn to dusk ($\dot{y} = \omega/k_y > 0$). As β gets larger the growth rate becomes comparable to the real part of the frequency. Shown in Fig. 6.7 are two eigenfunctions corresponding to two different parameter vectors. These perturbations are seen to be strongly ballooning, i.e., the maximum perturbation is confined to the equatorial region ($Z = 0$).

We did not consider a magnetic field model that has particles whose ion magnetic guiding-center drift is from dusk to dawn. We verify that an instability exists for these cases, by arbitrarily reversing the bounce-averaged drift velocity. An example of a model that does have drift reversal is given in [119] where a large localized magnetic pulse is applied to the Earth's dipole field. Figure 6.8 shows that for a flux-tube at $X = -5R_E$, corresponding to $R(\beta) \simeq -1$ a weakly unstable mode exists ($\gamma/\omega \ll 1$) for values of η_i predicted by the local Nyquist analysis. Also shown in this figure is the growth-rate estimate given by Eq. (6.36). These modes travel from dusk to dawn ($\dot{y} = \omega/k_y < 0$) in the direction of drifting protons. Since compressional disturbances are driven by the arrival of interplanetary shocks the existence

of marginally stable compressional drift waves may be of importance. The eigenfunctions corresponding to these two solutions to the dispersion relation are seen to also be strongly ballooning, with the maximum perturbation being in the equatorial plane.

6.7 1D Plasma Transport

Here we introduce a one dimensional transport model for the transient steepening of the pressure gradient in the magnetotail due to changes in the thermal sources deep in the tail. The model shows that pressure pulses steepen as the flow brakes against the stronger near Earthmagnetic field. Such pressure pulses are a natural source of transient steepening of the pressure gradient that can lead to magnetic driven pulses with guiding center drift reversal as shown by the models of Li *et al.* (1998) [119]. Li *et al.* (1998) modelled a dipolarization event with a Gaussian magnetic pulse which caused particles to reverse the direction of their magnetic drift and used this mechanism to explain dispersionless injection. We show that when particles reverse the direction of their magnetic drift, compressional/rarefraction waves can become unstable.

In the absence of turbulence the Earthward convection of the plasma flux tubes compresses the plasma against the Earth's dipolar magnetic field. In the MHD limit there is no heat loss from the flux tubes, and the pressure increases adiabatically with $p^{\rm ad}(x) \equiv p(V_0/V(x))^{\Gamma}$, where $V(x) = \int_0^L ds/B$ and $L = L(x)$ denotes the position of the ionosphere measured along B from the equatorial plane position $(x, y = 0, z = 0)$. In Fig. 6.9 we show $V(x)$

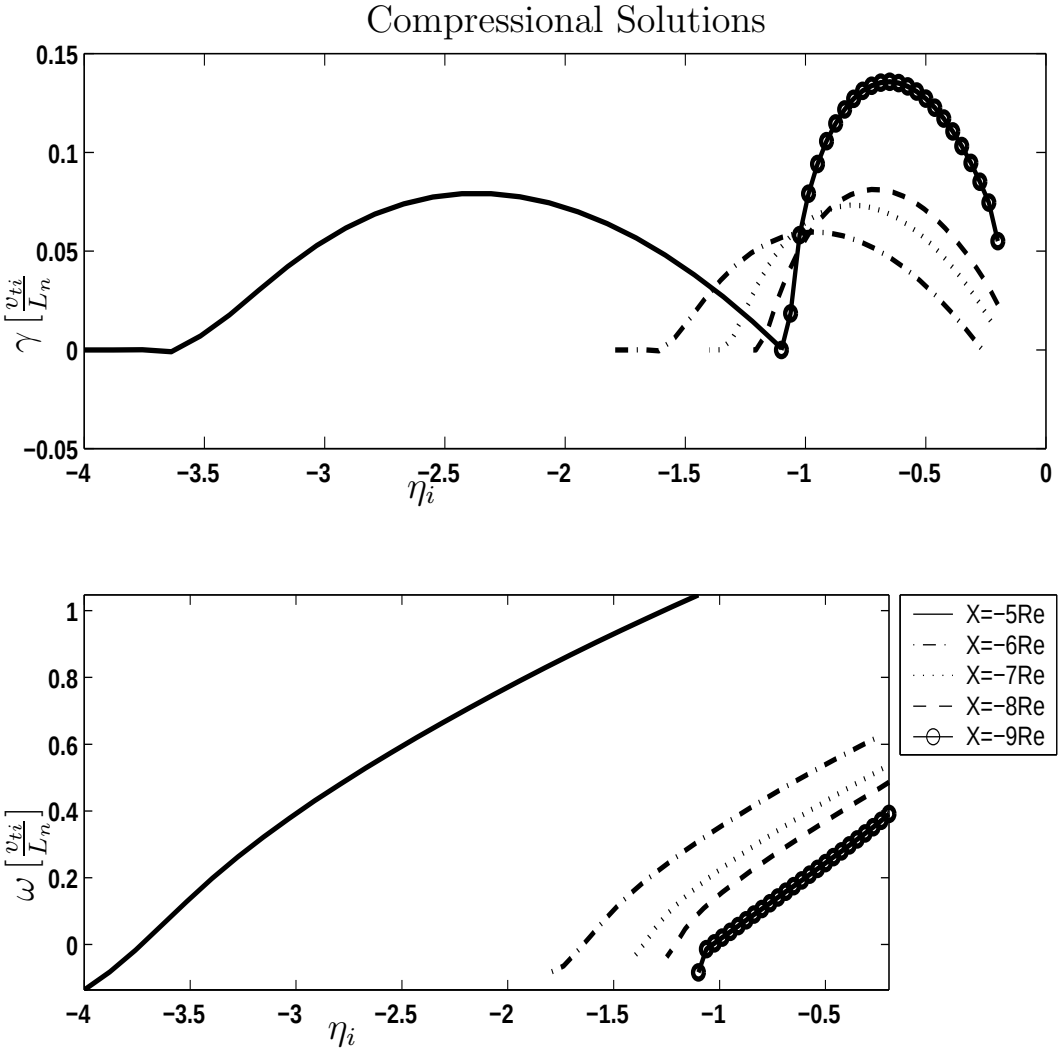

Figure 6.6: Growth rate γ (top panel) and the real part of the frequency ω (bottom panel) as a function of η_i, computed with the full non-local resonant particle dispersion relation given by Eq. (6.14). Here $k_y\rho_i = 0.5$, $T_e/T_i = 0$, and $L_n/R_c = 6$, and all other quantities were computed using Tsyganenko's (1996) model with $PS = 0$, $P_{\rm dyn} = 3.0\,$nPa, DST $= -50nT$, $B_y^{\rm IMF} = 0$, and $B_z^{\rm IMF} = 5.0$nT. There are five different curves corresponding to five different flux tubes at $X = -5, -6, -7, -8$, and $-9\,R_E$. The curves computed with flux tubes deeper in the tail have higher values of β, thus the stability parameter $R(\beta)$ is larger. This corresponds with moving up along the $R(\beta)$ axis in the marginal stability diagram of Fig. 6.5.

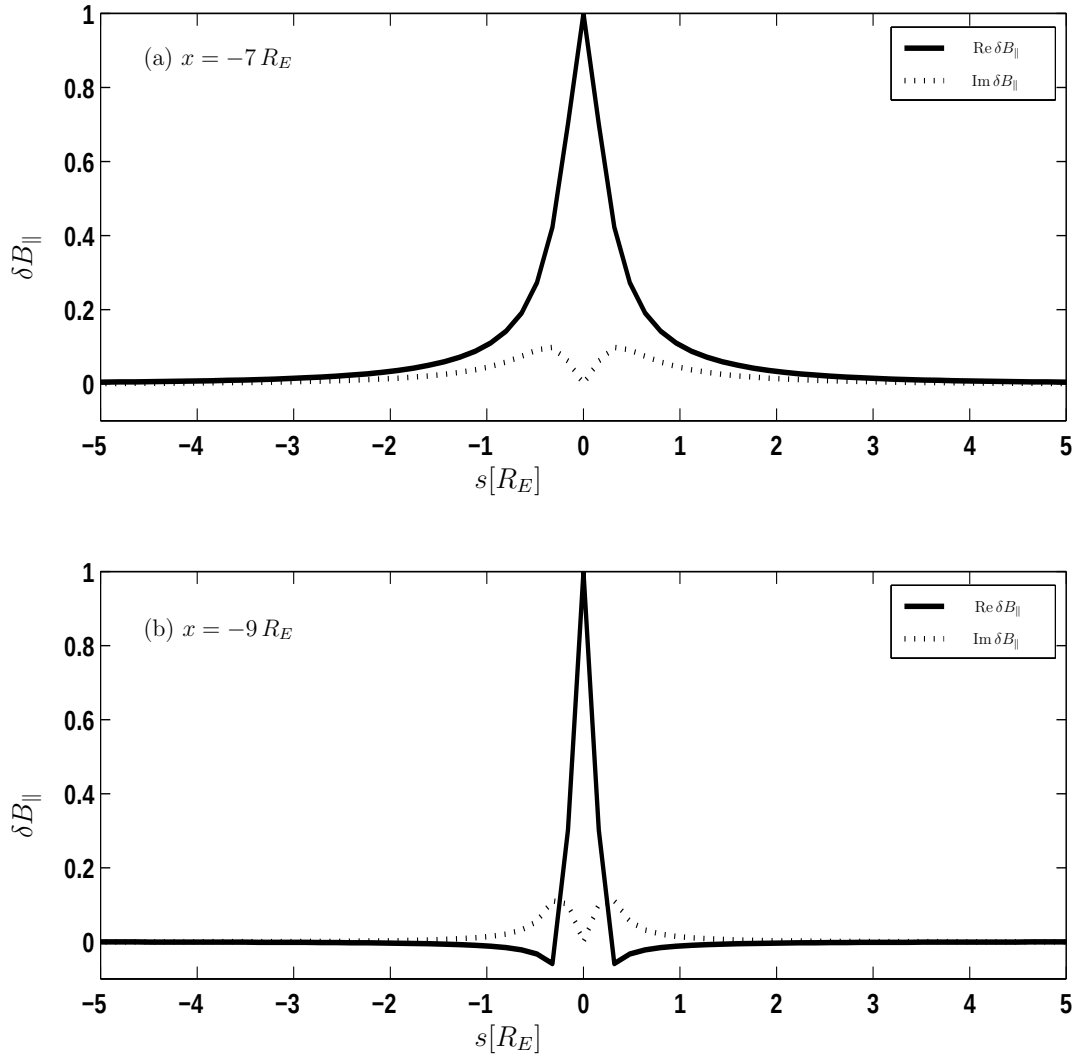

Figure 6.7: Real and imaginary parts of two different eigenfunctions $\delta B_\parallel$ as a function of the distance along the field line s (in units of R_E). These eigenfunctions were used to compute the solution to the dispersion relation found in Fig. 6.6. The first eigenfunction $\delta B_\parallel$ was computed with $\eta = -0.8$ at $x = -7R_e$, corresponding to $\beta = 7.6$. The second eigenfunction $\delta B_\parallel$ was computed with $\eta = -0.6$ at $x = -9R_E$, corresponding to $\beta = 24.2$. In this figure $k_y\rho_i = 0.5$, $T_e/T_i = 0$, and $L_n/R_c = 6$, and all other quantities were computed using Tsyganenko's (1996) model with $PS = 0$, $P_{\rm dyn} = 3.0\,$nPa, DST $= -50nT$, $B_y^{\rm IMF} = 0$, and $B_z^{\rm IMF} = 5.0$nT.

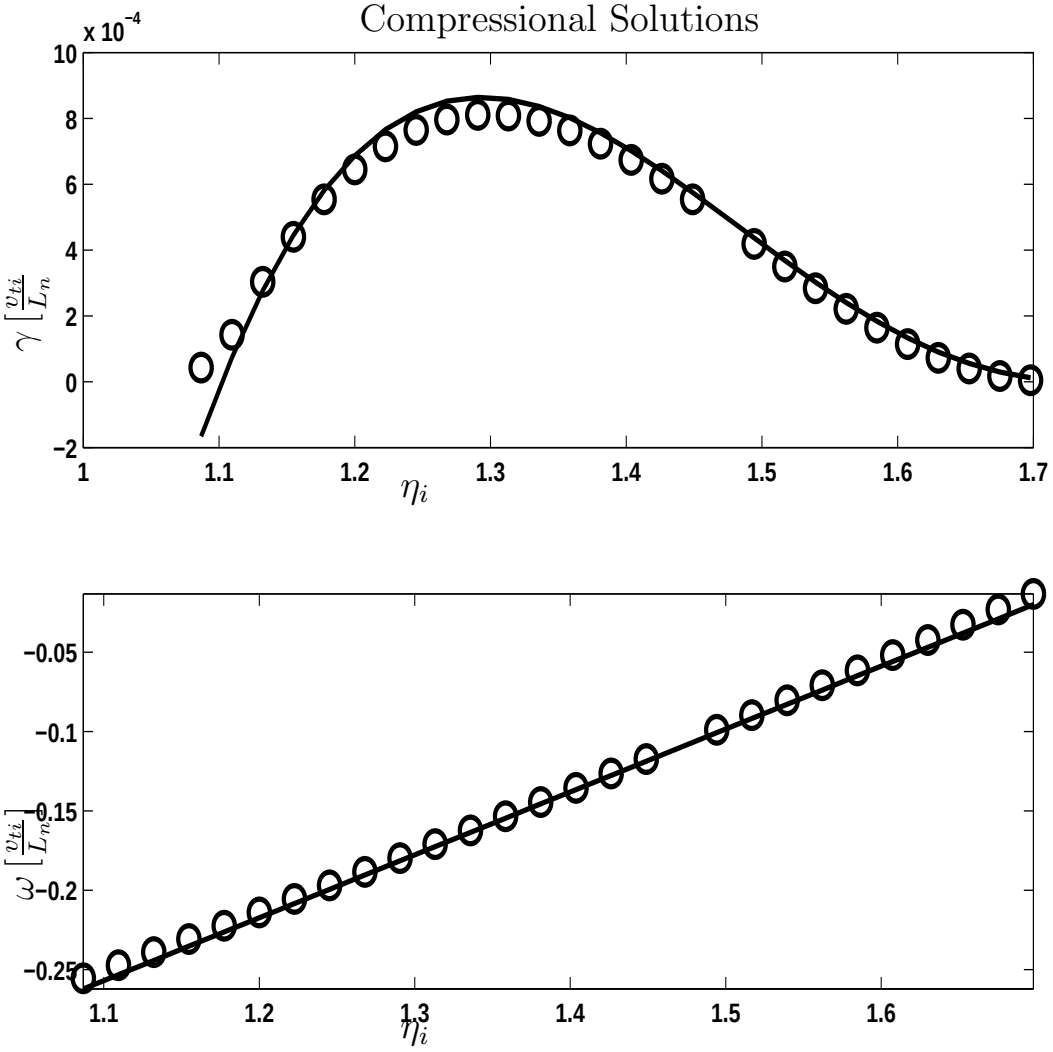

Figure 6.8: Growth rate γ (top panel) and the real part of the frequency ω (bottom panel) as a function of η_i, for a flux tube positioned at $X = -5\,R_E$. The circles show the results of the full non-local resonant particle dispersion relation given by Eq. (6.14), as compared to an approximate growth rate formula given by Eqs. (6.35) and (6.36). Here $k_y\rho_i = 0.5$, $T_e/T_i = 0$, and $L_n/R_c = 6$, and all other quantities were computed using Tsyganenko's (1996) model with $PS = 0$, $P_{\rm dyn} = 3.0\,$nPa, DST $= -50nT$, $B_y^{\rm IMF} = 0$, and $B_z^{\rm IMF} = 5.0$nT. To achieve drift-reversal the computed bounce-averaged magnetic guiding center drift was made eastward by increasing the Earthward pressure gradient arbitrarily by a factor of five.

and $p^{\rm ad}(x) = p_0(V_0/V(x))^\Gamma$ for $\Gamma = 5/3$ and $V_0 = V(x = -10)$. The sharp increase of the pressure gradient in the transition region $x = -6$ to $-12R_E$ is thought to drive drift-Alfvén ballooning mode instabilities over a spectrum of wavelengths $k_y\rho_i \leq 1$ and to produce a turbulent diffusivity D_Ψ that limits the pressure gradient. In this section we compute the Earthward gradient of the pressure distribution function relative to the adiabatic distribution. For higher energy ions with $\rho_i > R_c$, the chaotic motion of these ions breaks the magnetic moment invariant, giving a fairly isotropic distribution.

The distant neutral line (DNL) is a source region for entry of new solar wind ions into the geotail, which we model as $S_{\rm DNL}(x,t) = S_{\rm DNL}(t)\delta(x-x_{\rm DNL})$. Near the geosynchronous orbit region there is a sink of ions with respect to the geotail plasma. The ions cross from the geotail region into the inner magnetosphere through the Alfvén layer seperatrix. The ions are also lost through the dusk side low-latitude boundary layer. We write this net loss region as $S_{\rm NE}(t)\delta(x - x_{\rm NE})$ for the near Earth (NE) loss region.

Now the transport of ions is through the Earthward convective flow $u_x = \frac{E_y}{B_z(x)}$, and the turbulent velocity space diffusive flux is $-D_\Psi \partial p^{\rm ad}/\partial\Psi$. Thus, a one-dimensional model for the ion pressure is

$$\begin{aligned}\frac{\partial p}{\partial t} &= -\frac{\partial}{\partial\Psi}\left(E_y p - D_\Psi \frac{\partial p}{\partial\Psi}\right) - \frac{5}{3}\frac{pE_y}{V}\frac{{\rm d}V}{{\rm d}\Psi} \\ &\quad + S_{\rm DNL}(t)\delta(x - x_{\rm DNL}) - S_{\rm NE}(t)\delta(x - x_{\rm NE}) \qquad (6.40)\end{aligned}$$

where D_Ψ is the turbulent diffusivity due to low-frequency drift wave turbulence. For $D_\Psi = 0$ and $x_{\rm DNL} < x < x_{\rm NE}$, the solution of Eq. (6.40) is

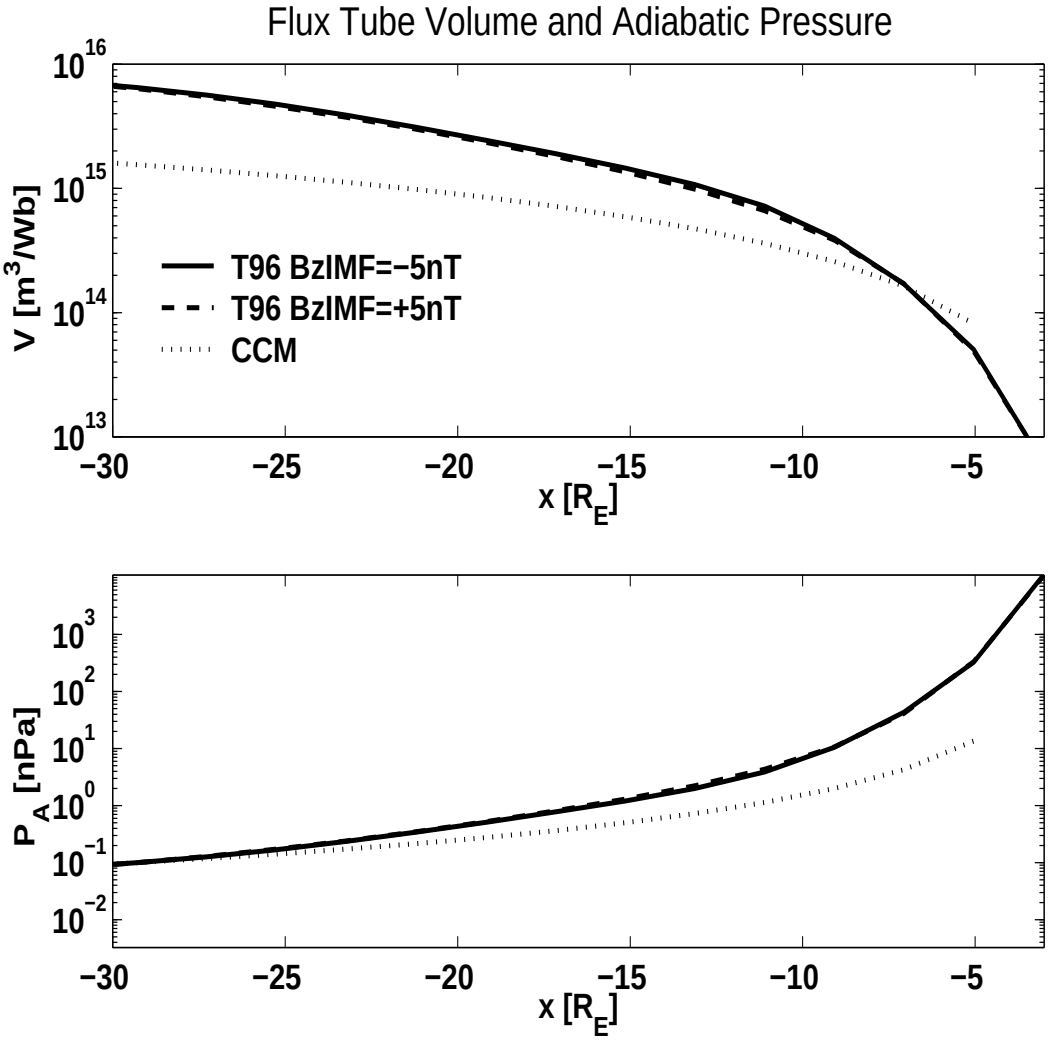

Figure 6.9: In the top panel the flux tube volume $V = \int ds/B$ is shown as a function of X in the geotail. The bottom panel shows $P^{\rm ad} = P_0(V_0/V)^\Gamma$ with $\Gamma = 5/3$ for the adiabatic pressure profile, and with P_0 chosen to be 0.1 nPa at -20 R_E in agreement with ISEE-2 measurements. The CCM model was used with the parameters $B'_x = 64{\rm nT}/R_E$, $B_n = 1.0{\rm nT}$, and $B_0 r_0^2 = 4000{\rm nT}R_E^2$, and the Tsyganenko 1996 model was used with $PS = 0$, $P_{\rm dyn} = 3.0{\rm nPa}$, ${\rm DST} = -50nT$, $B_y^{\rm IMF} = 0$, and $B_z^{\rm IMF} = \pm 5.0{\rm nT}$.

$p^{\rm ad}(x,t) = p^{\rm ad}(\Psi - \int_0^t E_y(t')dt')$ where $d\Psi = B_z dx = E_y dt$. This solution is the adiabatic convection of flux tubes in a time-varying convection electric field. We estimate the value of D_Ψ through

$$D_\Psi = \frac{\langle \delta\Psi^2 \rangle}{\tau_c} = B_z^2 \frac{\langle \delta x^2 \rangle}{\tau_c} \tag{6.41}$$

where $\langle \delta x^2 \rangle$ is the dominant wavelength in the fluctuation spectrum and τ_c is the correlation time.

The associated local $\mathbf{E} \times \mathbf{B}$ turbulent diffusivity is

$$D_x = \langle \delta x^2 \rangle^{1/2} \langle \tilde{v_E}^2 \rangle^{1/2} = \frac{\langle \delta x^2 \rangle}{\tau_c}. \tag{6.42}$$

For $\langle \delta x^2 \rangle \propto \rho_i L_p \approx (300\,\mathrm{km})(10^4\,\mathrm{km}) = 3 \cdot 10^6, \mathrm{km}^2$ and $\tau_c \approx 100\,\mathrm{s}$ we estimate that $D_x = 3 \cdot 10^4 \mathrm{km}^2/\mathrm{s}$. This compares with Borovsky's MHD estimate of $D_\perp \approx 10^7 \mathrm{km}^2/\mathrm{s}$. The corresponding $D_\Psi = 0.3(\mathrm{nT\,R_E})^2/\mathrm{s}$ for $B_z = 20$ nT gives a solution of Eq. (6.40),

$$\frac{1}{p}\frac{\partial p}{\partial \Psi} = \frac{E_y}{D_\Psi} = \frac{1\,\mathrm{mV/m}}{0.3(\mathrm{nT\,R_E})^2/\mathrm{s}} = \frac{0.5}{\mathrm{nT\,R_E}} \tag{6.43}$$

where $D_\Psi = \langle B^2 D_\perp \rangle$. Thus, we estimate the characteristic drift wave frequency as

$$\omega_* = k_y \frac{\langle E \rangle}{qp} \frac{\partial p}{\partial \Psi} \leq k_y \rho_i \frac{v_i}{L_p} \tag{6.44}$$

in the Westward direction for $1/L_{pi} = (1+\eta_i)/L_n > 0$. For $L_p^{-1} = \partial_x \ln p$ from Eq. (6.43) used in Eq. (6.44) we get

$$\begin{aligned} \omega_* &= k_y \rho_i \frac{400\mathrm{km/s}}{10^4\mathrm{km}} = 0.04\, k_y \rho_i\, \mathrm{rad/s} \\ f_* &= k_y \rho_i\, 6\mathrm{mHz} \end{aligned}$$

Typically the fastest growing waves have $k_y\rho_i \approx 0.4$ to 1.0.

Equation (6.40) was solved numerically using a grid in Ψ space with constant spacing. Tsyganenko's 1996 magnetic field model was used to compute the Δx_i's corresponding to $\Delta\Psi = 1\text{nT}\cdot R_E^2$. This choice of independent variable translated to variable spaced grid in x with many points placed closer to the Earth where the pressure pulses are predicted to pile up and steepen. Second order operator splitting was used so that a flux-corrected transport algorithm could be used to transport the pressure and a traditional finite-difference method to handle the source terms and the diffusion term.

Figure 6.10 shows five solutions to Eq. (6.40) for different times. An adiabatic pressure profile was taken as the initial condition and the tailward endpoint was taken to be time dependent, corresponding to a time dependent deposition of ions in the distant tail. The tailward source of ions is given mathematically by

$$S_{\text{DNL}}(t) = p^{\text{ad}}(x = x_{DNL}) + p^{\text{src}}\Theta(t - \tau/2)\sin(2\pi t/\tau) \tag{6.45}$$

where $p^{\text{ad}}(x = x_{DNL})$ is the adiabatic pressure at the distant neutral line taken here to be 0.06 nPa, $\Theta(t - \tau/2)$ is the step-function such that when $t > \tau/2$ the oscillating source is turned off.

$$\Theta(t - \tau/2) = \begin{cases} 1 & \text{for} \quad t < \tau/2 \\ 0 & \text{for} \quad t \geq \tau/2 \end{cases} \tag{6.46}$$

This choice of the argument of the step function ensures that the pressure pulse is entirely positive. The source pressure $p^{\text{src}} = 1\text{nPa/s}$ gives the height

of the pressure pulse with a period of $\tau = 60$ seconds. Given these parameters the energy density deposited over the duration of the pulse is computed to be 19 nPa. The pressure pulse then drifts Earthward by $\mathbf{E} \times \mathbf{B}$ convection, with a constant $E_y = 1mV/m$ applied along the tail, until it reaches the dipole braking region where the drift slows, due to the increase in B, and the pressure piles up. The axial $B_z(x, 0, 0)$ is taken from the Tsyganenko 1996 model with $PS = 0$, $P_{\rm dyn} = 3.0\,{\rm nPa}$, DST $= -50nT$, $B_y^{\rm IMF} = 0$, and $B_z^{\rm IMF} = -5.0{\rm nT}$ for this simulation. The turbulent diffusivity was taken to be zero, 0.05 $(nT\,R_E)^2/s$, and 0.3 $(nT\,R_E)^2/s$. The pressure pulse is significantly washed out for larger values of the turbulent diffusivity, though there is still some steepening.

In panel (e) of figure 6.10, which occurs at 891 seconds after the tailward source begins its half period oscillation, we see a sharp trailing edge pressure gradient. Such a pressure steepening could potentially be large enough to reverse the direction of the magnetic guiding center drift due the mechanism explained through Eq. (5.14) and shown by Li et al. (1998)[119]. In fact the pressure gradient shown in the trailing edge of the pulse in Figure 6.10 is over 5 times the adiabatic pressure gradient, which is approximately the same factor needed to produce drift reversal in Tsyganenko 1996. This drift reversal is then predicted to cause the drift compressional mode to go unstable. The steep transient gradient will also drive the ballooning/interchange mode unstable as explained in Chapter 3, which is the primary plasma energy release mechanism in this NGO region.

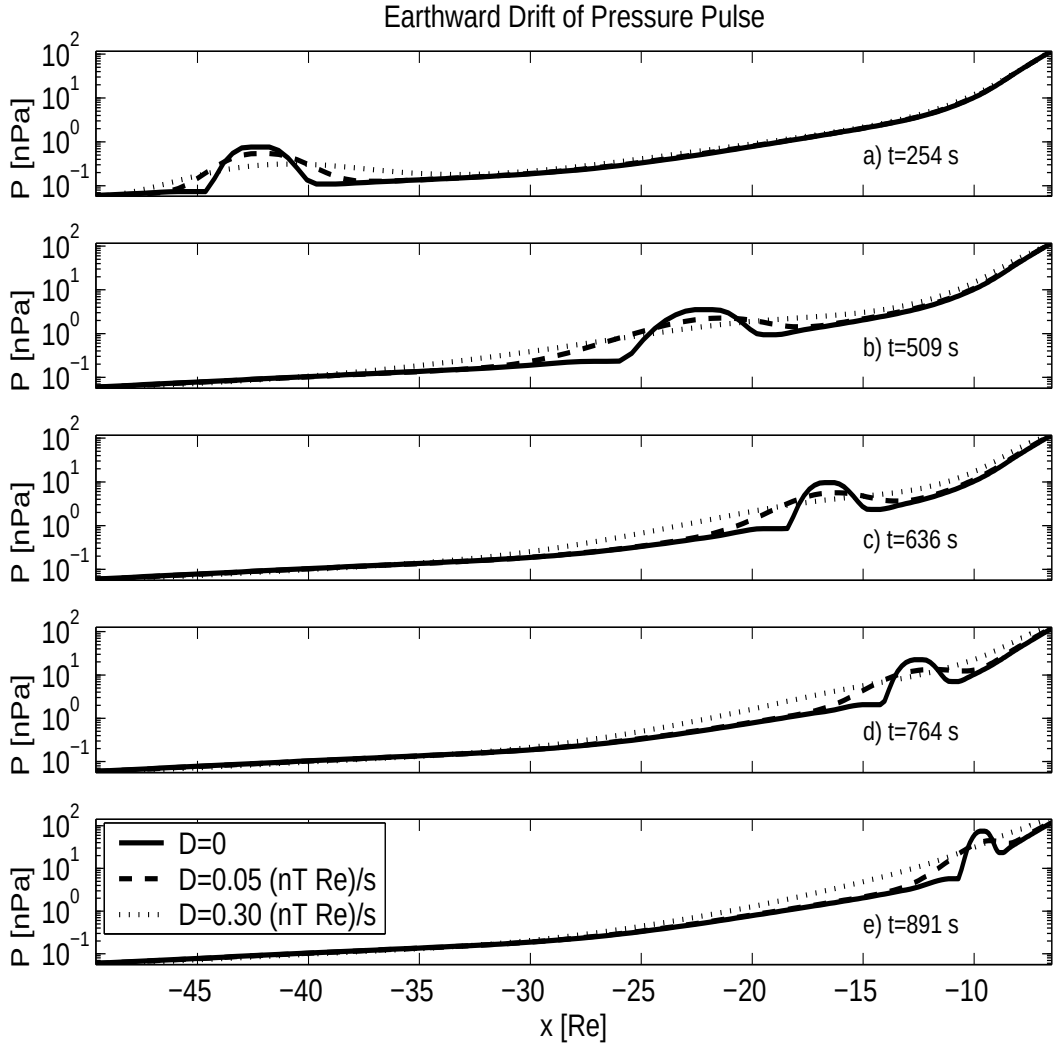

Figure 6.10: Earthward transport of pressure given by Eq. (6.40) due to $\mathbf{E}\times\mathbf{B}$ drift with $E_y = 1$ mV/m, with tailward source oscillating through a half period of a sine wave. The source term is given by Eq. (6.45) with $\tau = 60$ seconds and $p_{\text{source}} = 1nPa/s$. Panels (a) through (e) show the pressure profile at different times. Each panel shows three different curves corresponding to different values of the turbulent diffusivity D_Ψ. Due to the decrease in the $\mathbf{E}\times\mathbf{B}$ velocity, the pressure piles up in the tail/dipole transition region.

6.8 Conclusions

We have derived the kinetic equations for the low-frequency compressional/rarefraction drift-waves in the near geosynchronous orbit (NGO) region. These waves are thought to be responsible for the shorter period (30 seconds) magnetic oscillations reported in the CRRES data (see Maynard *et al.* (1996) [131]). At an early stage before the dipolarization event, there are longer period (60-90s) predominantly δE_y oscillations that are interpreted as the drift-Alfvén ballooning modes. The 30s magnetic oscillations that occur immediately following dipolarization are consistent with the properties of the drift compressional waves described herein. Sigsbee *et al.* (2002) [169] reported that strong compressional fluctuations of the magnetic field in the range of 7 to 30 mHz were observed at the distance of -10 to -13 R_E during the April 26, 1995 substorm. At Geotail the timing they reported is that dipolarization and compressional waves occur together and the large Earthward flows are a few minutes later. In the 10 minute interval following the initialization of dipolarization, the B_z (GSM) has large fluctuations ($\delta B_z \sim \langle B_z \rangle$), with $\langle B_z \rangle$ increasing from 5 nT to 20 nT and the total B dropping from 45 nT to 20 nT during the event. The Pi2 band from 7 to 30 mHz (40s to 150s period) is strongly excited during this event.

To understand this low-frequency compressional wave, the complex mirror orbits on the flux tubes need to be considered. To account for these orbits we have introduced matrix operators that act on the electromagnetic fields. We have computed the eigenvalues and eigenfunctions of these operators and

used these to form dispersion relations. We found that an unstable state, due to the $\omega = \overline{\omega}_{Di}$ resonance, can exist for a pressure gradient profile in which the guiding center particle drift is in the ∇B drift direction (Eastward) due to the large $\beta R_c/L_p$ (large β and R_c/L_p). We find that for typical time-averaged magnetic field models, particles do not reverse the direction of the Westward bounce-averaged guiding center drift velocity. In these cases, however, a density gradient that is in the opposite direction to the temperature gradient can support the growth of compressional waves. Theoretically, such an inversion of the density gradient may occur as a transient response to a sharp change in the convective flux of nE_y/B. We have found purely oscillating solutions when the frequency of the oscillation is well below and also well above the bounce-averaged guiding-center drift frequency; these results follow closely with traditional compressional waves.

We have numerically solved the non-local dispersion relation for the $\delta B_{\parallel}(s)$ eigenmodes for frequencies below the ion transit frequency, where the wave-particle resonance is responsible for the instability. We report these growth rates γ, real part of the frequency (ω), and growth per wave period $\gamma/\omega < 1$ as a function of η_i for different positions along the geotail axis, using the Tsyganenko (1996) [188] magnetic field model and a simple constant current magnetic field model to compute the properties of the different flux-tubes as well as the structure of the $\delta B_{\parallel}(s)$ drift compressional eigenmode. We find that the real part of the frequencies that we found correspond to the Pi2 frequency range of a few mHz. We found these magnetic perturbations

to be very strongly ballooning, with the maximum perturbation being at the equatorial plane. Our results for the growth rate reproduce well the stability boundaries determined in the local approximation from the Nyquist analysis for marginal stability. We have also presented approximate formulas for these growth rates for both $\eta_i > 0$ and $\eta_i < 0$.

We have proposed a transport model for the Earthward transport of the pressure distribution function. In this model, it is seen that sharp pressure gradients can form in the dipole/tail transition region from a small pressure oscillation in the deep tail boundary conditions. The maximum steepness of the pressure gradient is limited by the turbulent diffusivity $D_\perp$. We propose that this transient steepening of the pressure gradient could cause particles to reverse the direction of their magnetic drift, which, in turn induces an unstable compressional perturbation. Drift reversal from strong ∇B has been invoked by Li et al. (1998) [119] as the mechanism for the dispersionless injection of energetic electrons.

In this work we have considered modes dominated by $\delta B_\parallel$. When the ambient pressure gradient is steep enough, the coupling to other components of the electromagnetic field increases in importance. The ballooning/interchange mode characterized by a strong E_y perturbation and weak $\delta B_\parallel$ becomes active. The non-local behavior of these other modes and their coupling to the drift-compressional modes requires the extension of this work to the full 3×3 electromagnetic eigenmode equations. This full complex problem will be pursued in a later work.

Previously we found interchange/ballooning modes to be most unstable in the $x = -6$ to $-12R_E$ region [93, 94, 192]. As is well known, the interchange/ballooning modes also have a compressional component, $\delta B_{\parallel}$, due to inhomogeneities of the plasma. There are still two distinct drift modes, the drift interchange/ballooning mode and the compressional drift mode, with the compressional magneto-acoustic drift-waves having a higher frequency than the convective interchange mode [3]. Convective interchange motions of the flux tubes closer to the Earth are stabilized strongly by the energy required to bend the magnetic field, and flux tubes tail-ward of this region were found to be strongly stabilized by plasma compression. In contrast to the convective interchange mode instability, the compressional modes are unstable at high β from the plasma compression. The condition for the compressional modes to be unstable is complex and presented in this work. One mechanism is the ∇B drift reversal. We find the compressional mode is most unstable when the ∇B drift is large and opposite to the curvature drift. In the region Earthward of the transition region, the two drifts are in the same direction, and on the tail-ward side of this region the ∇B drift is in the opposite direction to the curvature drift, though it is not large enough to exhibit drift reversal. In our simulation of the transport of the pressure distribution, it was in this transition region, between dipole-like and tail-like magnetic field configurations, where the steepest gradients were observed. The other mechanism for compressional instability is inverted density and temperature gradients.

In conclusion, the role the compressional drift wave plays may be re-

quired to understand the Pi2 signals associated with substorm dynamics. The mode has some features, such as propagation in the ion diamagnetic direction, in common with the kinetic drift ballooning/interchange mode. The polarization and the stability conditions of the two modes are different as developed and discussed here. Integrated transport codes containing both the effects of the compressional drift modes and the ballooning interchange modes need to be developed to provide a clear interpretation of the complex signatures of observed low-frequency wave signals in the NGO to mid-tail region.

Bibliography

[1] *Basic Plasma Physics I*, chapter 1.4 MHD Description of Plasma. North-Holland Publishing Company, 1983.

[2] *Ideal Magnetohydrodynamics*. Plenum Pub. Corp., 1987.

[3] *Electromagnetic Instabilities in an Inhomogeneous Plasma*. Adam Hilger, 1992.

[4] *Introduction to Plasma Physics*. IOP publishing, 1995.

[5] *Introduction to Space Physics*. Cambridge University Press, 1995.

[6] *Classical Electrodynamics*. John Wiley and Sons, Inc., 1999.

[7] S.-I. Akasofu. The development of the auroral substorm. *Planetary Space Sciences*, 1964.

[8] T. M. Antonsen and B. Lane. Kinetic equations for low frequency instabilities in inhomogeneous plasmas. *Physics of Fluids*, 1980.

[9] T. M. Antonsen, B. Lane, and J. J. Ramos. Variational principle for low-frequency stability of collisionless plasmas. *Physics of Fluids*, 1981.

[10] K. Appert, D. Berger, R. Gruber, and J. Rappaz. A new finite element approach to the normal mode analysis in magnetohydrodynamics. *Journal of Computational Physics*, 1975.

[11] D. N. Baker, S. G. Kanekal, A. J. Klimas, D. Vassiliadis, and T. I. Pulkkinen. Collective phonmena in the inner magnetosphere. *Physics of Plasmas*, 1999.

[12] D. N. Baker and R. L. McPherron. Extreme energetic particle decreases near geostationary orbit: a manifestation of current diversion within the inner plasma sheet. *Journal of Geophysical Research*, 1990.

[13] D. N. Baker, T. I. Pulkkinen, J. Buchner, and A. J. Klimas. Substorms: A global instability of the magnetosphere-ionosphere system. *Journal of Geophysical Research*, 1999.

[14] D.N. Baker, P.R. Higbie, E.W. Hones Jr., and R.D. Belian. High resolution energetic particle measurements at 6.6 r_e, low-energy electron anisotropies and short-term substorm predictions. *Journal of Geophysical Research*, 1978.

[15] D.N. Baker and T. I. Pulkkinen. The earthward edge of the plasma sheet in magnetospheric substorms. In *Magnetospheric Substorms*.

[16] D.N. Baker, T. I. Pulkkinen, V. Angelopoulos, W. Baumjohann, and R. L. McPherron. Neutral line model of substorms: Past results and present view. *Journal of Geophysical Research*, 1996.

[17] I. Bar-On and . Ryaboy. Fast diagonalization of large and dense complex symmetric matrices, with applications to quantum reaction dynamics. *SIAM J. Sci. Comput.*, 1997.

[18] L. F. Bargatze, D. N. Baker, R. L. McPherron, and E. W. Hones. Magnetospheric impulse response for many levels of geomagnetic activity. *Journal of Geophysical Research*, 1985.

[19] N. Bekki. Torus knot in a dissipative fifth-order system. *Journal of the Physical Society of Japan*, 2000.

[20] N. Bekki and T. Karakisawa. Bifurcations from periodic solution in a simplified model of two dimensional magnetoconvection. *Physics of Plasmas*, 1995.

[21] A. D. Beklemishev. Nonlinear saturation of ideal interchange modes in a sheared magnetic field. *Physics of Fluids*, 1991.

[22] I. B. Bernstein, E. A. Frieman, M.D. Kruskal, and R. M. Kulsrud. An energy principle for hydromagnetic stability problems. *Proceedings of the Royal Society of London*, 1958.

[23] A. Bhattacharjee, Z. W. Ma, and Xiaogang Wang. Dynamics of thin current sheets and their disruption by ballooning instabilities: A mechanism for magnetospheric substorms. *Physics of Plasmas*, 1998.

[24] I. Birol and A. Hacinliyan. Signs and approximate magnitudes of lyapunov exponents in continuous time dynamical systems. *Journal of Mathematical Physics*, 1997.

[25] Joan Bolker. *Writing your dissertation in fifteen minutes a day.* Henry Holt and Company, Inc., 1998.

[26] J. P. Boris and D. L. Book. Flux-corrected transport. i. shasta, a fluid transport algorithm that works. *Journal of Computational Physics*, 1973.

[27] J. E. Borovsky, M. F. Thomsen, and R. C. Elphic. The driving of the plasma sheet by the solar wind. *Journal of Geophysical Research*, 1998.

[28] A. J. Brizard. Nonlinear bounce-gyrocenter hamiltonian dynamics in general magnetic field geometry. *Physics of Plasmas*, 2000.

[29] A. J. Brizard and A. A. Chan. Relativistic bounce-averaged quasi-linear diffusion equation for low-frequency electromagnetic fluctuations. *Physics of Plasmas*, 2001.

[30] D. Brock and W. Horton. Toroidal drift-wave fluctuations driven by ion pressure gradients. *Plasma Physics*, 1982.

[31] P. Cargo and G. Gallice. Roe matrices for ideal mhd and systematic construction of roe matrices for systemsof conservation laws. *Journal of Computational Physics*, 1997.

[32] J. R. Cary and R. G. Littlejohn. Noncanonical hamiltonian mechanics and its application to magnetic field line flow. *Annals of Physics*, 1983.

[33] C. Cattell, I. Roth, and M. Linton. The effects of low frequency waves on ion trajectories in the earth's magnetotail. *Geophysicl Research Letters*, 1995.

[34] A. A. Chan. Noncanonical hamiltonian methods for particle motion in magnetospheric hydromagnetic waves. *Journal of Geophysical Research*, 1998.

[35] A. A. Chan, M. Xia, and L. Chen. Anisotropic alfven-ballooning modes in earth's magnetosphere. *Journal of Geophysical Research*, 1994.

[36] C. X. Chen and R. A. Wolf. Interpretation of high-speed flows in the plasma sheet. *Journal of Geophysical Research*, 1993.

[37] L. Chen and A. Hasegawa. Kinetic theory of geomagnetic pulsations 1. internal excitations by energetic particles. *Journal of Geophysical Research*, 1991.

[38] L. Chen and A. Hasegawa. Kinetic theory of geomagnetic pulsations 2. ion flux modulations by transverse waves. *Journal of Geophysical Research*, 1994.

[39] L.-J. Chen, D. Larson, R. P. Lin, M. McCarthy, and G. Parks. Multicomponent plasma distributions in the tail current sheet associated with substorms. *Geophysical Research Letters*, 2000.

[40] L.-J. Chen, G. K. Parks, M. McCarthy, D. Larson, and R. P. Lin. Kinetic properties of bursty bulk flow events. *Geophysical Research Letters*, 2000.

[41] C. Z. Cheng. Mangetospheric equilibrium with anisotropic pressure. *Journal of Geophysical Research*, 1992.

[42] C. Z. Cheng. Three-dimensional magnetospheric equilibrium with isotropic pressure. *Geophysical Research Letters*, 1995.

[43] C. Z. Cheng and C. S. Lin. Eigenmode analysis of compressional waves in the magnetosphere. *Geophysical Research Letters*, 1987.

[44] C. Z. Cheng and A. T. Y. Lui. Kinetic ballooning instability for substorm onset and current disruption observed by ampte/cce. *Geophysical Research Letters*, 1998.

[45] B. V. Chirikov. A universal instability of many-dimensional oscillator systems. *Physics Reports*, 1979.

[46] J. W. Connor, R.J. Hastie, and J.B. Taylor. *Proc. R. Soc. London, Ser. A*, 1979.

[47] B. Coppi. Topology of ballooning modes. *Physical Review Letters*, 1977.

[48] L. N. Da Costa, E. Knobloch, and N. O. Weiss. Oscillations in double-diffusive convection. *Journal of Fluid Mechanics*, 1981.

[49] N. U. Crooker, G. L. Siscoe, M. A. Doyle, and W. J. Burke. Ring coupling model: implications for the ground state of the magnetosphere. *Journal of Geophysical Research*, 1984.

[50] J. W. Van Dam, M. N. Rosenbluth, and Y. C. Lee. A generalized kinetic energy principle. *Physics of Fluids*, 1982.

[51] R. C. Davidson. Electrostatic shielding of a test charge in a non-neutral plasma. *Journal of Plasma Physics*, 1971.

[52] R. C. Davidson and N. A. Krall. Vlasov equilibria and stability of an electron gas. *The Physics of Fluids*, 1970.

[53] A. L. Clua de Gonzalez and W. D. Gonzalez. Analytical study of the energy rate balance equation for the magnetospheric sotrm-ring current. *Annales Geophysicae*, 1998.

[54] D. del Castillo-Negrete. Chaotic transport in zonal flows in analogous geophysical and plasma systems. *Physics of Plasmas*, 2000.

[55] D. C. Delcourt, J.-A. Sauvaud, R. F. Martin Jr., and T. E. Moore. On the adiabatic precipitation of ions from the near-earth plasma sheet. *Journal of Geophysical Research*, 1996.

[56] J. DeLucia, S. C. Jardin, and A. M. M. Todd. An iterative metric method for solving the inverse tokamak equilibrium problem. *Journal of Computational Physics*, 1980.

[57] R. L. Dewar and A. H. Glasser. *Phys. Fluids*, 1983.

[58] J. Q. Dong, P. N. Guzdar, and Y. C. Lee. Finite beta effects on ion temperature gradient driven modes. *Physics of Fluids*, 1987.

[59] R. E. Ergun, Y.-J. Su, L. Andersson, C. W. Carlson, J. P. McFadden, F. S. Mozer, D. L. Newman, M. V. Goldman, and R. J. Strangeway.

Direct observation of localized parallel electric fields in a space plasma. *Physical Review Letters*, 2001.

[60] G. M. Erickson, N. C. Maynard, W. J. Burke, G. R. Wilson, and M. A. Heinemann. Electromagnetics of substorm onsets in the near-geosynchronous plasma sheet. *J. Geophys. Res.*, 2000.

[61] G. M. Erickson and R. A. Wolf. Is steady convection possible in the earth's magnetotail. *Geophysical Research Letters*, 1980.

[62] R. D. Elphinstone et al. Observations in the vicinity of substorm onset: Implications for the substorm process. *Journal of Geophysical Research*, 1995.

[63] M. O. Fillingim, G. K. Parks, L. J. Chen, M. Brittnacher, G. A. Germany, J. F. Spann, D. Larson, and R. P. Lin. Coincident polar/uvi and wind observations of pseudobreakups. *Geophysical Research Letters*, 2000.

[64] L. A. Frank, W. R. Paterson, J. B. Sigwarth, and S. Kokubun. Observations of magnetic field dipolarization during auroral substorm onset. *Journal of Geophysical Research*, 2000.

[65] L. A. Frank, W. R. Paterson, J. B. Sigwarth, and T. Mukai. Observations of plasma sheet dynamics earthward of the onset region with the geotail spacecraft. *Journal of Geophysical Research*, 2001.

[66] L. A. Frank and J. B. Sigwarth. Findings concerning the positions of substorm onsets with auroral images from the polar spacecraft. *Journal of Geophysical Research*, 2000.

[67] L. A. Frank, J. B. Sigwarth, and W. R. Paterson. High-resolution global images of earth's auroras during substorms. In *Substorms-4*.

[68] J. L. Friedman and B. F. Schutz. Lagrangian perturbation theory of nonrelativistic fluids. *The Astrophysical Journal*, 1978.

[69] J. L. Friedman and B. F. Schutz. Secular instability of rotating newtonian stars. *The Astophysical Journal*, 1978.

[70] Z. Gao, J. Q. Dong, G. J. Liu, and C. T. Ying. Study of electromagnetic instabilitied driven by ion temperature gradient and parallel sheared flows in high-β plasmas. *Physics of Plasmas*, 2001.

[71] T. Garner. Personal Communication.

[72] T. Garner. Turbulent transport as a possible solution to the pressure balance inconsistency.

[73] J. M. Greene and M. S. Chance. The second region of stability against ballooning modes. *Nuclear Fusion*, 1981.

[74] J. M. Greene and J. L. Johnson. Stability criterion for arbitrary hydromagnetic equilibria. *The Physics of Fluids*.

[75] P. N. Guzdar, R. G. Kleva, A. Das, and P. K. Kaw. Zonal flow and zonal magnetic field generation by finite β drift waves: a theory for low to high transitions in tokamaks. *Physical Review Letters*, 2001.

[76] E. Hameiri, P. Laurence, and M. Mond. The ballooning instability in space plasmas. *Journal of Geophysical Research*, 1991.

[77] G. W. Hammett and W. M. Tang. Kinetic and resistive effects on interchange instabilities for a cylindrical model spheromak. *Nuclear Fusion*, 1983.

[78] M. A. Hapgood. Space physics coordinate transformations: A user guide. *Planet. Spac. Sci.*, 1991.

[79] A. Hasegawa. Drift mirror instability in the magnetosphere. *The Physics of Fluids*, 1969.

[80] C. C. Hegna and S. R. Hudson. Loss of second-ballooning stability in three-dimensional equilibria. *Physical Review Letters*, 2001.

[81] B.-G. Hong, W. Horton, and D.-I. Choi. Drift-alfven kinetic stability theory in the ballooning mode approximation. *Physics of Fluids*, 1989.

[82] B. G. Hong, W. Horton, and D.-I. Choi. Pressure gradient-driven modes in finite beta toroidal plasmas. *Plasma Physics and Controlled Fusion*, 1989.

[83] W. Horton. Destabilization and quasilinear evolution of the ion flute mode. *The Physics of Fluids*, 1969.

[84] W. Horton. Drift modes in axisymmetric tandem mirrors. *The Physics of Fluids*, 1981.

[85] W. Horton. Chaos and structures in the magnetosphere. *Physics Reports*, 1997.

[86] W. Horton, L. Cheung, J.Y. Kim, and T. Tajima. Self-consistent plasma pressure tensors from the tsyganenko magnetic field model. *Journal of Geophysical Research*, 1993.

[87] W. Horton, D-I. Choi, and B.-G. Hong. Electromagnetic drift modes driven by pressure gradients in tokamaks. *Physics of Fluids*, 1983.

[88] W. Horton, R. D. Estes, and D. Biskamp. Fluid simulation of ion pressure gradient driven drift modes. *Plasma Physics*, 1980.

[89] W. Horton, B. G. Hong, and W. M. Tang. Toroidal electron temperature gradient driven drift modes. *Physics of Fluids*, 1988.

[90] W. Horton and M. Pekker. Magnetic energy storage and the night-side magnetosphere-ionosphere coupling. *Geophysical Research Letters*, 1998.

[91] W. Horton, J. E. Sedlak, Duk-In Choi, and B. G. Hong. Kinetic theory of the electromagnetic drift modes driven by pressure gradients. *Phys. Fluids*, 1985.

[92] W. Horton, R. S. Weigel, and J. C. Sprott. Chaos and the limits of predictability for the solar-wind-driven magnetosphere-ionosphere system. *Physics of Plasmas*, 2001.

[93] W. Horton, H. V. Wong, and J. W. Van Dam. Substorm trigger conditions. *Journal of Geophysical Research*, 1999.

[94] W. Horton, H. V. Wong, J. W. Van Dam, and C. Crabtree. Stability properties of high-pressure geotail flux tubes. *Journal of Geophysical Research*, 2001.

[95] W. Horton, H. Vernon Wong, R. Weigel, and I. Doxas. Interchange trigger for substorms in a nonlinear dynamics model. *Physics of Space Plasmas*, 1998.

[96] O. A. Hurricane. Mhd ballooning stability of a sheared plasma sheet. *Journal of Geophysical Research*, 1997.

[97] O. A. Hurricane, B. H. Fong, and S. C. Cowley. *Physics of Plasmas*, 1997.

[98] J. L. Johnson, C. R. Oberman, R. M. Kulsrud, and E. A Frieman. Some stable hydromagnetic equilibria. *The Physics of Fluids*, 1958.

[99] J. R. Kan, W. Sun, and W. Baumjohann. A hybrid equation of state for the quasi-static central plasma sheet. *Geophysical Research Letters*, 1992.

[100] T. Karakisawa, N. Bekki, and I. Shimada. Saddle-node bifurcation without reinjection process in the temporal intermittency. *Physics Letters A*, 1998.

[101] L. Kepko and M. Kivelson. Generation of pi2 pulsations by bursty bulk flows. *Journal of Geophysical Research*, 1999.

[102] L. Kepko, M. G. Kivelson, and K. Yumoto. Flow bursts, braking, and pi2 pulsations. *Journal of Geophysical Research*, 2001.

[103] J. Kesner. Stability of electrostatic modes in a levitated dipole. *Physics of Plasmas*, 1997.

[104] J. Kesner. Interchange modes in a collisional plasma. *Physics of Plasmas*, 2000.

[105] J. Kesner, A. N. Simakov, D. T. Garnier, P. J. Catto, R. J. Hastie, S. I. Krasheninnikov, M. E. Mauel, T. Sunn Pedersen, and J. J. Ramos. Dipole equilibrium and stability. *Nuclear Fusion*, 2001.

[106] J. Y. Kim, Y. Kishimoto, W. Horton, and T. Tajima. Kinetic resonance damping rate of toroidal ion temperature gradient mode. *Physics of Plasmas*, 1994.

[107] P. Kloucek and F. R. Toffoletto. The three dimensional non-conforming finite element solution of the chapman-ferraro problem. *Journal of Computational Physics*, 1999.

[108] E. Knobloch, N. O. Weiss, and L. N. Da Costa. Oscillatory and steady convection in a magnetic field. *Journal of Fluid Mechanics*, 1981.

[109] S. Kokubun and R.L. McPherron. Substorm signatures at synchronous altitude. *Journal of Geophysical Research*, 1981.

[110] Axel Konies. A kinetic magnetohydrodynamic energy integral in three dimensional geometry. *Physics of Plasmas*, 2000.

[111] M. D. Kruskal and R. M. Kulsrud. Equilibrium of a magnetically confined plasma in a toroid. *The PHysics of Fluids*, 1958.

[112] M. D. Kruskal and C. R. Oberman. On the stability of plasma in static equilibrium. *The Physics of Fluids*, 1958.

[113] D.-Y. Lee. Ballooning instability in the tail plasma sheet. *Geophysical Research Letters*, 1998.

[114] D.-Y. Lee. Effect of plasma compression on plasma sheet stability. *Geophysical Research Letters*, 1999.

[115] D.-Y. Lee and K.W. Min. On the possibility of the mhd-ballooning instability in the magnetotail-like field reversal. *Journal of Geophysical Research*, 1996.

[116] D.-Y. Lee and R. A. Wolf. Is the earth's magnetotail balloon unstable? *Journal of Geophysical Research*, 1992.

[117] W. W. Lee. Gyrokinetic approach in particle simulation. *Physics of Fluids*, 1983.

[118] J. Li, Y. Kishimoto, and T. Tuda. Separate structure of two branches of sheared slab η_i mode and effects of plasma rotation shear in weak magnetic shear region. *Plasma Physics and Controlled Fusion*, 2000.

[119] X. Li, D. N. Baker, M. Temerin, G. Reeves, and R. Belian. Simulation of dispersionless injections and drift echoes of energetic electrons associated with substorms. *Geophy. Res. Lett.*, 198.

[120] R. G. Littlejohn. Variational principles of guiding center motion. *Journal of Plasma Physics*, 1983.

[121] C. S. Liu. Low-frequency drift instabilities of the ring current belt. *Journal of Geophysical Research*, 1970.

[122] R. E. Lopez and A. T. Y. Lui. A multi-sattelite case study of the expansion of a substorm current wedge in the near-earth magnetotail. *J. Geophys. Res.*, 1990.

[123] A. T. Y. Lui. Extended consideration of a synthesis model for magnetic substorms. In *Magnetospheric Substorms*.

[124] A. T. Y. Lui and D. C. Hamilton. Radial profiles of quiet time magnetospheric parameters. *Journal of Geophysical Research*, 1992.

[125] A. T. Y. Lui, K. Liou, P. T. Newell, C.-I. Meng, S.-I. Ohtani, T. Ogino, and S. Kokubun. Plasma and magnetic flux transport associated with auroral breakups. *Geophysical Research Letters*, 1998.

[126] L. R. Lyons. A new theory for magnetospheric substorms. *Journal of Geophysical Research*, 1995.

[127] R. L. Lysak. Feedback instability of the ionospheric resonant cavity. *Journal of Geophysical Research*, 1991.

[128] R. L. Lysak. Generalized model of the ionospheric alfven resonator. *Auroral Plasma Dynamics*, 1993.

[129] R. L. Lysak and W. Lotko. On the kinetic dispersion relation for shear alfven waves. *Journal of Geophysical Research*, 1996.

[130] M. E. Mauel, D. T. Garnier, T. Sunn Pedersen, P. J. Catto, R. J. Hastie, J. Kesner, J. J. Ramos, A. N. Simakov, and S. I. Krasheninnikov. Dipole equilibrium and stability. In *18th IAEA Fusion Energy Conference*.

[131] N.C. Maynard, W.J. Burke, E.M. Basinska, G.M. Erickson, W.J. Hughes, H.J. Singer, A.G. Yahnin, D.A. Hardy, and F.S. Mozer. Dynamics of the inner magnetosphere near times of substorm onsets. *Journal of Geophysical Researc*, 1996.

[132] C. E. McIlwain. Coordinates for mapping the distribution of magnetically trapped particles. *Journal of Geophyiscal Research*, 1961.

[133] R. L. McPherron. Physical processes producing magnetospheric substorms and magnetic storms. In *Geomagnetism*.

[134] A. Miura. Conditions for the validity of the incompressible assumption for the ballooning instability in the long-thin magnetospheric equilibrium. *Journal of Geophysical Research*, 2000.

[135] A. Miura, S. Ohtani, and T. Tamao. Ballooning instability and structure of diamagnetic hydromagnetic waves in a model magnetosphere. *Journal of Geophysical Research*, 1989.

[136] T.S. Molinsky, W.E. Feero, and B.L. Damsky. "shielding grids from solar storms. *IEEE Spectrum*, 2000.

[137] P. J. Morrison and R. D. Hazeltine. Hamiltonian formulation of reduced magnetohydrodynamics. *Physics of Fluids*, 1984.

[138] T. Nagai, M. Fujimoto, Y. Saito, S. Machida, T. Terasawa, R. Nakamura, T. Yamamoto, T. Mukai, A. Nishida, and S. Kokubun. Structure and dynamics of magnetic reconnection for substorm onsets with geotail observations. *J. Geophys. Res.*, 1998.

[139] K.-I. Nishikawa. Global particle simulation study of substorm onset and particle acceleration. *Space Science Reviews*, 2001.

[140] K.-I. Nishikawa and S.-I. Ohtani. Global particle simulation for a space weather model: present and future. *IEEE Transactions on Plasma Science*, 2000.

[141] T. Ohkawa and M. Yoshikawa. Experimental observation and theoretical interpretation of low-frequency interchange instability in "average mininum-b" configurations. *Physical Review Letters*, 1967.

[142] S. Ohtani, A. T. Y. Lui, K. Takahashi, D. G. Mitchell, and T. Sarris. Ion dynamics and tail current intensification prior to dipolarization: The june 1, 1985, event. *Journal of Geophysical Research*, 2000.

[143] N. Padhye and W. Horton. Alfven-wave particle interaction in finite-dimensional self-consistent field model. *Physics of Plasmas*, 1999.

[144] W. R. Paterson, L. A. Frank, S. Kokubun, and T. Yamamoto. Geotail survey of ion flow in the plasma sheet: Observations between 10 and 50 re. *J. Geophys. Res.*, 1998.

[145] P. Perreault and S.-I. Akasofu. A study of geomagnetic storms. *Geophys. J. R. astr. Soc.*, 1978.

[146] D. Pfirsch and R. N. Sudan. Nonlinear ideal magnetohydrodynamics instabilities. *Physics of Fluids*, 1993.

[147] D. H. Pontius and R. A. Wolf. Transient flux tubes in the terrestrial magnetosphere. *Geophysical Research Letters*, 1990.

[148] P. L. Pritchett and F. V. Coroniti. Drift ballooning mode in a kinetic model of the near-earth plasma sheet. *Journal of Geophysical Research*, 1999.

[149] M. R. E. Proctor and N. O. Weiss. Magnetoconvection. *Reports on Progress on Physics*, 1982.

[150] Z. Y. Pu, K. B. Kang, A. Korth, S. Y. Fu, Q. G. Zong, Z. X. Chen, M. H. Hong, Z. X. Liu, C. G. Mouikis, R. W. H. Friedel, and T. Pulkkinen. Ballooning instability in the presence of a plasma flow: a synthesis of tail reconnection and current disruption models for the initiation of substorms. *Journal of Geophysical Research*, 1999.

[151] T. I. Pulkkinen and M. Wiltberger. Thin current sheet evolution as seen in observations and empirical models and mhd simulations. *Geophysical Research Letters*, 2000.

[152] T.I. Pulkkinen, D.N. Baker, D.H. Fairfield, R.J. Pellinen, J.S. Murphree, R.D. Elphinstone, R.L. McPherron, J.F. Fennell, R.E. Lopez, and T.Nagai. Modelling the growth phase of a substorm using the tsyganenko model and multi-spacecraft observations: Cdaw-9. *Geophysical Research Letters*, 1991.

[153] H. Qin, W. M. Tang, and W. W. Lee. Gyrocenter-gauge kinetic theory. *Physics of Plasmas*, 2000.

[154] S. C. Reddy, P. J. Schmid, and D. S. Henningson. Pseudospectra of the orr-sommerfeld operator. *Siam Journal of Applied Mathematics*, 1993.

[155] M. N. Rosenbluth. Magnetic trapped-particle modes. *Physical Review Letters*, 1981.

[156] M. N. Rosenbluth and C. L. Longmire. Stability of plasmas confined by magnetic fields. *Annals of Physics*, 1957.

[157] M. N. Rosenbluth and N. Rostoker. Theoretical structure of plasma equations. *The Physics of Fluids*, 1959.

[158] A. Roux, S. Perraut, P. Robert, A. Morane, A. Pedersen, A. Korth, G. Kremser, B. Aparicio, D. Rodgers, and R. Pellinen. Plasma sheet instability related to the westward traveling surge. *Journal of Geophysical Research*, 1991.

[159] C.T. Russell and R.L. McPherron. The magnetotail ans substorms. *Space Science Reviews*, 1973.

[160] P. H. Rutherford and E. A. Frieman. Drift instabilities in general magnetic field configurations. *The Physics of Fluids*, 1969.

[161] B. Saltzman. Finite amplitude free convection as an initial-value problem -i. *Journal of the Atmospheric Sciences*, 1962.

[162] J. C. Samson. Mapping substorm intensifications from the ionosphere to the magnetosphere. In *Proceedings of the Second International Conference on Substorms*.

[163] J. C. Samson, L. L. Cogger, and Q. Pao. Observations of field line resonances, auroral arcs, and auroral vortex structures. *Journal of Geophysical Research*, 1996.

[164] T. D. Sauer, J. A Tempkin, and J. A. Yorke. Spurious lyapunov exponents in attractor reconstruction. *Physical review letters*, 1998.

[165] K. Schindler and H. Goldstein. A nonlinear kinetic energy principle for two-dimensional collision-free plasmas. *Physics of Fluids*, 1983.

[166] J. J. Schott, N. G. Kleimenova, J. Bitterly, and O. V. Kozyreva. The strong pc5 geomagnetic pulsations in the initial phase of the great magnetic storm of march 24, 1991. *Earth Planets Space*, 1998.

[167] N. Sckopke. A general relation between the energy of trapped particles and the disturbance field near the earth. *Journal of Geophysical Research*, 1966.

[168] V. A. Sergeev, V. Angelopoulos, J. T. Gosling, C. A. Cattell, and C. T. Russell. Detection of localized, plasma-depleted flux tubes or bubbles in the midtail plasma sheet. *Journal of Geophysical Research*, 1996.

[169] K. Sigsbee, C. A. Cattell, D. Fairfeild, K Tsuruda, and S. Kokubun. Geotail observations of low frequency waves and high speed earthward flows during substorm onsets in the near magnetotail from 10 to 13 re. *J. Geophys. Res.*, 2002.

[170] P. Similon, J.E. Sedlak, D. Stotler, H.L. Berk, W. Horton, and D. Choi. Guiding-center dispersion function. *Journal of Computational Physics*, 1984.

[171] D. J. Southwood and M. G. Kivelson. Charged particle behaviour in low-frequency geomagnetic pulsations 1. transverse waves. *Journal of Geophysical Research*, 1981.

[172] H. E. Spence, M. G. Kivelson, and R. J. Walker. Static magnetic field models consistent with nearly isotropic plasma pressure. *Geophysical Research Letters*, 1987.

[173] H. E. Spence, M. G. Kivelson, and R. J. Walker. Magnetospheric plasma pressures in the midnight meridian: observations from 2.5 to 35 r_e. *Journal of Geophysical Research*, 1989.

[174] D. P. Stern and N. A. Tsyganenko. Uses and limitations of the tsyganenko magnetic field model. *Eos, Transactions, American Geophysical Union*, 1992.

[175] H. R. Strauss. Nonlinear, three-dimensional magnetohydrodynamics of noncircular tokamaks. *The Physics of Fluids*, 1976.

[176] H. R. Strauss. Dynamics of high β tokamaks. *The Physics of Fluids*, 1977.

[177] H. Sugama. Gyrokinetic field theory. *Physics of Plasmas*, 2000.

[178] H. Sugama, T.-H. Watanabe, and W. Horton. Collisionless kinetic-fluid closure and its application to the three-mode ion temperature gradient driven system. *Physics of Plasmas*, 2001.

[179] P. N. Swarztrauber. Symmetric ffts. *Mathematics of Computation*, 1986.

[180] T. Takeda, Y. Shimomura, M. Ohta, and M. Yoshikawa. Numerical analysis of magnetohydrodynamics by the finite element method. *Physics of Fluids*, 1972.

[181] P. Terry, W. Andersen, and W. Horton. Kinetic effects on the toroidal ion pressure gradient drift mode. *Nuclear Fusion*, 1982.

[182] P. W. Terry. Suppression of turbulence and transport by sheared flow. *Reviews of Modern Physics*, 2000.

[183] J.-L. Thiffeault and P. J. Morrison. Classification and casimir invariants of lie-poisson brackets. *Physica D*, 2000.

[184] N. A. Tsyganenko. Global quantitative models of the geomagnetic field in the cislunar magnetosphere for different disturbance levels. *Planetary and Space Sciences*, 1987.

[185] N. A. Tsyganenko. Modeling the earth's magnetospheric magnetic field confined within a realistic magnetopause. *Journal of Geophysical Research*, 1995.

[186] N. A. Tsyganenko. An empirical model of the substorm current wedge. *Journal of Geophysical Research*, 1997.

[187] N. A. Tsyganenko. Solar wind control of the tail lobe magnetic field as deduced from geotail, ampte/irm, and isee 2 data. *Journal of Geophysical Research*, 2000.

[188] N. A. Tsyganenko and D. P. Stern. Modeling the global magnetic field of the large-scale birkeland current systems. *Journal of Geophysical Research*, 1996.

[189] N. A. Tsyganenko and A. V. Usmanov. Determination of the magnetospheric current system parameters and development of experimental geomagnetic field models based on data from imp and heos satellites. *Planetary and Space Sciences*, 1982.

[190] G. Vetoulis and L. Chen. Kinetic theory of geomagnetic pulsations 3. global analysis of drift alfven-ballooning modes. *Journal of Geophysical Research*, 1996.

[191] S. Weinberg. Eikonal method in magnetohydrodynamics. *The Physical Review*, 1962.

[192] H. Vernon Wong, W. Horton, J. W. Van Dam, and C. Crabtree. Low frequency stability of geotail plasma. *Physics of Plasmas*, 2001.

[193] S. Zaharia and C.Z. Cheng. Physical limitations of empirical field models: force balance and plasma pressure.

[194] X. Zhu and M. G. Kivelson. Compressional ulf waves in the outer magnetosphere: 2. a case study of pc 5 type wave activity. *Journal of Geophysical Research*, 1994.

[195] S. M. Zoldi. Unstable periodic orbit analysis of histograms of chaotic time series. *Physical Review Letters*, 1998.

Index

Vita

Christopher Eugene Crabtree was born in Stillwater, Oklahoma on March 4, 1975, the son of Larry and Annie Crabtree. He graduated summa cum laude from Langham Creek High School in Houston, Texas in May of 1993.

In August of 1993 he began his undergraduate studies at Washington University in Saint Louis. He earned a Bachelor of Arts degree in Physics with honors in May of 1997 from Washington University in Saint Louis by completing a thesis on "Position Sensitive CdZnTe X-ray Detectors" under the supervision of Dr. Paul Hink.

He began his graduate studies at the University of Texas at Austin in September of 1997. In January of 1998 he began working with Professor Wendell Horton in the Institute for Fusion Studies, who served as his dissertation advisor.

In June of 2000 he married Kristine Amy Morong in Rochester New Hampshire. Kristine was born December 5, 1974 in Durham, New Hampshire.

Permanent address: 21911 Woodland Heights Lane
Spring, TX 77373

This dissertation was typeset with LaTeX[†] by the author.

[†]LaTeX is a document preparation system developed by Leslie Lamport as a special

version of Donald Knuth's TEX Program.